Title
A Transfer Function Model for Deformation Hazard Analysis of Earthen Dams

Author
Hale, Christina Denissen

Publication Date
2019

Peer reviewed|Thesis/dissertation

A Transfer Function Model for Deformation Hazard Analysis of Earthen Dams

By

Christina Denissen Hale

A dissertation submitted in partial satisfaction of the

requirements for the degree of

Doctor of Philosophy

in

Engineering – Civil and Environmental Engineering

in the

Graduate Division

of the

University of California, Berkeley

Committee in charge:

Professor Jonathan Bray, Chair
Professor Nicholas Sitar
Professor Douglas Dreger

Fall 2019

Abstract

A Transfer Function Model for Deformation Hazard Analysis of Earthen Dams

by

Christina Denissen Hale

Doctor of Philosophy in Engineering – Civil and Environmental Engineering

University of California, Berkeley

Professor Jonathan Bray, Chair

Dynamic analysis of earthen dams is performed to assess the seismic stability and vulnerability of dams during earthquakes, and a useful engineering demand parameter for this assessment is the shear-induced deformation of the dam. Although deformation assessments have historically been based on deterministic approaches, it is possible to combine the seismic hazard and dam response to compute the probabilistic deformation hazard of the dam. A significant challenge to quantifying probabilistic deformation hazard for an earthen dam is the need to perform hundreds of dynamic analyses to capture the response of the dam across the full range of ground motion intensities. When probabilistic deformation hazard assessments are used to prioritize resources for a portfolio of dams, there is the additional need to carry out the analyses with a consistent methodology that provides a basis for comparisons between dams. The objective of this research is to develop a simplified method that can be used to estimate shear-induced deformations with a large suite of ground motions, for the purpose of performing probabilistic deformation hazard assessments for earthen dams in a consistent manner.

The proposed methodology involves estimating the transfer function for a potential sliding mass of an earthen dam, which is applied to a user-defined input ground motion to estimate the average acceleration time history of the sliding mass and calculate a shear-induced deformation. The estimated transfer functions are defined at all frequencies and have a physical basis that captures the key mechanisms through which nonlinearity affects soil behavior, including dam period shift and damping increase. The methodology accommodates the entire time history of the ground motion, allowing the user to take advantage of available seismic hazard characterization through the use of site-specific ground motions. The proposed method is utilized to develop a transfer-function model, which represents one implementation of the methodology for a given set of assumptions about the characteristics of the earthen dam. The developed transfer-function model is based on a synthetic dataset generated by performing equivalent-linear dynamic analyses on two-dimensional finite element models of representative earthen dams. The shift in dam period and increase in damping observed in the modeled transfer functions is controlled by the shear-modulus reduction and material damping curves employed in the dynamic analyses, and adjustments can be made to the transfer-function model for alternative nonlinear behavior.

Implementation of the transfer-function model is demonstrated through two case histories where the estimated deformations from the model are compared with the observed shear-induced deformations at Austrian and Lexington Dams during the Loma Prieta earthquake. The analyses indicate that the estimated deformations are not only sensitive to the record chosen to represent the ground motions at the site, but also the azimuth of the input ground motion. The natural period of the sliding mass, represented in the model by the period corresponding to the peak of the transfer function, also has a large impact on the calculated deformations. Implementation of the transfer-function model in a probabilistic framework is then demonstrated for a hypothetical dam in the Sierra Mountain Region of California. The results from a site-specific probabilistic seismic hazard analysis are used to capture the expected ground motions at the dam site, the transfer-function model is used to perform incremental dynamic analyses for the dam, and the seismic hazard results are combined with the dynamic analyses results to compute probabilistic deformation hazard curves. Epistemic uncertainty in the deformation hazard is presented through alternative deformation hazard curves that reflect uncertainties in the seismic hazard and dam response. Epistemic uncertainty in the seismic hazard, which is characterized by different fractile hazard curves, is a significant contributor to the uncertainty in the deformation hazard. The nonlinear behavior of the transfer function model and yield coefficient of the sliding mass also contribute to the uncertainty in deformation hazard.

To Matt,

for every encouraging word
and supportive action.

TABLE OF CONTENTS

ACKNOWLEDGMENTS

I would like to express my sincere gratitude to my advisor, Professor Norm Abrahamson, for his teaching and guidance throughout the course of this work. He agreed to work with me when I decided to come back to school after five years of working, and to say I was a little rusty on integrals and statistics is kind. I have never met someone who can explain a concept in so many different ways, and his dedication to another's learning is inspiring. The completion of this dissertation would not have been possible without his support and I am grateful for his academic and professional guidance over the past five years.

I am also grateful to my committee members and professors at UC Berkeley: Professors Jonathan Bray, Nicholas Sitar, and Douglas Dreger. Professor Bray's Geotechnical Earthquake Engineering course was critical to my understanding of nonlinear soil behavior and provided a solid foundation for this research. His enthusiasm for subjects at the intersection of earthquakes and soil mechanics came through in every 50-minute energy-packed lecture, and I will forever remember the lecture where he acted out sand boil ejecta. It was through Professor Sitar's Engineering Geology course that I gained an appreciation for the complex geology of the San Francisco Bay Area and the influence of geologic origin on the engineering characteristics of soil and rock. I am grateful for the lessons taught in the classroom and the understanding gained in the field while mapping Grizzly Peak in Berkeley and trying to keep up with Professor Sitar on hikes around Tahoe. My very favorite course at UC Berkeley was Professor Dreger's Laboratory in Observational Seismology. While the idea of reproducing a record from an earthquake of your choosing seemed like a simple task on day one, numerical modeling of seismic waveform data proved to be a humbling experience by the end of the semester, and I am grateful for all of the learning that took place along the way.

A sincere thank you to Joseph Sun, Eng Sew Aw, and Albert Kottke of Pacific Gas and Electric Company. Their insights, ideas, and sharing of engineering knowledge and experience were instrumental in this work. I would also like to thank Fenggang Ma of Kleinfelder, Faiz Makdisi of Gannett Fleming, Inc., and Justin Phalen, Nathaniel Wagner, and Jennie Watson-Lamprey of Slate Geotechnical Consultants for their input on this research. A special thanks to Ziad Kteich at École Spéciale des Travaux Publics Paris and Pierre Labbe at Électricité de France for the many fruitful discussions and valuable feedback.

I would like to thank the GeoSystems PhD students on the 4th floor of Davis Hall during my time at Berkeley: Christine Beyzaei, Khaled Chowdhury, Julien Cohen-Waeber, Nella Pierre Louis Desruisseaux, Estéfan Garcia, Michael Gardner, Daniel Hutabarat, Robert Lanzafame, Greg Lavrentiadis, Roberto Luque, Jorge Macedo, Zorana Mijic, John Murphy, Chukwuebuka Nweke, Maggie Parks, and Ezra Setiasabda. I sincerely appreciate the opportunity to work with all of these individuals in a collaborative and supportive learning environment. I would also like to thank the Structural PhD students who took me in on the 5th floor, especially Jiang Jun Lee, Daniel Miller, Simon Kwong, Carlos Arteta, and Arnkjell Løkke.

Funding for this research was provided by Pacific Gas and Electric Company's Geosciences Department and Southern California Edison's Dam Safety Team. Their financial support is greatly appreciated.

1 INTRODUCTION

1.1 Background and Motivation

The potential dam failure modes related to earthquakes and their associated seismic hazard of ground shaking are often the driving design criteria for new dams in earthquake-prone regions, and the primary concern when evaluating the safety of many existing dams that were built before modern design and construction criteria were put in place. To visualize the importance of the seismic safety of dams, Figure 1.1 presents a map of California with historic earthquakes on the left, and a map of California showing the locations of its dams on the right. As seen in the figure, California is an active tectonic region characterized by high seismic hazard. The state is also heavily reliant on the nearly 1500 dams, the vast majority of which are earthen, that play a crucial role in California's water management.

One observation from Figure 1.1 is that many of the dams are built in the same areas where earthquakes occur. This overlap is not unique to California, as there are many seismically active regions worldwide with earthen dams constructed in the vicinity of nearby faults. Dams are often built in active earthquake areas due to favorable topographic features – specifically, long valleys along tectonically active faults in an otherwise young mountain terrain. Other seismically active regions with a large number of dams for irrigation, hydropower, and flood control use include the Pacific Northwest in the United States and Canada, China, India, Turkey, Mexico, Iran, and Japan, among others.

1.1.1 Evolution of Analyses

Many of the dams in California were built at a time when our understanding of tectonics, seismicity, and geotechnical earthquake engineering was in its infancy. Figure 1.2 presents a histogram of the percentage of dams built during various time periods for the state of California along with the time periods for an estimated world dam population. Approximately 40% of the earthen dams in California and 20% of the dams in the world were built before 1950. From 1950 – 1970 there was a major boom in the construction of dams, with many dams erected around the world, and most of the dams in California built in this period. Worldwide, the boom continued into the 1970s and 1980s, while in California the construction of dams slowed. It's worth noting that in 1962, when more than half of the dams worldwide had already been completed, computers were just beginning to be used to analyze soil stresses and the finite-element method had just been developed. The vintage of the California and world dam inventory means that some dams were originally designed with no consideration for the threat of earthquakes, and most were designed based on simplistic assumptions about geomechanics and earthquake forces.

Following the San Fernando earthquake in 1971, where both the Upper San Fernando and Lower San Fernando dams were significantly damaged, the standard of practice for dam seismic evaluation was re-examined and the Division of Safety of Dams (DSOD) in California began a seismic re-evaluation program, resulting in numerous seismic retrofits of dams in the state. Approaches to analyzing earthen dams have evolved in the last 50 years as the state-of-practice for both seismic hazard characterization and geotechnical earthquake engineering has rapidly changed. Dam seismic evaluation has advanced from simplistic static or pseudo-static analysis to performing dynamic analyses with a single ground motion (often the 1940 El Centro record) to performing dynamic analyses for a suite of ground motions specifically selected for the dam site.

1.1.2 Moving Toward Risk Assessment

Moving into the twenty-first century, dam owners and regulators recognized the need to prioritize dam safety evaluations and dam safety improvement investments. With an aging dam inventory and increasing demand on available resources, owners and regulators looked toward risk analysis to provide a systematic method for prioritizing engineering analyses and retrofit or rehabilitation projects for their dams. Owners and regulators have been using risk principles and concepts for years. Evaluations for large dams near population areas are often prioritized over small dams in rural areas, and the cost effectiveness of various remediation measures are often considered to determine which investment provides the most improvement for its value. In recent years, there has been a push toward more formalized, quantitative risk assessments. Similar to the chemical and nuclear industries, which have been using risk analysis methods for decades, the dam industry has recognized the potential benefits of risk analysis and risk management.

For a utility that owns and operates a large number of dams, one of the attractive attributes of keeping updated risk models for all of their dams is the potential to establish a risk reduction program. A risk reduction program is a long-term commitment to develop and update quantitative risk assessments and use those analyses to continually improve the overall risk. Through this framework, a company can act to measurably reduce their risk as they perform analyses, prioritize resources, and invest in improvement projects. As far as the risk from seismic hazard, performing seismic risk assessments in a comprehensive and quantitative manner is a useful tool to improve the quality and consistency of decisions on the seismic safety of dams (Federal Emergency Management Agency, 2005).

Despite the recognition and desire to move toward seismic risk assessments, little progress has been made in the past decade in terms of utilities and regulators quantifying the seismic risk for their portfolio of dams. Current seismic risk practices by owners and regulators of dams involve primarily qualitative categorization, where dams are binned into various performance groups based on readily available information. One of the limitations of the qualitative seismic risk assessment approach is that it typically does not treat uncertainty. Dams are categorized and placed in a box, but the process generally does not allow for an assessment of the uncertainties associated with that categorization. Decisions are then made based on the magnitude of the engineering judgments, without regard for reliability.

1.1.3 Deformation Hazard

Over the past decade, many utilities have developed quantitative Probabilistic Seismic Hazard Assessments (PSHA) for their portfolio of dams. While dam regulations remain largely deterministic in their seismic hazard requirements, PSHA provides a framework in which aleatory variability and epistemic uncertainty can be identified and combined in a rational manner to provide a more complete picture of the seismic hazard at a dam site, and many utilities have adopted this approach. Some utilities in California and the Pacific Northwest have developed internal PSHA processes designed to periodically update the PSHA for their dams with the most recent ground-motion and source characterization models.

Maintaining and improving probabilistic seismic hazard assessments allows utilities to characterize and understand the seismic hazard for their portfolio of dams, but the seismic hazard is only half of the equation when it comes to evaluating dam seismic safety for the purpose of prioritizing resources. Quantification of the dam response is also necessary and must be coupled with the seismic hazard at the site to provide an assessment of the seismic safety of the dam. A common approach is to characterize the seismic safety of the dam by an engineering design parameter. The engineering demand parameter of interest for evaluating the seismic performance of earthen dams is typically the seismically-induced deformation or displacement of the dam. Large deformations are problematic because they could lead to an uncontrolled release of reservoir water during an earthquake. Large deformations without catastrophic failure are also problematic because economic losses from damage can be substantial. The combination of the seismic hazard and the dam response in terms of deformation yields an assessment of the deformation hazard.

The term "seismically-induced deformations" encompasses a number of different mechanisms for movement in earthen dams caused by earthquakes – each playing a part in the seismic safety evaluation. Earthquake shaking that causes liquefaction of the materials within the dam embankment or its foundation is the most critical deformation because of the potential for instability that produces large, rapid movements. Once the primary concern of liquefaction has been addressed, significant deformations attributed to shear and volumetric mechanisms are used to assess the seismic stability of the dam. Movement caused by liquefaction and permanent deformations caused by volumetric compression are not discussed or addressed in this study. The focus of this study is on the shear-induced deformations, which are typically calculated using a Newmark-type procedure (Newmark, 1965).

Numerous studies have performed dynamic analyses and applied the Newmark method to estimate shear-induced deformations for a set of site-specific ground motions applied to a numerical model of an earthen dam. Historically, a limited number of ground motions – typically three to seven – have been run at the seismic hazard design or evaluation level. Details and results from these studies can be found in academic journals (e.g., Hadidi et al., 2014; Mejia et al., 2014) and consulting reports (e.g., URS Corporation, 2006; AMEC Geomatrix, Inc., 2011; TERRA / GeoPentech, 2012).

More recently, a few projects have been completed where significantly more ground motions were run to estimate shear-induced deformations across a wide range of ground-motion intensities, with the purpose of performing a probabilistic deformation hazard analysis for the dam (e.g., Phalen and Wagner, 2017; Conkle, 2017). In each of these studies, a detailed analysis

was performed for a single dam subjected to hundreds of expected ground motions, and those analyses were repeated to capture the epistemic uncertainty in the inputs. These types of studies are relatively new in the dam industry and are also expensive. Updating the deformation hazard by running hundreds of dynamic analyses at a frequency similar to what is done for seismic hazard is cost-prohibitive for the average utility and dam. Additionally, there's a wide range in the geotechnical data available for each dam as far as the level of detail and quality of the information about the dam materials, making it challenging to perform the studies in a consistent way for the various dams in a portfolio so that the results can be compared and used as part of a risk-reduction program. A simplified approach to estimate shear-induced deformations is needed to overcome these challenges and move from seismic hazard assessments to deformation hazard assessments for earthen dams.

1.2 Previous Simplified Procedures

Newmark (1965) proposed using a sliding block model to estimate displacements and evaluate the seismic performance of embankment dams during earthquakes. Many researchers have subsequently developed simplified procedures for estimating shear-induced displacements. For an extensive review of deformation-based methods used for calculating earthquake-induced displacements for slopes see Strenk (2010). Only simplified procedures applicable to deformable or flexible systems that could potentially be used in a probabilistic framework to compute deformation hazard curves for earthen dams are discussed here.

Makdisi and Seed (1978) introduced one of the most widely used simplified procedures for estimating the shear-induced deformation of an earthen dam. The procedure is based on the results of a limited number of dynamic analyses run using the two-dimensional finite-element method with the equivalent-linear scheme. In particular, the number of earthquake ground motions was extremely limited by today's standards with three empirical recordings and one artificial record. The estimated deformation is calculated from two charts that rely on the user-defined earthquake magnitude and sliding mass geometry, as well as user-estimated crest PGA, yield coefficient, and first natural period. Subsequent researchers have updated and improved upon the work of Makdisi and Seed by formulating the procedure in terms of a GMPE-like equation rather than look-up charts, predicting deformations from inputs that don't require the user to estimate the response at the crest of the dam or the first natural period, and running more ground motions when generating their dataset.

Bray and Travasarou (2007) developed predictive models that utilized a large ground-motion database and accounts for the response of the sliding mass. Their work uses the fully coupled, nonlinear, deformable stick-slip sliding model proposed by Rathje and Bray (2000). The dynamic response of the deformable sliding mass is based on one-dimensional equivalent-linear analyses with the shear-modulus reduction and material damping curves by Vucetic and Dobry (1991) for PI=30. Generation of their dataset included applying 688 earthquake records to eight sliding block systems with fundamental periods from 0 – 2.0 *s* and utilizing yield coefficients ranging from 0.02 – 0.4. Displacements are estimated from the initial fundamental period (T_s), the spectral acceleration of the ground motion at a degraded period of 1.5 times the fundamental period ($S_a(1.5T_s)$), the magnitude of the earthquake (M_w), and the yield coefficient (k_y). The standard deviation of the displacement is a constant 0.66 natural log units.

Saygili and Rathje (2008) developed a model to estimate Newmark displacements for rigid sliding blocks that was extended to the flexible case by Rathje and Antonakos (2011). The original rigid sliding block model utilized 2,383 input motions, used as is and additionally scaled by factors of 2.0 and 3.0, with the condition that the PGA could not exceed 1.0 *g*. For the flexible case, the response of the sliding mass is based on one-dimensional site response calculations using the equivalent-linear site response code Strata (Kottke and Rathje, 2008) with the shear-modulus reduction and material damping curves by Darendeli (2001) for PI=0. Site response calculations were performed for 80 input motions and five sites with site periods ranging from 0.15 – 1.5 *s*. Displacements for the flexible case are estimated from the initial fundamental period (T_s), the peak ground acceleration (*PGA*), the peak ground velocity (*PGV*), the mean period of the ground motion (T_m), and the yield coefficient (k_y).

An alternative model to the Saygili and Rathje (2008) model was presented in Rathje and Saygili (2009) for rigid sliding blocks and extended to the flexible case by Rathje and Antonakos (2011). The alternative model relies on the same dataset, but does not require the *PGV* of the ground motion, and instead requires the magnitude of the earthquake (M_w). All other predictor variables are the same. The Rathje and Saygili (2009) model represents a scalar (single) ground motion parameter model, while the Saygili and Rathje (2008) model represents a vector (two) ground-motion parameter model. For both models, the standard deviation of the displacement is a function of *PGA*, T_m, and k_y. The standard deviation of the scalar model is generally larger than the standard deviation of 0.66 from Bray and Travasarou (2007), while the standard deviation of the vector model is generally smaller.

Du et al. (2018) used the methodology from Bray and Travasarou (2007) to develop two different vector models for seismic slope displacements. Their models also use the fully coupled, nonlinear, deformable stick-slip sliding model by Rathje and Bray (2000) and a one-dimensional equivalent-linear approach for the soil response. The shear-modulus reduction and material damping curves are those by Darendeli (2001) for PI=30. Analyses were performed for 3,714 earthquake records. Displacements are estimated from T_s, k_y, and either $S_a(1.5T_s)$, Arias intensity (I_a), and M_w, or *PGA* and $S_a(2\ s)$. The standard deviations of the displacement are 0.69 and 0.74 natural log units, respectively.

Bray and Macedo (2019) updated the work by Bray and Travasarou (2007) with a larger ground-motion database of 6,711 two-component recordings. Their work again utilized the fully coupled, nonlinear, deformable stick-slip sliding model by Rathje and Bray (2000), which includes a one-dimensional equivalent-linear approach for the soil response. The shear-modulus reduction and material damping curves were updated to Darendeli (2001) for PI=15. Seismically induced shear slope displacements are estimated from T_s, $S_a(1.3T_s)$, M_w, and k_y for the general case; *PGV* is also included for near-fault pulse motions. The standard deviation of the displacement for the general model is 0.74 natural log units.

The simplified procedures described above all utilize ground motions from shallow crustal earthquakes. Because there are differences in ground motions from other tectonic environments beyond the ground-motion parameters used in the displacement procedures, strictly speaking, these models should not be applied to other tectonic environments. Bray et al. (2018) developed a model specifically for subduction zone interface earthquakes. Their work also relies on the fully coupled, nonlinear, deformable stick-slip sliding model by Rathje and Bray (2000) with its one-dimensional equivalent-linear approach for the soil response. The

shear-modulus reduction and material damping curves are those by Darendeli (2001) for PI=15. Analyses were performed for 810 two-component earthquake records. Displacements are estimated from T_s, $S_a(1.5T_s)$, M_w, and k_y. The standard deviation of the displacement is 0.73 natural log units.

These simplified procedures all use a similar approach where a large number of ground motions are run through an idealized sliding-mass model, and a Newmark analysis is performed to calculate the displacements. The generation of a dataset using numerical simulations is necessary because empirical observations of dam deformations are limited. The geometry and dynamic properties of the potential sliding mass are often varied to capture a range of natural periods, and the yield coefficient is also varied to capture a range of material strengths. Regression techniques are used to fit a curve through the resulting deformations, based on predictor variables that characterize the input ground motion and the potential sliding mass.

1.3 Basis for Proposed Methodology

Available simplified procedures are easy to use but provide limited flexibility to refine the input ground motion, which has a large impact on the estimated deformation. In the available simplified procedures, the input ground motion is replaced with a single proxy or in some cases a series of proxies after examining the dependence of the estimated deformations on various ground motion parameters from the ground motions used in the dataset. The simplification of the ground motion to a single proxy or series of proxies in the available deformation models does not allow for the incorporation of more information about the expected ground motions at a site. As seismic hazard assessments continue to move toward more regionalized and site-specific ground motions, it is desirable to use a simplified approach that maximizes information about the input ground motion and can reflect regional differences and refinements of site-specific ground motions in the estimated deformations.

Available simplified procedures use large datasets and multivariable regression techniques to fit a curve through the dataset of calculated seismic slope displacements, providing an estimate of the median deformation and the standard deviation of that deformation. Caution must be exercised when extrapolating the model beyond the range of the data that were generated to build it. To perform deformation hazard assessments for many dams in seismically active regions, it is necessary to estimate deformations for a wide range of ground motions, including rare ground motions, which are poorly represented in our ground-motion records databases. It is, therefore, desirable to use a simplified approach that has a physical basis beyond best-fit trends to the selected data, providing physical constraints on the extrapolation.

This study proposes an alternative to the available simplified procedures by developing a methodology that only simplifies the response of the earthen dam. With the proposed method, the dynamic analysis of the earthen dam is replaced with a simplified transfer function for a potential sliding mass. When applied to a user-defined ground motion, the simplified transfer function provides the time history of the average acceleration for the potential sliding mass, which can then be used to estimate a shear-induced deformation using a Newmark-type procedure. Through the de-coupled approach, the proposed methodology maximizes information about the input ground motion by accommodating the entire ground-motion time history.

Importantly, the simplified transfer functions have a physical basis routed in the nonlinear behavior of soil response.

The proposed methodology offers an intermediate procedure between a detailed dynamic analysis and available simplified procedures. It is similar in concept to the recently published work by Hayati and Moss (2017). The application of their proposed method is the computation of the surface response spectra for site response, rather than the shear-induced deformation of a potential sliding mass of an earthen dam, but there are similarities in the approach in terms of providing a model that accepts the entire ground-motion time history as an input. Hayati and Moss develop a simplified procedure that provides a five-point estimate of site amplification factor, providing an intermediate site response solution between generic site factors and rigorous numerical solutions. In contrast, the proposed transfer-function model is formulated to provide a continuous estimate of the transfer function across all frequencies, rather than a discrete estimate, and offers a means to obtain an estimate of the average acceleration time history for a potential sliding mass for a shear-induced deformation analysis.

1.4 Overview and Objectives

A simplified method for carrying out dynamic response analyses of earthen dams is proposed for performing shear-induced deformation assessments. The methodology involves estimating the transfer function for a potential sliding mass of an earthen dam, which is applied to a user-defined input ground motion to estimate the average acceleration time history of the sliding mass and calculate a shear-induced Newmark deformation. The proposed approach is utilized to build a transfer-function model, which represents one implementation of the methodology for a given set of assumptions about the characteristics of the earthen dam. The transfer-function model is based on a synthetic dataset generated by performing dynamic analyses for 950 input ground motions applied to 12 representative earthen dams using the equivalent-linear finite-element method. The transfer-function model can be applied to a suite of site-specific ground motions to ultimately calculate a deformation hazard curve. The approach is efficient enough that it can be used to calculate and regularly update mean deformation hazard with associated uncertainties for a large number of earthen dams. If fragility curves for the dams can be estimated, then the deformation hazard curves can be combined with the fragility curves to calculate mean seismic risk with uncertainties.

The proposed work meets the following four objectives. The first objective is to develop a methodology that can be used to move from seismic hazard assessments for a suite of earthen dams, to something that is a better predictor of dam performance. Rather than basing decisions on the quantitative seismic hazard assessments, which are typically performed for spectral acceleration, the proposed methodology provides a rational approach for bringing in information about the response of the dam. Shear-induced deformations calculated from a Newmark-type analysis are a better predictor of dam performance than the spectral acceleration of the ground motion alone.

The second objective is to develop a methodology that maximizes information about the input ground motion, which has a large impact on the estimated deformation. Although the de-coupled approach is unable to account for the simultaneous occurrence of the dynamic response with its seismically induced permanent deformation, it has the advantage of separating the input

ground motion from the response analysis. This separation allows shear-induced deformations to be computed for a suite of site-specific ground motions. Because the entire time history of the ground motion is an input to the model, the approach offers flexibility in applying the model to ground motions with a wide range of characteristics, including ground motions with different frequency content and durations, and those differences are reflected in the calculated deformations.

The third objective is to develop a methodology for shear-induced deformation hazard assessment that maintains a similar level of detail on both the ground motion and dam response sides. In seismic hazard analysis, ground-motion prediction equations make simplifying assumptions about the complicated dynamic rupture process of an earthquake and the 3D wave propagation through the crust. The ground-motion prediction equations are based on the Brune (1970) point-source model to provide a physical basis for the models and ensure proper extrapolation beyond the range of the empirical data. On the dam response side, the dynamic response of soil systems is a complex process, and estimating the response and deformation of the dam with a transfer function and Newmark-like procedure is likewise acknowledged as utilizing a simplified model. Similar to the physical basis behind the ground-motion prediction equations, the transfer-function model has a physical basis that captures the key mechanisms through which nonlinearity affects soil behavior.

The fourth objective is to develop a methodology that can be used in a consistent manner to compute shear-induced deformation hazard curves for a suite of earthen dams – providing a basis for comparisons between dams. Using the same approach with the same assumptions to compute deformation hazard curves adds value by providing a systematic approach for decision-making, even if those decisions are based on simplified analyses.

1.5 Organization

This dissertation is organized into eight chapters. The representative dams and input ground motions used in the dynamic analyses to generate a synthetic dataset are described in Chapter 2. The inputs and assumptions described in Chapter 2 form the basis for the transfer-function model, which represents one implementation of the transfer function methodology. The geometry and material properties of the representative dams are discussed, along with the selection process used for the suite of input ground motions.

The results of the dynamic analyses are discussed in Chapter 3 and the key behavior of the earthen dams when subjected to earthquake ground motions is highlighted. Amplification of the input ground motions through the dam materials is discussed in terms of earthquake-induced peak shear strains, earthquake-induced peak horizontal accelerations, and input motion vs. crest PGA comparisons. Shear-induced deformations calculated from the dynamic analyses and a Newmark-type procedure are also presented.

The development of the transfer-function model is explained in Chapter 4. The results of the dynamic analyses discussed in the previous chapter form the basis of the transfer-function model. The estimated transfer function is defined at all frequencies and captures the key mechanisms through which nonlinearity affects soil behavior, including period shift and damping increase. The methodology accommodates the entire time history of the ground motion, allowing

the user to take advantage of available seismic hazard characterization through the use of site-specific ground motions.

The results from a subset of dynamic analyses that were performed with alternative nonlinear curves are presented in Chapter 5. Because the functional form of the transfer-function model has a physical basis beyond best-fit trends to the selected data, the model can be altered in a straightforward manner, and adjustments are recommended for alternative nonlinear behavior.

The transfer-function model is applied to two case histories in Chapter 6, comparing the estimated deformations from the model with the observed deformations at two dams. Despite significant uncertainties in the required inputs, the case histories provide a valuable check on the reasonableness of the estimated deformations from the transfer-function model. The case histories also illustrate how the transfer-function model can be used to gain insights about the input ground motion and how the model can be calibrated using empirical observations of the natural period of the dam.

The transfer-function model is applied in a probabilistic framework to characterize the shear-induced deformation hazard for an earthen dam in Chapter 7. The results from a site-specific probabilistic seismic hazard analysis are used to capture the expected ground motions at a hypothetical dam site, the transfer-function model is used to perform incremental dynamic analyses for the dam, and the seismic hazard results are combined with the dynamic analyses results to compute shear-induced deformation hazard curves. Epistemic uncertainty in the seismic hazard and dam response is presented through a sensitivity analysis leading to alternative deformation hazard curves.

The main findings and conclusions from the research presented in this dissertation are summarized in Chapter 8 and plans for future work are laid out.

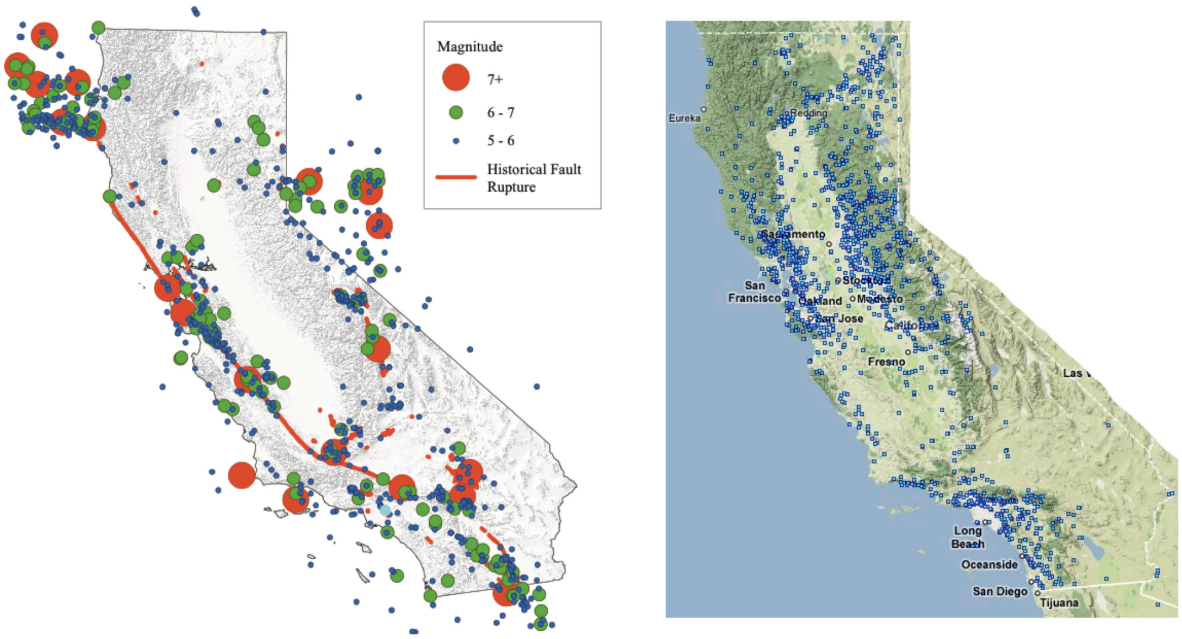

Figure 1.1 **California historic earthquakes (Branum et al., 2016) and California dam locations (US Army Corps of Engineers, 2017).**

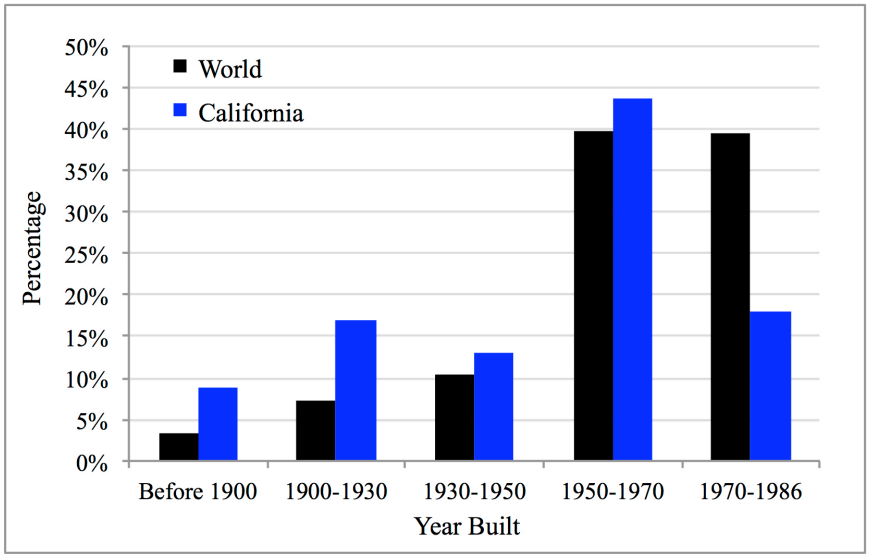

Figure 1.2 **Histogram showing when dams were built in California (Division of Safety of Dams, 2018) and worldwide (Foster et al., 2000).**

2 REPRESENTATIVE DAMS AND ACCELERATION TIME HISTORIES

2.1 Introduction

The transfer-function model will be built on the results of a series of dynamic analyses performed by running recorded earthquake ground motions through numerical models of representative dams. The generation of a dataset using numerical simulations is necessary because empirical observations of dam behavior during real earthquakes are limited. The results of the dynamic analyses constitute a synthetic dataset of the response of dams to earthquake ground motions. The transfer-function model developed from this synthetic dataset represents one application of the transfer function methodology, based on the dam properties and assumptions described in this chapter.

2.2 Selection of Representative Dams and Required Inputs

The geometry and material properties of the representative dams were chosen to reasonably reflect the range of earthen dams that the transfer-function model will be applied to for shear-induced deformation hazard analyses. To make the best use of computer time, properties known to greatly influence the dynamic response of the dam were varied, while single representative values were chosen for inputs found to be of lesser importance. Particular consideration was given to the height and shear-wave velocity profiles of the representative dams, and ultimately twelve representative dams were utilized. The twelve representative dams consist of combinations from four dam heights and three shear-wave velocity profiles.

2.2.1 Dam Geometry

The geometry of each dam is characterized by the dam height, crest width, downstream slope, and upstream slope. Dam heights from the Division of Safety of Dams (DSOD) database (Division of Safety of Dams, 2018) for the approximately 1100 earthen dams in California are displayed via a histogram plot in Figure 2.1. Four dam heights of 25 *ft*, 50 *ft*, 100 *ft*, and 150 *ft* were chosen to represent the range of dam heights from the larger database. The height selection notably includes dams on the smaller side. These shorter dams, particularly the older ones, are less likely to be prioritized for reevaluation, hence many have never had numerical models built or dynamic analyses performed for them, though they may make up half of a utility's portfolio. Representative dams taller than 150 *ft* were not included because numerical models for these taller dams are generally available.

A single representative crest width was selected for each dam height (see Table 2.1). The upstream slope for all dams is 3:1 horizontal to vertical and the downstream slope is 2.5:1. A diagram of the 100 *ft* dam is shown in Figure 2.2, annotated with these geometry specifications. The idealized earthen dam sits atop a firm foundation; therefore, the results of the dynamic analyses are applicable to earthen dams founded on competent rock, and are not applicable to dams founded on alluvial materials. Figure 2.2 includes the geometry specifications for the foundation material beneath the earthen dam. In reality the dam foundation exists in an infinite field condition; however, for modeling purposes, the material beneath the earthen dam consists of a finite foundation region. The foundation thickness was modeled as 40% of the dam height, and the lateral extent of the foundation beyond the base width of the earthen dam was modeled as 150% of the dam height.

The freeboard value, describing the vertical distance from the reservoir water level to the crest of the dam, was specified for each representative dam. A single freeboard value, representing an average high-reservoir water level was selected for each of the four dam heights. The representative freeboard values are described by the following equations:

$$H<100 \text{ ft} \qquad \text{Freeboard} = 3 \text{ to } 4 \text{ ft} \tag{2.1}$$

$$H\geq 100 \text{ ft} \qquad \text{Freeboard} = 10 + (H - 100)\cdot 5\% \text{ ft} \tag{2.2}$$

where H is the dam height in *ft*.

Each representative dam was modeled with a single phreatic surface. Although the representative dams are modeled as homogeneous embankments, the phreatic surface for each dam accounts for the engineering and drainage features common for a real embankment dam of that height. While shorter dams may be purely homogeneous, taller dams are generally better engineered with clay cores and internally placed pervious material to control seepage and the saturation within the dam. These features are not explicitly modeled in the representative dams, but the phreatic line of each dam implicitly accounts for filter and drainage elements with lower phreatic lines in the taller dams.

The phreatic surface for each representative dam is illustrated in Figure 2.3. The phreatic surface for the 25 *ft* dam is modeled simplistically as a straight line from the reservoir level to the downstream tow of the dam, reflecting the tendency for a higher phreatic line in a purely homogeneous embankment. The phreatic surface for the 50 *ft*, 100 *ft*, and 150 *ft* dams is modeled simplistically with a hinge point in the body of the dam, bringing the phreatic surface down. As seen in Figure 2.3, the phreatic surface hinge point moves progressively lower as the dam height increases, reflecting the increasing level of engineering and drainage features built into dams of greater heights.

The dynamic analyses are performed for pre-prescribed failure surfaces using the de-coupled approach. The computer program SLOPE/W (GEO-SLOPE International Ltd., 2008) was used to examine potential slip surfaces. A wide slip surface entry and exit range was defined. The entry range includes the upstream half of the crest width of the dam and extends down to half of the dam height on the upstream side. The exit range includes the tow of the dam and extends up to half of the dam height on the downstream side, and is shown in red on Figure 2.4 for the 100 *ft* dam. The critical slip surface is a deep failure that starts at the upstream edge of the crest and exits near the downstream toe. The critical slip surface is shown in Figure 2.4a, and the factor of safety for undrained loading is included on the figure ($\phi_u = 22°$, $c_u = 300$ *psf*, *FS* =

1.3). Four additional slip surfaces with slightly higher factors of safety for undrained loading (1.3 – 1.35) are shown along with the critical slip surface in Figure 2.4b.

Based on the results from the SLOPE/W analyses, and considering input from dam owners and practicing dam engineers (J.I. Sun, E.S. Aw, and F.I. Makdisi, personal communication, 2016) the dynamic analyses were run with two potential failure surfaces for each dam – one "deep" failure and one "shallow" failure. The deep failure is the critical failure surface described above, encompassing the crest width and the full dam height, which is in agreement with a critical dam failure scenario that could lead to a loss of safety function of the dam (i.e., not a maintenance issue). The shallow failure surface is a similar shape, but occupies half of the dam height, and is considered because although shallow failure surfaces are associated with higher yield coefficients, the response of the dam is also stronger in the upper half of the dam, so there is a potential for larger deformations. The two failure surfaces capture two distinct potential failures – that is two failure surfaces that produce meaningfully different average acceleration time histories. The final deep and shallow failure surfaces prescribed in the dynamic analyses are shown in Figure 2.5. Although the dynamic analyses were run for both failure surfaces, only the deep failure surface results were used to develop the transfer-function model. The transfer-function model can be expanded for the shallow failure surface in future work.

2.2.2 Dynamic Material Properties

The dynamic material properties required for the dynamic response analyses using the equivalent-linear approach are total unit weight, Poisson's ratio, shear-wave velocity, and relationships describing the shear-modulus reduction and material damping with cyclic shear strain. The representative dams are idealized as homogeneous embankments comprised of sand, silt, and clay. A single representative unit weight of 130 *pcf* was used for the embankment material and a unit weight of 150 *pcf* was used for the foundation. A wet Poisson's ratio of 0.47 was used for the embankment material below the phreatic surface and a dry Poisson's ratio of 0.33 was used above the phreatic surface. A Poisson's ratio of 0.3 was applied to the foundation. A sensitivity analysis was performed where the Poisson's ratio of the foundation was changed to 0.47, and the results indicated that this change has a negligible effect on the dynamic analyses. Results of the sensitivity analysis are presented in Appendix A.

Shear-wave velocity measurements from the Sykora database (Sykora, 1987) are plotted in Figure 2.6. The database consists of shear-wave velocity measurements obtained by the crosshole seismic method at 40 earthen dam sites across eight states in the United States, with seventy percent of the sites located in California. The database consists of measurements from 85 crosshole arrays made from the crest of the dam, resulting in 1257 data points, which are the data plotted in Figure 2.6. Three shear-wave velocity profiles were selected to represent the range of shear-wave velocities from the larger database. The three representative profiles are also shown in Figure 2.6 for the 150 *ft* dam, and are referred to as the low, medium, and high shear-wave velocity profiles. The velocity profiles for the shorter dams are the same, stopping at the appropriate depth below the dam crest, given the height of the dam.

The representative shear-wave velocity profiles utilize the functional form from Sawada and Takahashi (1975), calibrated to capture the range of the shear-wave velocities in the Sykora database, and are described by the following equations:

$$Z < 5 \text{ ft} \qquad V_s = a \tag{2.3}$$

$$Z \geq 5 \text{ ft} \qquad V_s = b \cdot Z^c \tag{2.4}$$

where V_s is the shear-wave velocity in *ft/s*, Z is the depth below the surface in *ft*, and a, b, and c are coefficients that differ between the low, medium, and high shear-wave velocity profiles as shown in Table 2.2.

The representative profiles are compared to individual measured velocity profiles in Figure 2.7. Note that only measurements in the embankment of the dam are shown; velocity measurements taken in the foundation and at bedrock are not included. The velocity measurements at Estates Dam in California (URS Corporation, 2006) are similar to the idealized medium velocity profile. The pre-compaction shear-wave velocity measurements at Jackson Lake Dam in Wyoming (Sirles, 1988a) are similar to the low velocity profile, while the post-compaction measurements are similar to the medium velocity profile. The measured values at Cold Springs Dam in Oregon (Sirles, 1988b) fall between the low and medium profiles, with a shape that follows the idealized profiles remarkably well up to a depth of about 60 *ft*. The shear-wave velocity measurements at Rye Patch Dam in Nevada (Sirles, 1988b) fall between the medium and high profiles, though exhibit more variation than the idealized profiles. The comparisons show that the idealized low, medium, and high velocity profiles are similar in shape to field measurements from real dams and can be used to reasonably represent the shear-wave velocities of an embankment dam.

The foundation was modeled with a shear-wave velocity of 3200 *ft/s*. A sensitivity analysis was performed where the top 15 *ft* of the foundation was modeled as a weathered rock zone with a shear-wave velocity of 2000 *ft/s*, and the shear-wave velocity of the deeper foundation was kept at 3200 *ft/s*. The results indicated that this change has a negligible effect on the dynamic analyses. Results of the sensitivity analysis are presented in Appendix A.

The maximum shear moduli of the embankment and foundation materials were obtained from their shear-wave velocities using the following equation:

$$G_{max} = \frac{\gamma \cdot V_s^2}{g} \tag{2.5}$$

where γ is the unit weight of the material, V_s is the shear-wave velocity of the material, and g is the acceleration of gravity.

The shear-modulus reduction and material damping curves used for the embankment materials are based on the confining-pressure-dependent relationships by Darendeli (2001) for PI=20. This relationship was selected based on the average characteristics of the embankment materials and the preference for a relationship that captures the stress-dependent nature of the dynamic response. Four curves at confining pressures of 0.5, 1, 2, and 4 *atm* were utilized based on the range of stresses present in the representative dams. The stress-dependent Darendeli (2001) PI=20 curves are compared with other commonly used nonlinear curves in Figure 2.8. The Darendeli (2001) PI=20 curves are most similar to the Seed and Idriss (1970) upper bound

G/G_{max} and lower bound damping curves for sands and the Vucetic and Dobry (1991) PI=15 curves.

The published Darendeli curves were modified using the procedure proposed by Yee et al. (2013) to adjust the soil backbone curve to transition toward a specified shear strength at large strains. Because the Yee et al. (2013) procedure relies on the shear-wave velocity of the material to calculate the values for the second hyperbola, the procedure was applied to each of the three representative shear-wave velocity profiles, resulting in V_s-profile-dependent shear-modulus reduction curves. Damping values were calculated from equation 9.2b in Darendeli (2001) and utilize the strength-adjusted G/G_{max} to come up with strength-adjusted material damping curves that are consistent with the strength-adjusted shear-modulus reduction curves. The hyperbolic functional form from equation 9.2b in Darendeli (2001) causes the damping curve to have a negative slope at high strains. This behavior was not allowed, and the damping was set equal to the maximum at high strains to prevent a negative slope. Figure 2.9 shows the final adjusted shear-modulus reduction and material damping curves used in the dynamic analyses for the three shear-wave velocity profiles. Figure 2.9 also presents the as-published Darendeli curves (without strength adjustment) for comparison. Strength-adjustments for the low and medium shear-wave velocity profiles are minimal, while the adjustments to the high shear-wave velocity profile are more significant and result in a steeper G/G_{max} curve. The foundation was modeled with a constant $G/G_{max} = 1$ and a constant material damping = 2%.

2.2.3 Material Strengths and Yield Coefficients

The dam material strength and yield coefficient are not required inputs for the de-coupled dynamic response analyses, but are necessary to apply the Newmark procedure and estimate shear-induced deformations. A range of material strengths and yield coefficients are discussed here in the context of the expected application of the Newmark procedure. Though the representative dams are idealized as homogeneous, the material strength parameters should be thought of as composite strengths – single values that represent the strength of two or more materials. Using composite strengths takes advantage of increased shear resistance from higher strength materials in the dam embankment, shell, or buttress without explicitly modeling multiple zones or materials.

The total stress undrained shear strengths of the embankment materials are characterized by the total stress friction angle, ϕ_u, and the apparent total stress cohesion, c_u. Based on discussions with dam owners and practicing dam engineers (J. Sun, E.S. Aw, and J. Phalen, personal communication, 2016) and a review of dam seismic stability evaluation reports, composite total stress friction angles of 16 - 25° and composite apparent total stress cohesion values of 100 - 800 *psf* reasonably represent the strengths for many existing earthen dams.

Lower material strengths are reflective of dams constructed with no formal compaction or light compaction, and include many dams built before 1920, where soil may have been placed by horse-drawn wagons. Medium material strengths are reflective of moderately compacted dams, and include many dams built between 1920 and 1950. For these dams, soil may have been placed and compacted by mechanical equipment but without compaction by rollers, or rolled in thick layers beyond the capability of the roller. Higher material strengths are reflective of dams that

were properly compacted, and include many dams built in the 1950s and 1960s, where modern vibration and compaction equipment was used.

The range of shear strengths utilized in this study (ϕ_u = 16 - 25° and c_u = 100 - 800 *psf*) represents low to medium material strengths. These shear strengths were used to perform a limited number of pseudo-static stability analyses to obtain yield coefficients for the deep sliding surface for the representative dams. The range of undrained material strengths utilized in this study correspond to factors of safety of about 1.25 – 1.5 and yield coefficients of about 0.12 – 0.24 for the potential deep sliding mass. These values are consistent with expected factors of safety using undrained shear strengths and yield coefficients for many existing earthen dams, and also compare well with those obtained from the simplified equation:

$$k_y = (FS - 1)\sin\alpha \tag{2.6}$$

where *FS* is the factor of safety and α is the angle between the slip direction of the center of mass and the horizontal (taken simplistically here as 21.8° from the downstream slope of the dam).

2.2.4 Analysis Methodology

The analysis methodology follows the de-coupled approach, which is used to assess the seismic performance of embankments constructed of soils that do not lose significant strength during earthquakes. This de-coupled approach includes pseudo-static stability analyses, dynamic analyses, and Newmark-type deformation analyses. Strictly speaking, only the dynamic analyses are necessary to build the transfer-function model, but the complete de-coupled approach is discussed here to place the dynamic analyses in the context of its application to estimating shear-induced deformations. The general approach consists of the following steps:

1. Perform a pseudo-static stability analysis to obtain the potential sliding surface and yield acceleration, k_y
2. Perform a dynamic analysis to obtain the average acceleration time history of the potential sliding mass
3. Perform a Newmark-type deformation analysis to estimate the accumulated permanent displacement of the embankment

Pseudo-static stability analyses were performed using the computer program SLOPE/W (GEO-SLOPE International Ltd., 2008). The program uses the two-dimensional limit equilibrium method of slices. Spencer's method (Spencer, 1967), which considers both normal and shear interslice forces, and satisfies both force and moment equilibrium, was used in the SLOPE/W analyses. The yield coefficient, k_y, is calculated as the seismic coefficient required to calculate a factor of safety equal to 1.0. The results from these analyses are discussed in the previous section. The yield coefficient is not an input to the transfer-function model, but is necessary to perform the Newmark-type deformation analysis.

The results from step 2 above form the basis of the transfer-function model. The computer program QUAD4MU (Hudson et al., 2003) was used to perform the dynamic analyses of the representative earthen dams, capturing the response of the embankment materials and providing an average acceleration time history for the potential sliding mass. QUAD4MU is an update to QUAD4 (Idriss et al., 1973) and QUAD4M (Hudson et al., 1994). The program models

the dam with two-dimensional finite elements. The finite-element procedure consists of numerically modeling a continuum with a finite number of elements interconnected at their common nodes. A typical embankment cross section is modeled as a plane strain section and the input motion is applied transversely in the upstream / downstream direction at the bedrock foundation.

The QUAD4MU program uses the equivalent-linear procedure to assign strain-compatible shear-modulus reduction and material damping properties to the dam. The equivalent-linear procedure consists of an analysis that begins with an initial estimate of the shear modulus and material damping ratio for each solid element representing the earthen dam. Using an iterative process, the system is analyzed using these shear modulus and damping ratio values, effective shear strains are calculated, and new shear modulus and damping ratio values at the effective shear strain are employed in the next iteration. The process is repeated until convergence is achieved. The final shear modulus and damping values for each element are used for the entire duration of the acceleration time series.

In this study, the effective shear strains in all dynamic analyses were calculated simplistically as the maximum shear strains multiplied by a strain reduction factor of 0.65. An expression relating the strain reduction factor to earthquake magnitude (e.g., (M-1)/10) was not utilized, as the constant strain reduction factor was preferred for its straightforward implementation and to simplify the examination of the results.

QUAD4MU allows for a compliant base through implementation of the Lysmer scheme (Lysmer and Kuhlemeyer, 1969), where dampers are used at the base of a vibrating footing. Transmitting boundaries were used for all of the nodes at the base of the modeled foundation and the finite-element mesh for the foundation was extended laterally to minimize the effects of side boundaries. The foundation rock that extends beneath the modeled portion of the foundation is treated as an elastic half-space.

One feature that makes QUAD4MU an attractive program for this study is the average acceleration time history output, which the program calculates for a user-defined potential sliding mass. As explained in Kramer (1996), the average acceleration time history, which may be of greater or smaller amplitude than the input ground motion acceleration time history (depending on the input motion characteristics and amplification characteristics of the slope), provides the most realistic input for a Newmark-type procedure. QUAD4MU calculates the average acceleration time history of a potential sliding mass from the time-dependent forces acting on the sliding surface. The force acting on the sliding surface is determined at each time step by summing the normal and shear forces of the finite elements along the boundary of the sliding mass. These normal and shear forces are calculated from the corresponding normal and shear stresses acting on the finite elements and the dimensions of the finite elements. The average acceleration is obtained by dividing the resultant force by the mass of the sliding block (Makdisi and Seed, 1977):

$$F(t) = \sum_{i=1}^{n} [\tau_{hvi}(t) w_i + \sigma_{hi}(t) d_i \tag{2.7}$$

$$k_{av}(t) = \frac{F(t)}{m} \tag{2.8}$$

where $F(t)$ is the time-dependent force acting on the sliding surface, n is the number of elements along the sliding surface, τ_{hvi} is the time-dependent shear stress of element i, w_i is the width of element i, σ_{hi} is the time-dependent normal stress of element i, d_i is the depth of element i, $k_{av}(t)$ is the time-dependent average acceleration of the potential sliding mass, and m is the mass of the sliding block. In this study, average acceleration time histories are calculated for the deep and shallow sliding masses.

The yield coefficient from step 1 is applied to the average acceleration time history from step 2 using the Newmark (1965) sliding block procedure modified for a flexible sliding block analysis (Makdisi and Seed, 1978) in a de-coupled approach (Kramer and Smith, 1997; Bray and Rathje, 1998). Following this approach, the average acceleration time history of the potential sliding mass is compared with the yield coefficient, k_y. Movement initiates when the average acceleration exceeds the yield coefficient and continues until the relative velocity of the sliding mass drops to zero. Integration of the average acceleration compared to the yield coefficient with time gives relative velocity, and integration of the relative velocity gives displacement. For each average acceleration time history, two seismic slope displacements are calculated – one for the standard polarity and one for the reverse polarity.

The de-coupled approach with the Newmark sliding block method is recognized as a simplification of the complex response of earthen materials to earthquake loading resulting in permanent deformations. The Newmark method does not account for volumetric settlement. The method also does not account for deformation due to liquefaction and should not be used if there are materials in the dam that will lose significant strength during earthquakes. Additionally, the method does not consider the variation of the strength in the earthen mass during seismic loading. Nonetheless, the approach provides a framework for carrying out a first-order approximation of shear-induced deformations and is a useful evaluation tool. The calculated Newmark-type deformations are approximate in nature and should be viewed as such.

2.3 Selection of Acceleration Time Histories

Acceleration time histories were used in the dynamic analyses to predict the response of the dams to earthquake loading. Selected records were chosen to reasonably represent the range of ground motions expected at dam sites, with consideration given to the intensity of the ground motion and the duration of strong shaking. All selected ground motions were either 1) recorded in past earthquakes, or 2) recorded in past earthquakes and then modified by scaling the amplitude to reach a desired PGA. The durations of the ground motions were not modified. A total of 475 earthquake recordings were selected based on the criteria discussed below. The horizontal 1 and horizontal 2 acceleration time histories from each of the 475 recordings were used separately to perform dynamic analyses of the modeled dams, for a total of 950 dynamic analyses per dam.

2.3.1 Minimum Screening Criteria

Ground-motion records were selected from the NGA-West2 database (Ancheta et al., 2014), a collection of worldwide ground-motion data recorded from shallow crustal earthquakes in active tectonic regions. The database includes 21,539 records, with metadata available via the PEER

website in the form of a flatfile. The information in the flatfile was used to select the subset of recordings used in this project. Starting with the 21,539 recordings, only records for events with magnitudes greater than or equal to M 5 were considered. Earthquakes with magnitudes less than 5 are not expected to damage well-engineered structures, primarily due to the short durations. Excluding magnitudes less than 5 is also consistent with standard probabilistic seismic hazard analysis calculations, which use a minimum magnitude of 5. From the remaining recordings, only records from sites with V_{S30} values greater than 300 *m/s* were kept. The selected recordings will serve as input rock motions at the dam foundation, so recordings at these soft soil sites were excluded as they are thought to not reasonably represent input rock motions.

The next screening criteria was to only consider recordings with a lowest usable frequency less than or equal to 0.8 *Hz*. This check was performed on both the H1 and H2 components. If the lowest usable frequency was unknown, the record was also removed. Recordings that do not have reliable frequency content down to at least 0.8 *Hz* can cause problems in the dynamic analysis. In particular, the transfer functions associated with these records are not well-behaved at the frequencies below the lowest usable frequency. Records without known PGA values and without known 5–75% durations were also removed. The number of records left after applying these initial screening criteria are shown in Table 2.3.

2.3.2 Peak Ground Acceleration

A total of 6,177 records meet the minimum screening criteria discussed above. A histogram of the distribution of PGAs for these records is shown in Figure 2.10a. The limits of the bins were defined so that the PGA bins are equally spaced on a log axis. As shown in Figure 2.10a, the distribution of 6,177 records at PGAs ranging from 0.01 *g* to 2 *g* is not uniform. There are many more available records at low PGAs than there are at high PGAs. To make the best use of computer time, and to build a model that works well at all anticipated ground-motion levels, equal numbers of records were chosen from each bin. Figure 2.10b shows a histogram of the distribution of PGAs for the 475 selected records. Between PGAs of 0.01 *g* and 0.05 *g*, 3 records were chosen per bin. Above a PGA of 0.05 *g*, 17 records were chosen per bin. Preliminary analyses indicated that the shape of the transfer function was dependent on the intensity of the rock input motion above a PGA of about 0.05 *g*. Therefore, more records were selected from the bins with PGAs greater than 0.05 *g*. The records with PGAs less than 0.05 *g* were included for completeness and to demonstrate that the shape of the transfer function is approximately the same at these lower intensity levels.

Because very few recordings are available at the highest PGA levels, some records had to be scaled to get to 17 records in each bin. As illustrated in Figure 2.10b, 82 of the selected records were scaled while 393 records were used as is, for a total of 475 selected records. Note that all of the 475 selected records have unique record sequence numbers, meaning that if a record was used as is, it was not also used with a scaled ground motion.

2.3.3 Ground-Motion Duration and Arias Intensity

In addition to spanning the range of expected PGAs, the selected recordings should sample from the range of durations observed in the larger dataset. In Figures 2.11a, 2.12a, and 2.13a the 5–75% duration is plotted against the PGA of the ground motion for three magnitude ranges: M 5–

6, M 6–7, and M 7–8. The PGA dependence of duration for a given magnitude range results from the distance dependence of duration and the correlation of PGA and distance. The data plotted in Figures 2.11a, 2.12a, and 2.13a are the 6,177 records that meet the minimum screening criteria. The median of the observed data is plotted as a solid line, and the standard deviation of the duration from the data is noted on each figure. Similar plots were generated for the selected (scaled and unscaled) records to examine whether the selected ground motions retained the variability in duration of the larger dataset. Records were then reselected as necessary until the median and standard deviation of the selected records was similar to the larger dataset for each magnitude range.

Figures 2.11b, 2.12b, and 2.13b show the 5–75% durations against PGA for the final selected records. The median of the observed data is plotted along with the median of the selected records, and for all magnitude ranges the median lines from the data and selected records are very similar. The standard deviations of the duration from the selected records are also noted on the figures and compare well with the standard deviations from the data. As shown in Figures 2.11b, 2.12b, and 2.13b, scaled records were carefully chosen so that the duration of the record was appropriate for the scaled PGA.

Ground-motion records were selected based on the 5–75% durations. The 5–95% durations, 5–75% Arias intensities, and 5–95% Arias intensities of the selected ground motions were also checked. The purpose of these checks is to make sure that the selected ground motions are not biased and have adequate variability compared to the larger dataset. The checks are also important to ensure that the scaled ground motions have reasonable duration and Arias intensity characteristics. Figures 2.14 – 2.16 show the 5-95% durations against PGA for the observed data and selected records at the three magnitude ranges. Figures 2.17 – 2.19 similarly show the 5-75% Arias intensities against PGA, and Figures 2.20 – 2.22 show the 5-95% Arias intensities. The slope of the Arias intensity versus the PGA on a log-log scale for a given magnitude range is close to 2, as expected due to the squared acceleration in the definition of Arias intensity. In all cases the median of the observed data is similar to the median of the selected ground motions and the standard deviations of the data and selected records are in reasonable agreement.

2.4 Summary

Numerical models were built for twelve representative dams, comprised of combinations from four dam heights and three shear-wave velocity profiles. The geometry and material properties of the representative dams were selected to reflect average characteristics for many earthen dams built over the past century. Recorded earthquake ground motions from the NGA-West2 database were selected, and in some cases scaled, for the dynamic analyses. The set of input ground motions span a wide range of intensity levels and include variability in the duration and Arias intensity characteristics of the records. Dynamic analyses are performed by running the recorded earthquake ground motions through numerical models of the representative dams to capture the key behavior of earthen dams subjected to seismic loading.

Table 2.1 Representative dam heights and crest widths.

Dam Height [ft]	Crest Width [ft]
25	12
50	16
100	20
150	26

Table 2.2 Coefficients for representative dam shear-wave velocity profiles.

Coefficient	Low	Med	High
a	450	625	800
b	350	475	600
c	0.17	0.18	0.20

Table 2.3 Minimum screening criteria.

Criteria	Records Remaining
All NGA-West2 records	21,539
Magnitude ≥ 5	8,494
V_{S30} ≥ 300 m/s	6,364
H1 and H2 lowest usable freq ≤ 0.8 Hz (remove if unknown)	6,210
Remove if PGA unkown	6,182
Remove if 5 – 75% duration unknown	6,177

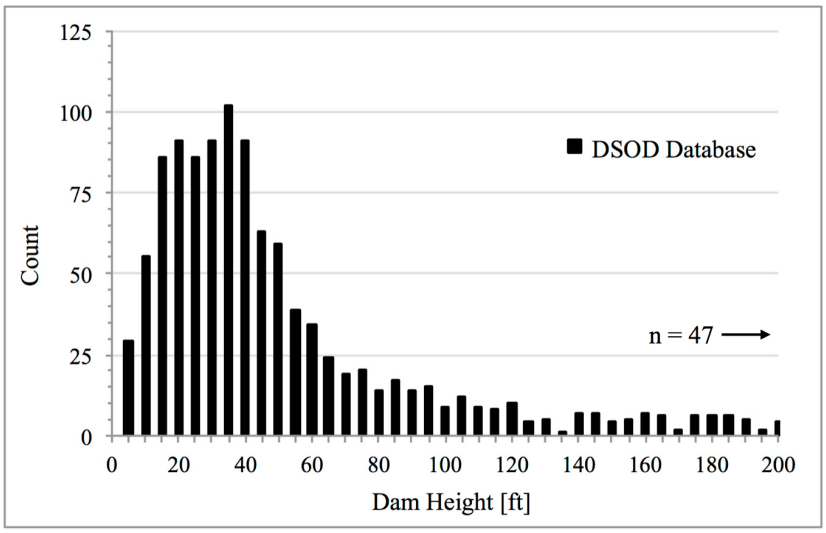

Figure 2.1 **Histogram of dam heights from the Division of Safety of Dams (DSOD) for the approximately 1100 earthen dams in California.**

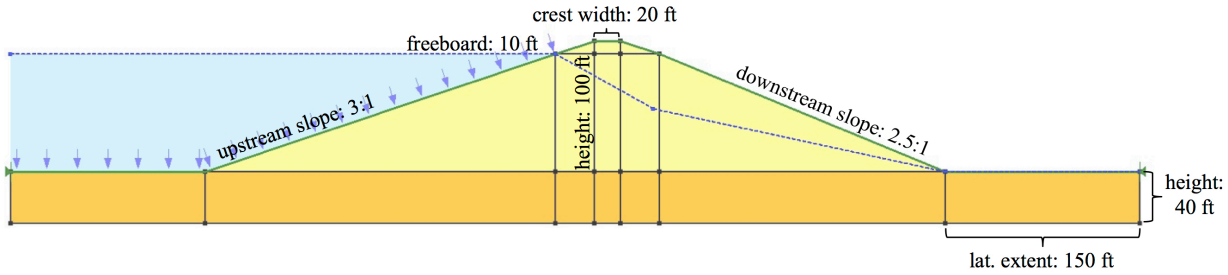

Figure 2.2 **Numerical model of representative dam with height of 100 *ft* annotated with geometry specifications.**

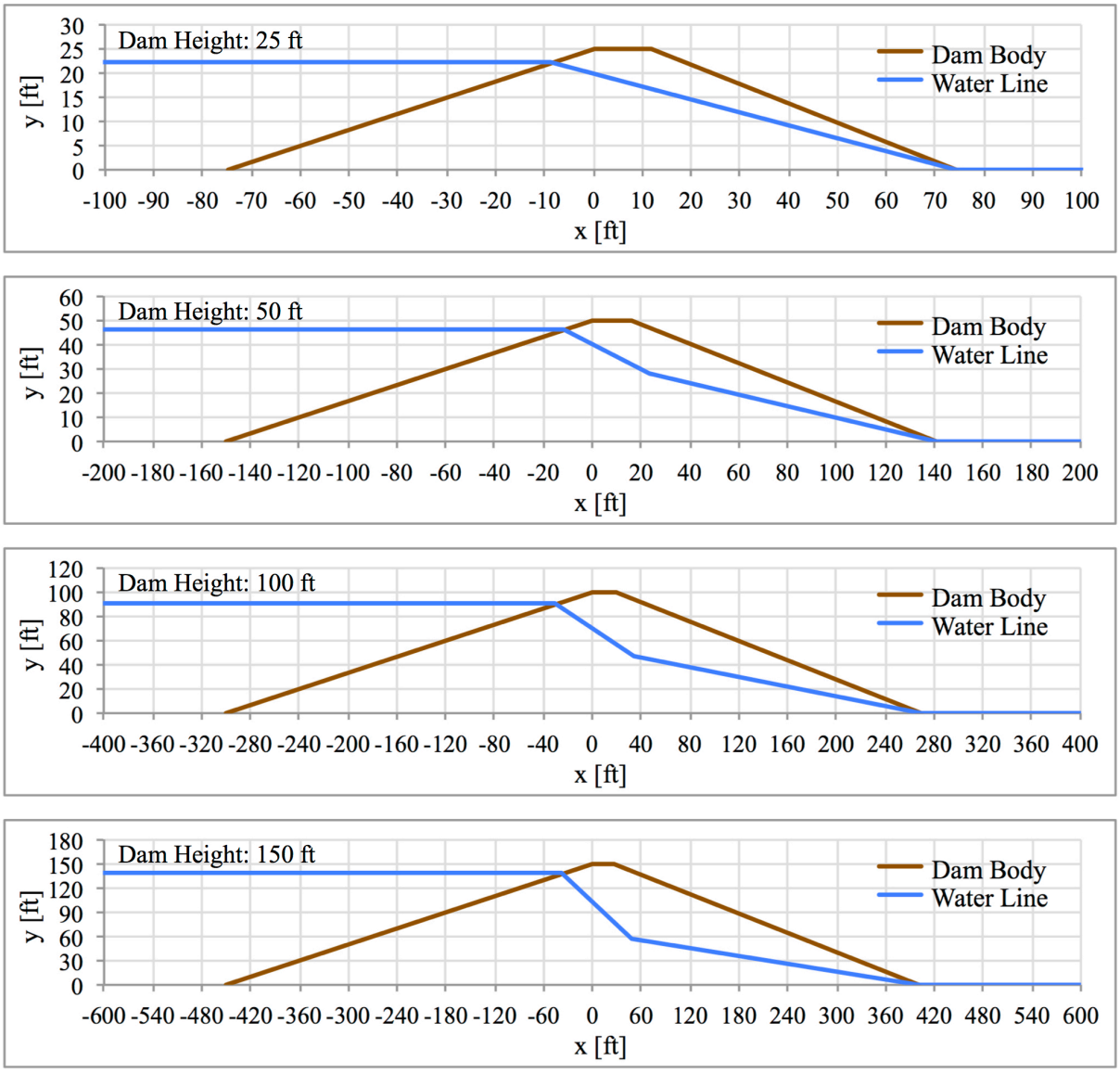

Figure 2.3 Phreatic surface for representative dams of different heights.

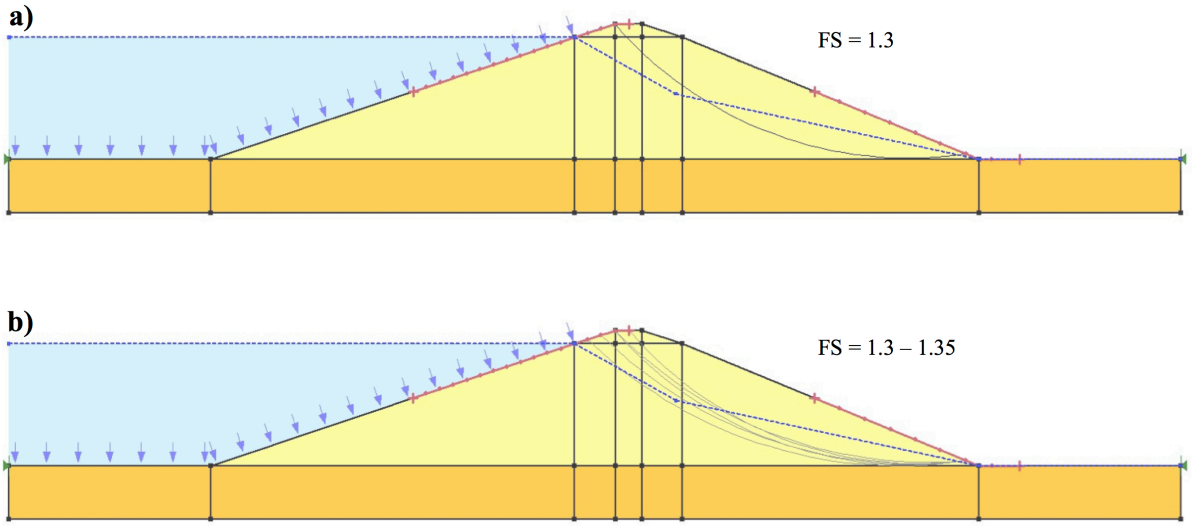

Figure 2.4 **Examination of potential deep failure surfaces for representative dam with height of 100 *ft* including a) critical slip surface and b) five slip surfaces with lowest factors of safety (factors of safety are for ϕ_u = 22° *and* c_u = *300 psf)*.**

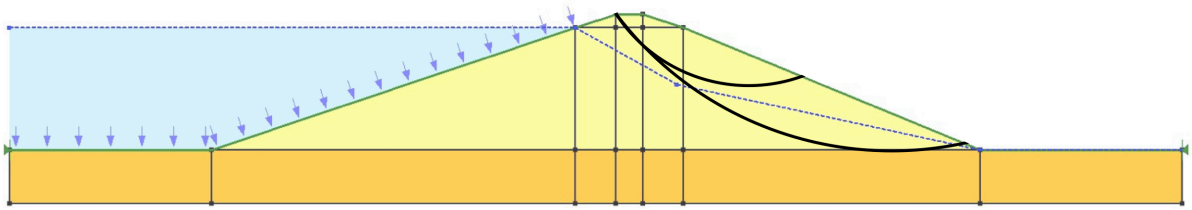

Figure 2.5 **Potential deep and shallow failure surfaces prescribed in dynamic analyses for representative dam with height of 100 *ft*.**

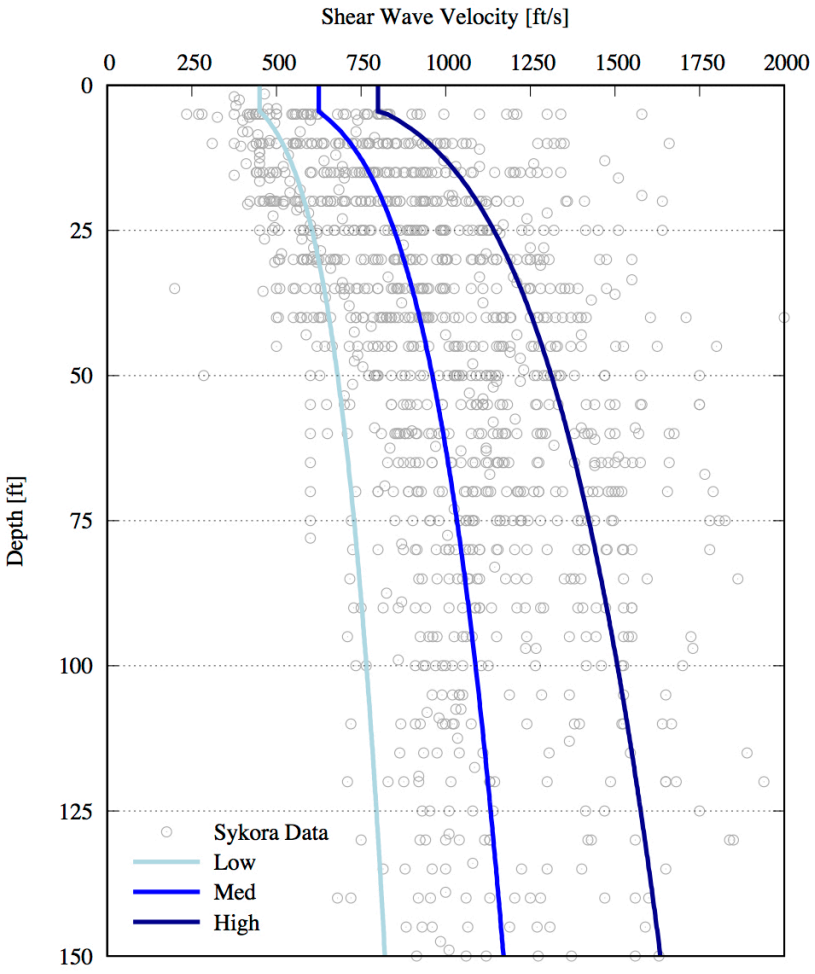

Figure 2.6 **Shear-wave velocity profiles for representative dams, along with measurements from Sykora database.**

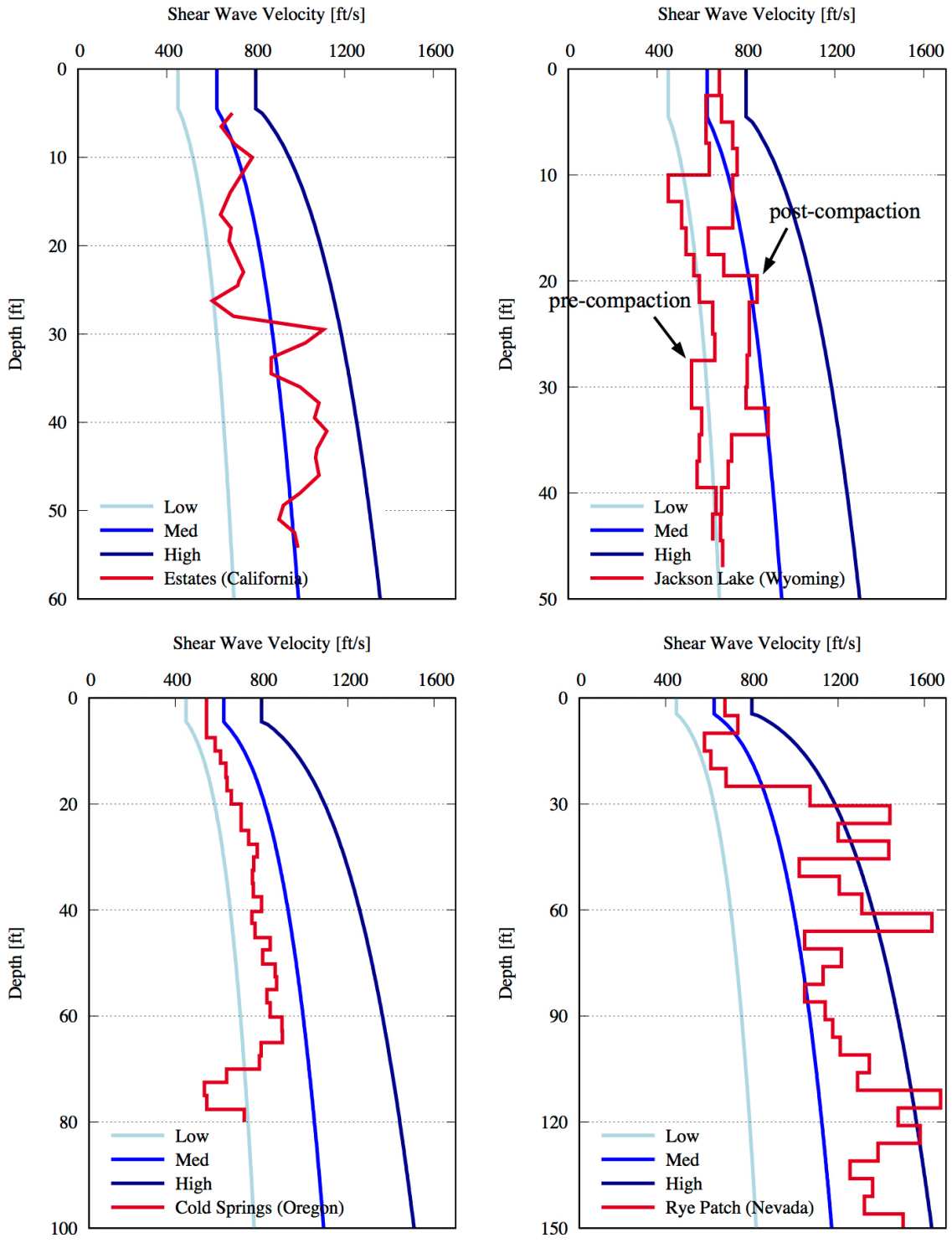

Figure 2.7 **Comparison of shear-wave velocity profiles for representative dams and individual measured velocity profiles from real dams.**

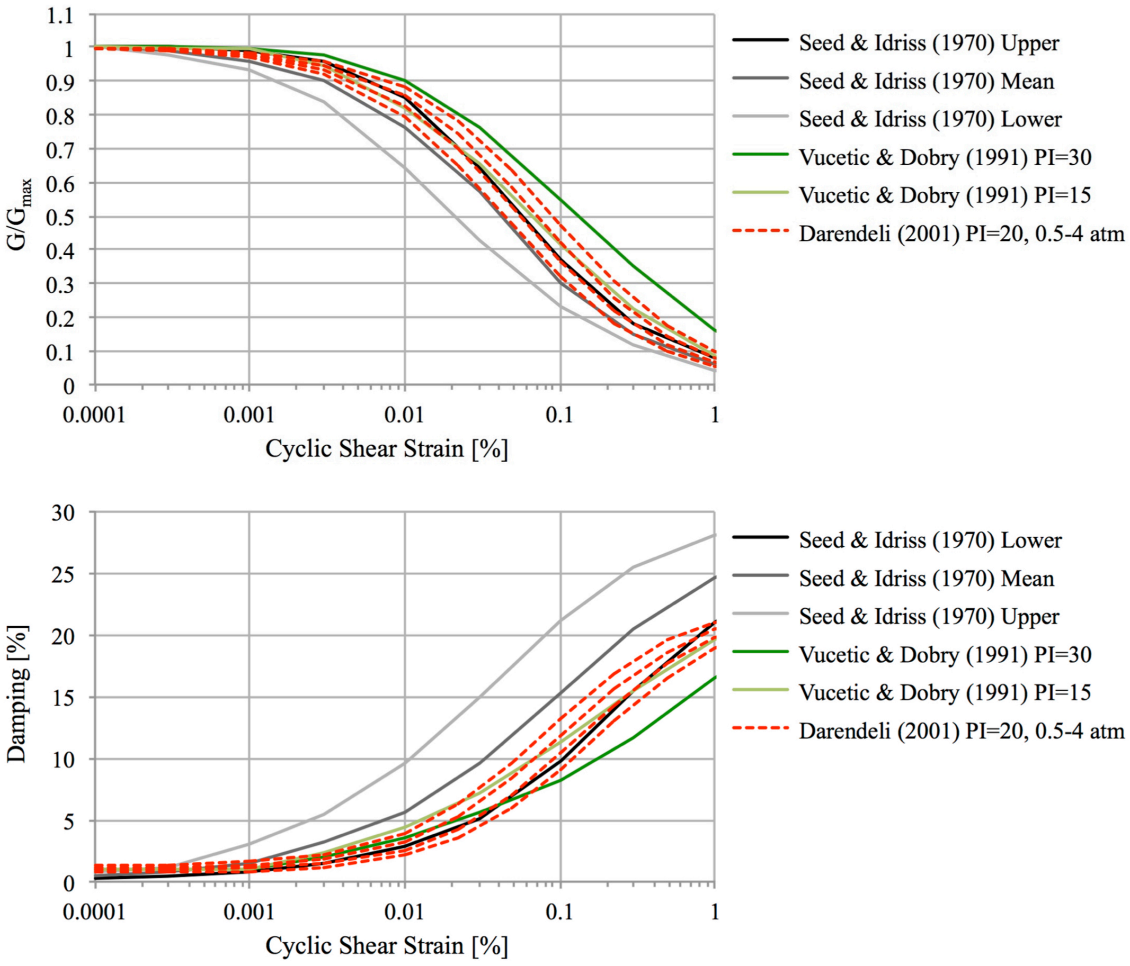

Figure 2.8 **Comparison of Darendeli (2001) PI=20 shear-modulus reduction and material damping curves with other commonly used nonlinear curves.**

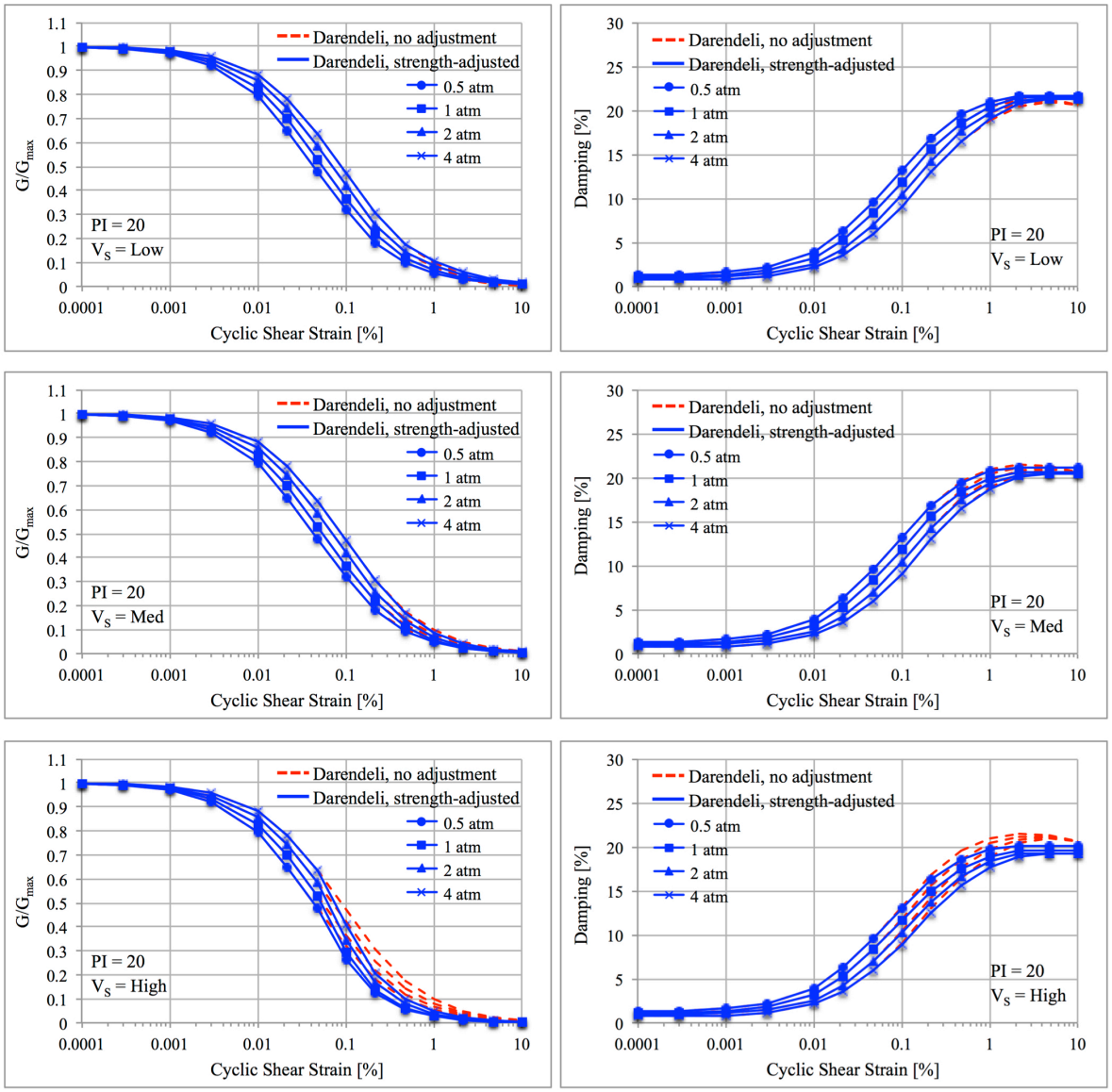

Figure 2.9 **Final strength-adjusted Darendeli (2001) PI=20 shear-modulus reduction and material damping curves used in dynamic analyses, along with as-published Darendeli (2001) PI=20 curves for comparison.**

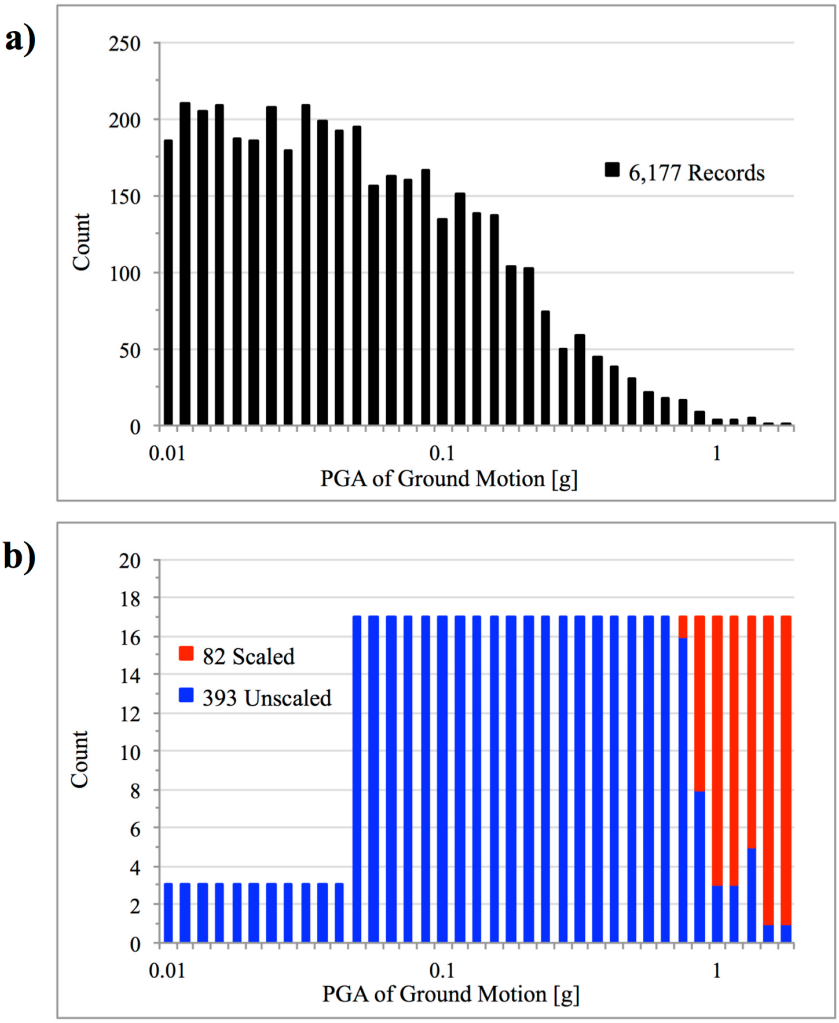

Figure 2.10 **Histograms of PGA for a) data comprising 6,177 records that meet minimum screening criteria and b) 475 selected records.**

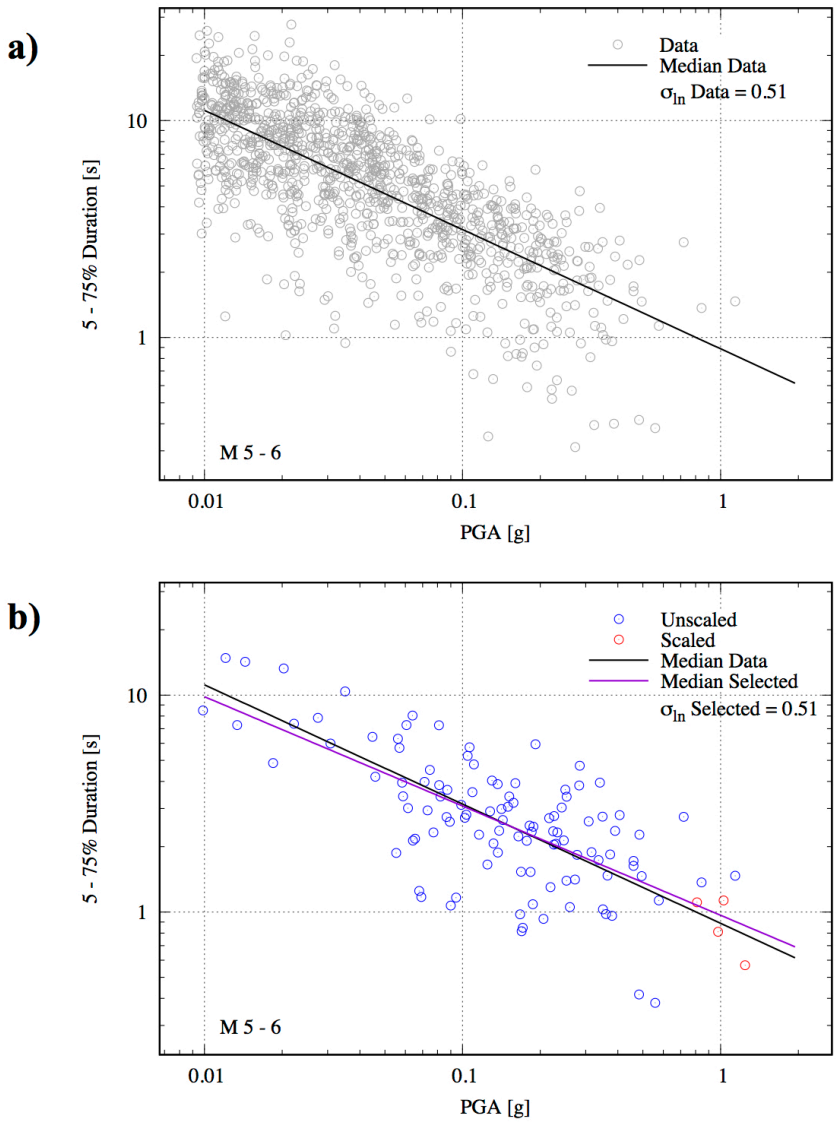

Figure 2.11 **5-75% durations for a) data and b) selected records with M 5-6.**

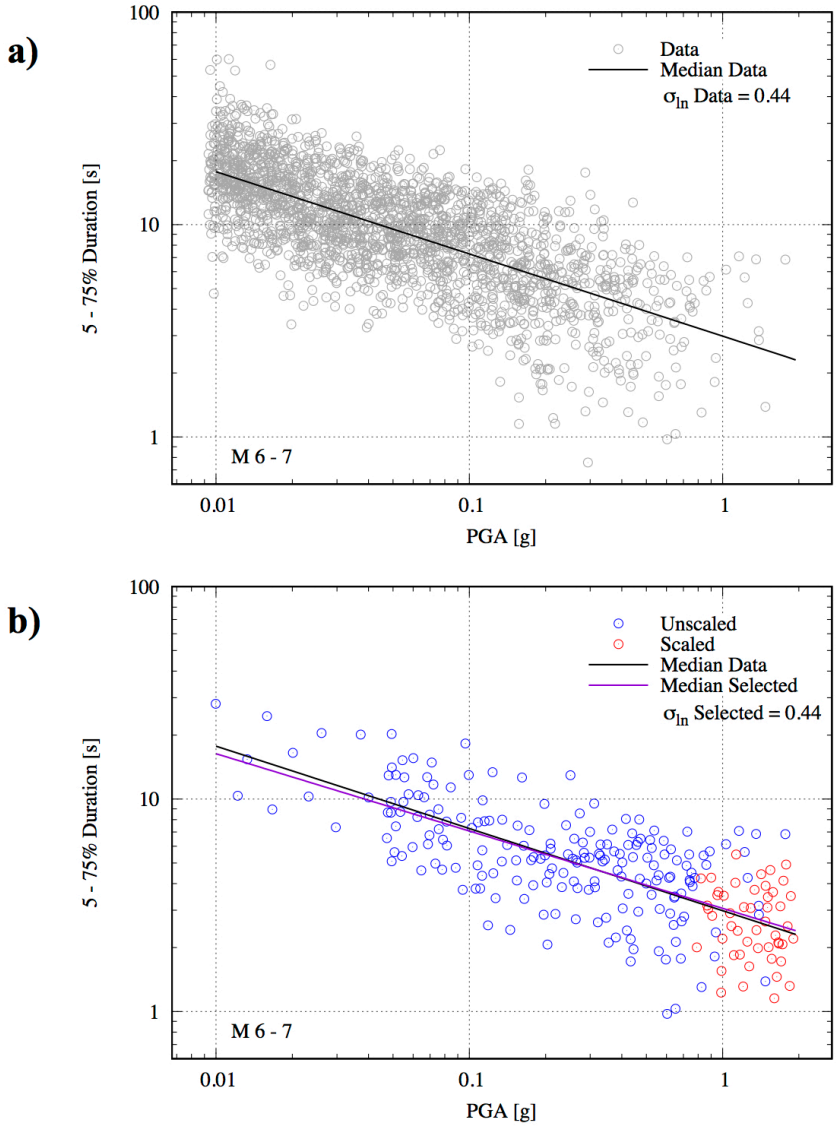

Figure 2.12 5-75% durations for a) data and b) selected records with M 6-7.

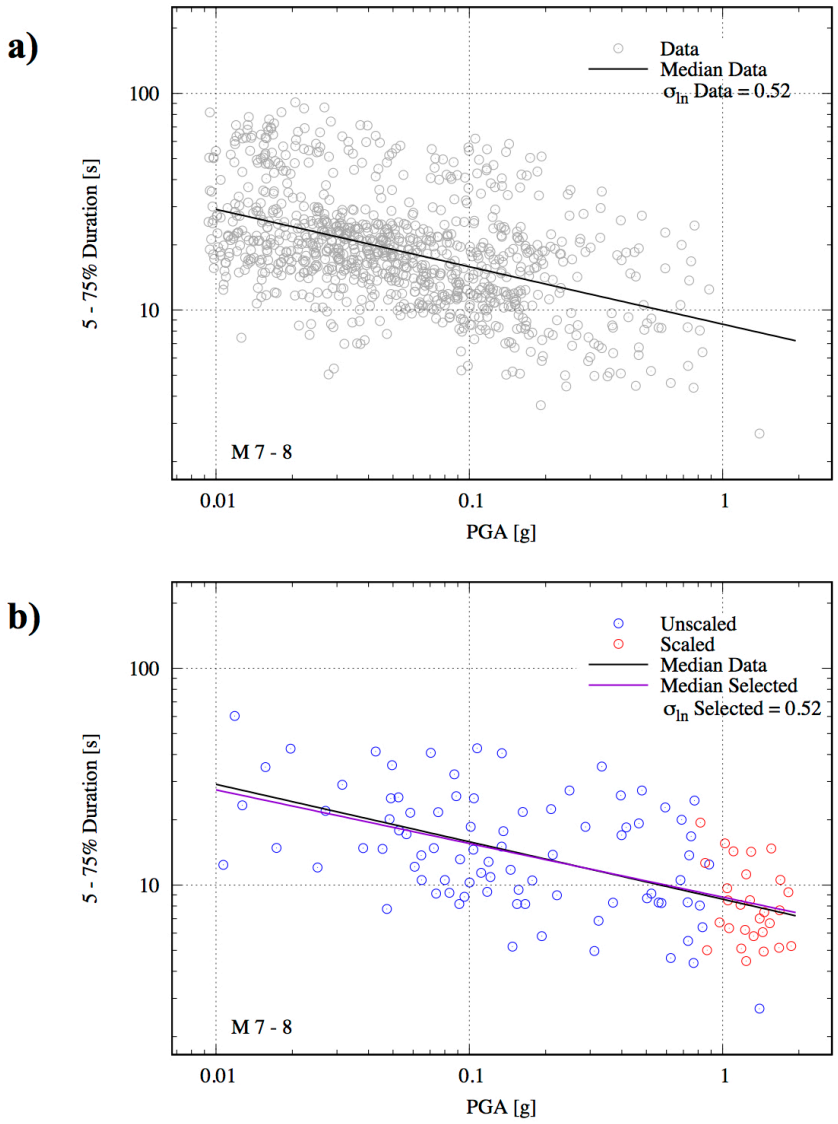

Figure 2.13 **5-75% durations for a) data and b) selected records with M 7-8.**

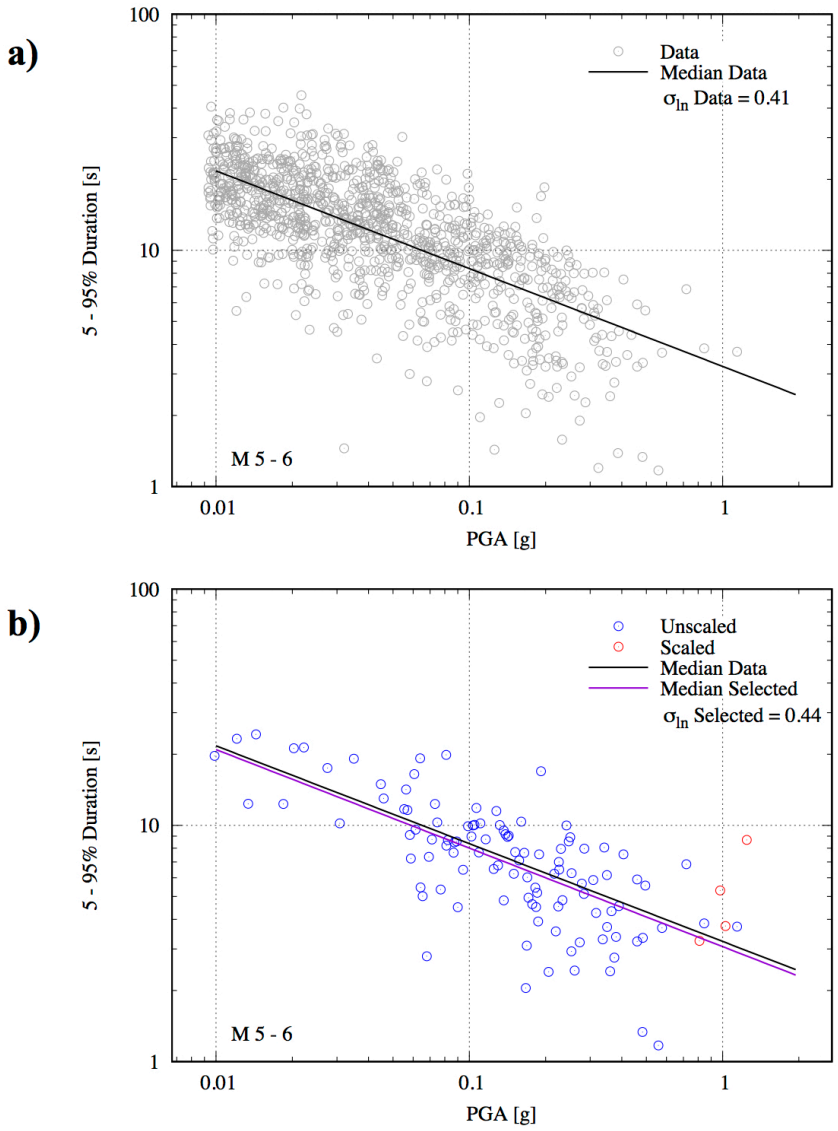

Figure 2.14 5-95% durations for a) data and b) selected records with M 5-6.

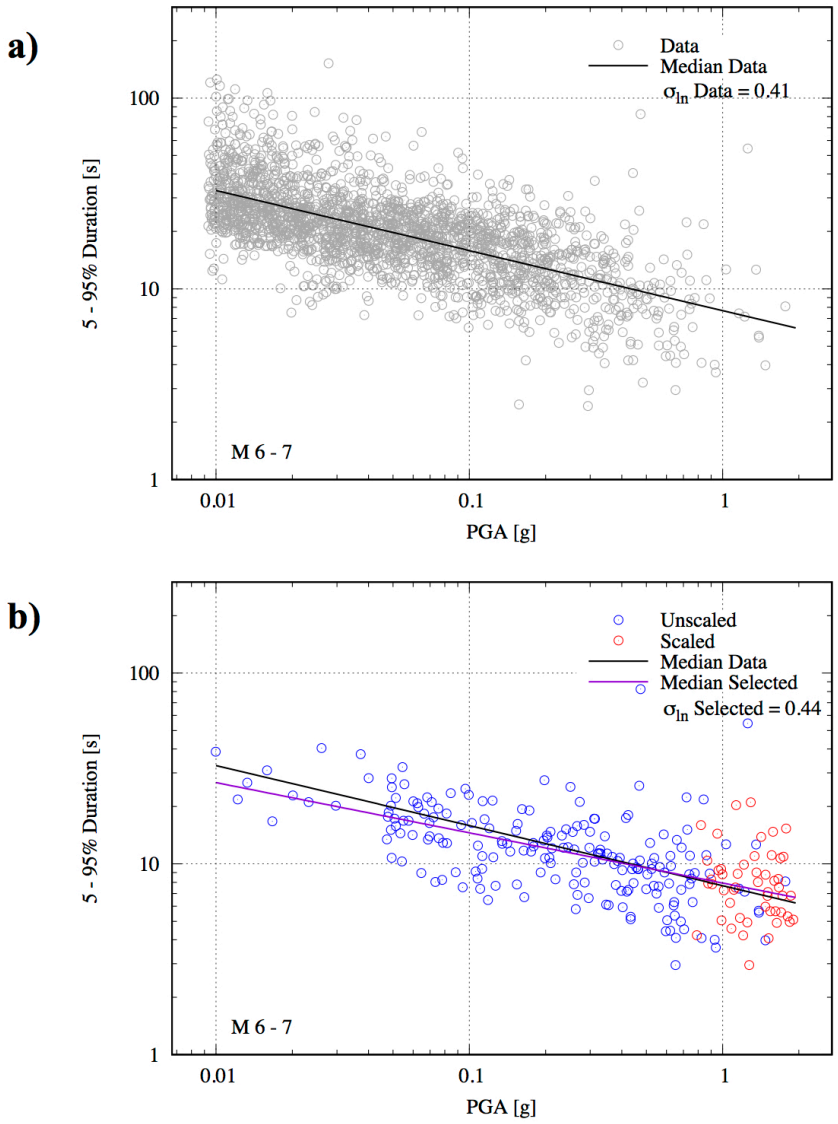

Figure 2.15 5-95% durations for a) data and b) selected records with M 6-7.

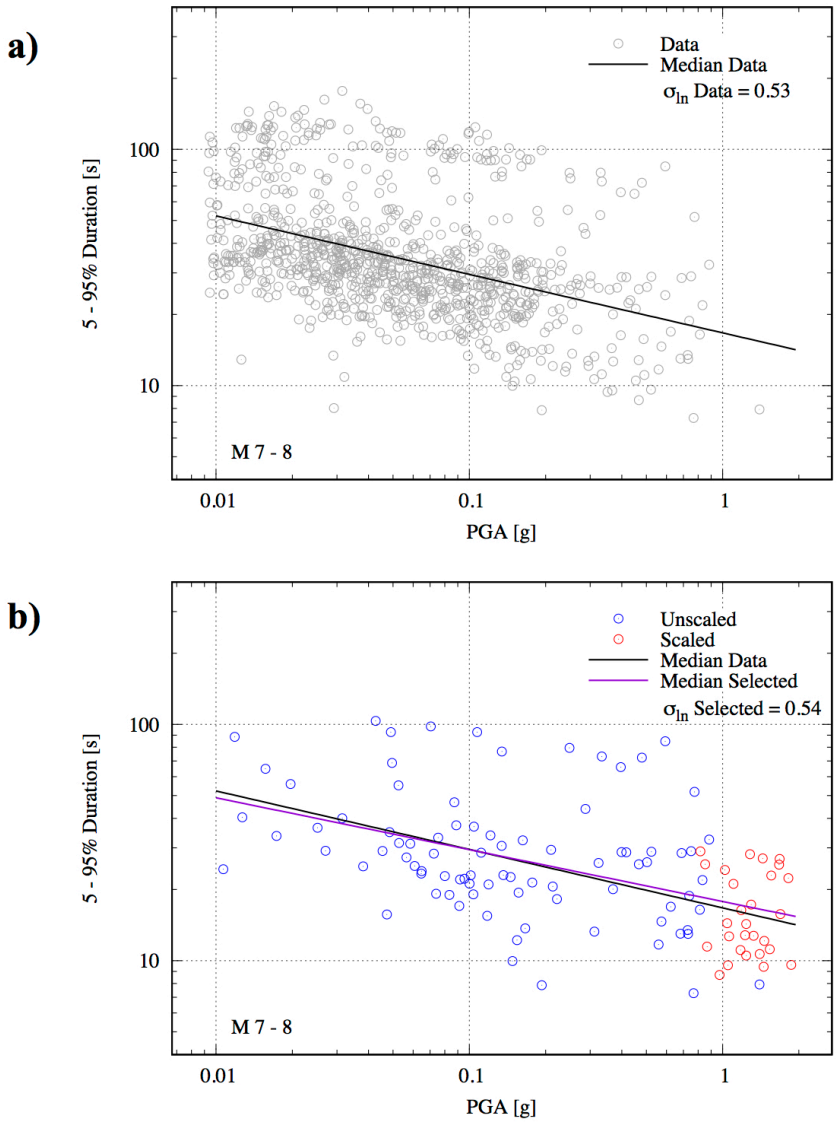

Figure 2.16 **5-95% durations for a) data and b) selected records with M 7-8.**

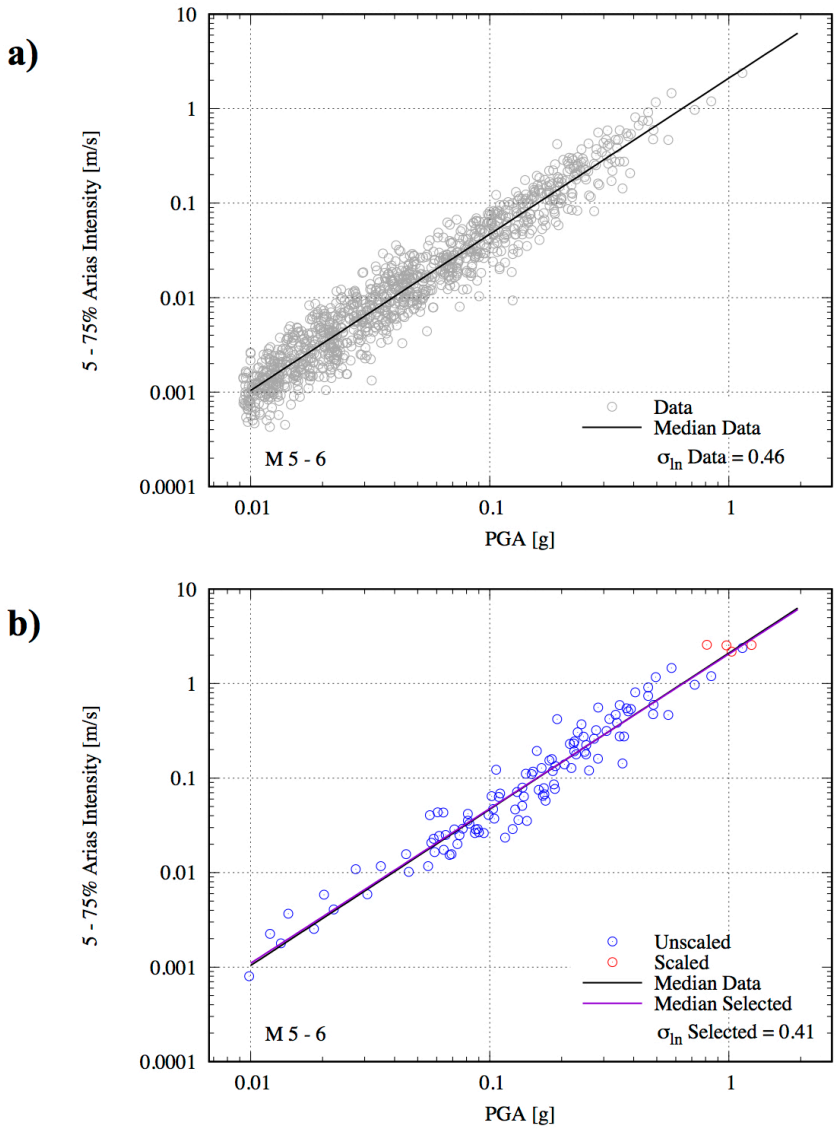

Figure 2.17 **5-75% Arias intensities for a) data and b) selected records with M 5-6.**

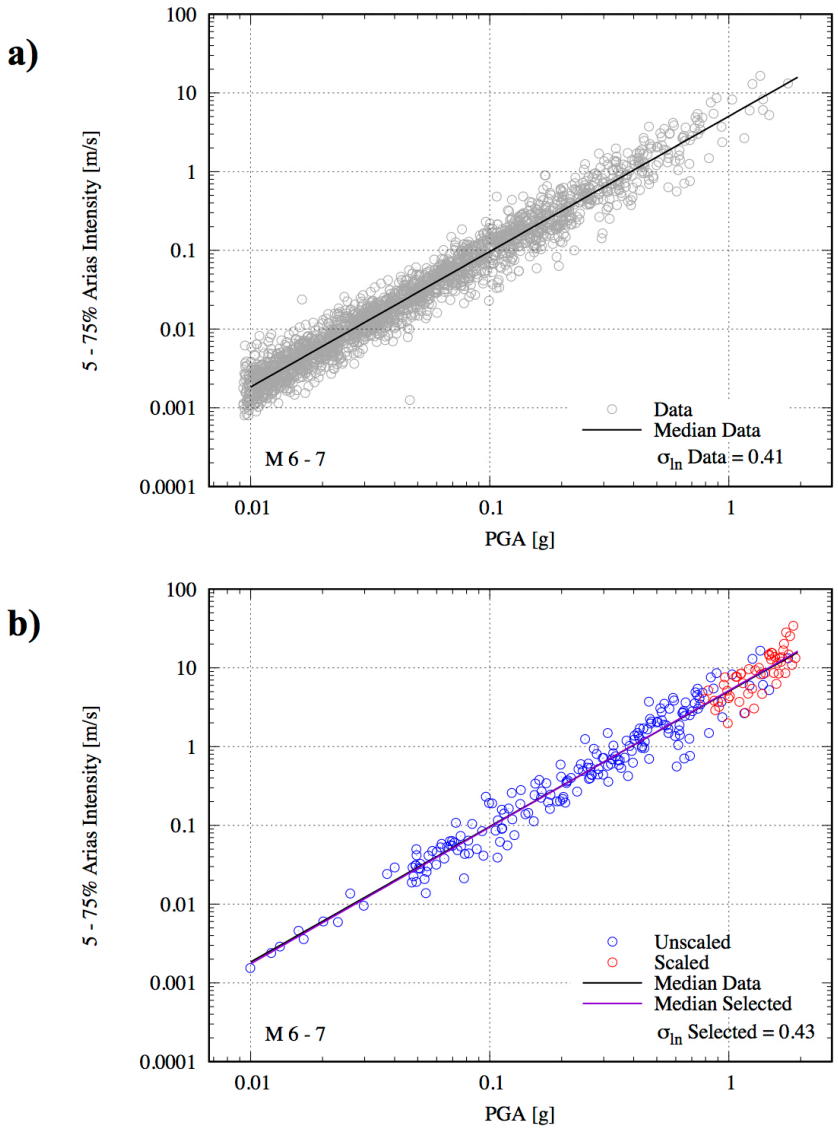

Figure 2.18 5-75% Arias intensities for a) data and b) selected records with M 6-7.

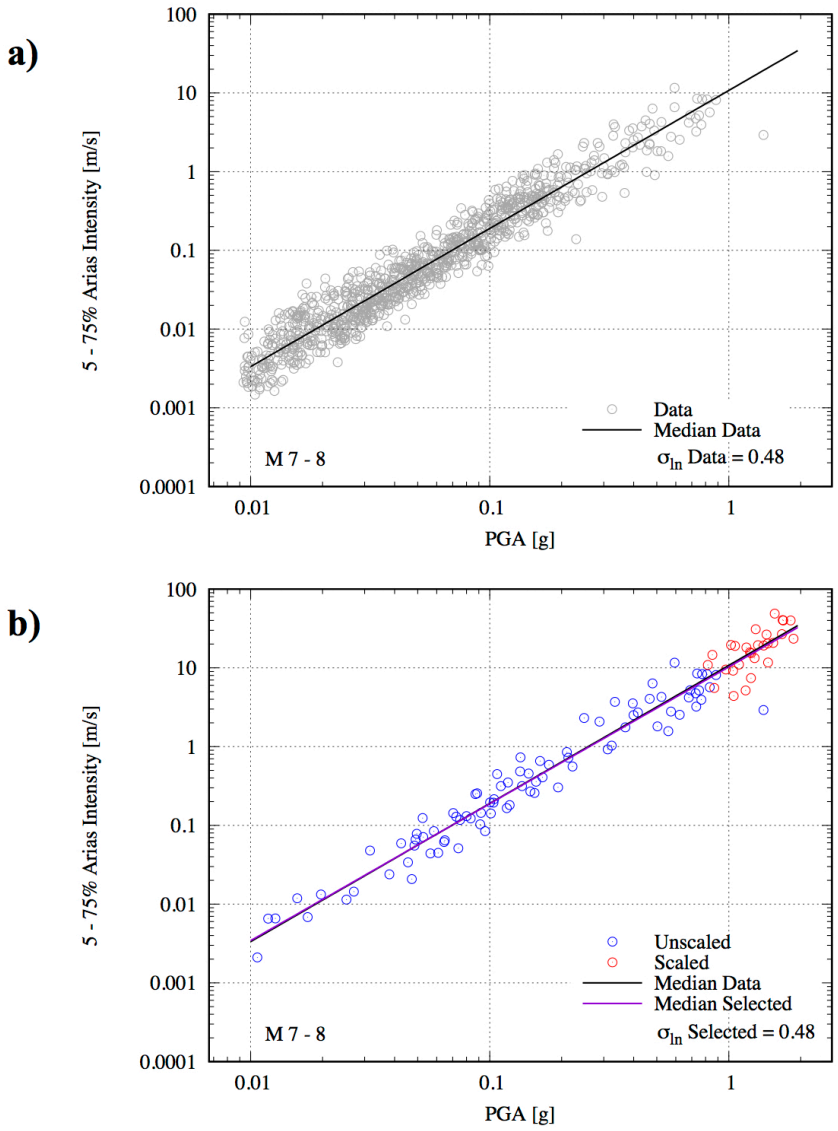

Figure 2.19 **5-75% Arias intensities for a) data and b) selected records with M 7-8.**

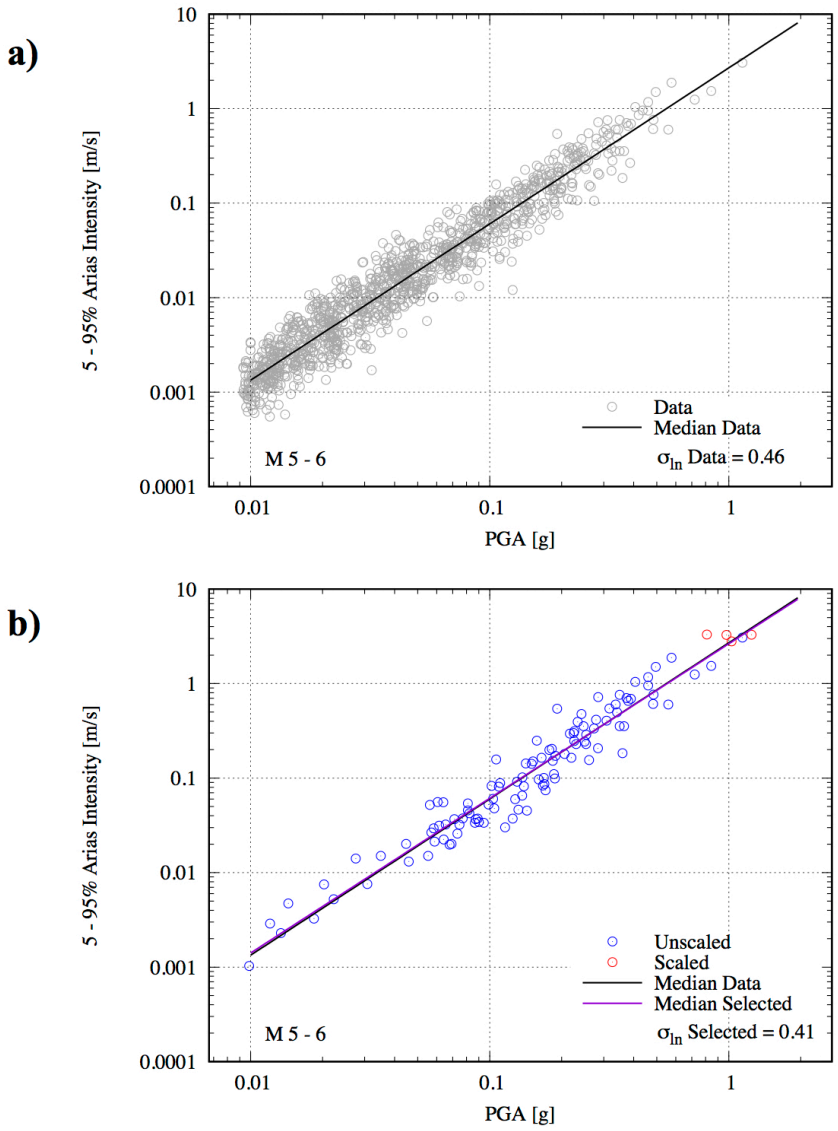

Figure 2.20 **5-95% Arias intensities for a) data and b) selected records with M 5-6.**

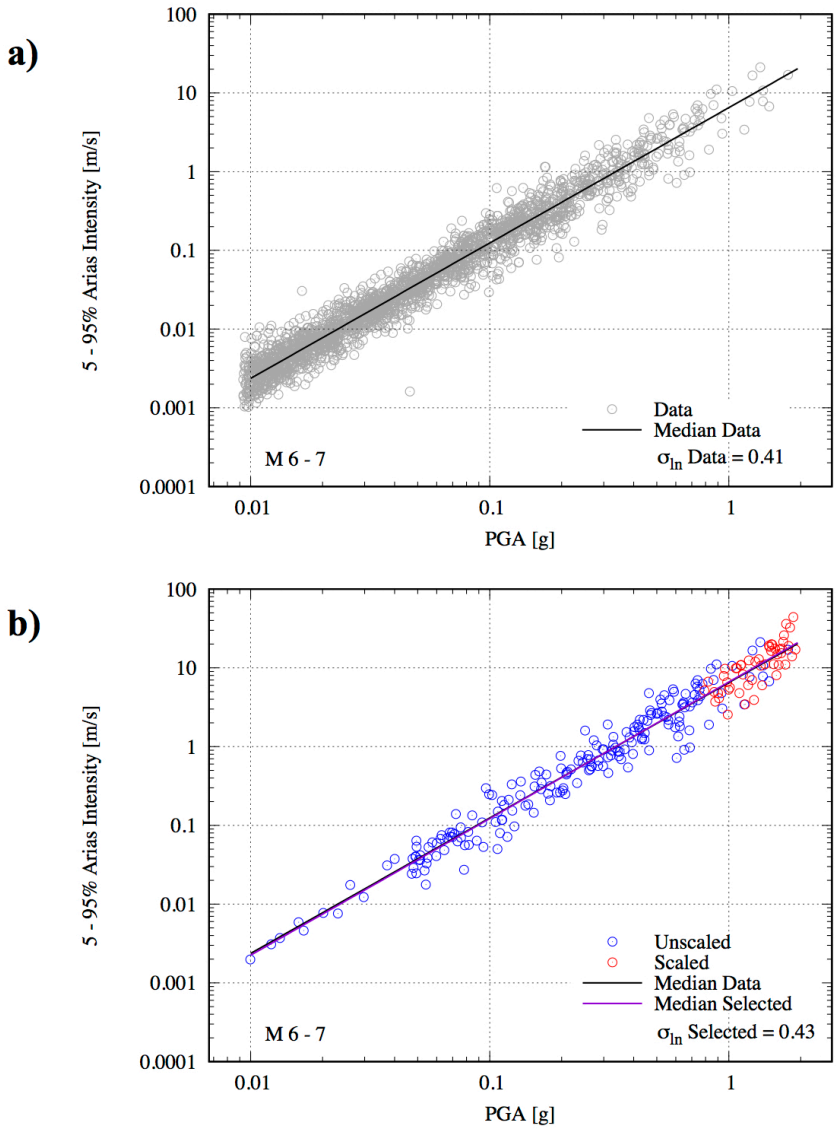

Figure 2.21 **5-95% Arias intensities for a) data and b) selected records with M 6-7.**

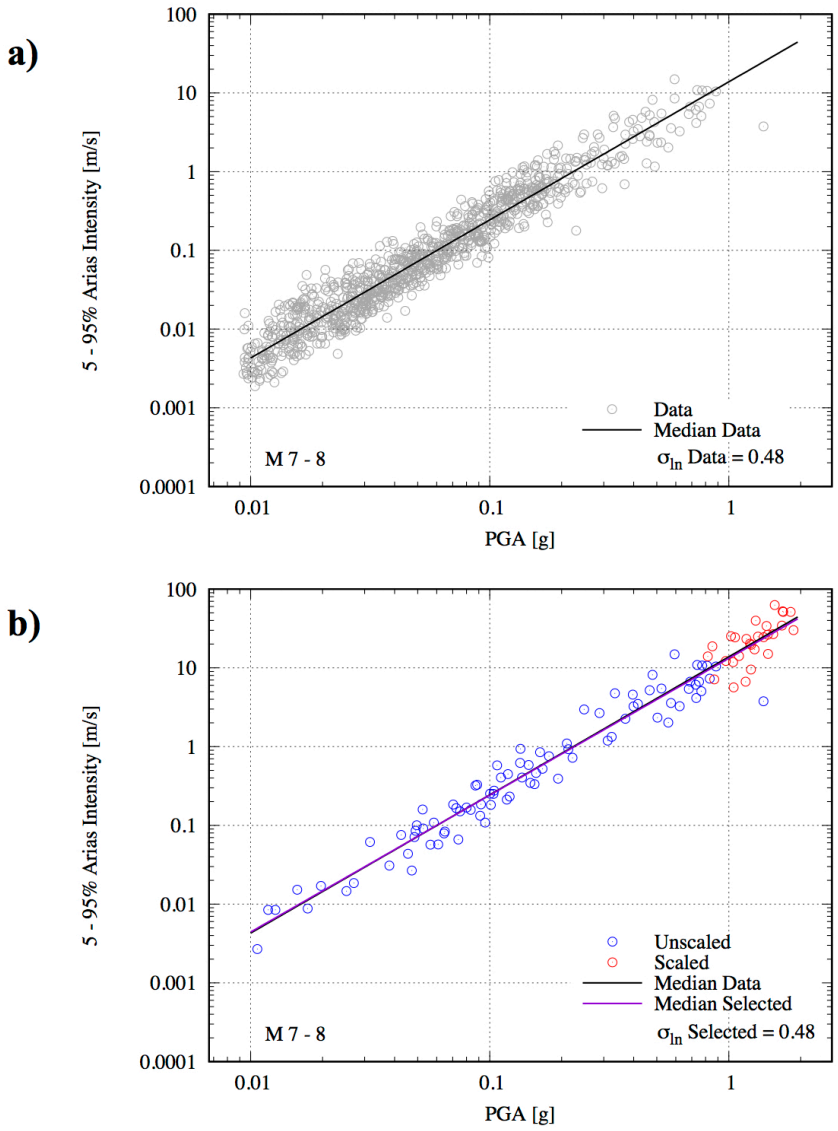

Figure 2.22 **5-95% Arias intensities for a) data and b) selected records with M 7-8.**

3 RESULTS OF DYNAMIC ANALYSES

3.1 Introduction

The 950 input ground motions were propagated through the twelve representative dams, each with two potential sliding surfaces, resulting in 22,800 average acceleration time histories of potential sliding masses. The results of the dynamic analyses are discussed herein and the key behavior of the earthen dams when subjected to earthquake ground motions is highlighted.

Many of the plots and comparisons presented here are similar to those typically found in a consulting report for a dynamic analysis of an earthen dam (i.e., individual input acceleration time histories and subsequent response time histories at nodes within a dam). Other results are presented with a more macroscopic view and look at overall trends in dam response across a large range of input ground-motion intensities (i.e., input motion and crest PGAs for a given representative dam subjected to 950 input ground motions with PGAs ranging from 0.01 to 2.0 *g*). Transfer functions are computed and used to build the transfer-function model in Chapter 4. Although many of the results presented here are not necessary to build the transfer-function model, they are presented to highlight trends in the data and to demonstrate that the dynamic behavior of the representative dams is reasonable.

3.2 Amplification through Dam Materials

In addition to computing time histories of the potential sliding masses, the QUAD4MU program was used to compute acceleration time histories at designated nodes within the representative dams. These designated nodes were specified at approximately the centerline of the dam, between the foundation and crest, in a vertical array. Figure 3.1 shows the locations of the designated nodes for the representative dam with a height of 50 *ft* as an example. This was done to examine how the materials in the dam amplify the input motion.

The results from three dynamic analyses are presented as representative examples of the full suite of dynamic runs. The examples use Dam 5, which has a height of 50 *ft* and a medium shear-wave velocity profile. The three example ground motions include a record with a PGA of 0.15 *g* from the 2004 M 6 Parkfield, CA earthquake, a record with a PGA of 0.42 *g* from the 1989 M 6.9 Loma Prieta, CA earthquake, and a record with a scaled PGA of 1.12 *g* from the 1999 M 7.6 Chi-Chi, Taiwan earthquake. The results from each dynamic analysis are presented as a single figure with eight plots. The four plots on the left display the acceleration time histories from the designated nodes, along with the input acceleration time history record, which is an outcropping motion, applied below the finite element mesh with a compliant base. The top right plots display a profile view of the dynamically-induced peak horizontal accelerations and a

profile view of the dynamically-induced effective shear strains (in percent). The effective shear strains are the maximum shear strains multiplied by 0.65. The bottom right plots display the final iterated values of damping and normalized shear modulus for each finite element in the numerical model of the dam. These nonlinear values are plotted versus shear strain, which is the same effective shear strain displayed in the profile view.

The results from the first example dynamic analysis are shown in Figure 3.2. The input acceleration time history is the Parkfield record with a PGA of 0.15 *g*. The nodal time histories show the amplification of the record as the ground motion is propagated through the materials of the dam, reaching a PGA of 0.52 *g* at the crest. This corresponds to an amplification ratio of 3.47 between the input motion PGA, which is an outcropping rock motion, and the crest response PGA. The profile view of dynamically-induced peak horizontal accelerations shows the relatively uniform amplification of the input ground motion through the materials of the dam up to the crest. This behavior is expected, given the idealized shear-wave velocity profile where the minimum shear-wave velocity is at the crest and the shear-wave velocity increases gradually with depth. The profile view of the dynamically-induced effective shear strains shows that the highest shear strains occur in the body of the dam, toward the center. The effective shear strains induced in the embankment range from less than 0.01% to 0.04%, with an average of 0.03%. The final iterated values of damping and G/G_{max} are shown for each element within the embankment of the dam. Material damping values range from 2 to 8%.

The results from the second example dynamic analysis are shown in Figure 3.3. The input acceleration time history is the Loma Prieta record with a PGA of 0.42 *g*. The PGA at the crest of the dam is 1.23 *g*, corresponding to an amplification ratio of 2.93 between the input motion PGA and the crest response PGA. The effective shear strains induced in the embankment range from less than 0.01% to 0.18%, with an average of 0.10%. Material damping values range from 3 to 16%.

The results from the third example dynamic analysis are shown in Figure 3.4. The input acceleration time history is the scaled Chi-Chi record with a PGA of 1.12 *g*. The PGA at the crest of the dam is 2.07 *g*, corresponding to an amplification ratio of 1.85 between the input motion PGA and the crest response PGA. These results indicate that the dynamic analyses are overestimating the amplification in the dam materials, as empirical observations of PGAs measured at the crests of real dams exhibit a decrease in amplification ratio with increasing ground motion intensity. This is discussed further in the following section. The effective shear strains induced in the embankment range from less than 0.01% to 2.58%, with an average of 0.44%. Material damping values range from 3 to 21%.

Many of the high intensity ground motions, including the Chi-Chi record used in the third example dynamic analysis, induce shear strains in the dam that are beyond the strain range where the equivalent-linear procedure is typically considered applicable. Additionally, whether an equivalent-linear or fully nonlinear procedure is used, there are considerable uncertainties associated with the shear-modulus reduction and material damping curves used to describe the nonlinear behavior of the dam materials at these high strains. Despite these concerns, and given that the purpose of the dynamic analyses is to provide a basis for a simplified model, it is preferred to keep these analyses and include them in the development of the transfer-function model. To address the epistemic uncertainty associated with the nonlinear curves at high shear strains, future work includes running dynamic analyses with alternative nonlinear curves and

expanding the transfer-function model for these different relationships. To address the impact of using the equivalent-linear procedure for high intensity ground motions, future work includes running fully nonlinear analyses, assessing the impact of the equivalent-linear method on the resulting deformations, and proposing appropriate adjustments to the transfer-function model.

3.3 Peak Crest Accelerations

Figures 3.5 and 3.6 plot the PGA at the crest of the dam from the dynamic analyses versus the input motion PGA for the twelve representative dams. The input motion is an outcropping rock acceleration time history. Figures 3.7 and 3.8 plot the input-to-crest amplification ratio versus the input motion PGA for each of the dams. The results are displayed for each dam individually, and each plot contains 950 data points from the 950 input ground motions. Overall, dams with different heights and shear wave velocity profiles behave similarly with respect to the peak crest accelerations and amplification ratios over a range of input motion intensities. Shorter dams exhibit more scatter in the crest PGAs at low input motion intensities. Dams with high shear wave velocities have a more distinct flattening trend in the crest PGAs at high input motion intensities. This somewhat unusual flattening trend is discussed further in the following paragraphs.

Figures 3.9 and 3.10 plot the crest PGA versus input motion PGA and input-to-crest amplification ratio versus input motion PGA for all dams on the same graph, making it easier to observe general trends. Figure 3.9 shows an increasing slope region, followed by a flat trend in the crest versus input motion PGAs. The flat amplification region for high-intensity motions is unusual. Examination of the results revealed that this flat behavior is caused by performing dynamic analyses for high-intensity motions using the equivalent-linear method, combined with the use of shear-modulus reduction curves that model significant strength reduction at high shear strains. Note that the Darendeli (2001) nonlinear curves are consistent with stress-strain behavior that models a strength envelope, and at high shear strains the stresses in the dam materials – especially near the crest of the dam – are in the flat region of the stress-strain curves. These factors result in significant softening of the system, causing a break in the crest PGA curve.

The flat amplification region for high-intensity motions is exacerbated by the use of confining-pressure dependent shear-modulus reduction curves, which assign very low shear strengths to the finite elements near the crest of the dam. The flat amplification region is also exacerbated by the use of the Yee et al. (2013) procedure with relatively low shear strengths. The Yee et al. (2013) procedure further reduces the shear modulus at high shear strains – particularly for the dams with high shear wave velocities – which is why dams with high shear wave velocities have a more distinct flattening trend in the crest PGAs at high input motion intensities.

Figure 3.10 shows the large range in amplification ratios for input ground motions ranging from a PGA of 0.01 *g* to about 0.6 *g*. The amplification ratios range from about 1 to 7 up to an input motion PGA of 0.6 *g*, after which the range appears to narrow and the slope changes from a relatively flat slope at low to moderate PGAs, to a decreasing slope at high PGAs. The amplification ratios start to drop below 1 when the input motion PGA is about 1 *g*, indicating that the PGA at the crest is actually less than the input motion PGA. Although amplification ratios less than 1 are consistent with empirical observations at high input motion intensities, this expected behavior is not necessarily a sign that the equivalent-linear method is modeling the

nonlinear behavior at high shear strains in a meaningful way, but rather a result of using the equivalent-linear method with shear-modulus reduction curves that model significant strength reduction at high shear strains, as discussed previously.

In a typical site-specific study, available empirical observations are used to calibrate the numerical model of the dam. While the idealized dams used to produce the synthetic dataset are not models of specific physical dams, it is worthwhile to compare the PGAs at the crest of the representative dams from the dynamic analyses to recorded PGAs from case histories of earth and rockfill dams that experienced real earthquakes. The case histories used for this comparison come from three primary sources. The first is Harder et al. (1998), who presented more than 20 case histories of earth and rockfill dams, including many from the Loma Prieta earthquake. The second is the WES data, which was added to the Harder plot by Cameron (1996). The third is Yu et al. (2012), who performed an extensive review of earth and rockfill dam case histories and compiled 43 measurements of peak crest accelerations and peak ground accelerations from the literature, including many from earthquakes in Japan and China. Recorded measurements were reproduced from these three sources and are plotted along with the results from the dynamic analyses in Figure 3.11 (log scales) and Figure 3.12 (linear scales). Some of the Yu et al. (2012) case histories were duplicates of the case histories from the first two sources – these duplicates were removed prior to plotting.

Note that for the dynamic analysis results, the value on the x-axis is the PGA from the input acceleration time history, which is an outcropping motion. For the empirical observations, some of the x-axis PGAs are outcropping rock motions but some of the x-axis PGAs are within motions recorded by an instrument located at the base of the dam. The majority of the California data are outcropping motions, while data from Japan tends to be within motions recorded by an instrument at the interface of the embankment and foundation. The PGA for a within motion is approximately 15% lower than the PGA from an outcropping motion. In other words, the dynamic analysis results would all shift approximately 15% to the left for a direct comparison with those empirical observations that utilize a within motion.

The results from the dynamic analyses overlap with the majority of the crest PGA records for input PGAs less than about 0.2 *g*. Both the dynamic-analysis results and the empirical observations display significant scatter in the crest PGAs. This variability in the response of the dams is primarily caused by variability in the input ground motion, and secondarily by differences in properties of the dams. There are several observed differences between the dynamic-analysis results and the empirical observations. The dynamic-analysis results are all above the 1:1 line until the input PGA exceeds about 0.6 *g*, while some empirical observations are below the 1:1 line. Interestingly, these low crest PGAs are primarily from the WES data. The most significant difference between the results is the over amplification of the crest PGAs from the dynamic analyses compared to the empirical observations for high-intensity motions. Though crest recordings at dams for high intensity ground motions are sparse (there are very few empirical observations beyond PGA = 0.4 *g*), it is clear that the dynamic analyses are overestimating the amount of amplification beyond PGAs of about 0.2 *g*. Compared to the empirical observations, the dynamic-analysis results produce higher crest PGAs, and this difference increases with increasing levels of input acceleration. The overestimation of the amplification in the dynamic analyses is a limitation of the equivalent-linear method. Specifically, the equivalent-linear method does not capture the decrease in amplification ratio of

input rock to response crest PGAs with increasing ground motion intensity observed in the empirical data.

3.4 Small-Strain Fundamental Period

The fundamental period of the dam is the period at which the earthen dam would resonate with harmonic loading. The small-strain fundamental period, T_o, is the fundamental period of the dam in the linear range of the dynamic stress-strain relationship of the embankment materials. Eighteen input ground motions that will induce small-strain amplitudes in the linear range were identified. The eighteen input ground motions have peak ground acceleration values less than 0.015 *g*. The level of strain associated with the linear range is approximately 10^{-3} percent cyclic shear strain or less. Figure 3.13 plots the shear-modulus reduction and material damping curves used in the dynamic analyses, along with the final iterated dam mesh values for one of the eighteen small-strain ground motions for Dam 5. As seen in the figure, the shear strains induced in the dam are approximately 10^{-3} percent, where the curves are flat, implying that the dam response is in the linear range. For comparison, shear-strain amplitudes estimated in dams during forced vibration testing performed to measure fundamental periods are typically on the order of 10^{-4} to 10^{-5} percent (i.e., Öner and Erdik, 1981).

The fundamental period of the finite element model is provided as an output of the dynamic analysis. These fundamental periods were compiled for each of the eighteen small-strain input ground motions, and for each of the twelve representative dams. The small-strain fundamental period is approximately constant for each dam, and does not change when the dam is subjected to the eighteen different ground motions. This means that T_o is not dependent on the properties of the ground motion when the shear-strain amplitudes induced in the dam are in the linear range. The T_o values from the eighteen ground motions were averaged to compute a single small-strain fundamental period for each dam. These values are summarized in Table 3.1. As expected, the small-strain fundamental period increases as dam height increases, and decreases as the shear-wave velocity of the dam increases. Hatanaka (1955) and Ambraseys (1960) both showed that the analytical expression for the fundamental period of an earth dam modeled as a triangular homogeneous shear-beam is expressed as:

$$T_o = \frac{2.61H}{V_S} \tag{3.1}$$

This equation is often used to approximate the small-strain fundamental period of an earthen dam. The small-strain fundamental periods calculated from the dynamic analyses in this study are about 15% higher than those calculated from Equation 3.1, with coefficients ranging from 2.89 to 3.05 rather than 2.61. This is because the representative dams are not symmetrical triangles. These coefficients are also included in Table 3.1. For simplicity, a coefficient of 3 rather than 2.61 can be used to obtain an estimate of the fundamental periods calculated from the dynamic analyses in this study.

3.5 Fundamental Period Shift

With increasing ground-motion intensity, the strains induced in the dam materials move into the nonlinear range and the fundamental period of the dam shifts to longer periods. This shift in the fundamental period of the dam is a key behavior of the dam, and it is worthwhile to compare the period shift modeled in the dynamic analyses with empirical observations at real dams. Unfortunately, empirical observations of dam period shift at real dams are sparse. Characterization of the period shift at a dam site requires multiple observations from ground motions at a range of intensity levels. Additionally, two instruments must record those ground motions – generally one at the crest of the dam to measure the system response, and one that represents the input motion at the foundation level. Fourier spectral ratios can then be computed for each event to examine changes in the natural period of the dam due to different levels of shaking.

Two case histories that characterize the dam period shift are used to compare the results of the synthetic dataset with empirical observations. The first is the analysis of Lexington Dam in California during the 1989 Loma Prieta earthquake and 1989 Lake Elseman earthquake (Makdisi et al., 1991). The second is the analysis of Kawanishi Dam in Japan during ten earthquakes, including the 2004 Chuetsu earthquake (Park and Kishida, 2019). The results from these two case histories are presented in Figure 3.14, along with the results from the most similar representative dam in the synthetic dataset for comparison. It is important to note that in the case of Lexington Dam, the input motion is a record from an instrument at the left abutment, while in the case of Kawanishi Dam, the input motion is a record from an instrument at the toe of the downstream slope. The input motions for the dynamic analyses are outcropping motions applied below the finite element mesh with a compliant base; therefore, a direct comparison to the empirical observations is not possible. Because only limited case histories are available to characterize the dam period shift, the comparison with empirical observations is still extremely valuable, despite the approximation of the abutment or toe records to actual foundation input motions.

The dam period shift is presented as T_1/T_o, which is the fundamental or first-mode period normalized by the small-strain period. For Kawanishi Dam, the natural period of the dam is close to the small-strain fundamental period up until a *PGA* of about 0.4 *g*. At these intensity levels the ratio of T_1/T_o ranges from 1.0 to 1.2. At higher levels of shaking, the dam period shifts away from the small-strain period more significantly with T_1/T_o ratios of 1.6 and 1.7. These observations fall within the range of dam period shift modeled by the dynamic analyses. The onset of nonlinearity observed in the Kawanishi dataset occurs at a slightly higher *PGA* than the dynamic analyses, but the dam period shift for an input motion *PGA* of about 0.6 *g* is consistent with the median of the dynamic analysis data. For Lexington Dam, there are not enough observations to discern when the natural period of the dam begins to shift away from the small-strain period – the observations only indicate that the onset of nonlinearity occurs somewhere between 0.08 *g* and 0.45 *g*. For the Loma Prieta event, the dam period shift is significant with a T_1/T_o ratio of 2.8. This is at the high end of the range in period shift modeled by the dynamic analyses.

Though the empirical observations from Kawanishi and Lexington Dam are not inconsistent with the range of period shift modeled by the dynamic analyses, the number of observations at high intensity ground motions is very limited. Additionally, the dynamic analysis

results presented here use shear-modulus reduction curves that model significant strength reduction at high shear strains, resulting in relatively high T_1/T_o ratios for high-intensity ground motions. To model a more moderate loss of shear strength and corresponding dam period shift, a set of dynamic analyses were carried out with the Vucetic and Dobry (1991) PI=30 curves, the results of which are discussed in Chapter 5.

3.6 Effective Shear Strains

The dynamically-induced effective shear strains were compiled for all dynamic analyses. Each finite element in the numerical model of the dam has an effective shear strain value from the final iteration of a given dynamic analysis. The log-mean of the effective shear strains from all elements were computed and these average effective shear strains are plotted against the PGA of the input ground motion for the twelve representative dams in Figures 3.15 and 3.16. Note that only the mesh elements that comprise the embankment were used to compute the average – the foundation elements were excluded. The results are displayed for each dam individually, and each plot contains 950 data points from the 950 input ground motions.

The average effective shear strains are plotted against additional ground-motion intensity measures in Figures 3.17 – 3.22. The additional ground-motion intensity measures are PGV, PSA(T_o), and PSA($2T_o$). Overall, the PGA of the ground motion is a good predictor of shear strain for all dams when the input ground motion has a low intensity. PGV is generally a worse predictor of shear strain, except for the tallest dams with the lowest shear-wave velocities, where PGV does a good job of explaining shear strain across the full range of intensities. When the shear strains are plotted against the pseudo-spectral acceleration of the ground motion, PSA(T_o) generally does a better job of explaining strains at low ground-motion intensities, while PSA($2T_o$) does a better job of explaining strains at high ground-motion intensities.

As mentioned previously, many of the high intensity ground motions induce shear strains in the dam that are beyond the strain range where the equivalent-linear procedure is typically considered applicable. Given that the purpose of the dynamic analyses is to provide a basis for a simplified model, it is preferred to keep these analyses and include them in the development of the transfer-function model. Future work can address the impact of using the equivalent-linear procedure for high intensity ground motions and propose appropriate adjustments to the model.

3.7 Shear-Induced Deformations

Each dynamic analysis from QUAD4MU produces two time histories of average acceleration – one for the potential deep sliding mass and one for the potential shallow sliding mass. A shear-induced permanent deformation can be estimated using the average acceleration time history, yield acceleration, and Newmark-type procedure. The QUAD4MU program provides the average acceleration time history for the potential sliding mass. The yield acceleration, k_y, is determined from a limit-equilibrium, pseudo-static slope stability analysis, and represents the acceleration at which a potential sliding surface would develop a factor of safety of one. For a specified potential sliding mass, the average acceleration time history of that mass is compared with the yield acceleration. When the average acceleration of the sliding mass exceeds the yield acceleration, downslope movement is assumed to occur along the direction of the failure plane.

Movement decelerates as the level of the induced acceleration drops below the yield acceleration, and stops when the relative velocity of the sliding mass reaches zero. The accumulated shear-induced permanent deformation is calculated by double-integrating the average acceleration time history of the sliding mass over the area where k_y is exceeded. This deformation utilizes the standard polarity of the average acceleration time history. A second deformation is computed from the reverse polarity case.

Figures 3.23 to 3.25 illustrate the Newmark-type procedure and report the resulting standard polarity Newmark deformations for the three example dynamic analyses discussed previously for Dam 5. Each figure contains a time history of the input ground motion, the average acceleration of the potential sliding mass, the velocity of the potential sliding mass, and the accumulated Newmark deformation. These examples all use a yield coefficient of 0.1, but the yield coefficient can be changed, or a range of yield coefficients can be used. The deformations notably increase from 2 *cm*, to 11 *cm*, to 158 *cm* as the intensity of the input ground motion increases from a PGA of 0.15 *g*, to 0.42 *g*, to 1.12 *g*. Another observation from Figures 3.23 to 3.25 is that the average acceleration time history of the potential sliding mass contains less high-frequency content compared to the input time history, particularly for the Loma Prieta and Chi-Chi records. The change in frequency content can be explained in part by the cumulative effect of incoherent motion in the sliding mass, resulting in an average or equivalent acceleration for the sliding mass as a whole, without all of the detail of the motions from each element within the block. Additionally, the softer soil layers in the dam embankment de-amplify or filter out some of the high frequency motions.

Figures 3.26 and 3.27 plot the Newmark deformations from all dynamic analyses against the PGA of the input ground motion for each dam. Each plot displays both the standard and reverse polarity Newmark deformations calculated from the average acceleration time histories. These results are for the deep failure surface and utilize a yield coefficient of 0.1. The yield coefficient can be changed, but it is useful to use the same k_y here in order to make comparisons. The deformations occupy a wide range at a given ground-motion intensity, and the variability of the input ground motion leads to variability in the estimated deformations.

PGA is a better predictor of shear-induced deformation for shorter dams and dams with high shear-wave velocities than it is for taller dams and dams with low shear-wave velocities, indicating that PGA works well for dams with short natural periods. This is consistent with the work by Saygili and Rathje (2008), who found that PGA was one of the most efficient scalar ground motion parameters for their dataset of Newmark displacements calculated for rigid sliding masses (i.e., systems with short natural periods). The deformations can be plotted against any intensity measure from the input ground motions. The deformations are plotted against PSA($1.5T_o$) and PGV in Figures 3.28 – 3.31. PSA($1.5T_o$) is a better predictor of shear-induced deformation than PGA and overall works well across all dam heights and shear-wave velocities. This is consistent with Travasarou (2003), who found that PSA($1.5T_o$) was overall the most efficient ground motion parameter when a range of stiff and flexible slopes were considered. PGV does a good job explaining the shear-induced deformations for high intensity ground motions, but is not a good predictor of deformations for low intensity ground motions. The predictive power of PGV for high intensity ground motions is consistent with Saygili and Rathje (2008) for rigid sliding masses and Travasarou (2003) for rigid and deformable sliding masses.

Looking at the magnitude of the deformations for different dams, the 25 and 50 *ft* dams generally have higher estimated deformations than the 100 and 150 *ft* dams. This is because, for the shorter dams, the natural period of the dam tends to align with the periods of the ground motion that have the highest amplitudes, while for the taller dams, the natural period of the dam is generally longer than the periods of the ground motion with the most energy. Figures 3.32 and 3.33 illustrate this point by plotting the mean period (T_m) of every input ground motion on top of the first-mode period of the dam (T_1) from every dynamic analysis for each dam. The first-mode period of the dam is extracted from the QUAD4MU output file for each dynamic analysis. The mean periods of the 950 input ground motions range from 0.1 to 1.0 *s*, with a log-mean of 0.4 *s*. The shorter dams have natural periods that elongate or shift into the range of mean periods from the ground motions, while the first-mode periods of the taller dams shift to periods longer than 1.0 *s*, away from the mean periods of the ground motions. This is consistent with Rathje and Antonakos (2011), who developed a predictive model for sliding displacement of flexible slopes based on one-dimensional site response calculations. Their model estimates the largest displacements when the small-strain natural period of the sliding mass, T_s, is about 0.1 – 0.2 *s* (similar to the T_o values of the 25 and 50 *ft* dams in this study). Sliding masses with these small-strain natural periods have an opportunity to elongate into the range of the mean periods of the ground motion. Their model estimates significantly smaller displacements for sliding masses with small-strain natural periods of 0.3 *s* or longer, which elongate past the range of the mean periods of the ground motion.

3.8 Summary

Representative dams were subjected to earthquake ground motions, and the results were discussed in terms of the dynamic behavior of the dams. Amplification trends were presented with plots of input motion vs. crest PGA, and included comparisons with recorded base and crest PGAs from case histories. The crest PGAs from the dynamic analyses are consistent with empirical recordings at low to moderate ground motions, and potentially over-predict the crest PGAs at high ground motions, where no empirical recordings are available. Small-strain fundamental periods for the representative dams were calculated from the dynamic analyses and can be approximated as $3H/V_S$. Shear-induced deformations were calculated from the average acceleration time history for a potential sliding mass using a yield acceleration and the Newmark sliding-block procedure. When subjected to the same input ground motions, dams with natural periods that line up with periods of the ground motion that have the highest amplitudes experience higher deformations.

Table 3.1 **Small-strain fundamental period, T_o, of representative dams.**

Dam No.	Height [ft]	V_S Profile	V_S Avg [ft/s]	T_o [s]	coeff. x: $T_o = xH/V_S$
1	25	Low	500	0.15	3.04
2	25	Medium	700	0.11	3.05
3	25	High	915	0.08	3.04
4	50	Low	550	0.27	2.96
5	50	Medium	770	0.19	2.97
6	50	High	1025	0.15	2.97
7	100	Low	610	0.49	2.90
8	100	Medium	860	0.34	2.92
9	100	High	1160	0.26	2.96
10	150	Low	660	0.68	2.91
11	150	Medium	920	0.48	2.89
12	150	High	1255	0.35	2.95

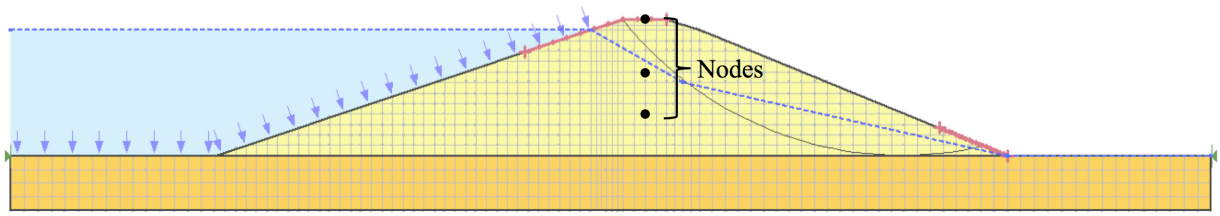

Figure 3.1 **Locations of designated nodes within the dam to examine acceleration time history response.**

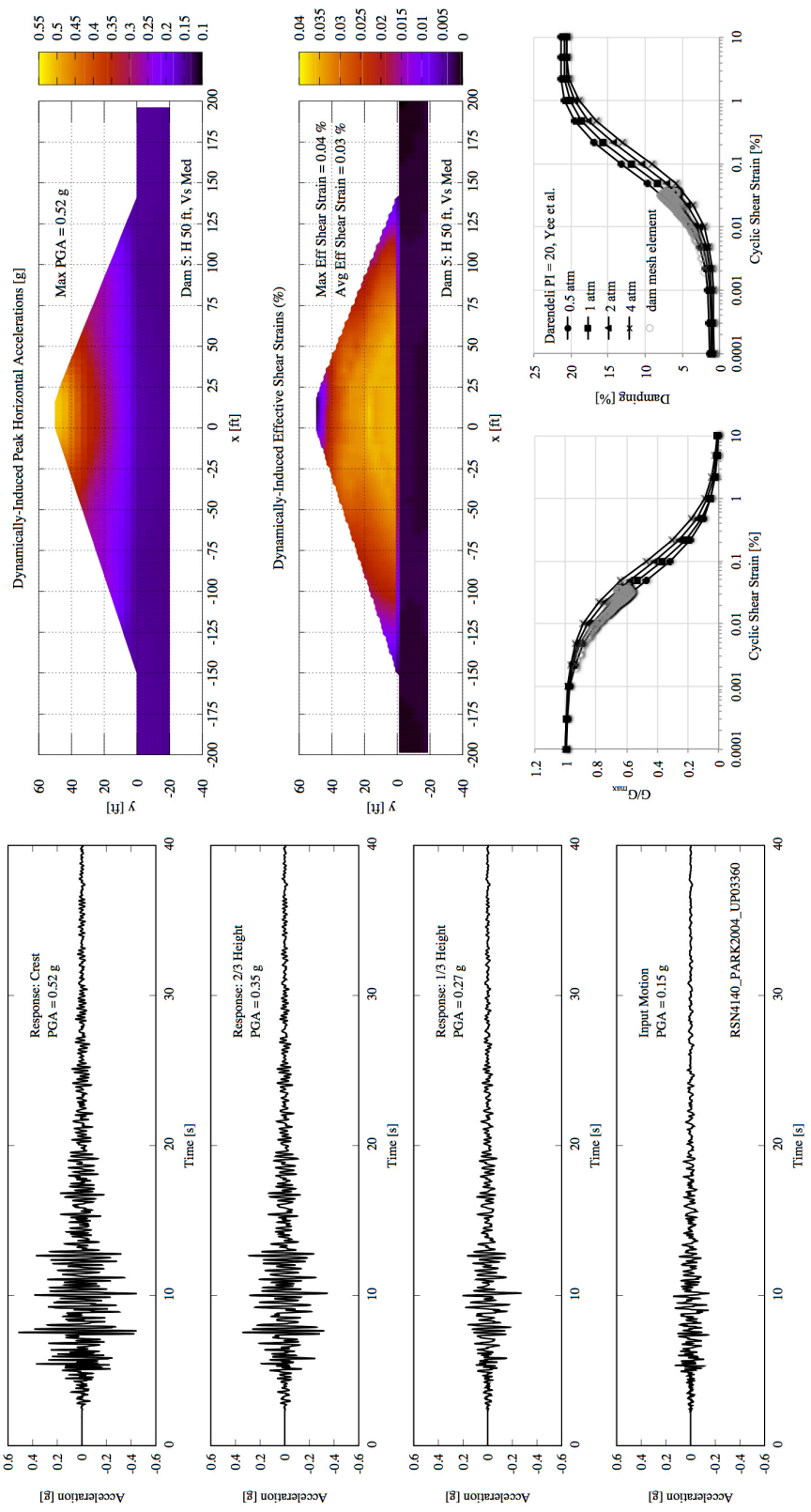

Figure 3.2 Example results from dynamic analysis with input PGA = 0.15 *g*.

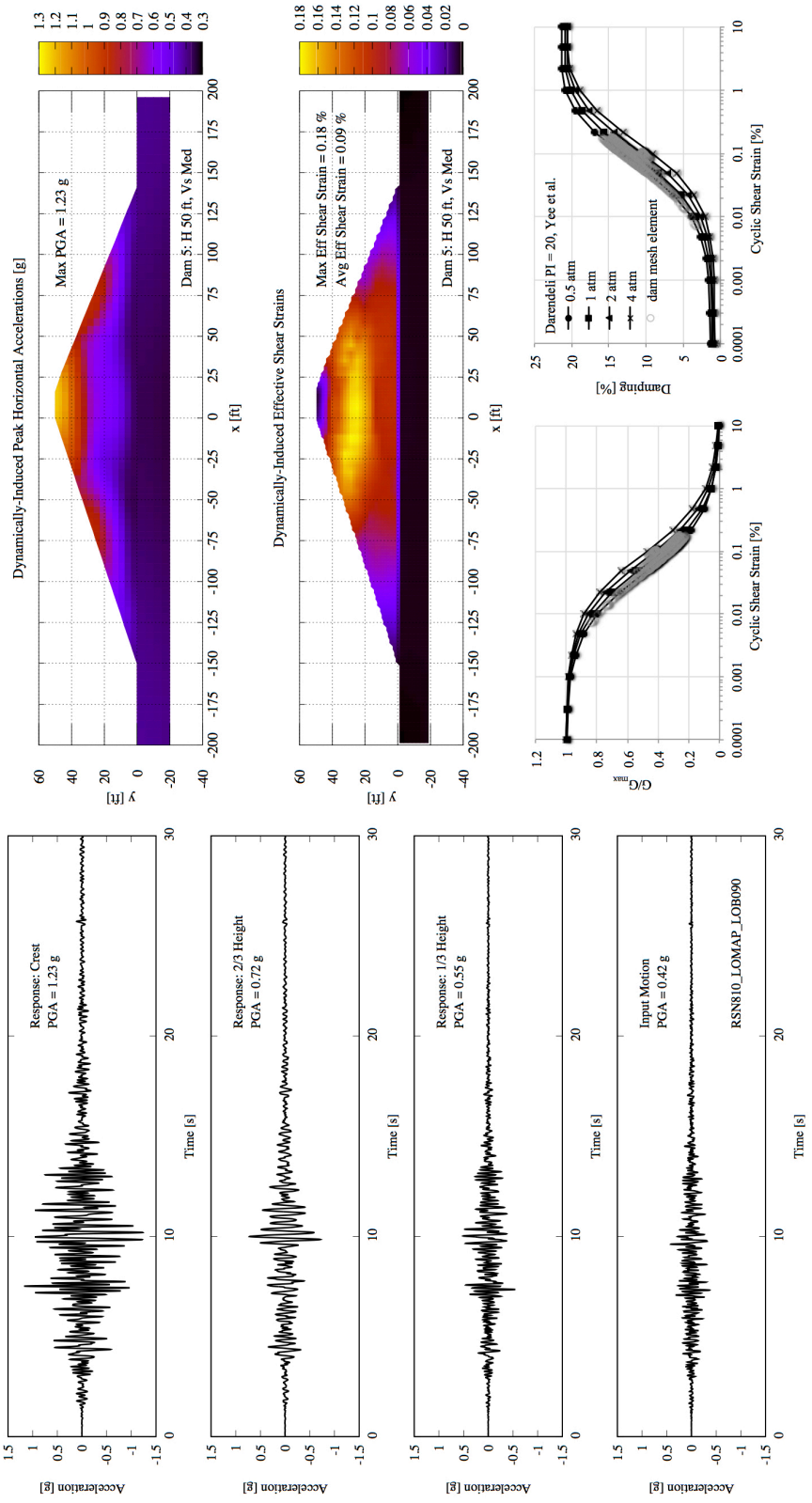

Figure 3.3 Example results from dynamic analysis with input PGA = 0.42 *g*.

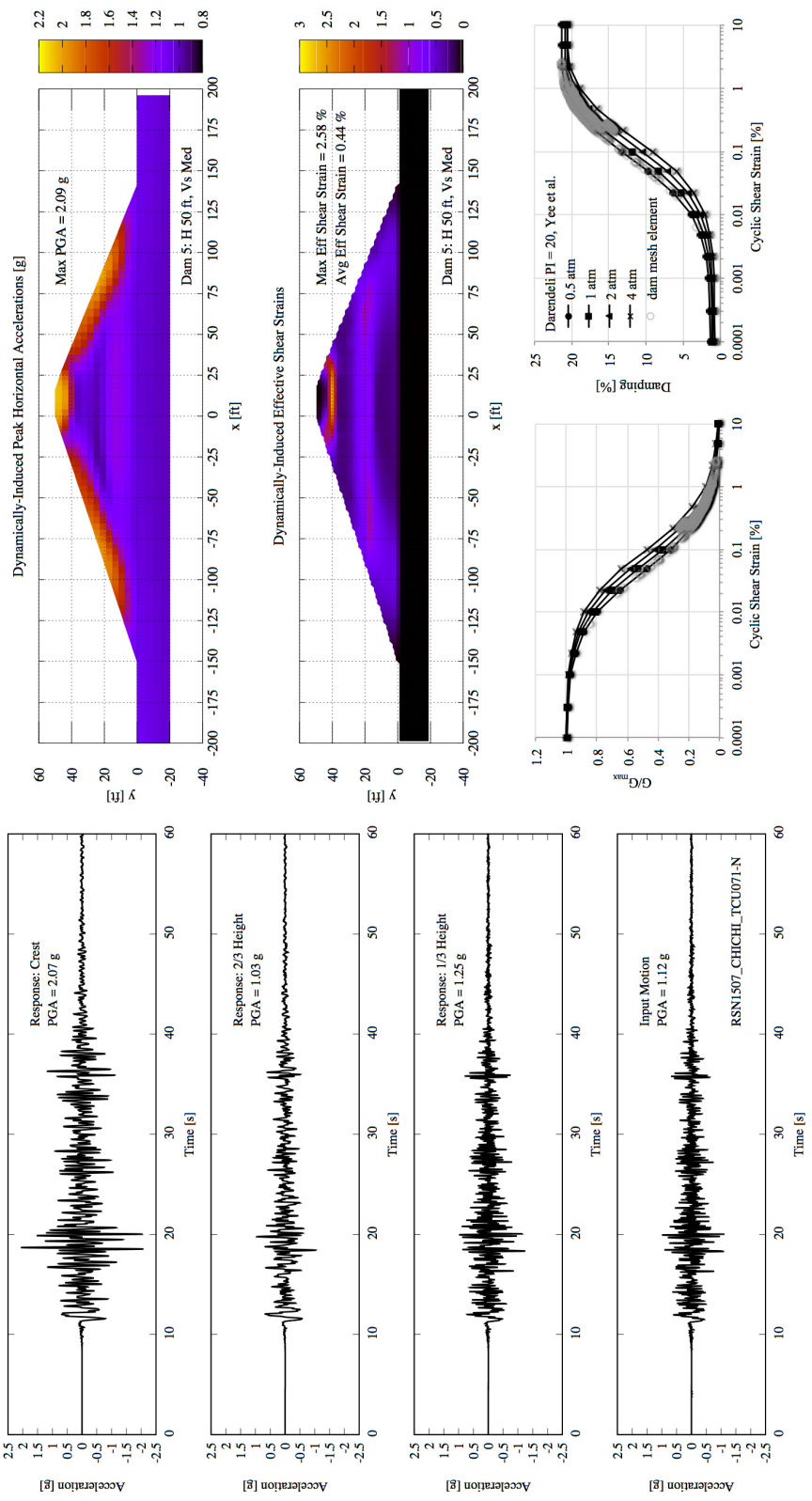

Figure 3.4 Example results from dynamic analysis with input PGA = 1.12 *g*.

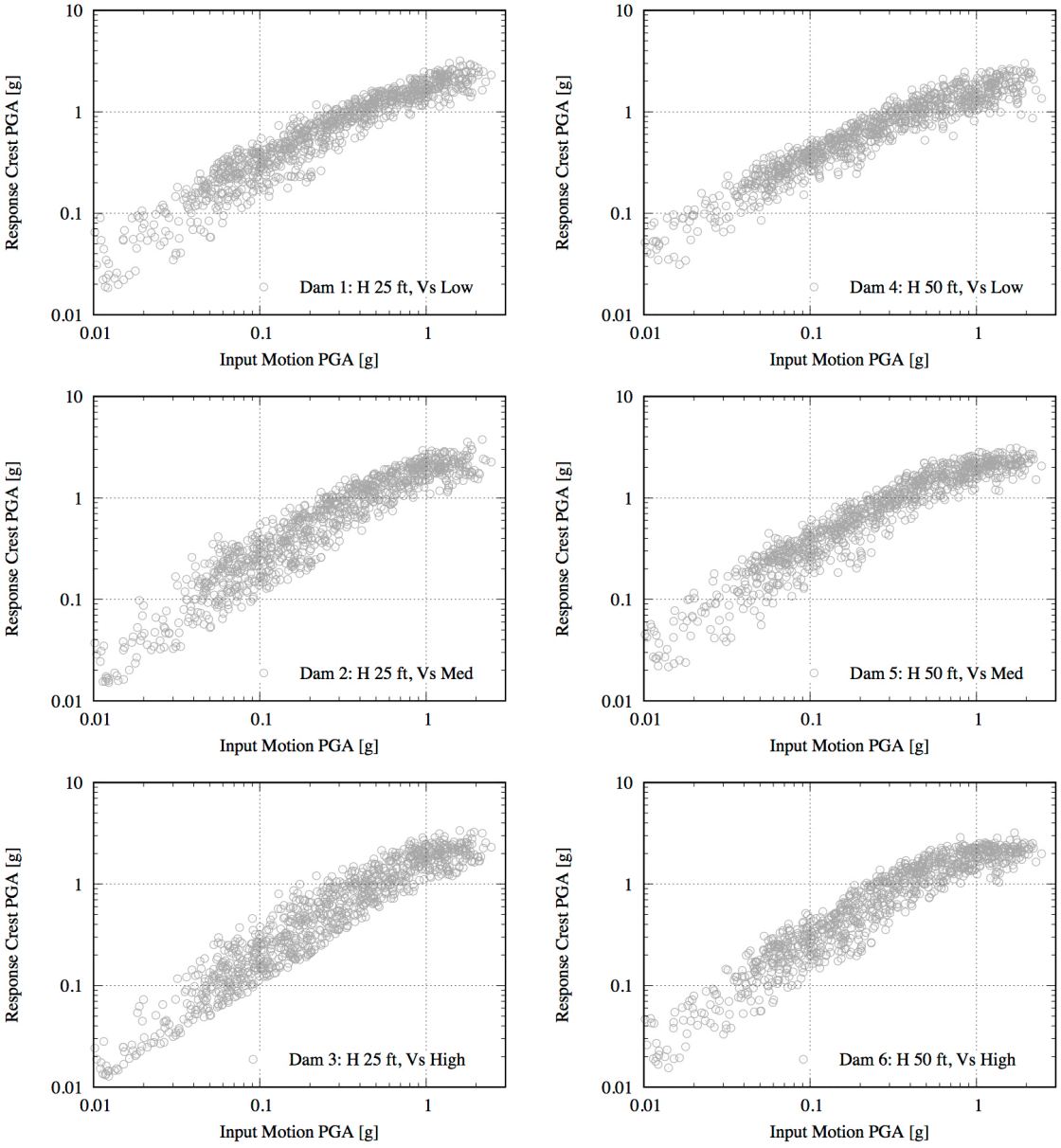

Figure 3.5 **Input motion PGA and response crest PGA from dynamic analyses for representative dams with heights of 25 and 50 *ft*.**

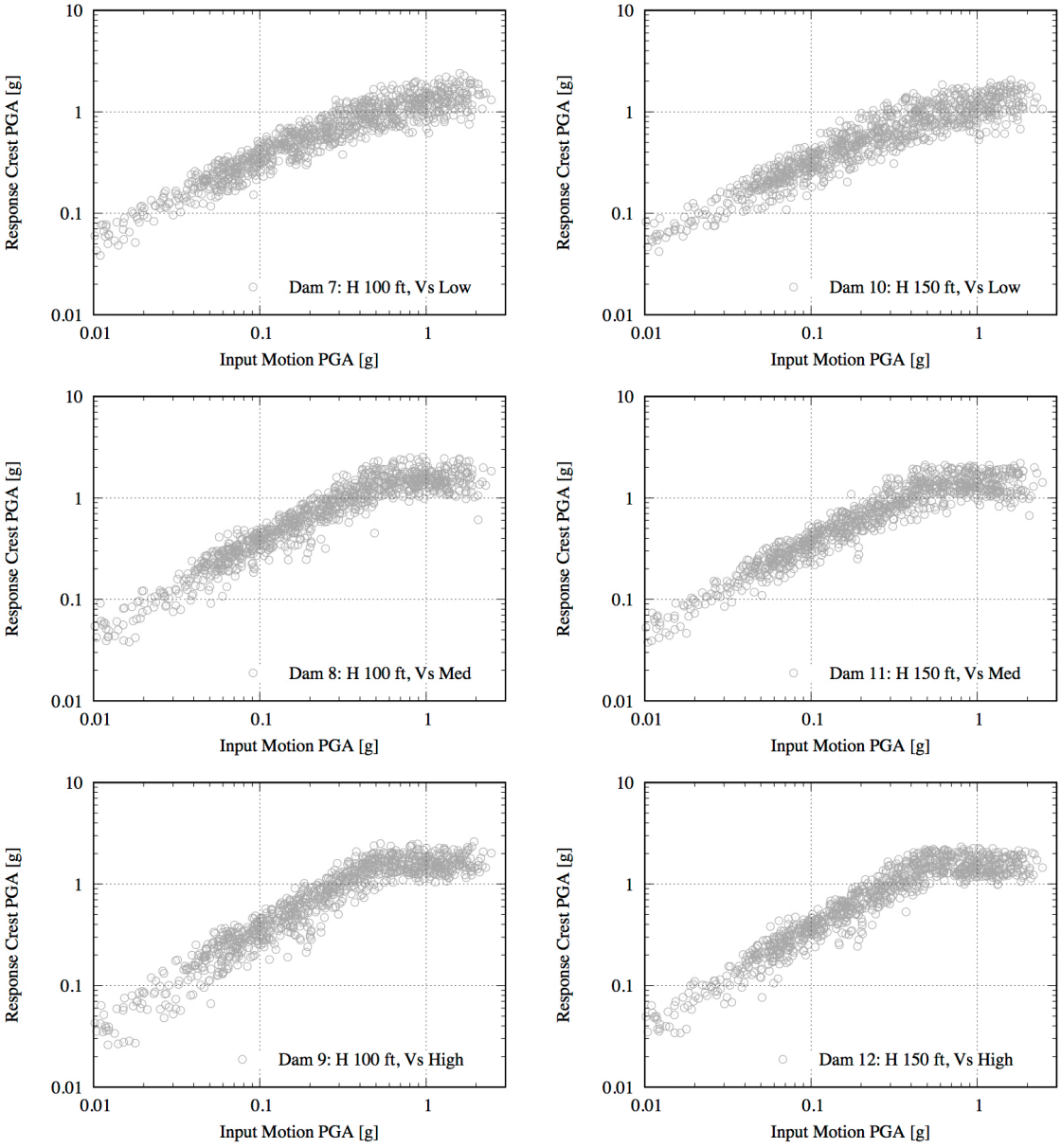

Figure 3.6 **Input motion PGA and response crest PGA from dynamic analyses for representative dams with heights of 100 and 150 *ft*.**

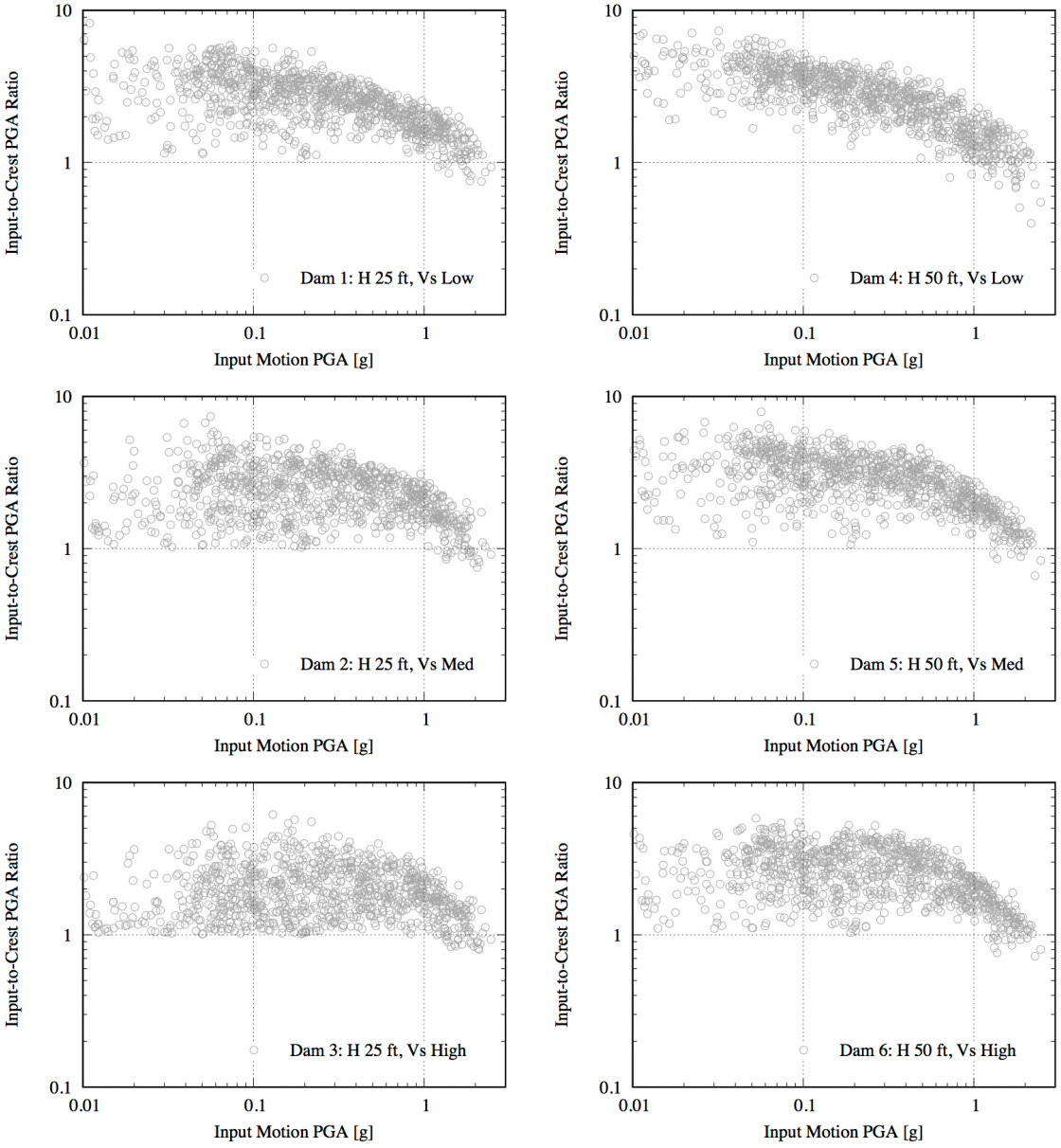

Figure 3.7 **Input motion PGA and input-to-crest PGA ratio from dynamic analyses for representative dams with heights of 25 and 50 *ft*.**

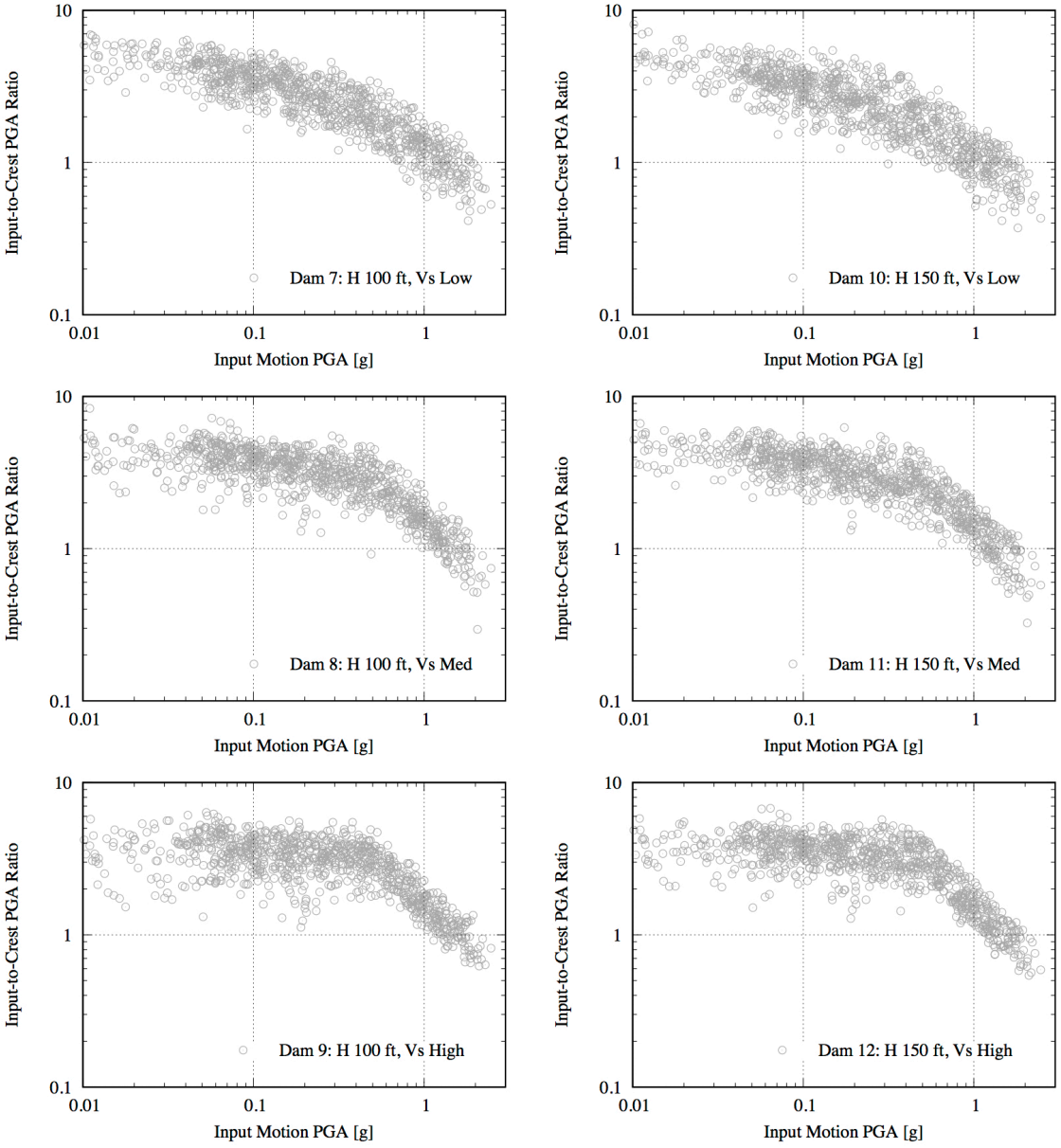

Figure 3.8 **Input motion PGA and input-to-crest PGA ratio from dynamic analyses for representative dams with heights of 100 and 150 *ft*.**

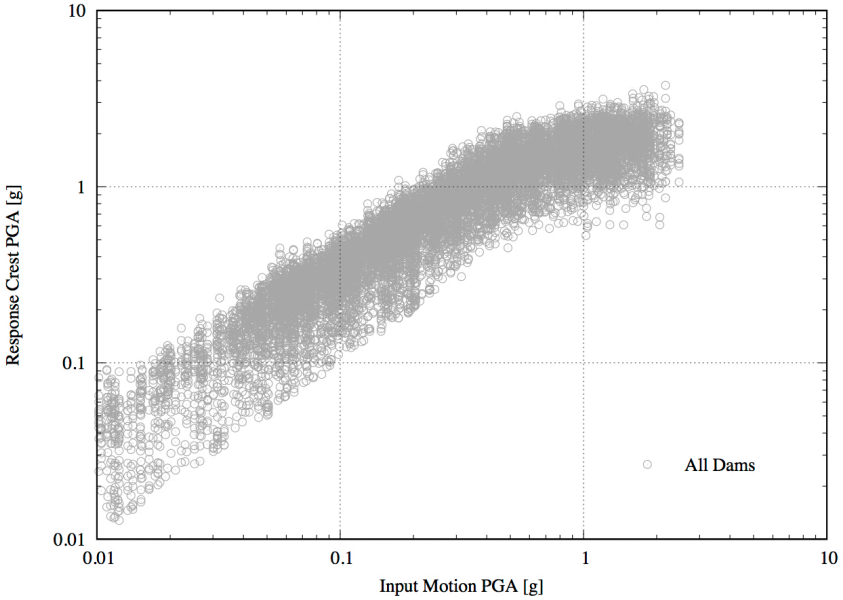

Figure 3.9 **Input motion PGA and response crest PGA from dynamic analyses for all representative dams.**

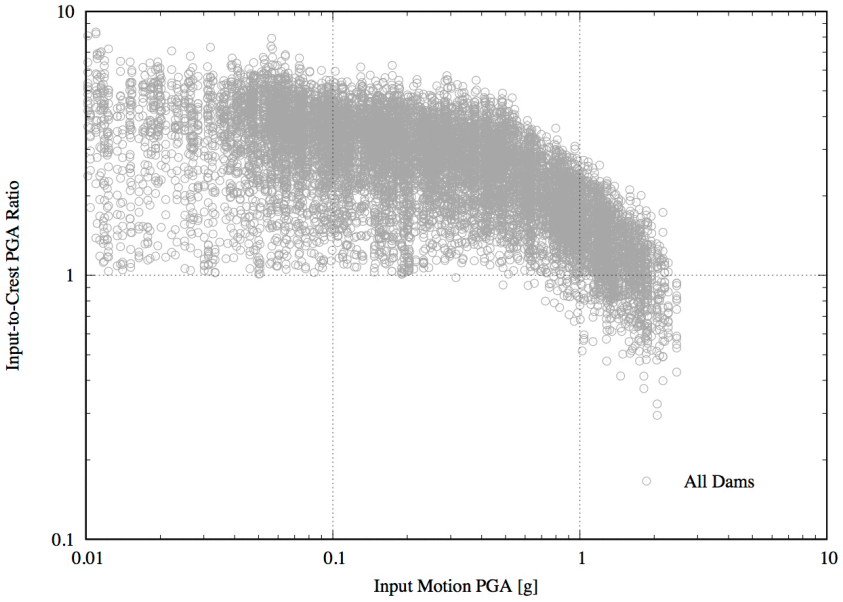

Figure 3.10 **Input motion PGA and input-to-crest PGA ratio from dynamic analyses for all representative dams.**

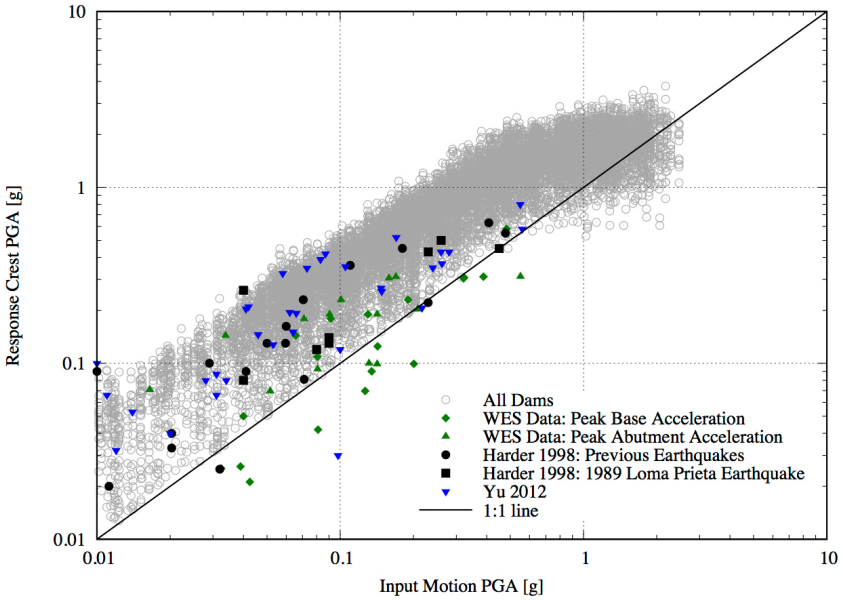

Figure 3.11 **Input motion PGA and response crest PGA from dynamic analyses along with empirical recordings measured at real dams during earthquakes for reference (log scales).**

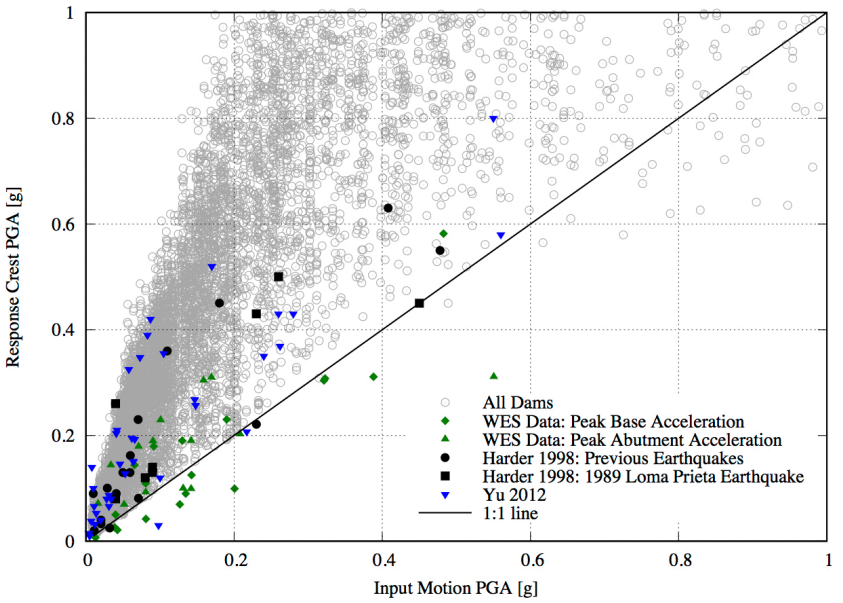

Figure 3.12 **Input motion PGA and response crest PGA from dynamic analyses along with empirical recordings measured at real dams during earthquakes for reference (linear scales).**

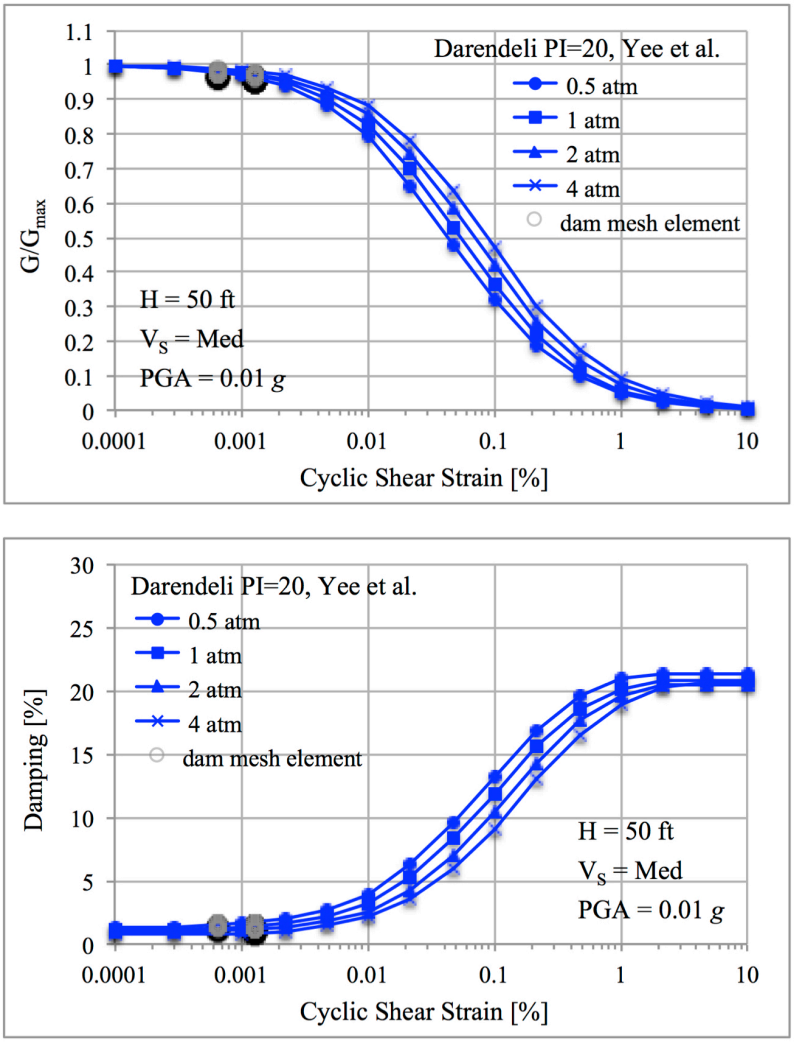

Figure 3.13 **Shear-modulus reduction and material damping curves used in dynamic analyses, along with final iterated dam mesh values for one of the small-strain ground motions.**

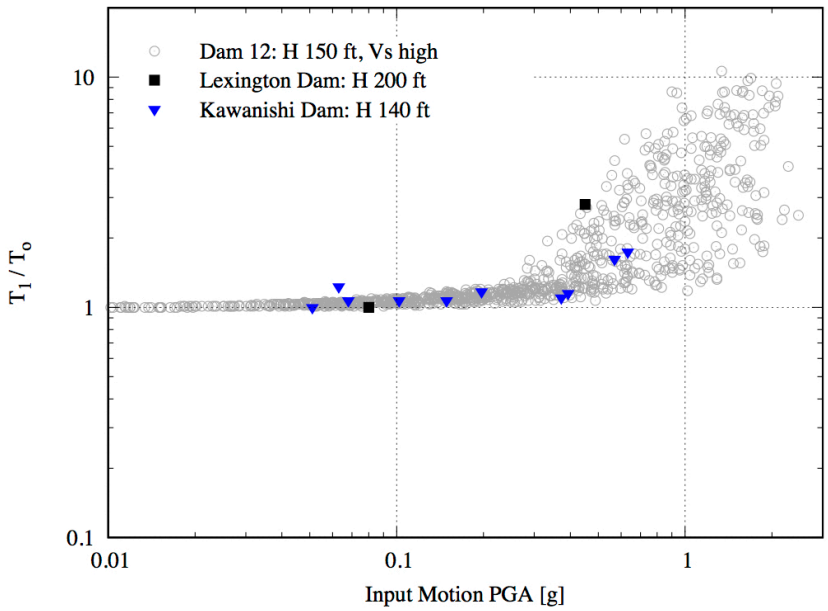

Figure 3.14 **Comparison of empirical observations of dam period shift with dynamic-analysis results for a similar representative dam.**

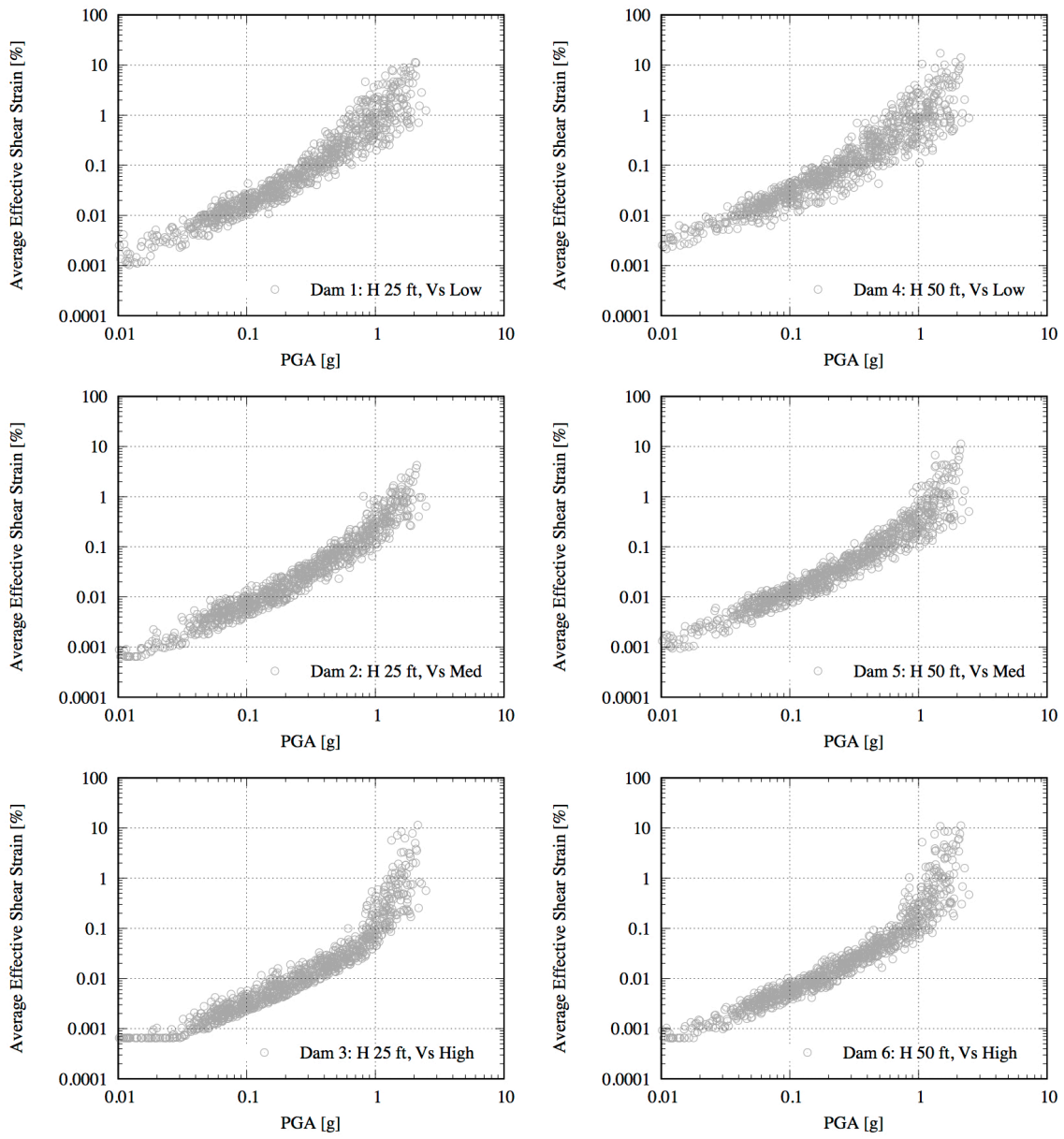

Figure 3.15 **Average (log-mean of all finite elements) effective shear strain vs. PGA from dynamic analyses for representative dams with heights of 25 and 50 *ft*.**

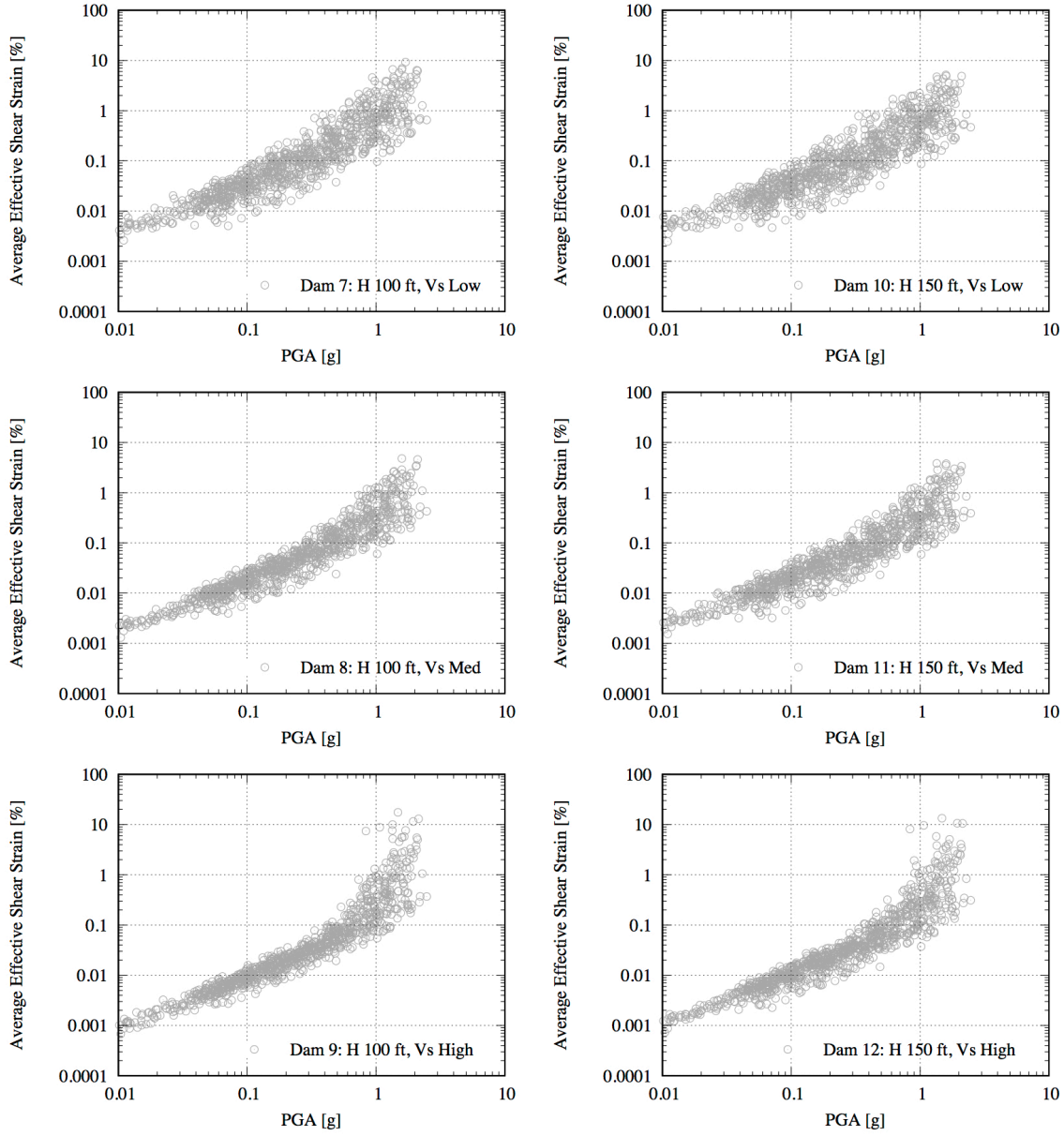

Figure 3.16 **Average (log-mean of all finite elements) effective shear strain vs. PGA from dynamic analyses for representative dams with heights of 100 and 150 *ft*.**

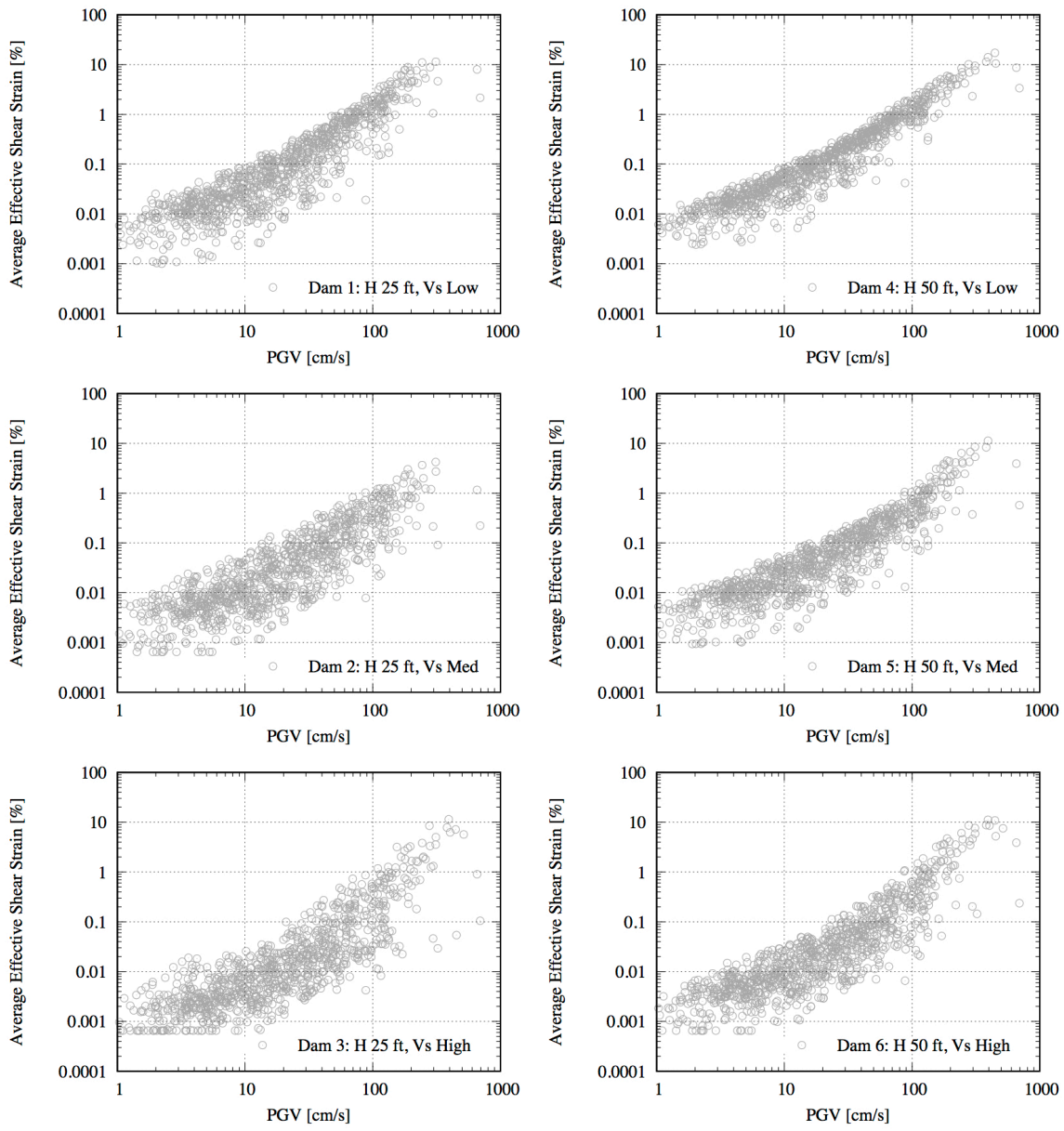

Figure 3.17 **Average (log-mean of all finite elements) effective shear strain vs. PGV from dynamic analyses for representative dams with heights of 25 and 50 *ft*.**

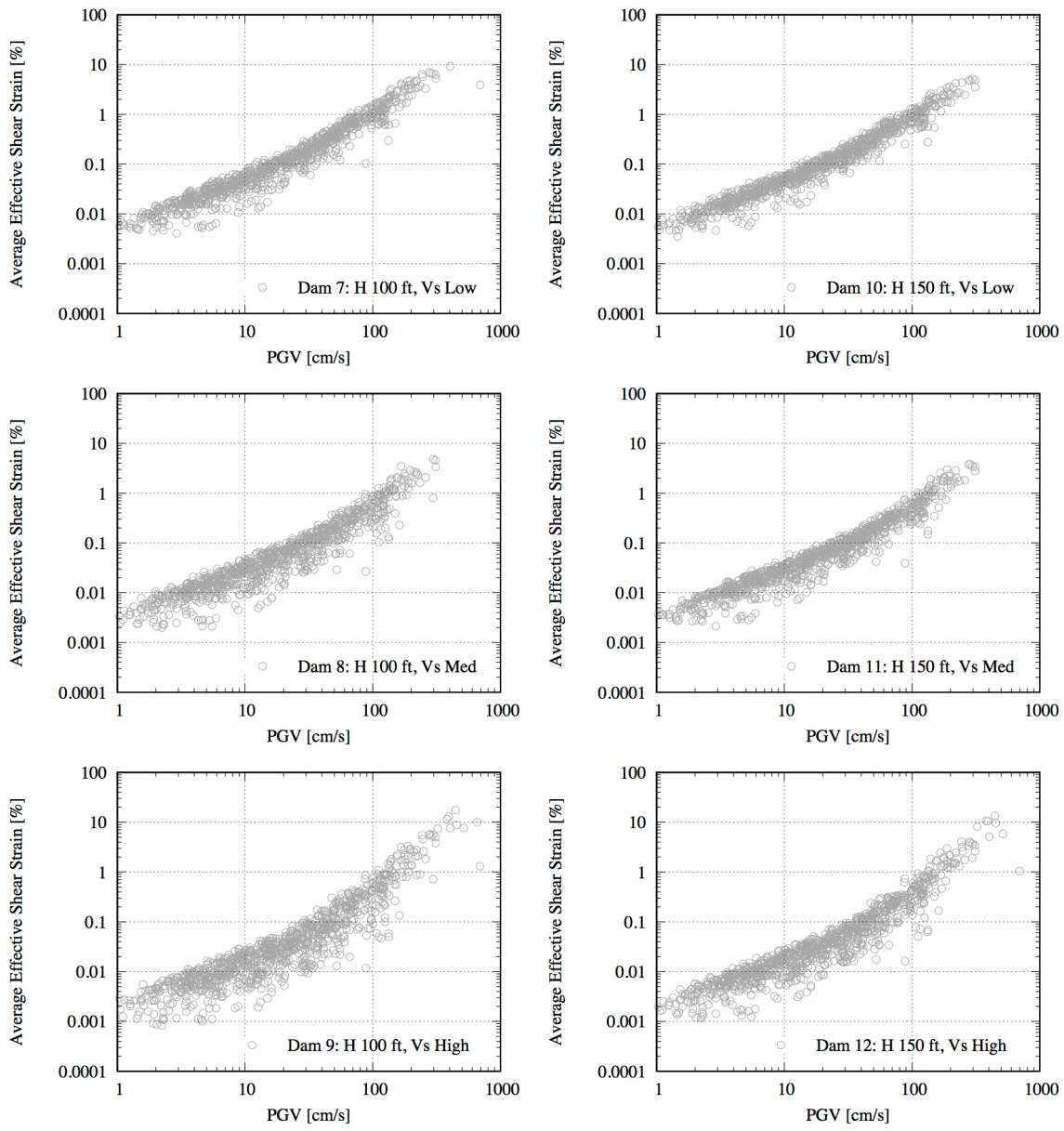

Figure 3.18 **Average (log-mean of all finite elements) effective shear strain vs. PGV from dynamic analyses for representative dams with heights of 100 and 150 *ft*.**

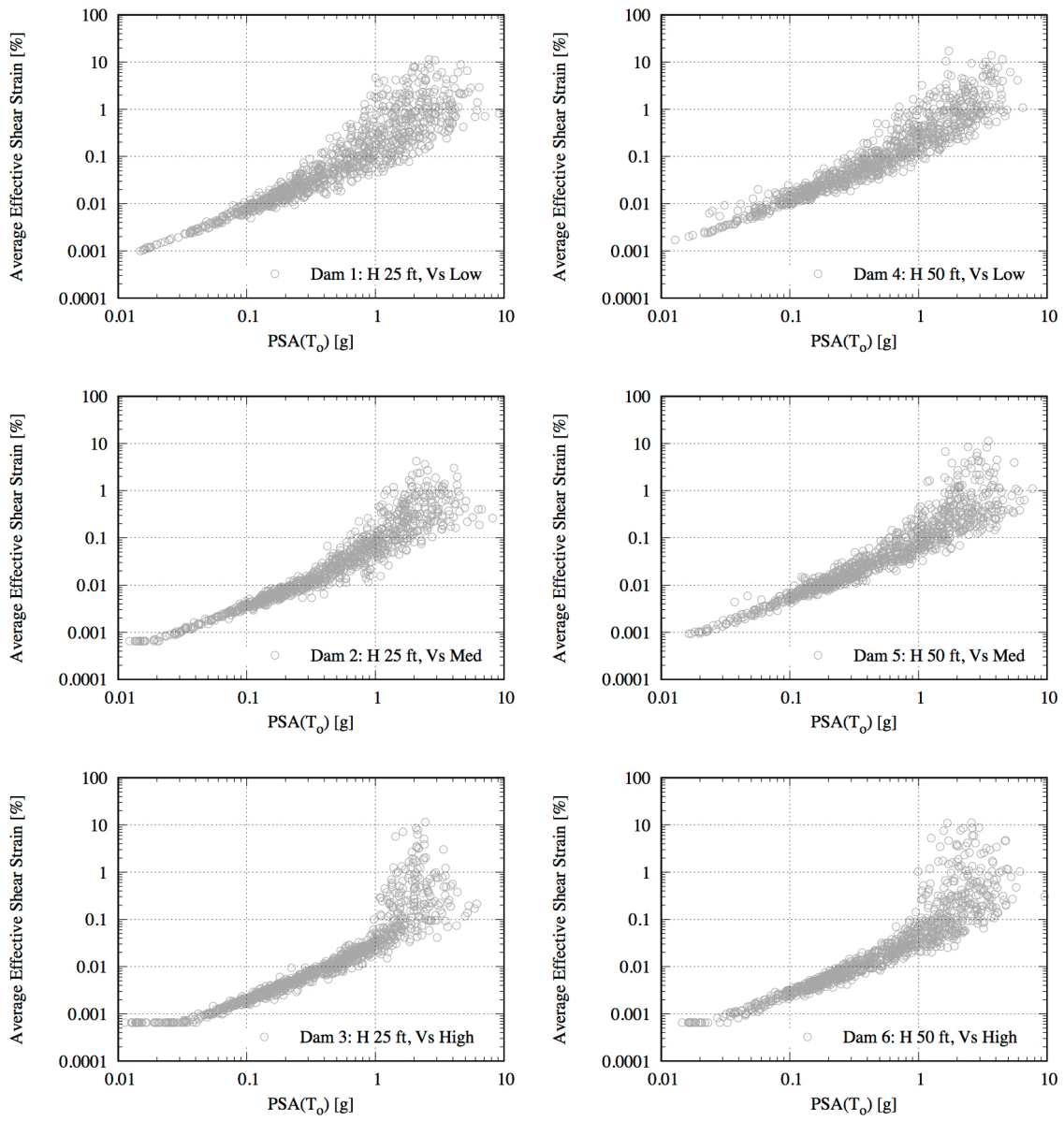

Figure 3.19 **Average (log-mean of all finite elements) effective shear strain vs. PSA(T_o) from dynamic analyses for representative dams with heights of 25 and 50 *ft*.**

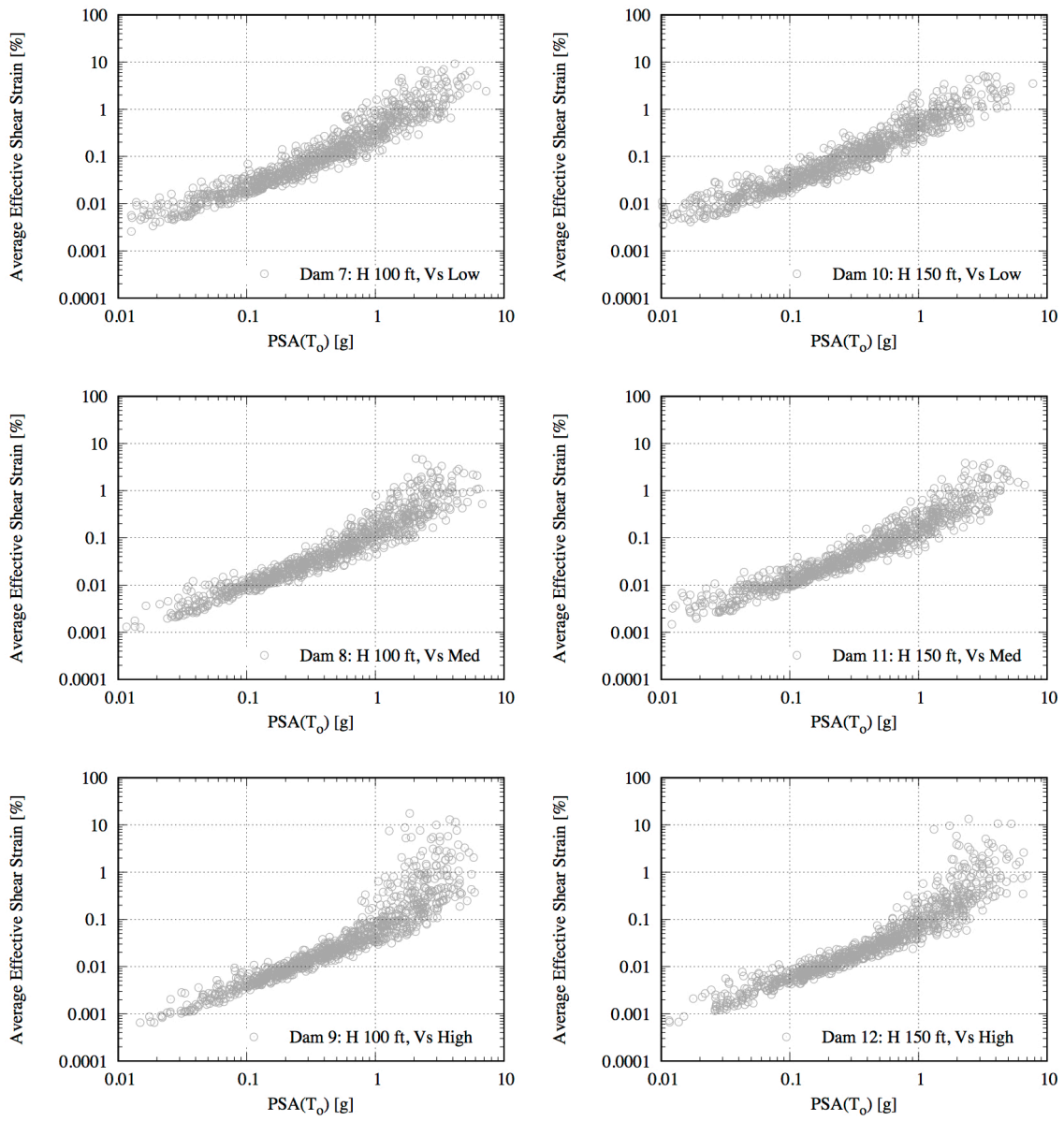

Figure 3.20 **Average (log-mean of all finite elements) effective shear strain vs. PSA(T_o) from dynamic analyses for representative dams with heights of 100 and 150 *ft*.**

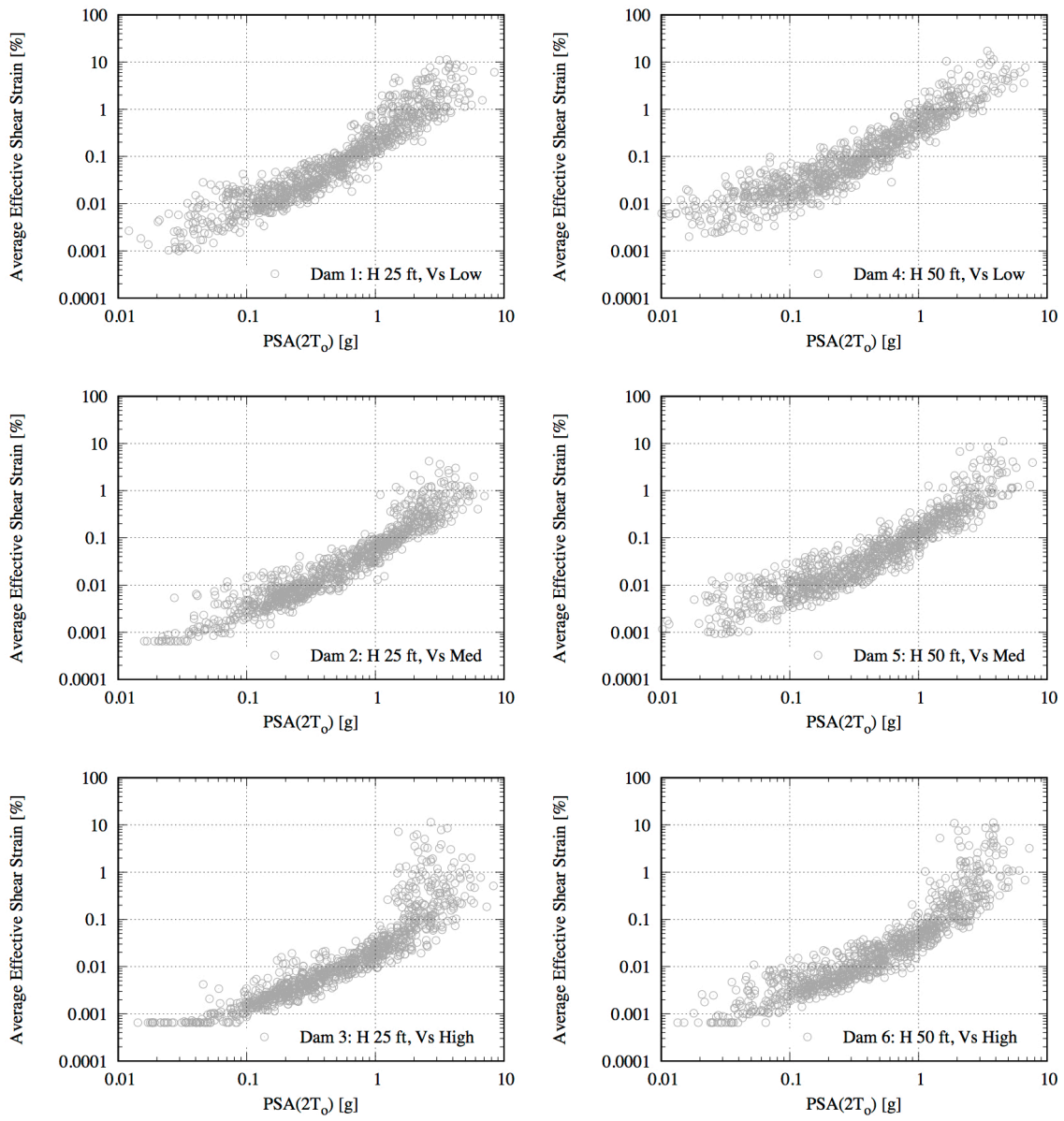

Figure 3.21 **Average (log-mean of all finite elements) effective shear strain vs. PSA($2T_o$) from dynamic analyses for representative dams with heights of 25 and 50 *ft*.**

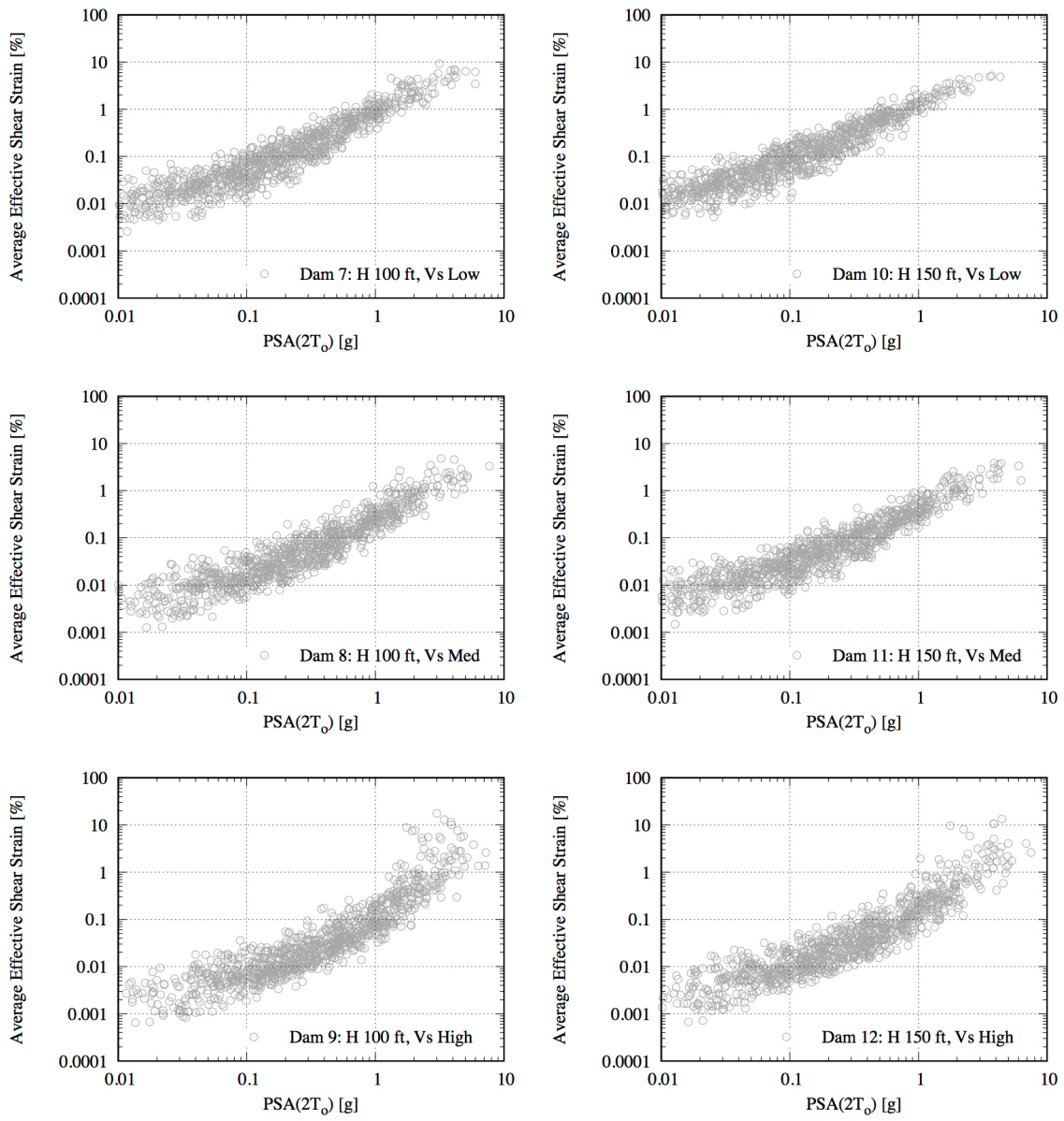

Figure 3.22 **Average (log-mean of all finite elements) effective shear strain vs. PSA(2T_o) from dynamic analyses for representative dams with heights of 100 and 150 *ft*.**

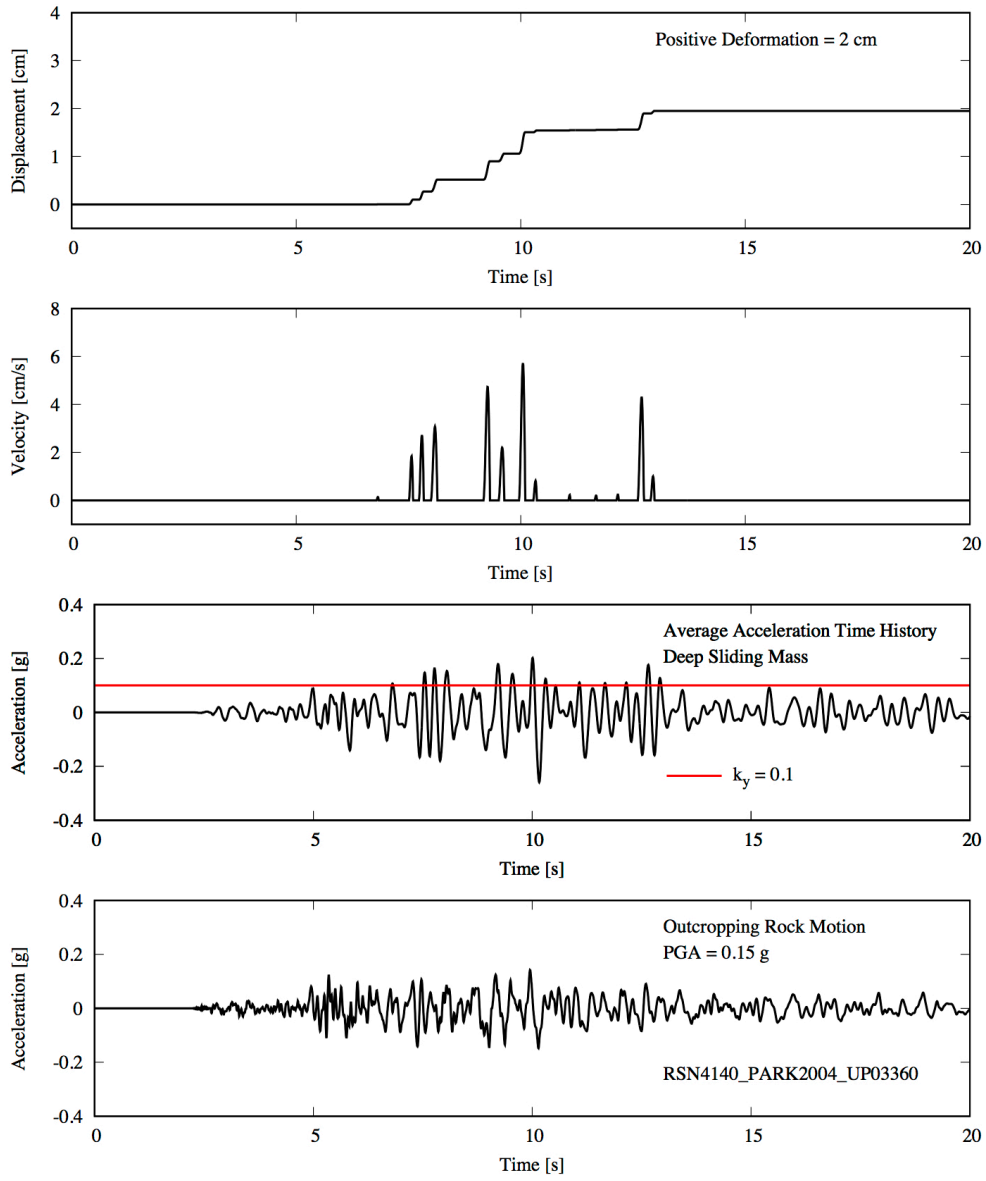

Figure 3.23 **Example of Newmark-type procedure applied to dynamic-analysis results with input PGA = 0.15 *g*.**

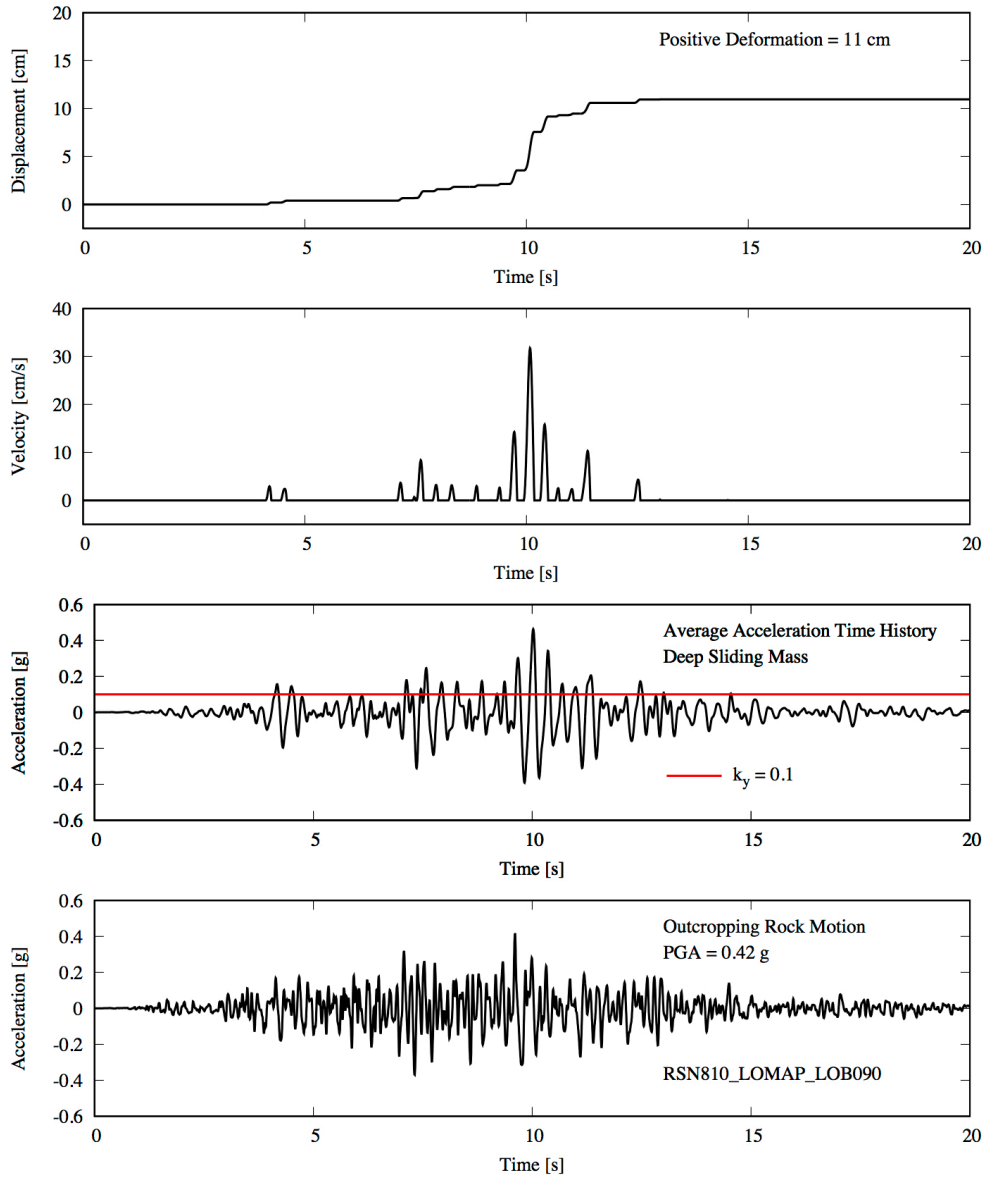

Figure 3.24 **Example of Newmark-type procedure applied to dynamic-analysis results with input PGA = 0.42 *g*.**

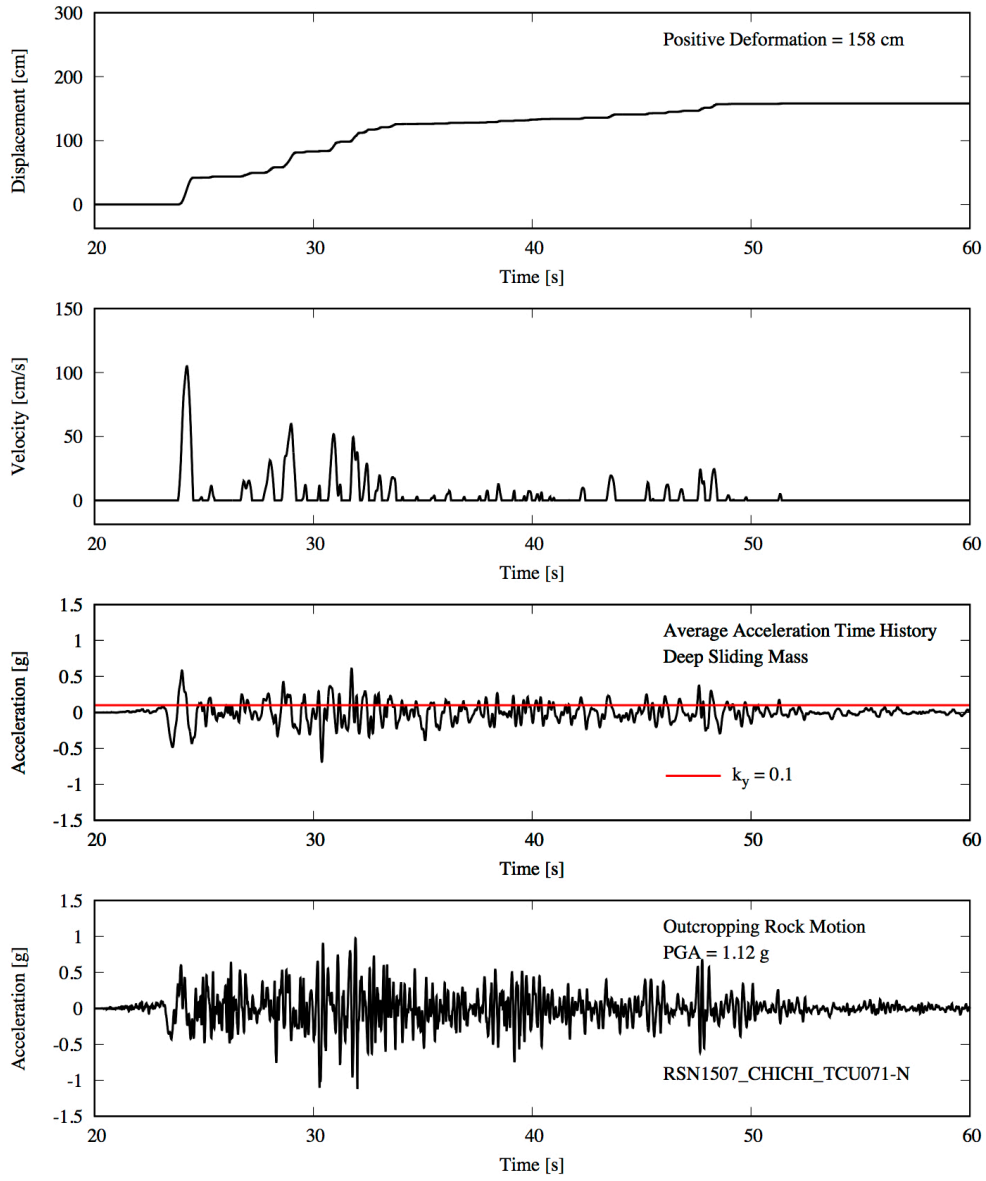

Figure 3.25 **Example of Newmark-type procedure applied to dynamic-analysis results with input PGA = 1.12 *g*.**

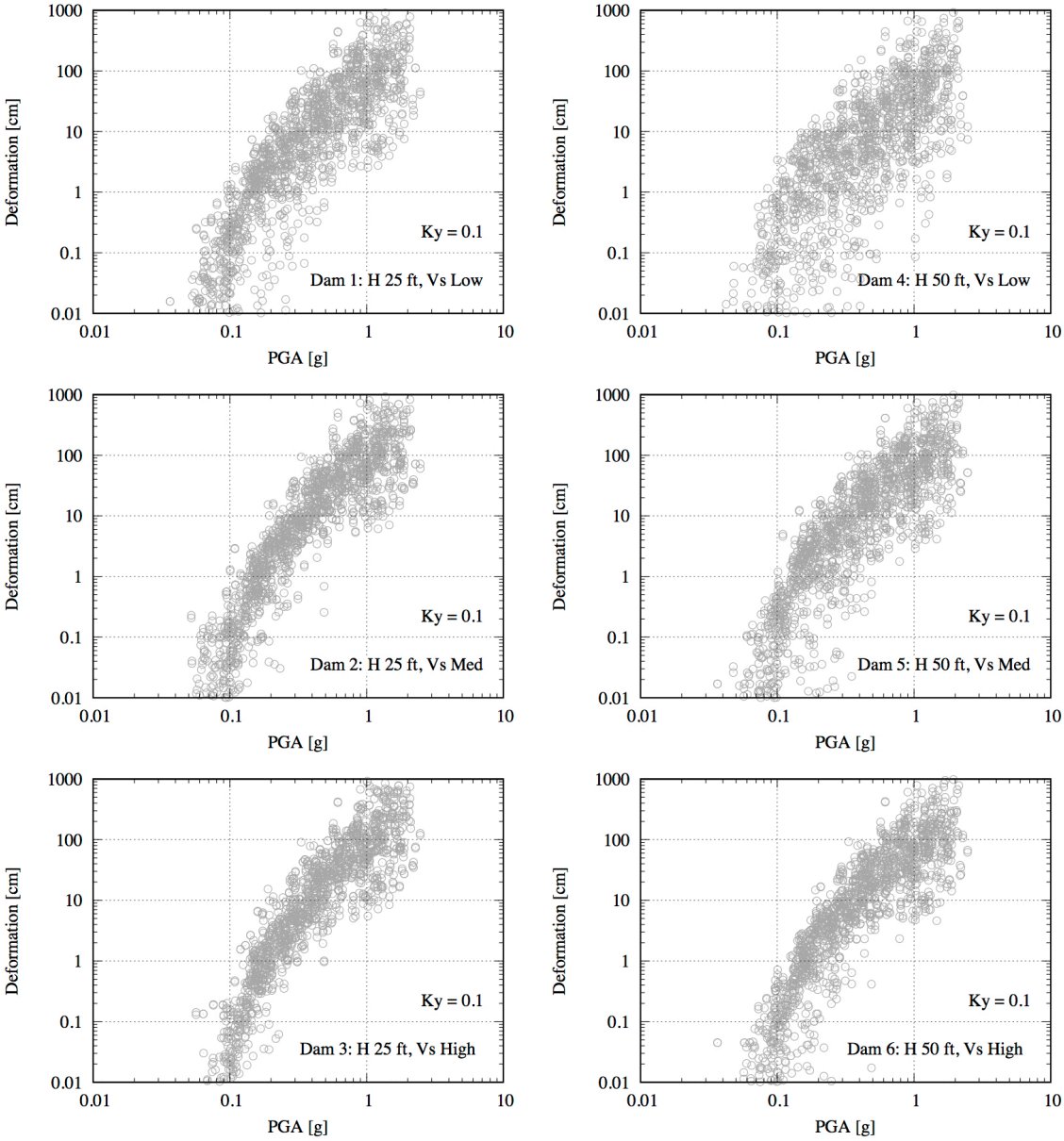

Figure 3.26 **Newmark deformations vs. PGA for representative dams with heights of 25 and 50 *ft*.**

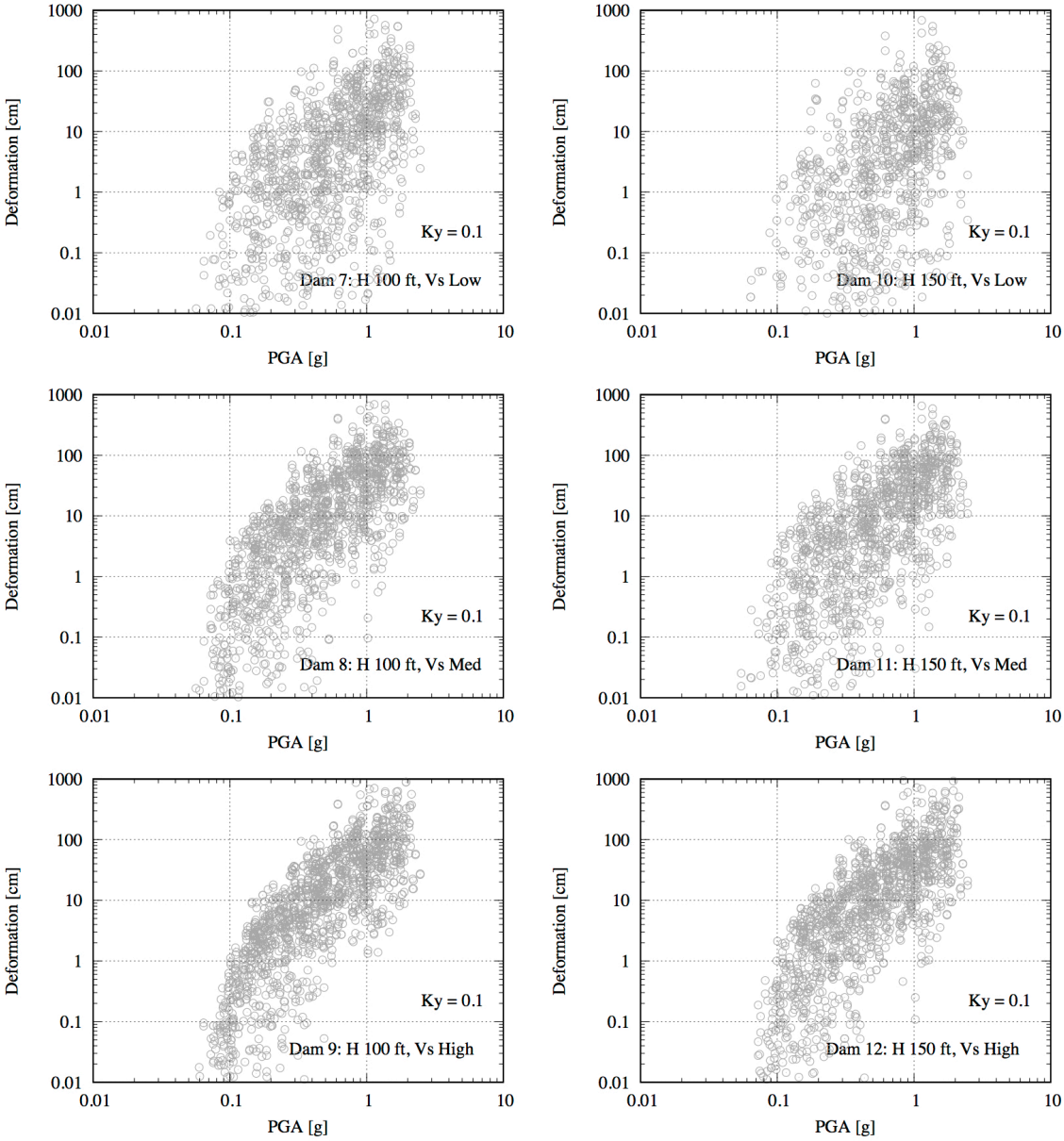

Figure 3.27 **Newmark deformations vs. PGA for representative dams with heights of 100 and 150 *ft*.**

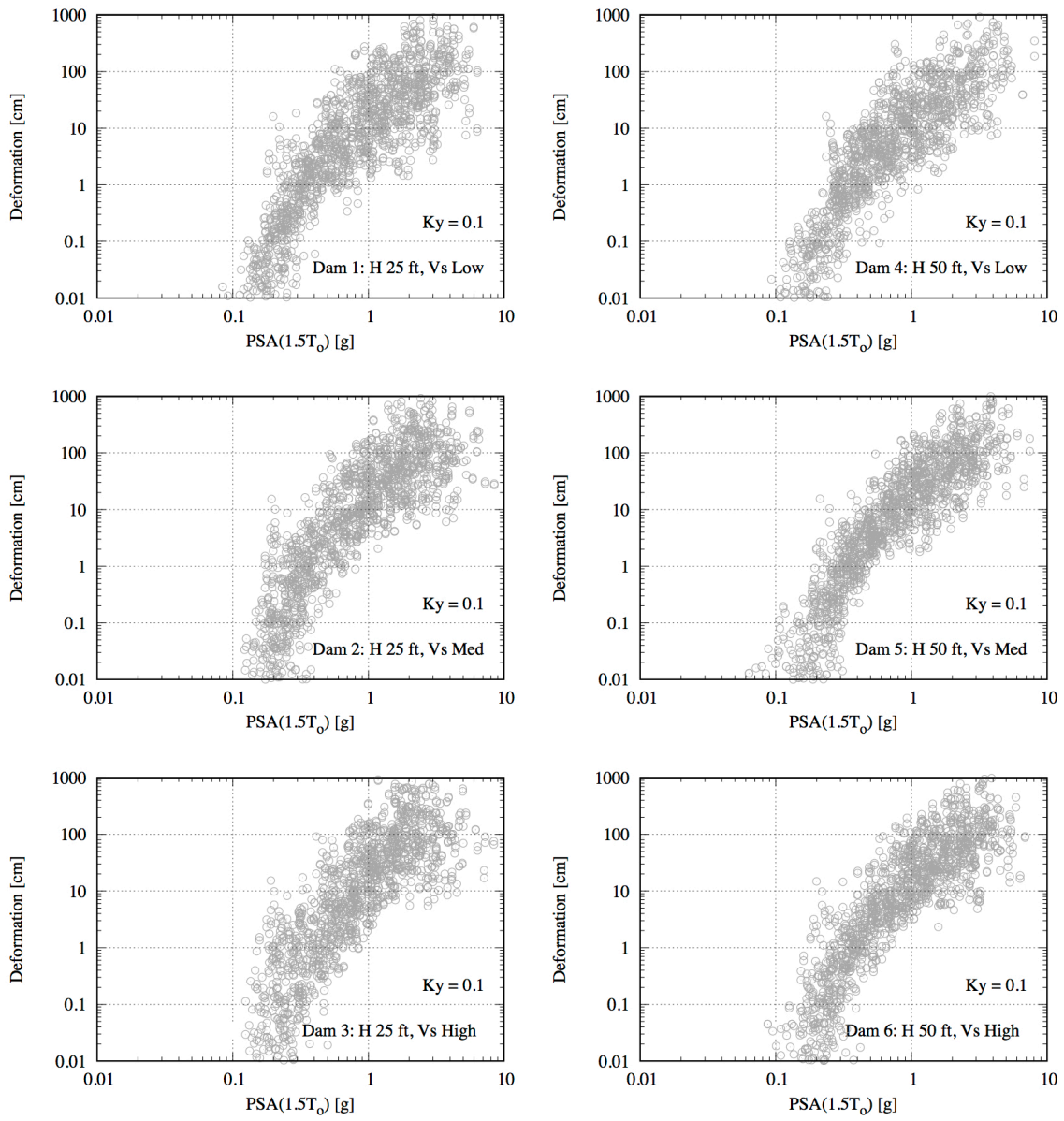

Figure 3.28 **Newmark deformations vs. PSA(1.5T_o) for representative dams with heights of 25 and 50 *ft*.**

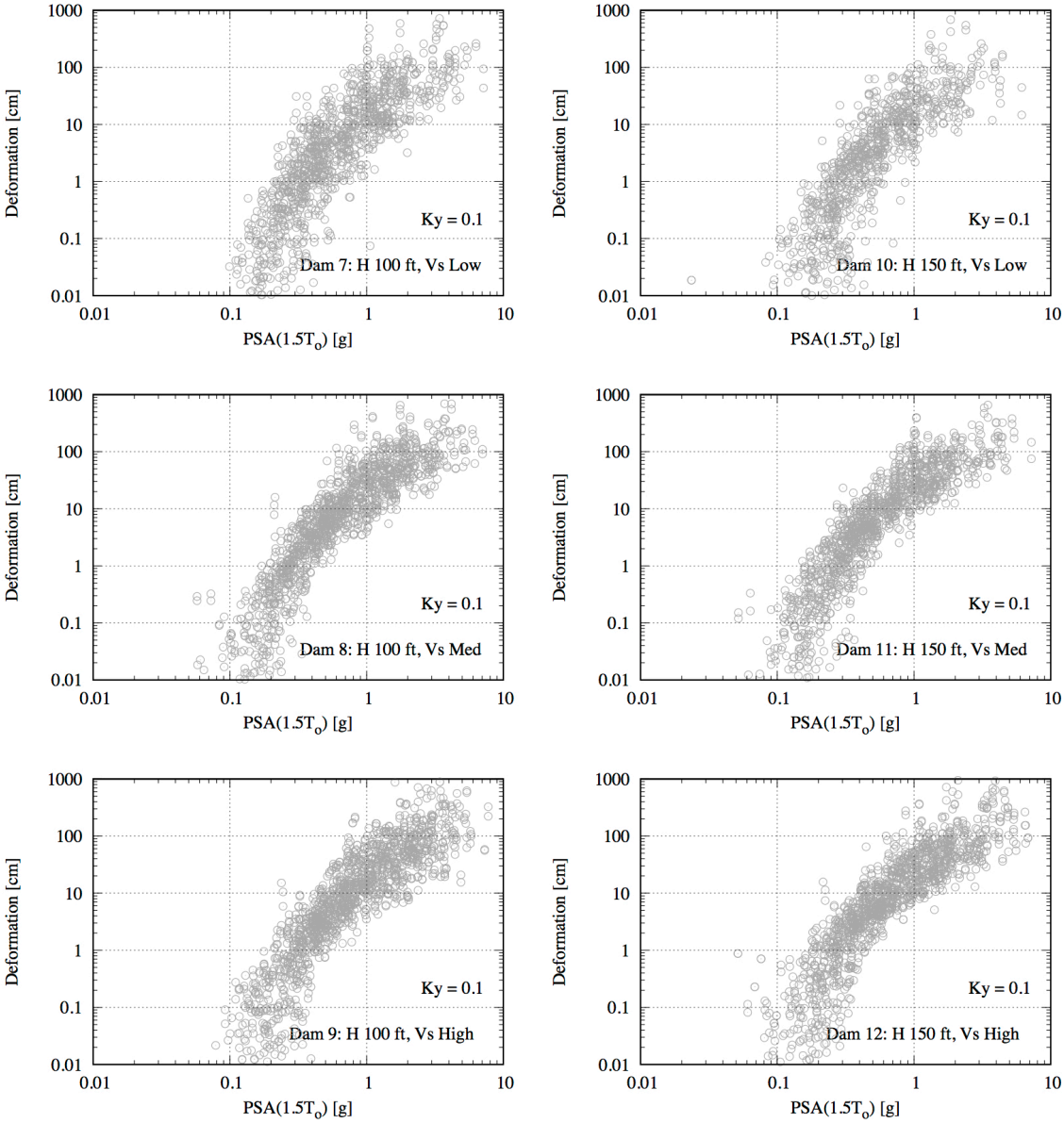

Figure 3.29 **Newmark deformations vs. PSA(1.5T_o) for representative dams with heights of 100 and 150 *ft*.**

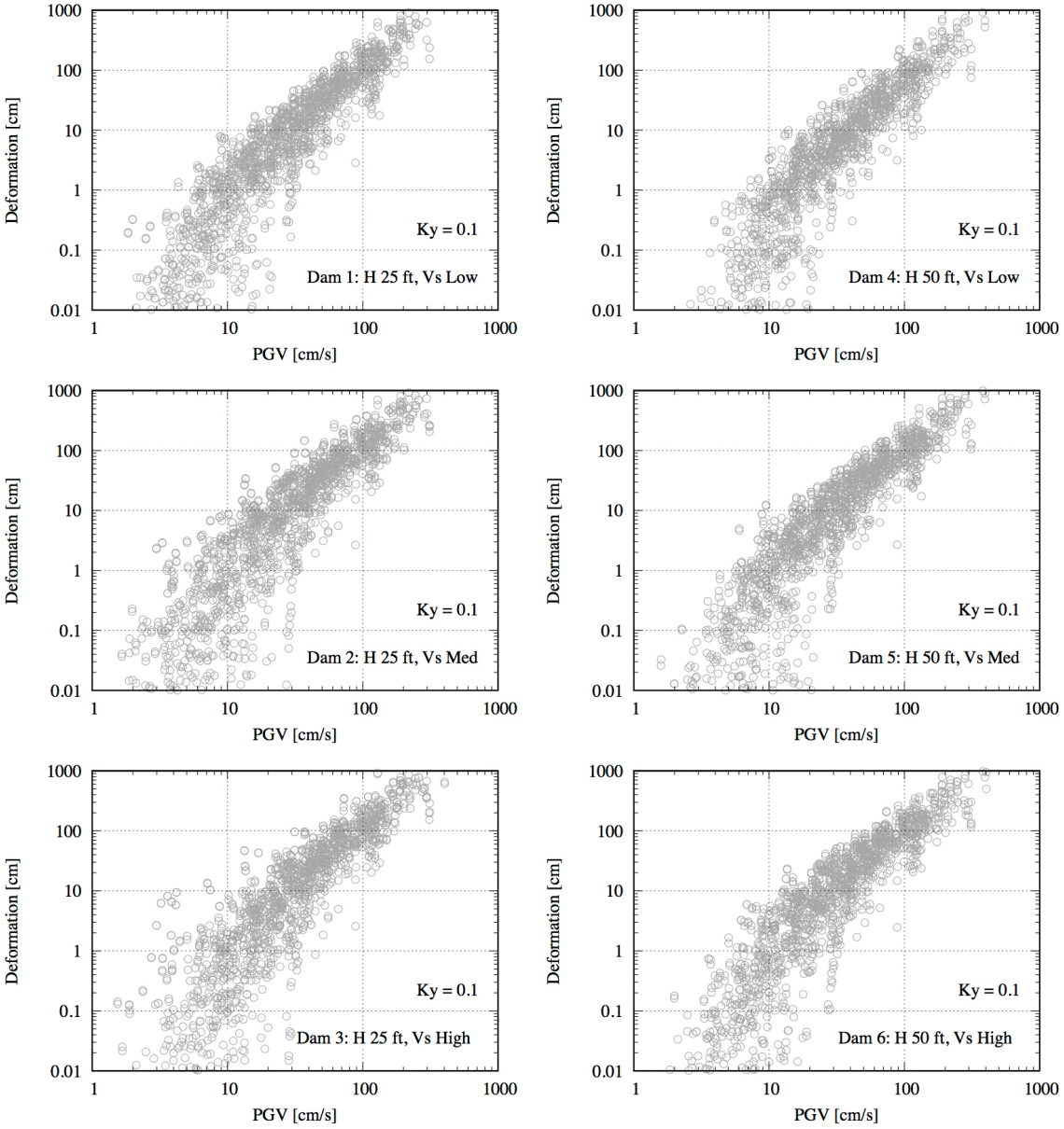

Figure 3.30 **Newmark deformations vs. PGV for representative dams with heights of 25 and 50 *ft*.**

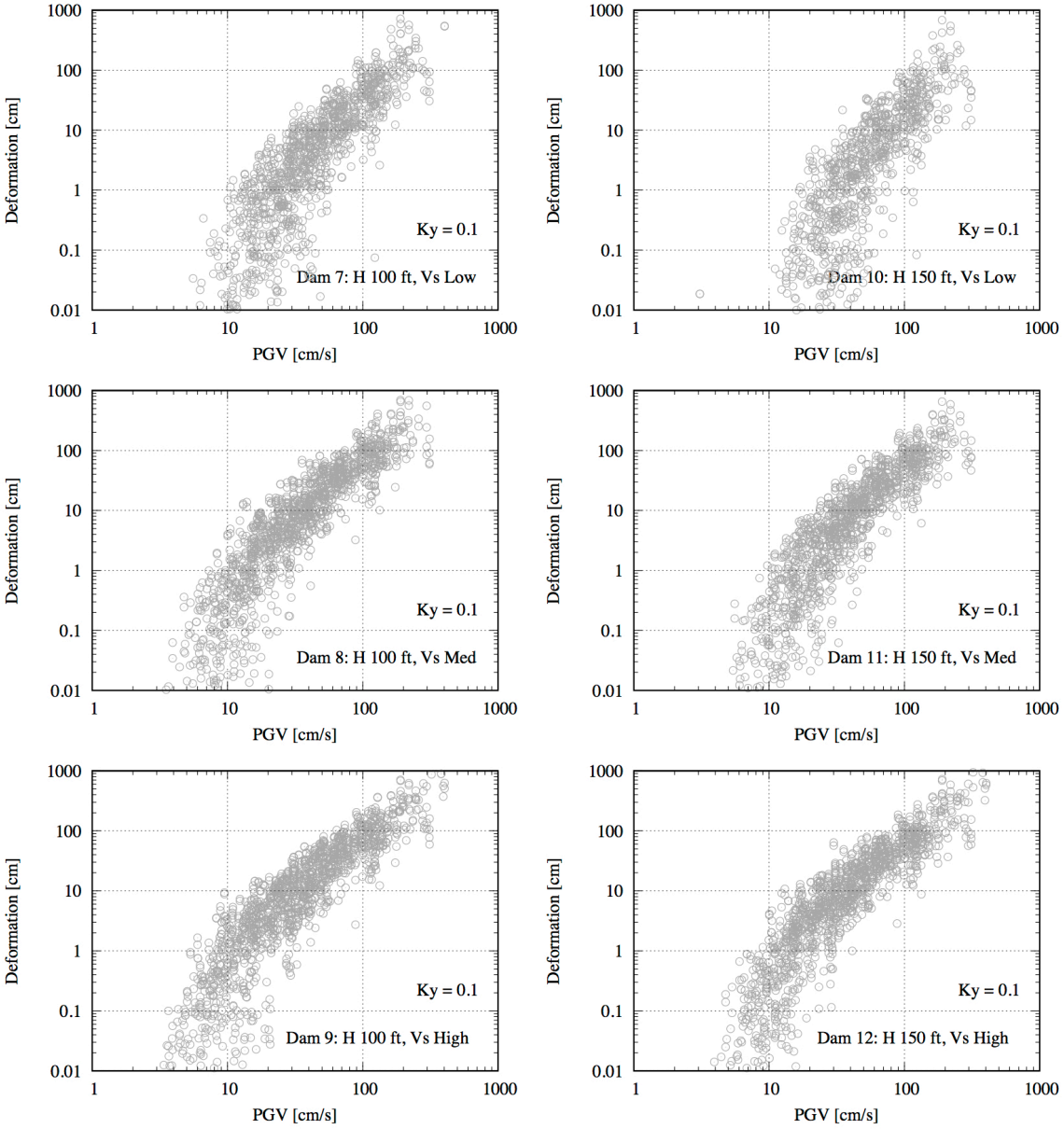

Figure 3.31 **Newmark deformations vs. PGV for representative dams with heights of 100 and 150 *ft*.**

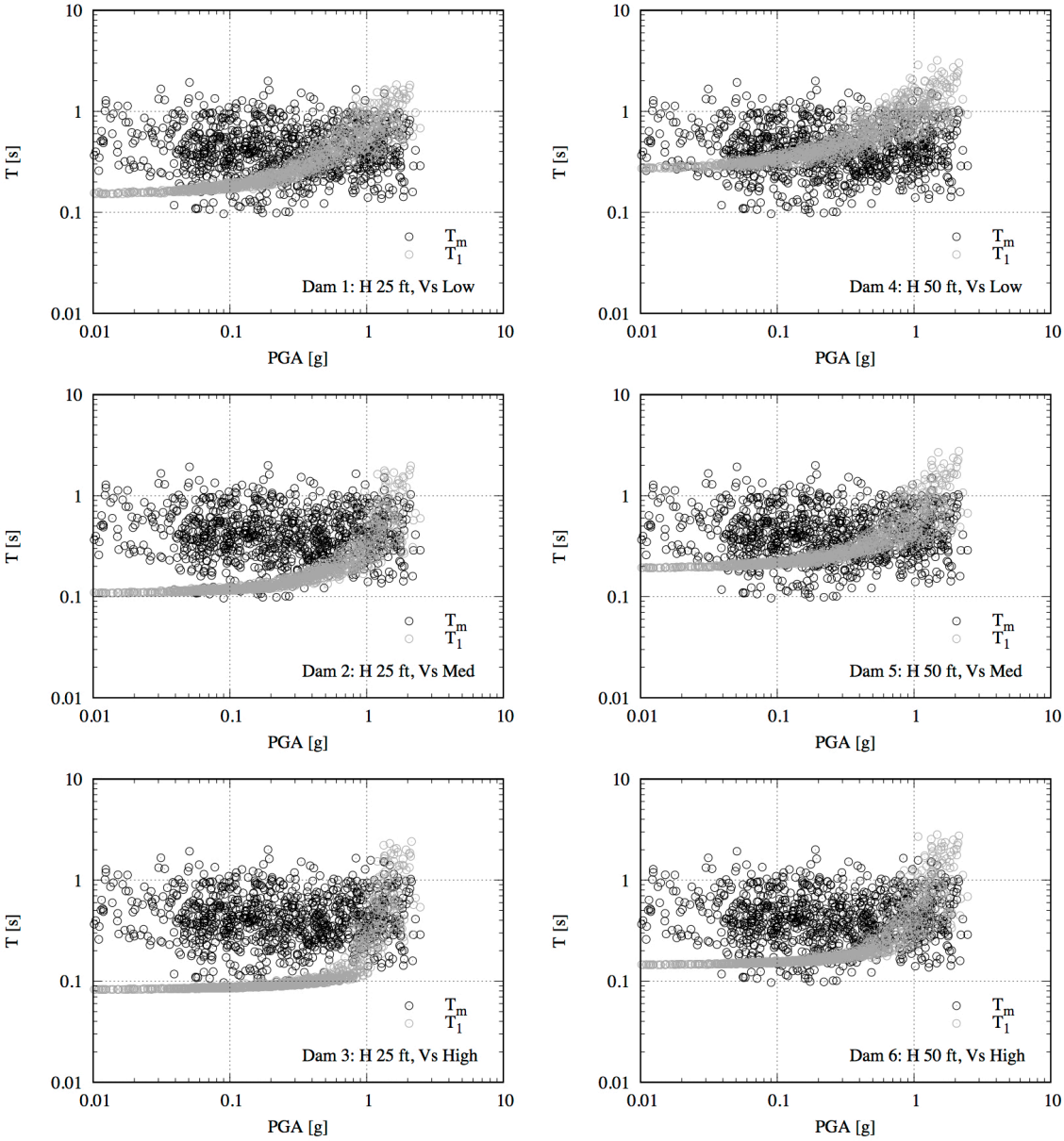

Figure 3.32 **Comparing mean period of ground motion (T_m) with first-mode period of dam from dynamic analysis (T_1) for representative dams with heights of 25 and 50 *ft*.**

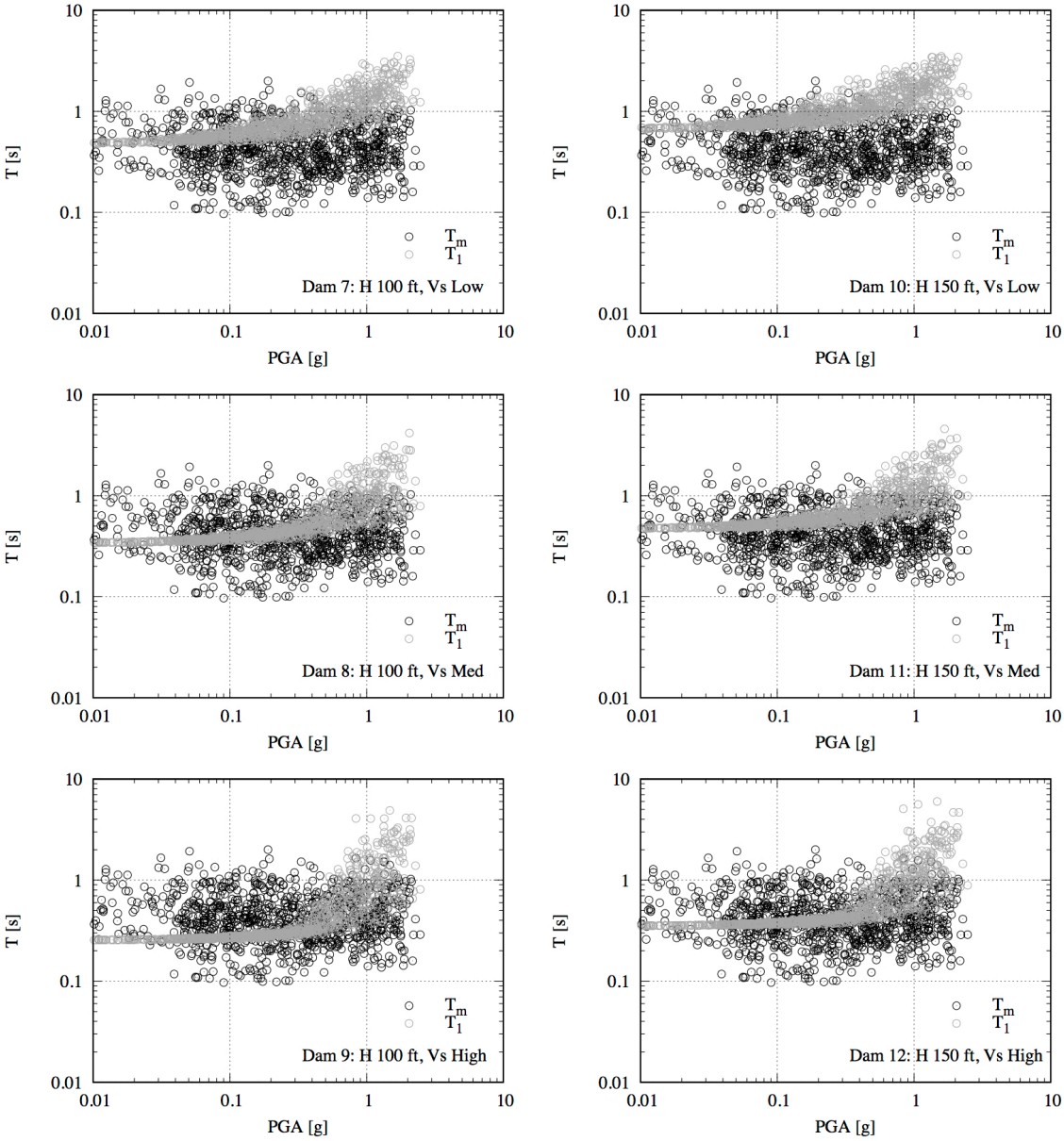

Figure 3.33 **Comparing mean period of ground motion (T_m) with first-mode period of dam from dynamic analysis (T_1) for representative dams with heights of 100 and 150 *ft*.**

4 DEVELOPMENT OF A TRANSFER-FUNCTION MODEL TO ESTIMATE DEFORMATION OF EARTHEN DAMS TO SEISMIC LOADING

4.1 Introduction

Dynamic analysis of earthen dams is performed to assess the seismic vulnerability and potential consequences of a dam failure during an earthquake. Once the primary concern of liquefaction has been addressed, the evaluation focuses on the potential for instability and the engineering demand parameter of interest is the permanent deformation or displacement of the dam. Large deformations are problematic because they could lead to an uncontrolled release of reservoir water during an earthquake.

Over the years, dam seismic evaluation has advanced from simplistic static or pseudo-static analysis to performing dynamic analyses with a single ground motion to performing dynamic analyses for tens of ground motions specifically selected for a dam site. The industry now looks to increase the number of ground motions again and perform hundreds of dynamic analyses to capture the response across the full range of expected intensity levels and ultimately characterize the deformation hazard at a dam site. Even further, utilities and regulators are recognizing the need to prioritize dam safety evaluations and dam safety improvement investments, which necessitates performing these evaluations not for a single dam but for a portfolio of dams, and with a consistent methodology that provides a basis for comparisons between dams.

There are two general approaches used in seismic stability evaluations of earthen dams. The first is a dynamic analysis where the seismic hazard assessment and ground-motion selection is site-specific and the dam material properties are project-specific and based on field and laboratory measurements. The dynamic analysis is performed by either equivalent-linear or nonlinear methods and in most cases a two-dimensional numerical model of the dam is utilized. Expected deformations are calculated for a limited number of ground motions using best-estimate material properties. Uncertainties are generally not characterized or provided, and instead the traditional approach has been to provide a discussion on the sources of conservatism in the inputs. These advanced analyses are usually only performed in the final design stages of new dams, in the evaluation of an existing dam that has been flagged as a high priority, or in the case of an accident analysis for a dam that has already failed. The dynamic analysis approach is numerically rigorous but time-consuming and expensive.

The second approach is to use a simplified procedure where the deformation is estimated from a GMPE-like equation that relies on variables or proxies to describe the input ground

motion and system response. Simplified procedures are developed by running a large number of ground motions through a simple system response to create a dataset of deformations, which are then fit with a functional form using regression techniques. The generation of a dataset using numerical simulations is necessary because empirical observations of dam deformations are limited. The procedures generally provide an estimate of the median deformation and the standard deviation of that deformation, with an assumed log-normal distribution. These simplified procedures are typically used to gain insights about the dam performance in the early stages of a project or as a quick check by reviewers. The semi-empirical equations are easy to use but provide limited flexibility to refine the input ground motion and were generally not developed with physical constraints on the extrapolation, making the models useful over a limited intensity range.

The model developed in this chapter utilizes an approach that falls between the dynamic analysis approach and currently available simplified procedures. The model estimates the transfer function for a potential sliding mass of an earthen dam, which is applied to a ground motion to estimate the average acceleration time history and calculate a shear-induced Newmark deformation. This definition of a transfer function as the ratio between the average acceleration of the potential sliding mass and the input ground motion is a key concept of the model, as discussed further in Section 4.2.3. The methodology accommodates the full time history of the ground motion, allowing the user to take advantage of available seismic hazard characterization through the use of site-specific ground motions. Because the full time history is utilized, the approach provides flexibility in applying the model to a wide range of different ground motions, including ground motions with different frequency content and durations.

The estimated transfer function is dependent on readily available properties of the dam, including dam height and average shear-wave velocity, as well as properties that characterize the intensity of the input motion. The transfer-function model captures the key mechanisms through which nonlinearity affects soil behavior, including dam period shift and damping increase, providing a physical basis for the model and constraints on its extrapolation. The proposed approach allows the user to perform hundreds of simplified dynamic analyses without building a detailed finite-element model for a dam and without the extensive run times of advanced analyses. The approach is efficient enough that it can be used to calculate and regularly update mean shear-induced deformation hazard with uncertainties for a portfolio of dams.

4.2 Previous Studies and Model Concept

Previous studies are discussed to place the proposed model in the context of current research, consulting practices, and available procedures. A sample of recent site-specific studies and the most common simplified procedures are summarized. An overview of the transfer-function model concept is presented, and the key advantages of the proposed approach are discussed.

4.2.1 Previous Site-Specific Studies

Numerous studies have performed dynamic analyses and applied the Newmark method to estimate shear-induced deformations for a set of site-specific ground motions applied to a numerical model of an earthen dam. Historically, a limited number of ground motions – typically

three to seven – have been run at the seismic hazard design or evaluation level. Details and results from these studies can be found in academic journals (e.g., Hadidi et al., 2014; Mejia et al., 2014) and consulting reports (e..g., URS Corporation, 2006; AMEC Geomatrix, Inc., 2011; TERRA / GeoPentech, 2012). More recently, a few projects have been completed where significantly more ground motions were used to estimate the permanent deformations across a wide range of ground-motion intensities, with the purpose of performing a probabilistic deformation hazard analysis for the dam. One such study was performed for an embankment dam at a nuclear facility in the Eastern United States (Phalen and Wagner, 2017). The probabilistic deformation analysis of the embankment was a small task of a larger site risk assessment for the nuclear facility. Another recent study was performed for a rockfill embankment dam on the West Coast of the United States as part of an ongoing dam safety and risk assessment program (Conkle, 2017).

In each of these two studies, the computer program QUAD4MU (Hudson et al., 2003) was used to model the dam with a two-dimensional finite-element mesh and perform the dynamic analyses with the equivalent-linear method. A detailed analysis was performed for a single dam subjected to tens or hundreds of expected ground motions. These types of studies are relatively new in the dam industry with respect to quantifying probabilistic deformation hazard. These studies are also expensive, and updating the deformation hazard by performing dynamic analyses at a frequency similar to what is done for seismic hazard (every 5-10 years) is cost-prohibitive for the average utility and dam. It is also challenging to perform these studies in a consistent way for the tens or hundreds of dams in a portfolio so that the results can be compared and used as part of a risk-reduction program.

A better use of resources may be to evaluate the deformation hazard with the transfer-function model for all dams in a portfolio and use those results to identify or flag high-priority dams. Resources can then be spent measuring dam material properties and performing state-of-the-art studies such as nonlinear, fully coupled analyses for those dams estimated to carry the highest seismic risk in the portfolio. The results of the transfer-function model analyses can also be used to inform the ground-motion selection for the advanced analyses so that fewer sophisticated runs are necessary.

4.2.2 Previous Simplified Procedures

Makdisi and Seed (1978) introduced one of the most widely used simplified procedures for estimating the shear-induced deformation of an earthen dam. The procedure is based on the results of a limited number of dynamic analyses run using the two-dimensional finite-element method with the equivalent-linear scheme. In particular, the number of earthquake ground motions was extremely limited by today's standards with three empirical recordings and one artificial record. The estimated shear-induced deformation is calculated from two charts that rely on the user-defined earthquake magnitude and sliding mass geometry, as well as user-estimated crest PGA, yield coefficient, and first natural period.

Subsequent researchers have updated and improved upon the work of Makdisi and Seed by formulating the procedure in terms of a GMPE-like equation rather than look-up charts, predicting deformations from inputs that don't require the user to estimate the response at the crest of the dam or the first natural period, and running more ground motions when generating

their dataset (e.g., Bray and Travasarou, 2007; Saygili and Rathje, 2008; Du et al., 2018; Bray and Macedo, 2019). These simplified procedures all use a similar approach where a large number of ground motions are run through an idealized sliding-mass model, and a Newmark analysis is performed to calculate the displacements. The geometry and dynamic properties of the potential sliding mass are often varied to capture a range of natural periods, and the yield coefficient is also varied to capture a range of material strengths. The approaches can differ on whether the sliding mass is assumed to be rigid or flexible, whether a coupled or de-coupled analysis is utilized, and how the resulting deformations from two possible horizontal components and two polarities are treated. Regression techniques are used to fit a curve through the resulting deformations, based on predictor variables that characterize the potential sliding mass and ground motion.

4.2.3 Transfer-Function Model Concept

Figure 4.1 provides a schematic of the transfer-function model concept, with a comparison that illustrates how the transfer-function model is used in place of a finite-element model of a dam to estimate the average acceleration time history for a potential sliding mass. The top portion of the figure shows the basic steps performed in a dynamic analysis. An appropriate acceleration time history is selected based on the characteristics of the expected ground motion at the dam site. A finite-element model of the dam is built and appropriate material properties are selected, including shear-wave velocity values and shear-modulus reduction and material damping curves. The dynamic analysis is performed and the output of the program is the average acceleration time history for the pre-determined potential sliding mass. The yield coefficient, typically calculated from a pseudo-static stability program such as SLOPE/W (GEO-SLOPE International Ltd., 2008), is applied to the average acceleration time history using the Newmark (1965) sliding block procedure modified for a flexible sliding block analysis (Makdisi and Seed, 1978) in a de-coupled approach (Kramer and Smith, 1997; Bray and Rathje, 1998). Two shear-induced deformations are calculated – one for the standard polarity and one for the reverse polarity.

The bottom portion of Figure 4.1 shows the basic steps performed using the transfer-function model. The input acceleration time history is the same, and the full description of the ground motion is used in the application of the model. The finite-element mesh and dynamic analysis has been replaced by an estimate of the transfer function for the potential sliding mass, describing how the earthen dam amplifies and filters input motions at different frequencies. The transfer function estimated from the model depends on the properties of the input ground motion and on the properties of the dam. The transfer function is applied to the input time history and an estimate of the average acceleration time history for the potential sliding mass is obtained. The Newmark sliding block procedure is then applied in the same way as it was for the dynamic analysis, and two shear-induced deformations are again calculated.

The transfer function depicted in the bottom portion of Figure 4.1 is estimated from the transfer-function model, which is developed based on the results of a series of dynamic analyses depicted by the finite-element mesh of the earthen dam in the top portion of the figure. It is important to define this specific transfer function and emphasize that this definition of a transfer function is unique and is not typically calculated or presented in dam seismic stability evaluation reports. The transfer function utilized in this study is defined as the ratio of the Fourier transform of the average acceleration time history of the potential sliding mass to the Fourier transform of

the input ground motion time history, as illustrated in Figure 4.2. This transfer function is not the transfer function between the crest and input motion (i.e., the spectral ratio) as is typical when analyzing vibration periods of dams, and it is not the amplification factor between the crest and input motion response spectra as is typical in site response. The transfer function in this study is between the average acceleration time history of the potential sliding mass and the input ground motion.

The proposed transfer-function model offers an intermediate procedure between a detailed dynamic analysis and available simplified procedures, and is similar in concept to the recently published work by Hayati and Moss (2017). The application of their proposed method is the computation of the surface response spectra for site response, rather than the shear-induced deformation of a potential sliding mass of an earthen dam, but there are similarities in the approach in terms of providing a model that accepts the full ground-motion time history as an input. Hayati and Moss develop a simplified procedure that provides a five-point estimate of site amplification factor, providing an intermediate site response solution between generic site factors and rigorous numerical solutions. In contrast, the proposed transfer-function model is formulated to provide a continuous estimate of the transfer function across all frequencies, rather than a discrete estimate, and offers a means to obtain an estimate of the average acceleration time history for a potential sliding mass for a shear-induced deformation analysis.

4.2.4 Advantages and Limitations of Transfer-Function Model

The key difference between an advanced analysis and the proposed transfer-function model is that the transfer-function model provides the response of an average dam. The representative dams are idealized earthen dams and are not modeled with the same level of detail as a site-specific study. The proposed approach is not expected to reproduce the response of dams with unique features or shear-wave velocity profiles that differ significantly from those utilized in the seed dynamic analyses, but it should provide a reasonable first-order approximation of an average earthen dam response. The advantage of running the transfer-function model in place of more rigorous and detailed dynamic analyses is that hundreds of ground motions can be run in a few seconds with basic inputs that characterize the dam. Additionally, the proposed approach allows the model to be applied to multiple dams with a consistent methodology, which is advantageous when the goal is to make comparisons between dams.

The key differences between available simplified procedures and the proposed transfer-function model are that the transfer-function model accepts the full description of the ground motion and the model simplifies the dam response only. The full acceleration time history of a potential future earthquake is an input to the transfer-function model. The ground motion is not simplified or replaced with a proxy or series of proxies. The output of the transfer-function model is an estimate of the average acceleration time history for a potential sliding mass, which can be used to apply the Newmark sliding block procedure to estimate shear-induced deformations. The Newmark sliding block procedure is not simplified and is not part of the model. These differences lead to maximum flexibility in the application of the model, which is the key advantage of the proposed approach. The flexibility of the model allows for the most information of the input that has the biggest effect on the deformation – the input ground motion.

The proposed transfer-function model is based on the results of 2D equivalent-linear analyses utilizing the de-coupled approach, and limitations of this approach are carried through to the transfer-function model. The de-coupled approach is necessary to accommodate the entire time history of the ground motion as an input to the model, but is an approximation of fully coupled response interaction. The equivalent-linear method is also an approximation of the fully nonlinear behavior of soils. These approximations are acknowledged as limitations of the proposed approach, and are acceptable given that the intended application of the model is to carry out a first-order approximation of shear-induced deformations to characterize the deformation hazard and its associated uncertainties for a portfolio of dams.

Importantly, the average acceleration time history of a potential sliding mass that is estimated from the transfer-function model is only as good as the dynamic analyses that the transfer-function model is based on. The transfer-function model presented in this chapter represents one implementation of the transfer function methodology for a given set of assumptions about the characteristics of the earthen dam. Future work can expand the methodology by considering a range of assumptions about the characteristics of the earthen dam to broaden its applicability.

4.3 Synthetic Dataset

The model is built on the results of a series of dynamic analyses performed by running recorded earthquake ground motions through numerical models of representative dams. In particular, the transfer function for a potential sliding mass is extracted from each dynamic analysis and the model estimates this transfer function from properties of the dam and input ground motion. Permanent Newmark deformations are also calculated from the average acceleration time histories of the dynamic analyses and these deformations are used to calibrate the model by comparing them with the Newmark deformations that are calculated when the modeled transfer function is applied to the same input ground motions. The results of the dynamic analyses constitute a synthetic dataset of the response of dams to earthquake ground motions.

4.3.1 Dynamic Analysis Methodology

The computer program QUAD4MU was used to perform the dynamic analyses of the representative earthen dams, capturing the response of the embankment materials and providing an average acceleration time history for the potential sliding mass. The program models the dam with two-dimensional finite elements and uses the equivalent-linear procedure to assign strain-compatible shear-modulus reduction and material damping properties to the dam. The equivalent-linear procedure consists of a time-stepping analysis that begins with an initial estimate of the shear modulus and damping ratio for each element. Using an iterative process, the system is analyzed using these shear modulus and damping ratio values, effective shear strains are calculated as 65% of the maximum shear strain, and new shear modulus and damping ratio values at the effective shear strain are employed in the next iteration. The process is repeated until convergence is achieved. The final shear modulus and material damping values for each element are used for the entire duration of the acceleration time series.

One of the features that makes QUAD4MU an attractive program for this study is the average acceleration time history output, which the program calculates for a user-defined potential sliding mass. The average acceleration is the ratio of the force induced by an earthquake in a block of mesh, over the mass of that block. The summation of forces acting on a block is computed as a function of time, and the average acceleration is then computed for each time step. The shear-induced deformation of the failure surface can be estimated using the yield-acceleration concept employed by a Newmark sliding block analysis on the average acceleration time history of the potential sliding mass.

4.3.2 Representative Dams and Input Ground Motions

Twelve representative dams were used to perform dynamic response analyses and obtain transfer functions for average acceleration time histories of selected potential sliding masses within the dam. The twelve representative dams consist of combinations from four dam heights and three shear-wave velocity profiles. Dam heights from the Division of Safety of Dams database (Division of Safety of Dams, 2018) were used to select the four representative dam heights of 25 *ft*, 50 *ft*, 100 *ft*, and 150 *ft*. Shear-wave velocity measurements from the Sykora (1987) database were used to select the three representative shear-wave velocity profiles for each dam height. The representative shear-wave velocity profiles for the various dam heights are shown in Figure 4.3 along with the associated velocity profile equations, which are modified from Sawada and Takahashi (1975). The average shear-wave velocities of the dams are summarized in Table 4.1. Two potential failure surfaces were considered for each dam – one "deep" failure at the full dam height and one "shallow" failure at half of the dam height. Both failure surfaces occupy the full crest width and occur on the downstream side of the dam.

The representative dams are idealized as homogeneous embankments comprised of sand, silt, and clay. A single representative unit weight of 130 *pcf* was used for the embankment material and a unit weight of 150 *pcf* was used for the foundation. The shear-modulus reduction and material damping curves used for the embankment materials are the confining-pressure-dependent relationships by Darendeli (2001) for PI=20, modified at large strains using the procedure proposed by Yee et al. (2013). Four curves at confining pressures of 0.5, 1, 2, and 4 *atm* were utilized based on the range of stresses present in the representative dams. Figure 4.4 presents the shear-modulus reduction and material damping curves.

A total of 950 ground motions were run through each representative dam. The ground motions were selected from the NGA-West2 database (Ancheta et al., 2014) and include the horizontal 1 and horizontal 2 components for 475 records from 122 earthquakes. Minimum screening criteria included a lowest usable frequency of 0.8 *Hz* or less and a V_{S30} value greater than 300 *m/s*. The earthquake magnitudes range from M 5.0 to M 7.9 and the geometric mean PGAs for the records range from 0.01 *g* to 2.0 *g*. To build a model that works well at all anticipated ground-motion levels, records were selected to obtain a uniform distribution of PGAs from 0.01 *g* to 2.0 *g*. (i.e., the same number of records were chosen at a PGA of 0.1 *g* as a PGA of 1.0 *g*). Because very few recordings are available at the highest PGA levels, some records had to be modified by scaling the amplitude to reach the desired PGA. The durations of the ground motions were not modified. The records were also selected to retain the variability in duration and Arias intensity of the larger dataset, meaning that the median and standard deviation for the

duration and Arias intensity of the 475 selected recordings is consistent with that of the larger NGA-West2 database.

4.3.3 Transfer-Function Behavior

The transfer functions from the dynamic analyses form the basis of the proposed model. For each dynamic analysis, an acceleration transfer function for each potential sliding mass is computed. This section presents a sample of the transfer functions computed from the dynamic analyses to examine the key changes in transfer-function shape. The dam height, dam shear-wave velocity, failure surface, and intensity of the input ground motion all influence the behavior of the transfer function.

Figure 4.5a shows that when the same input ground motion is propagated through dams of varying heights, the first-mode frequency of the transfer function shifts to lower frequencies, or longer periods, as the dam height increases. Figure 4.5b shows that when the same input ground motion is propagated through dams of varying shear-wave velocity profiles, the first-mode frequency of the transfer function shifts to higher frequencies, or shorter periods, as the dam shear-wave velocity increases. Both of these behaviors are expected, as taller dams are more flexible and have larger mass, leading to longer natural periods, and dams characterized by higher shear-wave velocities are stiffer in their response, leading to shorter natural periods. Note that the first-mode frequency of the transfer function reflects the natural period of the potential sliding mass, which is similar, but not equal to the natural period of the dam.

Figure 4.5c shows that when a given dam is subjected to the same input ground motion, the transfer functions for a deep and shallow failure surface are centered on similar first-mode frequencies, but the transfer function for the shallow failure surface exhibits stronger amplification. The increased amplification associated with the shallow failure surface is also expected because the shallow failure surface is located toward the top of the dam, where amplification is higher. Though dynamic analyses were completed for two failure surfaces, the remainder of this chapter and the proposed model will focus on the results from the deep failure surfaces.

Figure 4.5d shows that when a given dam is subjected to input ground motions of varying intensity, the dam response is different, resulting in dramatically different transfer functions. As the input ground-motion intensity increases, there is a shift in the first-mode frequency of the transfer function to lower frequencies, or longer periods. This trend is caused by the nonlinear response of soils, characterized by a decrease in stiffness as shear strain increases, leading to a downward shift in the first-mode frequency response. Additionally, as the ground-motion intensity increases, the shape of the transfer function becomes less peaked, and the amplification factor at the first-mode frequency is reduced. This trend is also explained by the nonlinear response of soils, characterized by an increase in damping as shear strain increases, leading to a reduced response or amplification of the ground motion.

4.3.4 Shear-Induced Deformations

Shear-induced Newmark deformations are calculated from the average acceleration time histories for the potential deep sliding mass for a suite of yield coefficients ranging from 0.05 to

0.30. For each yield coefficient, two deformations are calculated – one for the standard polarity of the average acceleration time history, and one for the reverse polarity. Figure 4.6 plots the deformations from the representative dam with a height of 150 *ft* and medium shear-wave velocity profile when a yield coefficient of 0.05 is applied. The deformations are plotted against various ground-motion intensity measures that are useful predictors of deformation including peak ground acceleration, peak ground velocity, and Arias intensity (Saygili and Rathje, 2008; Armstrong, 2017). The results follow the expected trend of increasing deformation with increasing ground-motion intensity. When deformations greater than 5 *cm* are considered, peak ground velocity is the most efficient predictor, with a standard deviation of 0.61 natural log units. When all twelve representative dams are analyzed with the full suite of yield coefficients, peak ground velocity remained the single best predictor of shear-induced deformations, with an average standard deviation of 0.65 natural log units.

4.4 Matched Transfer Functions

A simplified transfer function is fit to each dynamic-analysis transfer function, resulting in a dataset of matched transfer functions. The matching process is summarized and an illustrative example is presented. The predictor variables of the matched transfer functions are compiled and trends are observed.

4.4.1 Matching Process

The free variables to fit the matched transfer function to the dynamic-analysis transfer function are the natural angular frequency of damped vibration (ω_D), the damping ratio (β), and a scale factor (α). Later, these parameters will be predicted with basic information about the dam and the ground motion. The functional form of the matched transfer function is defined in the frequency domain as:

$$H(\omega) = \alpha \left[1 + \frac{(i\omega)^2}{\omega^2 - \omega_n^2 - 2i\beta\omega_n\omega}\right] \tag{4.1}$$

where ω is angular frequency, i is the unit imaginary number, ω_n is the natural angular frequency of the system, β is the damping ratio, and α is a scale factor. The transfer function described by equation 4.1 is for spectral acceleration response, not pseudo-spectral acceleration response. This difference is important given the relatively high matched damping ratios that provide the best fit to the dynamic-analysis transfer functions. Note that equation 4.1 is complex-valued. Although the fitting is performed on the dynamic-analysis transfer function (ratio of amplitudes), there is also a phase shift between the input ground motion and the sliding mass response. The phase contribution from equation 4.1 is adequate to capture the phase shift in the dynamic analyses, so the focus of the matching is on the amplitudes.

The matching process starts by finding the first-mode frequency of the transfer function for the deep failure surface and converting it to the first-mode angular frequency, ω_1. The first-mode frequency corresponds to the peak of the transfer function. ω_1 is equivalent to the natural angular frequency of damped vibration, ω_D. The natural angular frequency of damped vibration, ω_D, is related to the natural angular frequency, ω_n, by the equation:

$$\omega_n = \frac{\omega_D}{\sqrt{1-\beta^2}} \tag{4.2}$$

This ω_n is input into equation 4.1, and an algorithm was developed to find the combination of damping ratio, β, and scale factor, α, that when plugged into equations 4.2 and 4.1, provides the best fit to the dynamic-analysis transfer function. Initial results indicated that the scale factor, α, does not depend on the properties of the dam or the input ground motion. Instead, α depends on the failure surface. A constant scale factor of 0.85 provided the best fit for the deep failure surface results. The matching process was repeated to find the damping ratio that provided the best fit to the dynamic-analysis transfer function when the constant scale factor of 0.85 was applied.

4.4.2 Illustrative Example of Matching

Figure 4.7 illustrates an example of the matching process. The example uses the dynamic-analysis results for the representative dam with a height of 50 *ft*, the medium shear-wave velocity profile, and the deep potential sliding surface. The input ground motion is the 1994 Northridge earthquake record NORTHR\TPF270 with a PGA of 0.32 *g*. The dynamic-analysis transfer function is computed as the ratio of the average acceleration of the potential sliding mass to the input ground motion (both transformed into Fourier amplitude spectra in the frequency domain). Recall that this is a unique definition of a transfer function that is utilized in this study for the sole purpose of developing a model that estimates the average acceleration of a potential sliding mass. Figure 4.7a presents the dynamic-analysis transfer function and denotes the first-mode angular frequency, ω_1, and its equivalent first-mode frequency, f_1, of about 3 *Hz*. This first-mode frequency is consistent with the peak of the transfer function and is used in the calculation of the matched transfer function.

A search is performed on the damping ratio and scale factor that produce a transfer function that best fits the dynamic-analysis transfer function. Figure 4.7b shows the resulting transfer function from three trial damping ratios. Here the scale factor, α, is kept constant at 1 to isolate the change in the transfer-function shape when the damping ratio is varied. These three trial transfer functions were computed from Equation 4.1. The natural angular frequency, ω_n, was re-computed from equation 4.2 for each damping ratio. Figure 4.7b illustrates that a lower damping ratio produces a transfer function with a high peak amplification factor while a higher damping ratio produces a transfer function with a low peak amplification factor. When looking at how well the trial transfer functions match the dynamic-analysis transfer function, a damping ratio of 0.25 provides the best fit at the first-mode frequency. All three of the trial transfer functions are broader than the dynamic-analysis transfer function at frequencies that neighbor the first-mode frequency.

Figure 4.7c shows the resulting transfer function from three trial scale factor values. Here the damping ratio, β, is set to 0.25 to isolate the change in the transfer-function shape when the scale factor is varied. As expected, the scale factor simply scales the entire transfer function up and down. The scale factor causes the matched transfer function not to equal unity at low frequencies. To correct this undesirable behavior, an adjustment is later applied to set the amplitude spectrum equal to one at low frequencies.

Figure 4.7d shows the matched transfer function with the best fit to the QUAD4MU transfer function for this example. When a scale factor of one was used in Figure 4.7b, a damping ratio of 0.25 provided the best fit, but the trial transfer function was too broad. In Figure 4.7d, the best fit is achieved with a scale factor of 0.85 and a damping ratio of 0.20. The combination of a lower scale factor and lower damping ratio results in a transfer function that better matches the QUAD4MU transfer function across the entire first mode. Also note that the adjustment was applied to set the amplitude spectrum equal to one at low frequencies.

4.4.3 Matched Transfer-Function Deformations

To calculate shear-induced deformations from a matched transfer function, the input ground motion is multiplied by the matched transfer function, an inverse Fourier transform is performed, and the resulting estimate of the average acceleration time history for the potential sliding mass is used to calculate standard and reverse polarity Newmark deformations. As an example, the average acceleration time histories from the illustrative example are presented in Figure 4.8. The dynamic-analysis average acceleration time history for the potential sliding mass comes from the QUAD4MU output file. The modeled average acceleration time history for the potential sliding mass comes from applying the matched transfer function ($f_1 \cong 3$ Hz, $\beta = 0.20$, $\alpha = 0.85$) to the input ground motion. A yield coefficient of 0.12 is used and the resulting standard and reverse polarity shear-induced deformations are displayed on Figure 4.8.

The difference between the dynamic-analysis deformations and the matched transfer-function deformations comes from the differences in the average acceleration time histories and can be attributed to two sources. First, the transfer function amplitudes are not identical. Figure 4.7d shows that the matched transfer function is slightly lower than the QUAD4MU transfer function at frequencies below the natural frequency, and slightly higher at frequencies above the natural frequency. At the higher frequencies, the matched transfer function splits the difference between the first and second mode. The matched transfer function does not have the same details as the QUAD4MU transfer function, but does a good job of reproducing the amplification around the first mode.

Second, the phase shift modeled by Equation 4.1 is not the same as the phase shift that occurs in the dynamic analysis. Figure 4.9 presents the phase of the input ground motion, the phase of the average acceleration time histories, and the shifts between the two from the illustrative example. The phases are presented as phase difference distribution plots rather than phase angle plots. The phase difference of the average acceleration time history from the dynamic analysis has a similar distribution as the phase difference of the input ground motion, meaning that the phase shift from the input motion to the average acceleration time history of the potential sliding mass is minimal. Equation 4.1 results in essentially no phase shift between the input ground motion and the modeled average acceleration time history. The model does not reproduce the shift seen in the dynamic analysis, but does result in an average acceleration time history with approximately the right phase.

The parameters that define the matched transfer functions will be used to build the transfer-function model. To ensure that these matched transfer functions are a good basis for the model, the deformations obtained from the matched transfer functions were checked against the deformations from the dynamic analyses by computing residuals. The matching process was

adjusted until the resulting residuals were unbiased and a minimum standard deviation was reached. Specifically, different frequency ranges were used in the matching process and different constant scale factors (α) were applied to the matched transfer functions. Matching the transfer functions over a frequency range corresponding to amplification factors higher than one and using a constant scale factor of 0.85 produced the lowest unbiased residuals.

4.4.4 First-Mode Period Trends

To observe the trend in period shift, the first-mode period normalized by the small-strain period, T_1/T_o, is plotted against $SA(T_{NL})$ of the ground motion for each of the dynamic analyses. T_o is the small-strain fundamental period of the deep sliding mass. T_o of the deep sliding mass can be approximated as T_o of the dam, which can be estimated as $3H/V_S$. There is a single T_o value for each dam. T_1 is the first-mode period corresponding to the peak of the transfer function for the deep failure surface. A T_1 value is obtained for each dynamic analysis, resulting in 950 T_1 values per dam – one for each input ground motion. $SA(T_{NL})$ is the spectral acceleration of the input ground motion used in the dynamic analysis and is explained further in section 4.4.6 below. Figure 4.10 presents the resulting plots for four of the representative dams.

When the input ground motion has a low spectral acceleration, T_1/T_o is approximately equal to one, meaning that the first-mode period of the sliding mass is equal to the small-strain fundamental period. This response indicates that when the dam is subjected to low intensity ground motions that induce small strains in the dam, the dam behaves linearly and there is no period shift in the response of the deep sliding mass. As the input ground-motion intensity increases, the dam response reaches a spectral acceleration where the onset of nonlinearity occurs and T_1/T_o is greater than one. As the input ground-motion intensity increases further, T_1/T_o continues to increase and the dam behavior becomes highly nonlinear.

As shown in Figure 4.10, the nonlinear behavior of the dam with respect to the shift of the first-mode period of the deep sliding mass is dam-dependent. Dam height and dam shear-wave velocity profile impact how the period elongates with increasing ground-motion intensity. For dams with high shear-wave velocities, the onset of nonlinearity occurs at a higher spectral acceleration and the slope in the nonlinear region is steeper than dams with low shear-wave velocities. For short dams, the onset of nonlinearity also occurs at a higher spectral acceleration and the slope in the nonlinear region is steeper than tall dams. Both of these behaviors can be explained in the context of ductile versus brittle behavior. High shear-wave velocities and a short height lead to a stiffer system, which responds in a more brittle manner. The dam stays in the linear range up to a higher spectral acceleration, the onset of nonlinearity is abrupt, and the degradation in the nonlinear region is severe. On the other hand, low shear-wave velocities and a tall height lead to a flexible system, which responds in a more ductile manner. The dam begins to exhibit nonlinear behavior at a lower spectral acceleration, the onset of nonlinearity occurs over a wider transition zone between the linear region and nonlinear region, and the degradation in the nonlinear region is gradual.

4.4.5 Matched Damping Ratio Trends

To observe the trend in damping increase, the matched damping ratio, β, is plotted against the $SA(T_{NL})$ of the ground motion for each of the dynamic analyses. β is the damping ratio that

produces a transfer function that best matches the transfer function from the QUAD4MU dynamic analysis over the frequency range spanning the first mode. It is not a direct output from the QUAD4MU file, but instead is found by calculating the transfer function for the deep sliding mass from the QUAD4MU output and then matching a transfer function as described in Section 4.4.1. A matched β value is obtained for each dynamic analysis, resulting in 950 β values per dam – one for each input ground motion. The $SA(T_{NL})$ is the spectral acceleration of the input ground motion used in the dynamic analysis. Figure 4.11 presents the resulting plots for four of the representative dams.

When the input ground motion has a low spectral acceleration, β is at its minimum. The constant damping ratio at low intensity ground motions indicates that the dam behaves linearly and there is no change in the transfer-function shape for ground motions with low intensity. The damping ratio stays at a minimum until the ground-motion intensity reaches the onset of nonlinearity and β begins to increase. As the input ground-motion intensity increases further, β continues to increase and the dam exhibits nonlinear behavior. The damping ratio increase corresponds to reduced amplification of the input ground motion through a less peaked transfer function. When the input ground motion has a very high spectral acceleration, β reaches an approximate maximum and the damping ratio is relatively constant again.

As shown in Figure 4.11, the nonlinear behavior of the dam with respect to the matched damping is dam-dependent. Consistent with the trend for T_1/T_o, the onset of nonlinearity with respect to damping occurs at a lower spectral acceleration and the increase in damping in the nonlinear region occurs over a wider range of spectral accelerations for dams with lower shear-wave velocities (more ductile behavior). The trend with dam height is less pronounced but still consistent with the trend for T_1/T_o, where the onset of nonlinearity occurs at a lower spectral acceleration for taller dams (also exhibiting more ductile behavior).

4.4.6 SA(T_{NL})

To capture the nonlinear behavior of the dam materials, the parameters of the transfer-function model must depend on the input ground motion. The first-mode periods and damping values from the matched transfer functions were plotted against a variety of ground-motion intensity measures to determine which intensity measure best explained the two parameters. Ground-motion intensity measures that were considered included PGA, PGV, and a suite of nine spectral accelerations (SA) at periods ranging from 0.1 to 2.0 *s*.

While PGA and PGV were the best dependent variables for some dams, overall spectral acceleration did a better job at explaining the two parameters. This is consistent with the work by Travasarou (2003), though in this study the spectral acceleration is used to estimate the period shift and increase in damping, while in Travasarou (2003) the spectral acceleration is used to estimate the Newmark displacement. At low ground-motion intensity levels, shorter periods did a better job explaining the nonlinear behavior, and at higher ground-motion intensity levels, longer periods did a better job explaining the nonlinear behavior. This indicates that the period of the spectral acceleration that best explains the first-mode period of the deep sliding mass is the first-mode period of the sliding mass itself, which creates a circular logic problem. Rather than formulate a model that requires an iterative procedure to calculate T_1, a single best spectral acceleration period was chosen for each dam. The period of this spectral acceleration is referred

to as T_{NL}, the single period that when used to compute a spectral acceleration, best explains the nonlinear behavior of the dam. T_{NL} is different for each dam, and is calculated as:

$$\ln(T_{NL}) = a_1 \ln(T_o) + a_2 \tag{4.3}$$

where T_o is the small-strain fundamental period of the dam in seconds, and coefficients a_1 and a_2 are provided in the first two rows of Table 4.2. The T_{NL} values calculated from Equation 4.3 for the range of small-strain fundamental periods of the representative dams are shown in Figure 4.12a. The ratios of T_{NL}/T_o are plotted against T_o in Figure 4.12b. As an example, for representative dam number 8, which has a height of 100 *ft* and a medium shear wave velocity profile, T_o = 0.34 *s* and T_{NL} = 0.63 *s*. The ratio of T_{NL}/T_o is 1.84. These example values are highlighted on Figure 4.12.

4.5 Transfer-Function Model

The model provides an estimate of the transfer function for a potential sliding mass of an earthen dam. The transfer function specifically describes the change in the amplitude and phase from the input motion to the average acceleration time history for a potential sliding mass over a full range of frequencies. The complex-valued transfer function is calculated from three parameters: the natural angular frequency of the system (ω_n), the damping ratio of the system (β), and a scale factor (α).

4.5.1 Functional Form

The ratio of the first-mode period of the deep sliding mass to the small-strain fundamental period is calculated from Equation 4.4. The functional form of Equation 4.4 can be described as a continuous hinge function, where two straight lines are connected with a smooth curve. This functional form is ideal for describing the behavior of the period shift, which is characterized by two distinct regions – linear and nonlinear – and a transition region in between. The ratio of T_1/T_o is estimated as:

$$T_1/T_o = 1 + exp^{c_1(c_2 + \ln(SA(T_{NL})))} \tag{4.4}$$

where $SA(T_{NL})$ is the 5% damped pseudo-spectral acceleration of the input ground motion at the nonlinear period of the dam in *g*, c_1 describes the slope of the nonlinear region, and c_2 is inversely related to the onset of nonlinearity. The c_1 and c_2 parameters are calculated as:

$$c_1 = (a_3\ lnH + a_4)V_S + (a_5\ lnH + a_6) \tag{4.5}$$

$$c_2 = a_7\ c_1 + a_8 \tag{4.6}$$

where H is the height of the dam in *ft*, V_S is the average shear-wave velocity of the dam in *ft/s*, and coefficients $a_3 – a_8$ are provided in Table 4.2.

The T_1/T_o values calculated from Equation 4.4 for all representative dams and a range of spectral accelerations are shown in Figure 4.13. The period of the spectral acceleration (T_{NL}) on the x-axis is different for each dam. The range of T_{NL} for all representative dams is about 0.2 – 1.0 *s*. As an example, for a magnitude 7 earthquake at 5 *km*, the NGA-West2 ground motion models estimate spectral accelerations of about 0.1 – 1.65 *g* for the range of T_{NL} from 0.2 – 1.0 *s*

and considering plus and minus one standard deviation of the ground motion. At these spectral accelerations, T_1/T_o ranges from 1 to 3.3 for the representative dams.

The T_1/T_o ratio is multiplied by an estimate of T_o to get T_1. The recommended relationship for estimating the small-strain fundamental period of the dam is:

$$T_o = \frac{3H}{V_S} \tag{4.7}$$

where H is the height of the dam and V_S is the average shear-wave velocity of the dam. The first-mode period is converted to the first mode angular frequency by:

$$\omega_1 = \frac{2\pi}{T_1} \tag{4.8}$$

The damping ratio is calculated from Equation 4.9. The functional form of Equation 4.9 can be described as an "s"-shaped curve, where an increasing slope is constrained by a pair of horizontal asymptotes. This functional form is well suited for describing the nonlinear behavior of the dam with respect to damping, which is characterized by a linear region with constant damping and a nonlinear region with increasing damping followed by saturation. The damping ratio, β, is estimated as:

$$\ln(\beta) = b_1 + \frac{b_2}{(1+exp^{b_3+b_4 \ln\left(SA(T_{NL})\right)})} \tag{4.9}$$

where $SA(T_{NL})$ is the 5% damped pseudo-spectral acceleration of the input ground motion at the nonlinear period of the dam in g, b_1 is a constant that shifts the entire curve up or down, b_2 controls the value of the lower linear region, b_3 shifts the entire curve left or right (controlling the onset of nonlinearity and onset of saturation), and b_4 controls the slope of the nonlinear region, which also impacts the onset of nonlinearity and saturation. The $b_1 - b_4$ parameters are calculated as:

$$b_1 = a_9 V_S + a_{10} \tag{4.10}$$

$$b_2 = a_{11} V_S + a_{12} \tag{4.11}$$

$$b_3 = (a_{13}\ lnH + a_{14}) V_S + (a_{15}\ lnH + a_{16}) \tag{4.12}$$

$$b_4 = a_{17} V_S + a_{18} \tag{4.13}$$

where H is the height of the dam in *ft*, V_S is the average shear-wave velocity of the dam in *ft/s*, and coefficients $a_9 - a_{18}$ are provided in Table 4.2.

4.5.2 Example Calculation

The transfer-function model is applied to a hypothetical dam with a single ground motion in this example calculation. The hypothetical dam has a height of 100 *ft* and an average shear-wave velocity of 1160 *ft/s*. A yield coefficient of 0.1 has been determined from a pseudo-static stability analysis. The transfer-function model is applied in the following steps:

1. Estimate T_o from Equation 4.7

   $T_o = 0.259\ s$

2. Calculate T_{NL} from Equation 4.3

T_{NL} = 0.508 *s*

3. Select an input ground motion

   LOMAP\BRN090 (PGA = 0.50 *g*)

4. Calculate $SA(T_{NL})$

   $SA(T_{NL})$ = 1.392 *g*

5. Calculate $b_1 – b_4$ from Equations 4.10 – 4.13 and β from Equation 4.9

   b_1 = -0.866, b_2 = -0.874, b_3 = 0.793, b_4 = 2.399, β = 0.363

6. Calculate c_1 and c_2 from Equations 4.5 and 4.6 and T_1/T_o from Equation 4.4

   c_1 = 1.388, c_2 = 0.008, T_1/T_o = 2.601

7. Calculate T_1 and convert to ω_1 from Equation 4.8

   T_1 = 0.673 s, ω_1 = 9.341 *rads/s*

8. Calculate ω_n from Equation 4.2

   ω_n = 10.023 *rads/s*

9. Estimate the transfer function for a potential deep sliding mass from Equation 4.1. For frequencies less than the first-mode frequency, if the transfer function is less than 1, set the transfer function equal to 1.

   See Figure 4.14a

10. Apply the transfer function to the input ground motion. Perform an Inverse Fast Fourier Transform to get the estimate of the average acceleration time history of the potential sliding mass. Use the yield coefficient to perform a Newmark sliding block analysis on the average acceleration time history to estimate the standard polarity shear-induced deformation. Repeat to calculate a deformation for the reverse polarity.

    See Figure 4.14b

    Standard polarity deformation = 24.0 *cm*

    Reverse polarity deformation = 33.5 *cm*

To look at how the modeled transfer function changes with ground-motion intensity, the input ground motion from this example is scaled up and down with five scale factors, and the resulting transfer functions from the model are presented in Figure 4.15. As shown in the figure, the peak of the transfer function shifts to lower frequencies, or longer periods, and the peak amplification factor decreases, as the intensity of the ground motion increases, demonstrating that the modeled transfer functions are consistent with the nonlinear behavior of soil response characterized by a shift in period and increased damping.

4.5.3 Comparisons with Synthetic Dataset

The transfer-function model is built on the results of the synthetic dataset and should reasonably reproduce the dynamic-analysis results. To make comparisons between the two, the model is used to estimate a transfer function and resulting average acceleration time history for every dynamic analysis in the synthetic dataset. The necessary inputs are the dam height, average shear-wave velocity, and input ground motion. Each average acceleration time history is used to perform multiple Newmark sliding block analyses by applying a suite of yield coefficients. Comparisons are made between the model and the synthetic dataset at each stage of the calculation by first comparing the transfer-function parameters, then maximum average accelerations, and finally the estimated shear-induced deformations.

The estimated first-mode period, T_1, and damping, β, are the essence of the transfer-function model. The T_1 and β residuals for all dams and all ground motions are presented in Figure 4.16. The residuals are defined as the observed minus the predicted values, where the observed value is the T_1 or β obtained by matching a transfer function to the dynamic-analysis results and the predicted is the T_1 or β defined by Equations 4.4 or 4.9. The median of the residuals at various ground-motion intensity levels is also shown in Figure 4.16 and indicates that the model is unbiased.

The average acceleration time histories are compared via their maximum values (k_{max}). Figure 4.17 presents the dynamic-analysis k_{max} values and applied transfer-function model k_{max} values for one representative dam. The k_{max} values from the transfer-function model are similar to those from the dynamic analyses, displaying a comparable trend with ground-motion intensity, albeit with more scatter. The k_{max} residuals for all dams and all ground motions are presented in Figure 4.18. The residuals are defined as the observed minus the predicted values, where the observed is the dynamic-analysis k_{max} and the predicted is the applied transfer-function model k_{max}. The median of the residuals at various ground-motion intensity levels is also shown in Figure 4.18 and indicates that the model is unbiased.

The average acceleration time histories are used with different yield coefficients to calculate Newmark deformations. Standard and reverse polarity deformations are calculated for every average acceleration time history. Figure 4.19 presents the dynamic-analysis deformations and transfer-function model deformations for one representative dam. The transfer-function model does a good job of reproducing the dynamic-analysis results across a wide range of ground-motion intensities. The distribution of deformations from the transfer-function model exhibits slightly more scatter, which is a consistent finding when comparisons are made across all dams, as discussed in the next paragraph. The deformation residuals for all dams, all ground motions, and all yield coefficients are presented in Figure 4.20. The median of the residuals at various ground-motion intensity levels is also shown in Figure 4.20 and indicates that the model is unbiased.

The transfer-function model leads to a distribution of deformations with a slightly higher standard deviation than the dynamic analyses (i.e., more scatter in the results shown in the plot on the right in Figure 4.19 than the plot on the left). This increase in scatter is the penalty for using a simplified model. The standard deviations of the deformations from the transfer-function model are about 0.07 ln units higher than the standard deviations of the dynamic-analysis deformations. This bias is consistent whether the deformations are plotted against PGA, PGV, or

Arias intensity. It is also consistent whether the minimum deformation considered is 1 cm, 5 cm, or 10 cm. Figure 4.21 compares the mean standard deviations from all dams for various ground-motion intensity measures and minimum deformations. The 0.07 ln bias is highlighted. Note that PGV is associated with the smallest standard deviations and PGA is associated with the largest standard deviations.

4.5.4 Model Application

The transfer-function model differs from other simplified approaches in that it does not provide a direct estimate of the median deformation and standard deviation of that deformation. Instead, the transfer-function model provides an efficient way to perform a simplified or pseudo dynamic analysis. This allows the user to select an appropriate suite of input ground motions and perform many simplified dynamic analyses in a matter of seconds. In the same way that it would not be appropriate to select a single input ground motion and run only one sophisticated dynamic analysis, the transfer-function model should not be used with a single input ground motion to characterize the shear-induced permanent deformations of a dam.

The transfer-function model should be applied to multiple input ground motions that appropriately characterize the seismic hazard of the site. The model is well suited for incremental dynamic analysis, where a suite of ground motions are scaled to several levels of seismic intensity to evaluate the response of the dam through a range of behavior. When combined with probabilistic seismic hazard curves, the results of the incremental dynamic analysis can be used to calculate probabilistic deformation hazard curves for an earthen dam. The deformation hazard curves can then be combined with fragility curves as part of a seismic risk assessment. Running the transfer-function model within a framework that uses logic trees to describe alternative models for the seismic hazard, dam response, and fragility curves has the added benefit of quantifying the uncertainties in risk assessments, a step that is rarely completed in current dam engineering practice.

The transfer-function model is also a powerful tool that can be used to gain insights and perform sensitivity studies. In particular the model can be used to look at the sensitivity of the estimated deformations to different aspects of the input ground motion. Comparisons can be made between deformations calculated from a set of ground motions matched to an ergodic target spectrum versus a non-ergodic target spectrum. The variability of the ground motion can also be accounted for by using ground-motion selection techniques that return a set of ground motions with a desired median and standard deviation. Other potential sensitivities include azimuthal direction of the ground-motion record, fault-normal and fault-parallel ground motions, pulse and non-pulse motions, and different conditional-spectrum based approaches (e.g., Baker, 2011; Arteta and Abrahamson, 2019).

4.6 Conclusions

A simplified model for running dynamic analyses is proposed to address the need to perform shear-induced deformation assessments for a large number of dams with a consistent methodology that provides a basis for comparisons between dams. The approach is based on the dynamic-analysis results from 950 input ground motions applied to 12 representative earthen

dams using the equivalent-linear finite-element method. The model estimates the transfer function for a potential sliding mass of an earthen dam, which is applied to a ground motion to estimate the time history of the average acceleration of the potential sliding mass and calculate a shear-induced Newmark deformation.

The proposed method provides a rational approach for performing hundreds of simplified dynamic analyses and estimating shear-induced Newmark deformations for earthen dams. The model should be applied to a large number of input ground motions sufficient to capture the expected aleatory variability of the seismic hazard, and should not be used to estimate deformations from a single ground motion. Use of the model requires an estimate of the small-strain fundamental period of the dam, T_o, the height of the dam, H, and the average shear-wave velocity of the dam, V_S. The full time history of the ground motion is an input to the transfer function, and leads to maximum flexibility in the application of the model.

The modeled transfer functions are recognized as a simplification of the complex process of how soil systems respond to dynamic loading; however, the transfer-function model captures the key mechanisms through which nonlinearity affects soil behavior, including dam period shift and damping increase, providing a physical basis for the model and constraints on its extrapolation. The model is an ideal tool for utilities or regulators who want to move from seismic hazard curves to shear-induced deformation hazard curves as a means to prioritize seismic safety evaluations for a large number of dams.

Table 4.1 **Small-strain fundamental period, T_o, calculated from dynamic analyses of representative dams.**

Dam No.	Height [ft]	V_S [ft/s]	T_o [s]
1	25	500	0.15
2	25	700	0.11
3	25	915	0.08
4	50	550	0.27
5	50	770	0.19
6	50	1025	0.15
7	100	610	0.49
8	100	860	0.34
9	100	1160	0.26
10	150	660	0.68
11	150	920	0.48
12	150	1255	0.35

Table 4.2 Transfer-function model coefficients.

Coefficient	TF Model
a_1	0.76
a_2	0.35
a_3	-0.00049
a_4	0.00329
a_5	-0.03558
a_6	0.35297
a_7	-0.89726
a_8	1.25375
a_9	0.00024
a_{10}	-1.14426
a_{11}	0.00090
a_{12}	-1.91824
a_{13}	0.00145
a_{14}	-0.00993
a_{15}	0.86560
a_{16}	0.57934
a_{17}	0.00172
a_{18}	0.40392
α	0.85

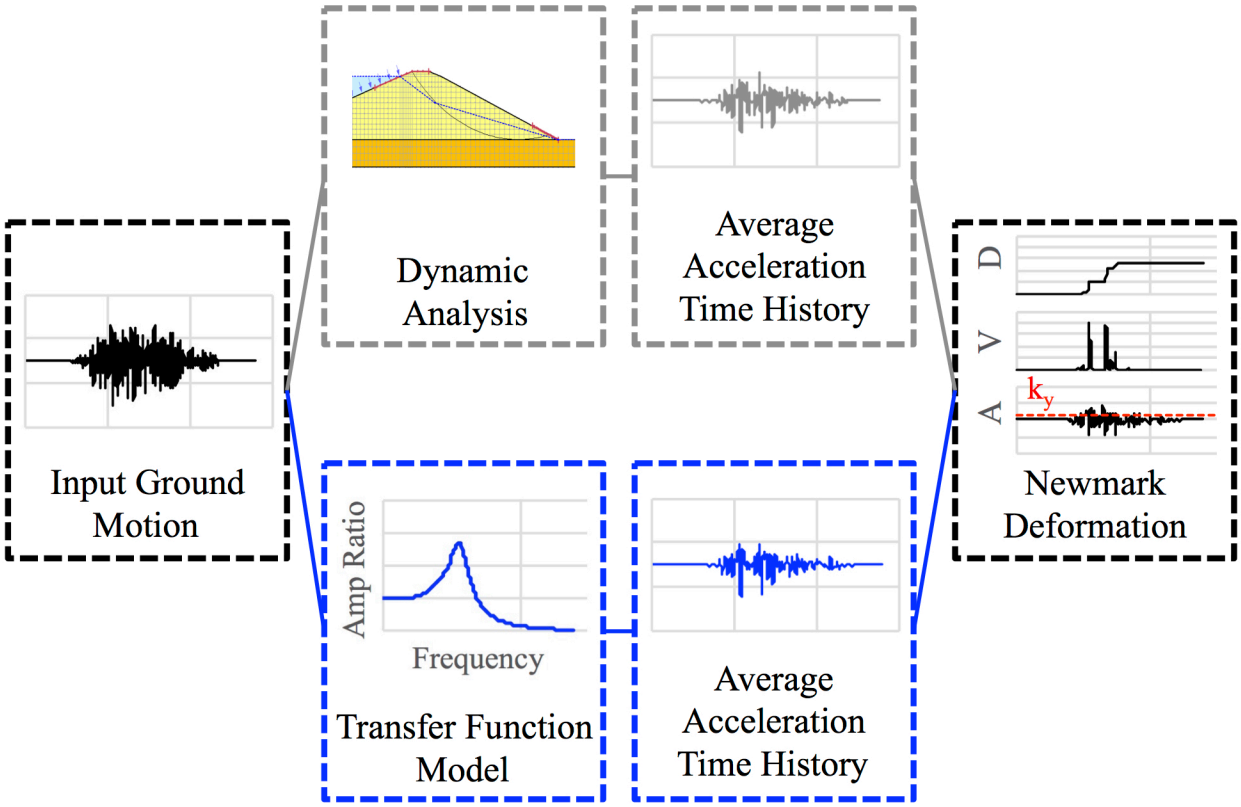

Figure 4.1 **Transfer-function model concept.**

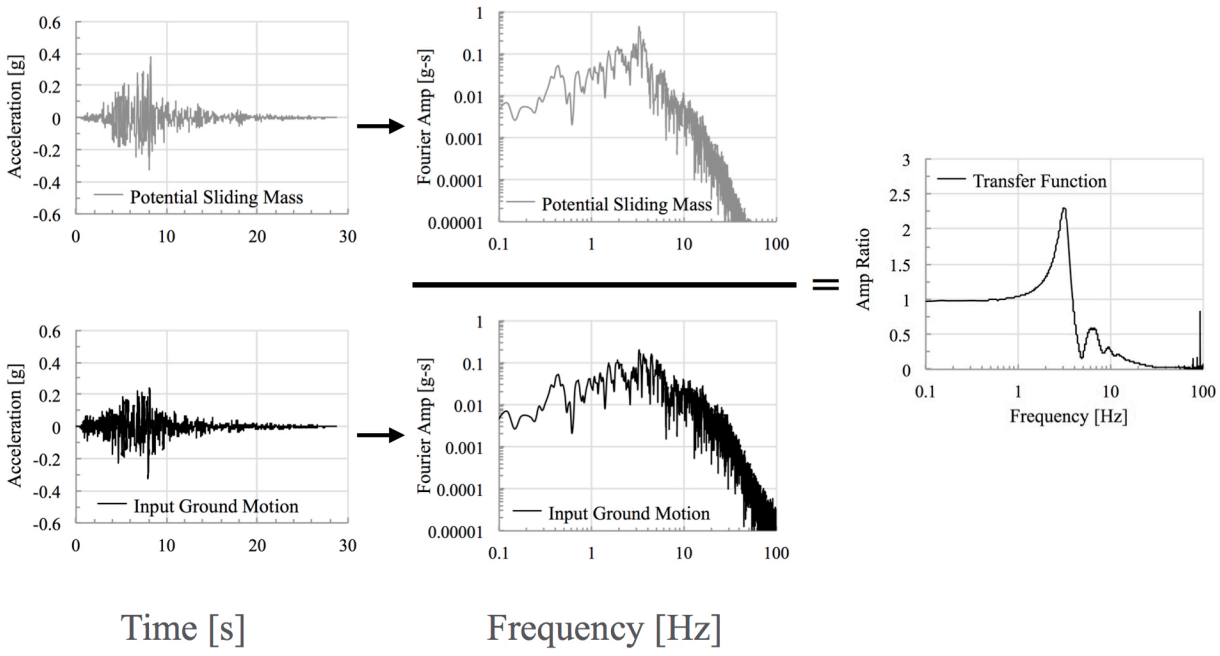

Figure 4.2 Definition of specific transfer-function utilized in this study.

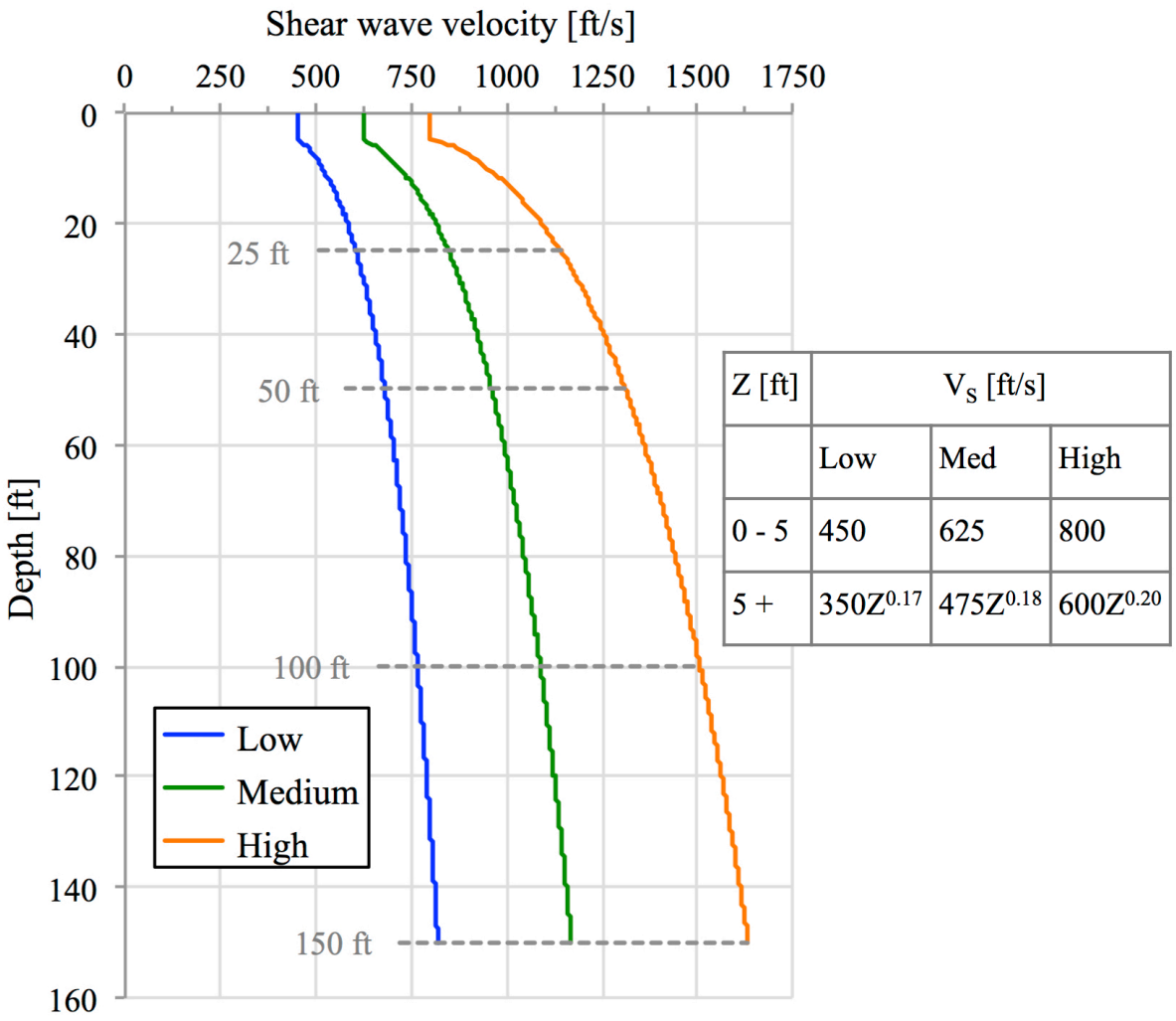

Z [ft]	V_S [ft/s]		
	Low	Med	High
0 - 5	450	625	800
5 +	$350Z^{0.17}$	$475Z^{0.18}$	$600Z^{0.20}$

Figure 4.3 **Shear-wave velocity profiles of representative dams.**

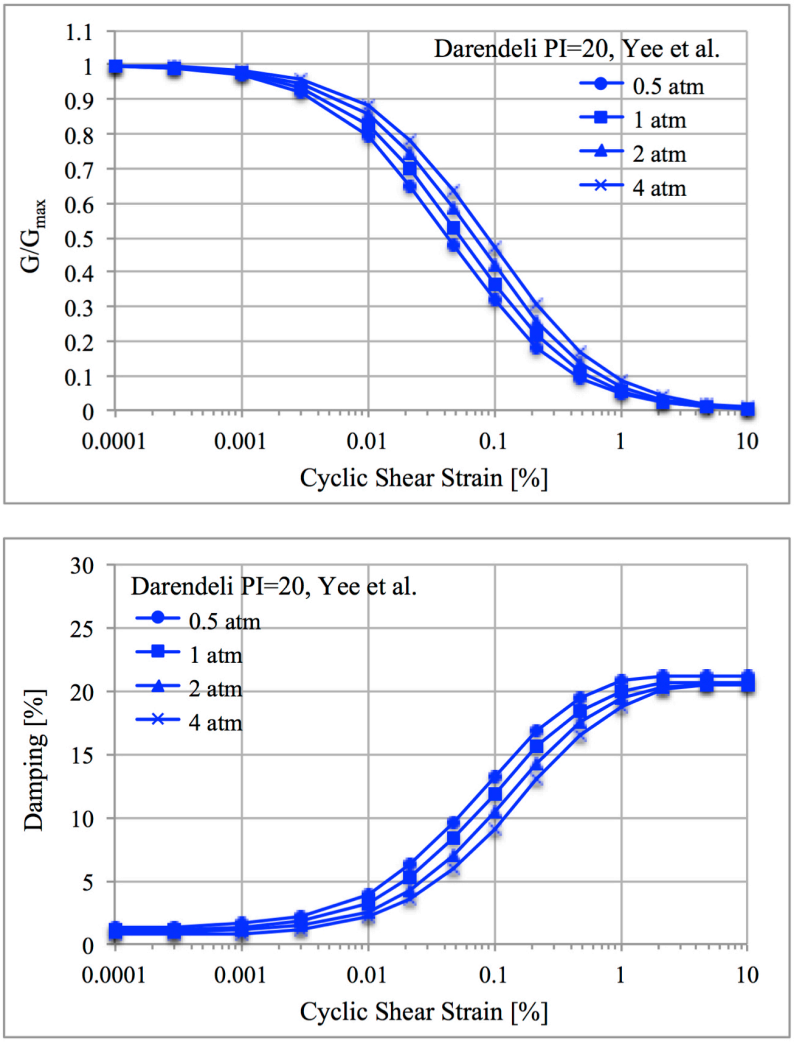

Figure 4.4 **Shear-modulus reduction and material damping curves applied to the representative dams in the dynamic analyses.**

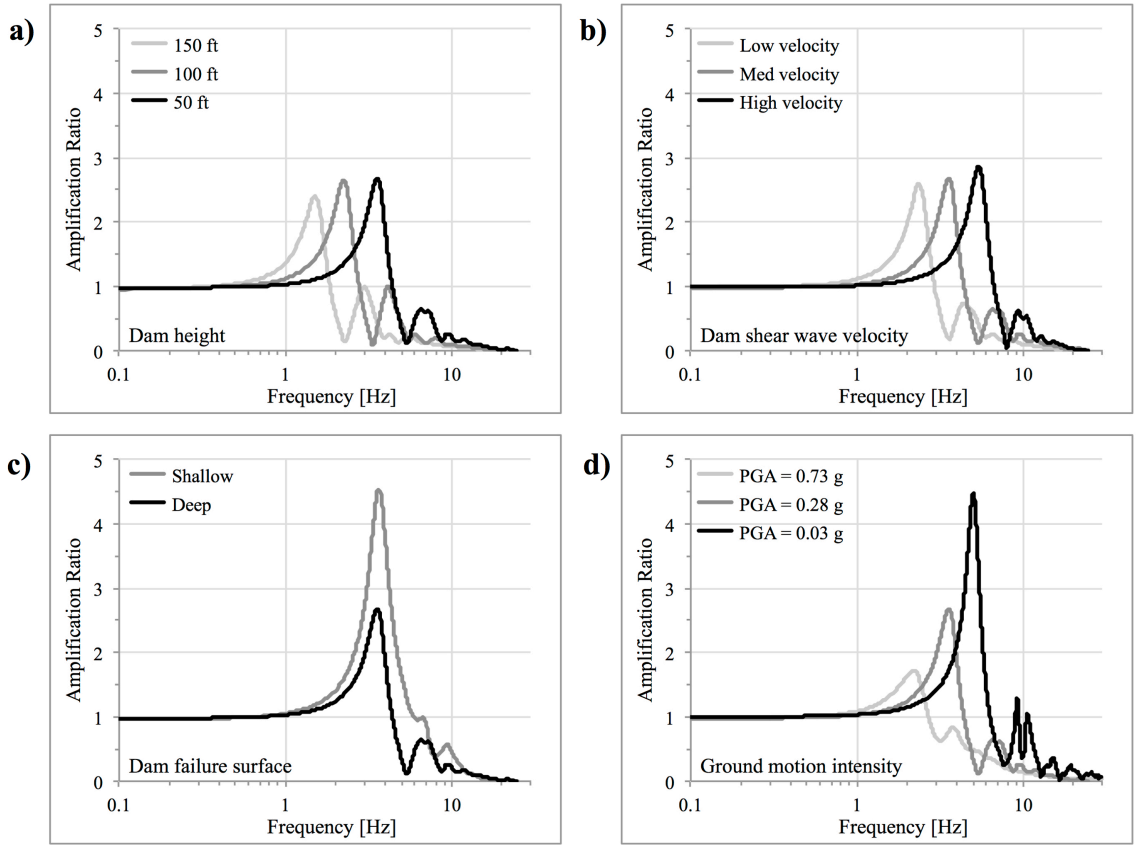

Figure 4.5 **Transfer functions from dynamic analyses demonstrating the change in transfer-function shape with a) dam height, b) dam shear-wave velocity, c) dam failure surface, and d) ground-motion intensity.**

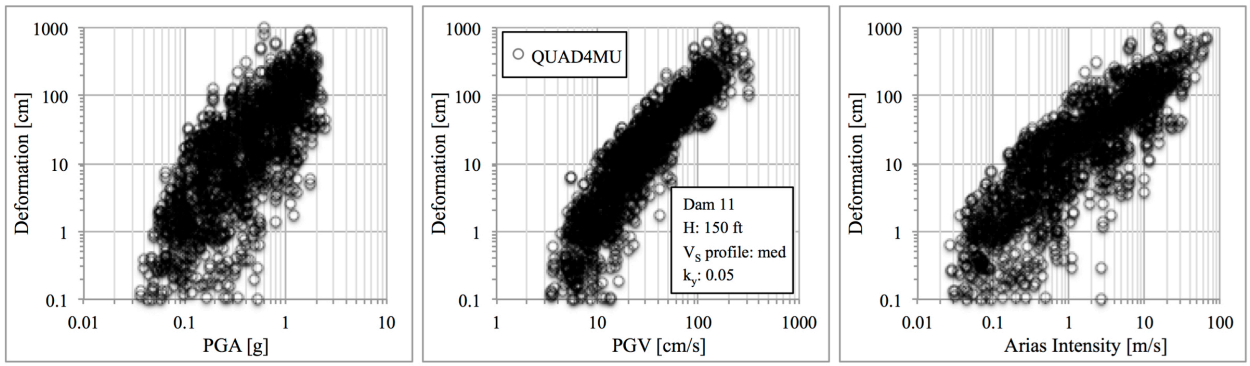

Figure 4.6 **Shear-induced Newmark deformations calculated from QUAD4MU dynamic analyses plotted against various intensity measures of the input ground motion.**

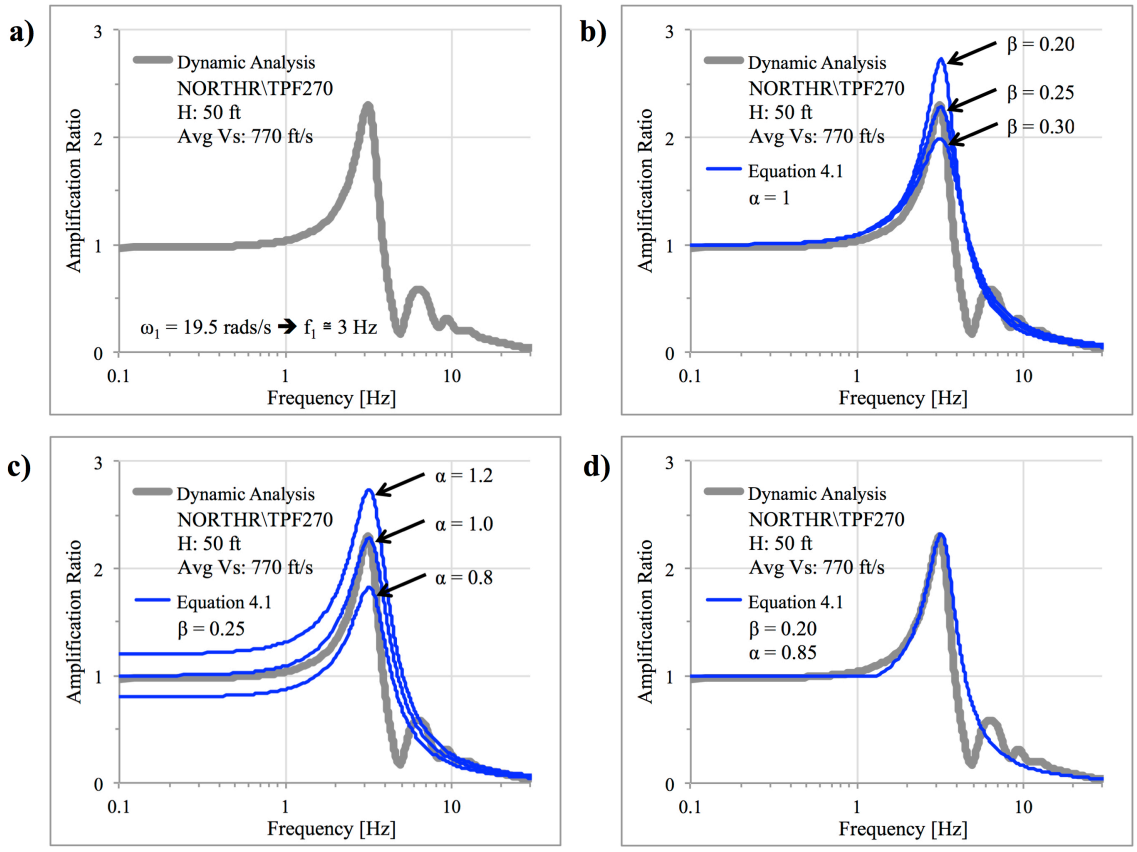

Figure 4.7 **Illustrative example of the matching scheme used to match a simplified transfer function to the transfer function of each dynamic analysis.**

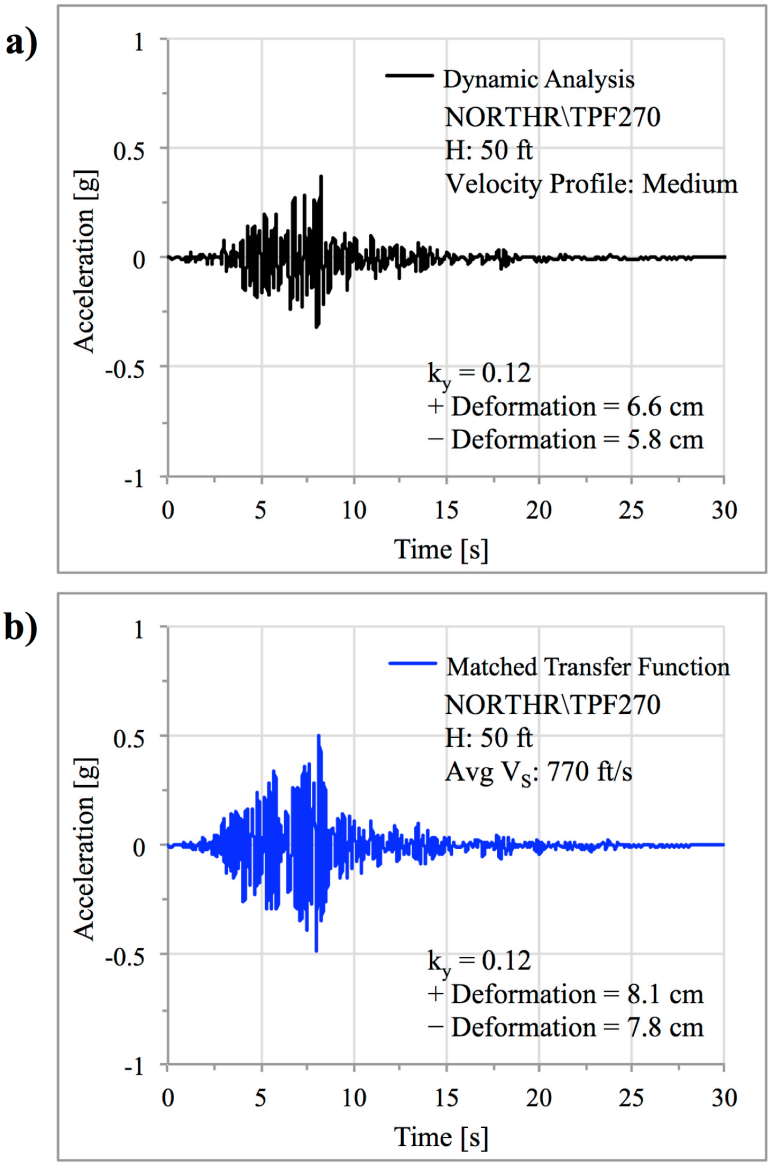

Figure 4.8 **Average acceleration time histories of a potential sliding mass from a) QUAD4MU dynamic analysis and b) matched transfer function used in the illustrative example and applied to the same input ground motion.**

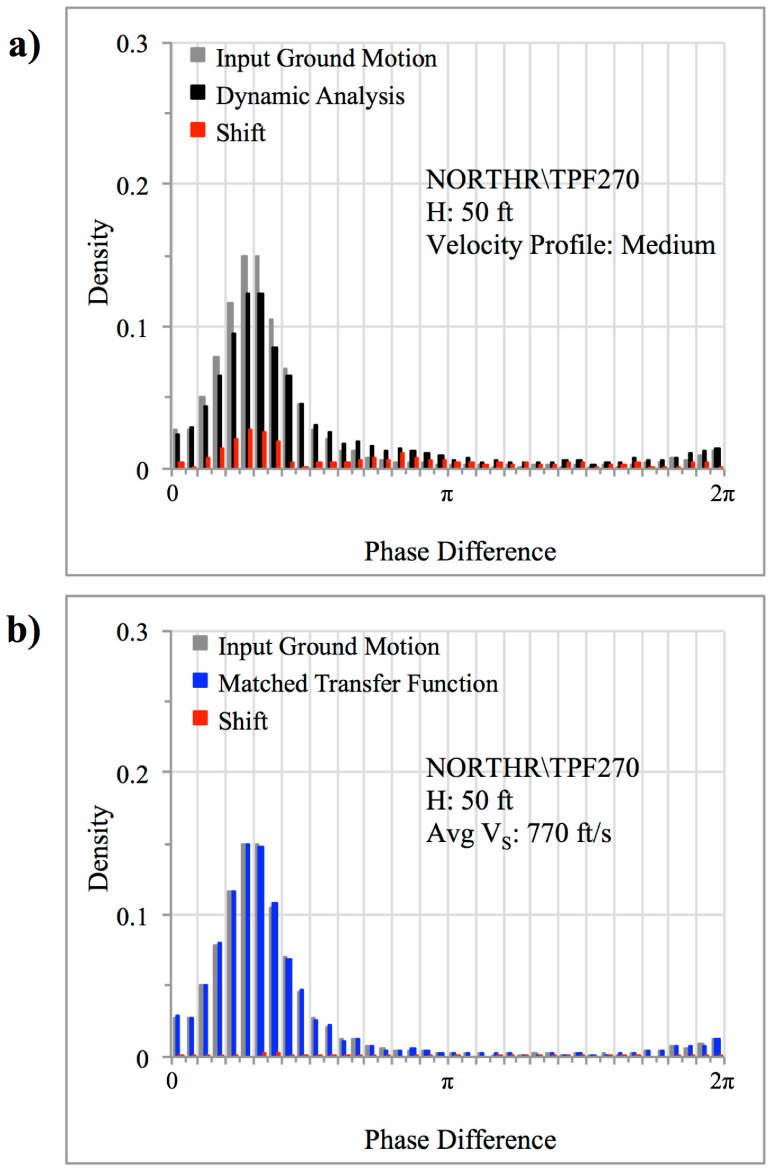

Figure 4.9 **Phase difference distributions from a) QUAD4MU dynamic analysis and b) matched transfer function used in the illustrative example and applied to the same input ground motion.**

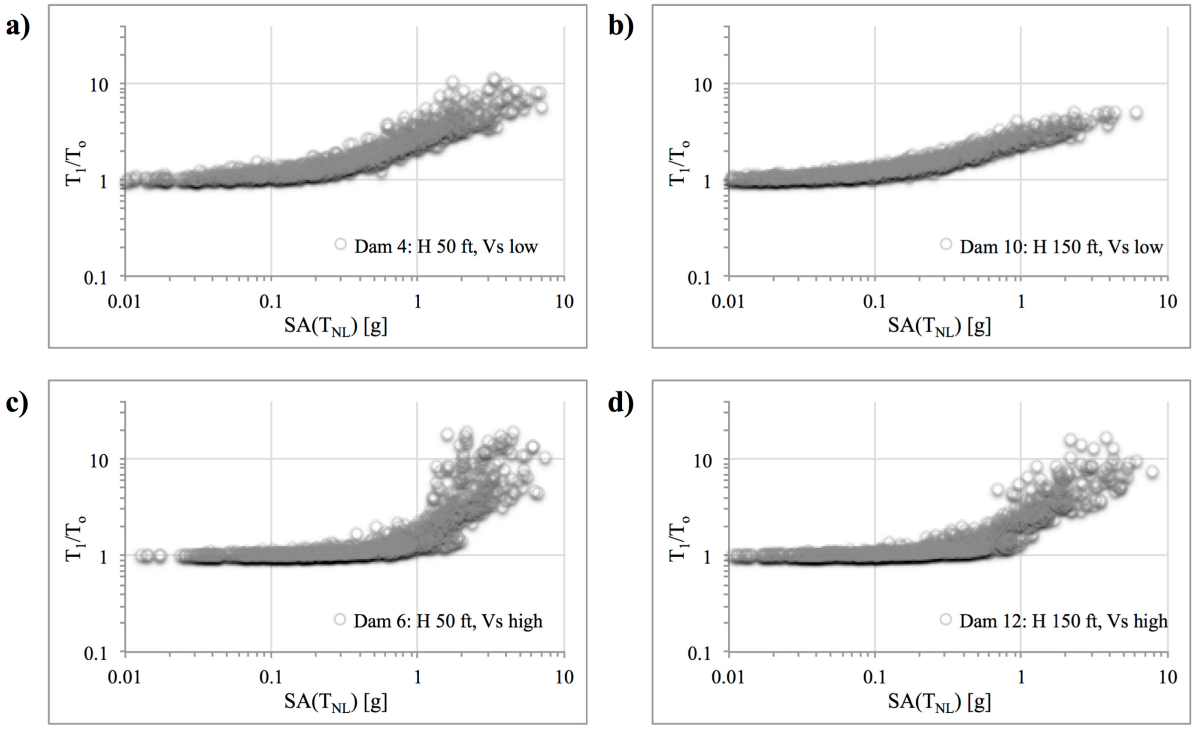

Figure 4.10 **Trends in dam period shift: T_1/T_o from transfer functions matched to dynamic analyses for representative dams with different heights and shear-wave velocity profiles.**

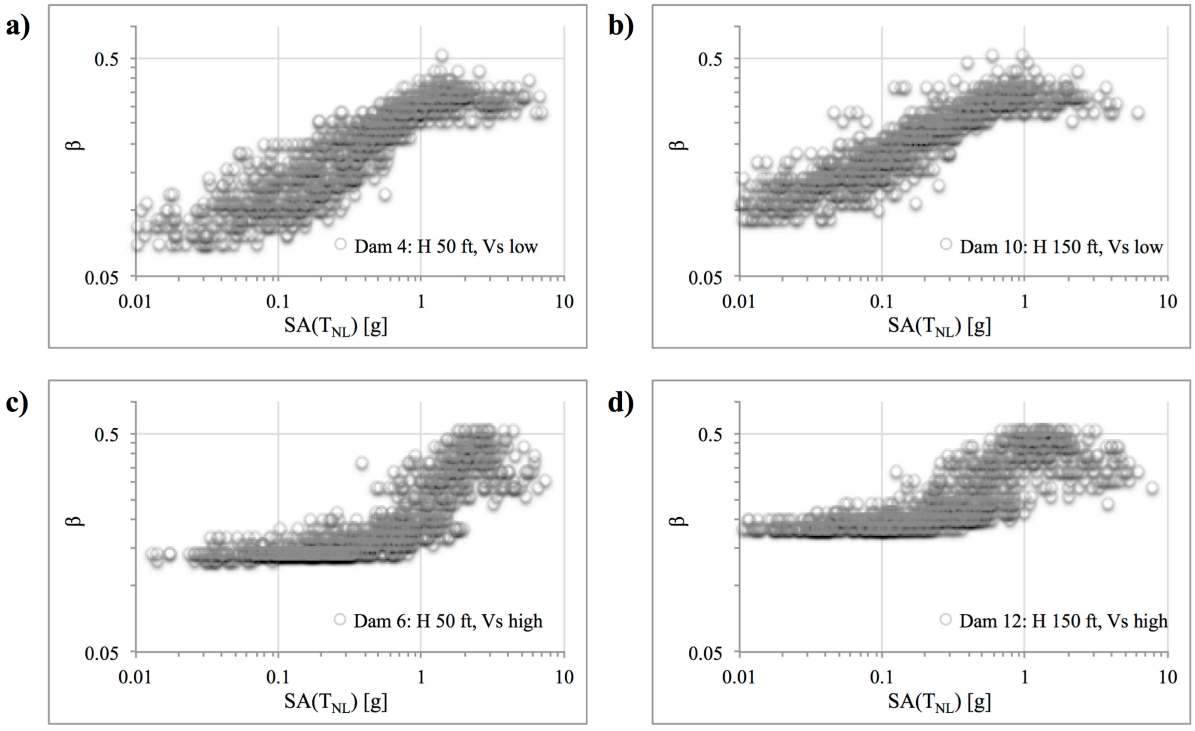

Figure 4.11 **Trends in matched damping: *β* from transfer functions matched to dynamic analyses for representative dams with different heights and shear-wave velocity profiles.**

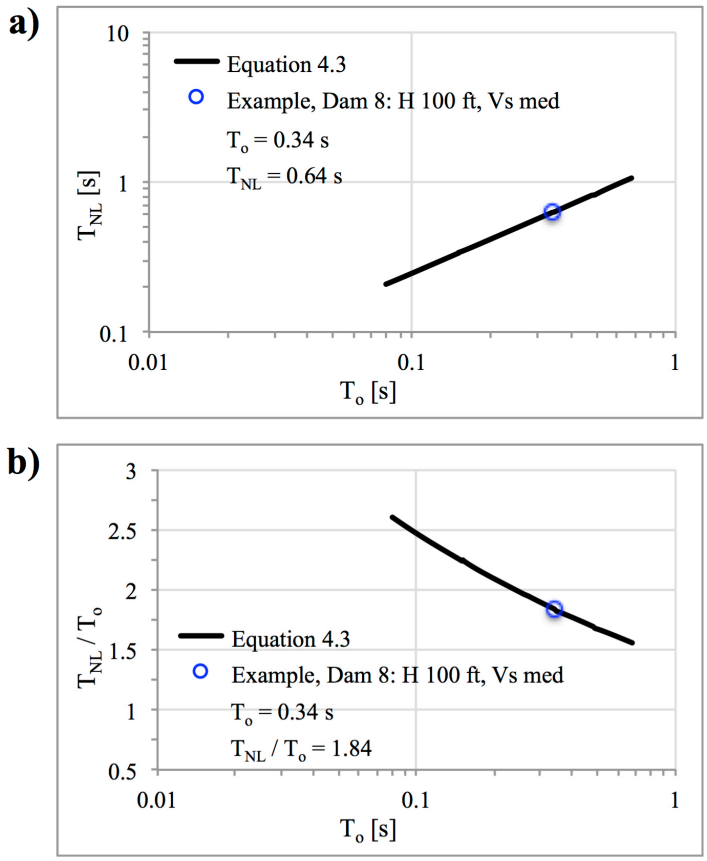

Figure 4.12 **Trends in T_{NL}, the single period that when used to compute a spectral acceleration, best explains the nonlinear behavior of the dam. T_{NL} is calculated from Equation 4.3 for the range of T_o of the representative dams.**

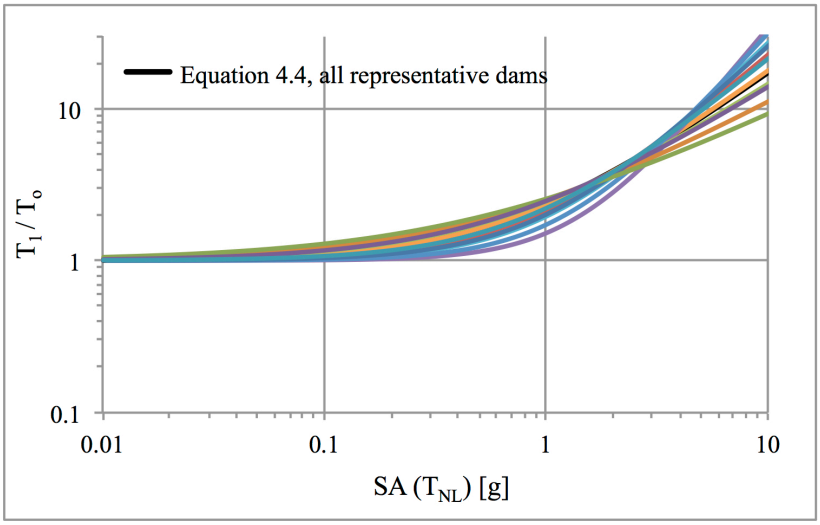

Figure 4.13 **Trends in T_1/T_o, the shift in the dam period. T_1/T_o is calculated from Equation 4.4 for all representative dams.**

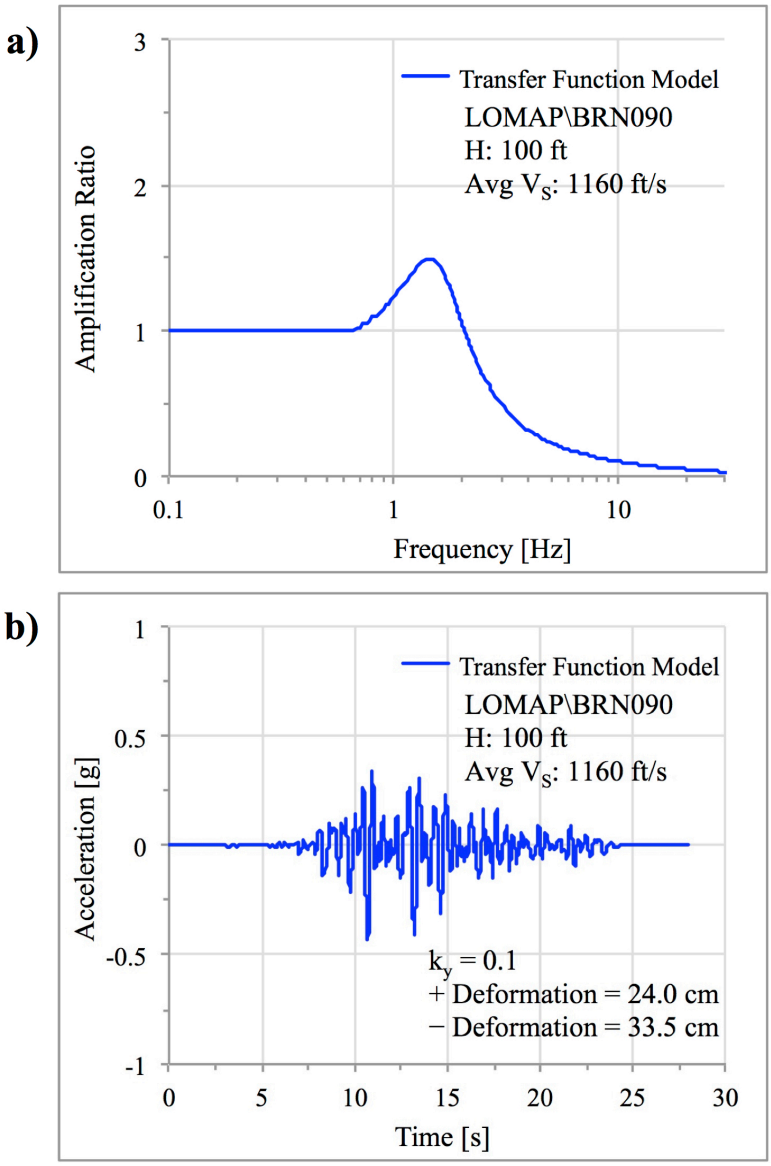

Figure 4.14 **Estimated transfer function and time history of average acceleration for a potential sliding mass from example calculation.**

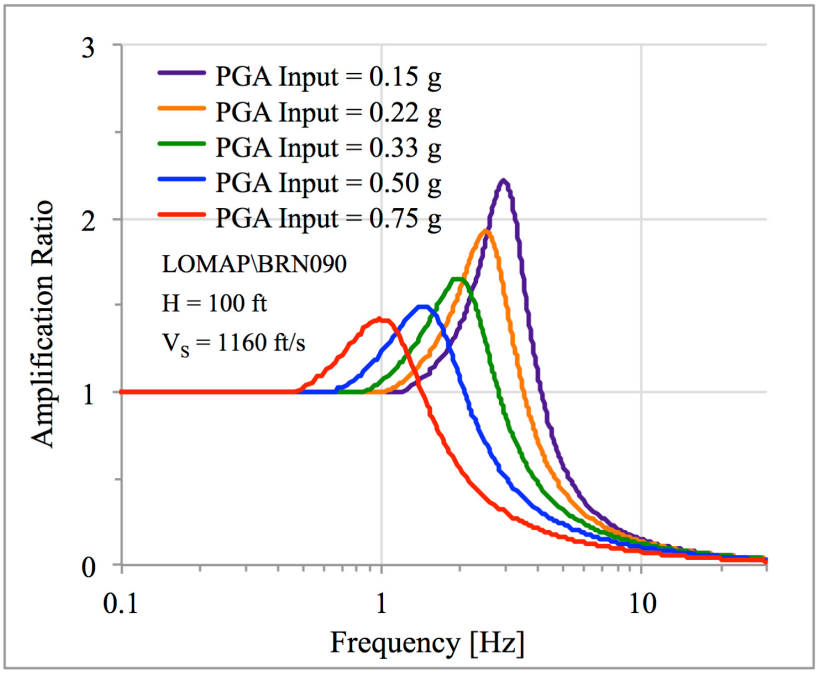

Figure 4.15 **Changes in modeled transfer function with increasing ground-motion intensity include a shift in the natural period of the system and an increase in damping.**

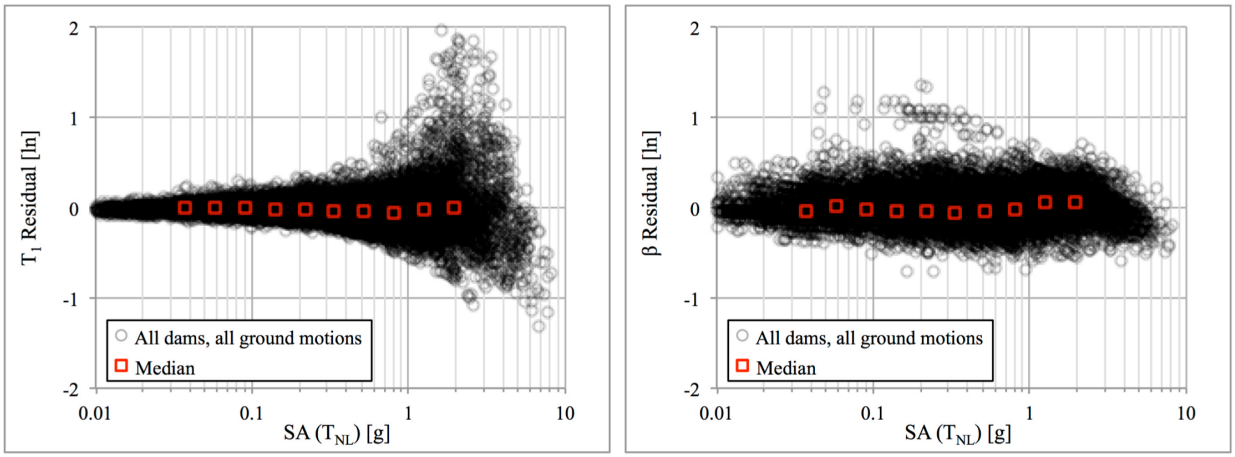

Figure 4.16 **Residuals and median of residuals for transfer-function model parameters T_1 and β showing that the transfer-function model is overall unbiased. A residual is calculated as the parameter matched to the QUAD4MU transfer function – parameter predicted from the transfer-function model.**

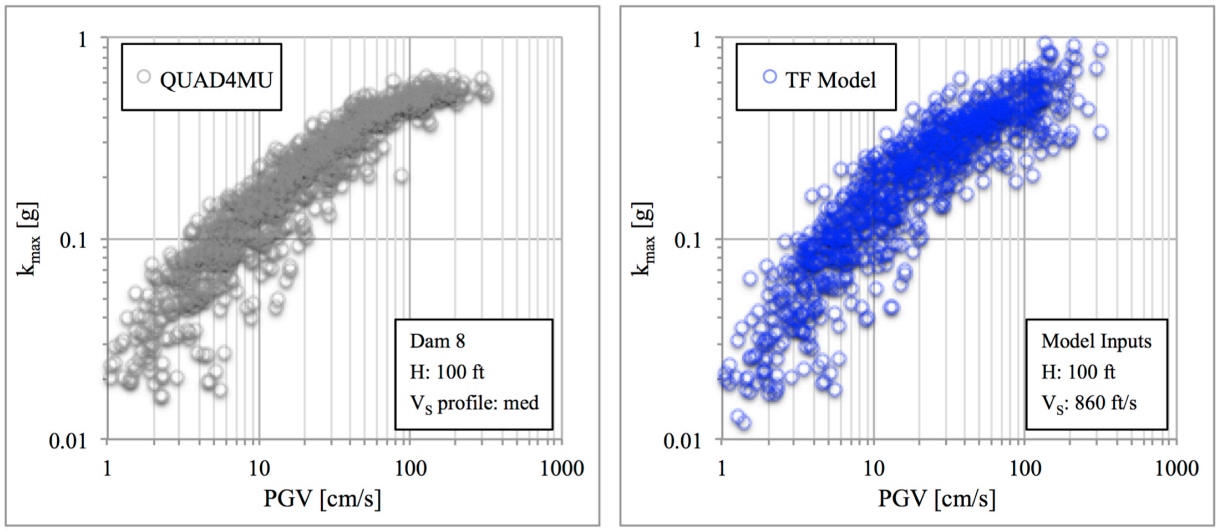

Figure 4.17 **Comparison of k_{max} values calculated from time histories of average acceleration for a potential sliding mass for QUAD4MU dynamic analyses (left) and transfer-function model (right) for one representative dam.**

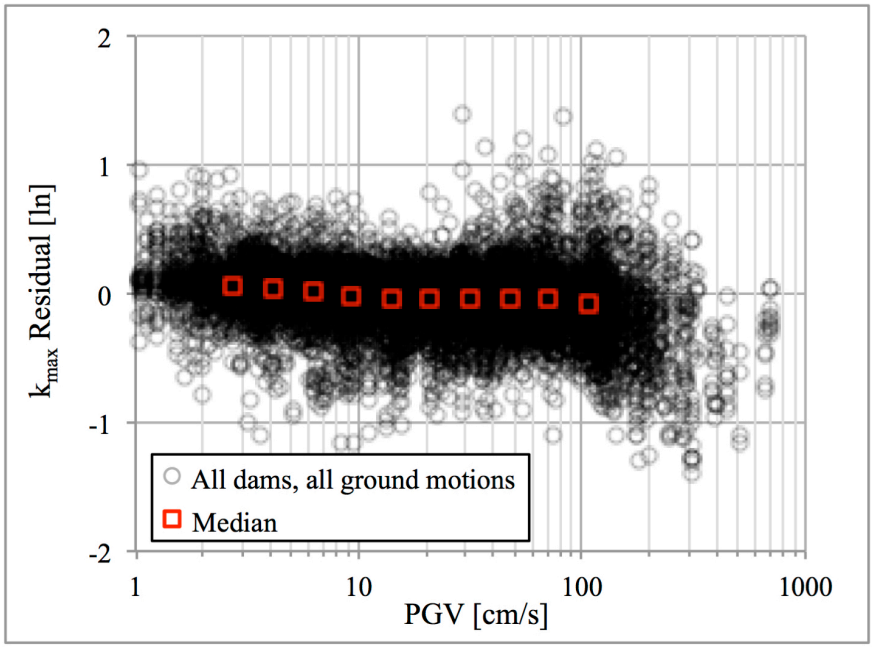

Figure 4.18 **K_{max} residuals and median of residuals showing that the transfer-function model is overall unbiased. A residual is calculated as k_{max} of QUAD4MU average acceleration time history – k_{max} of transfer-function model average acceleration time history.**

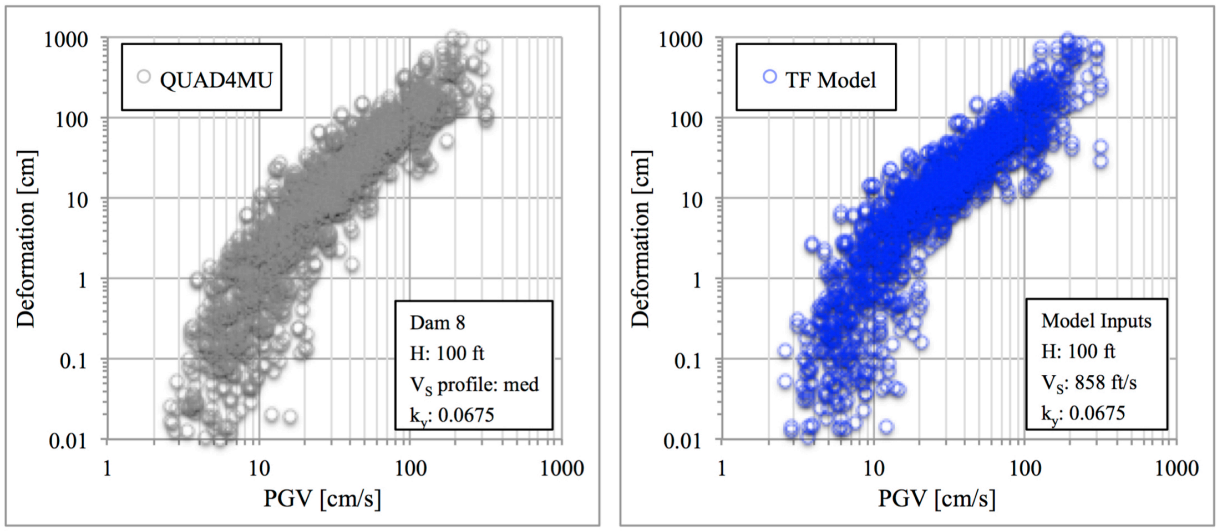

Figure 4.19 **Comparison of shear-induced deformations calculated from QUAD4MU dynamic analyses (left) and transfer-function model (right) for one dam.**

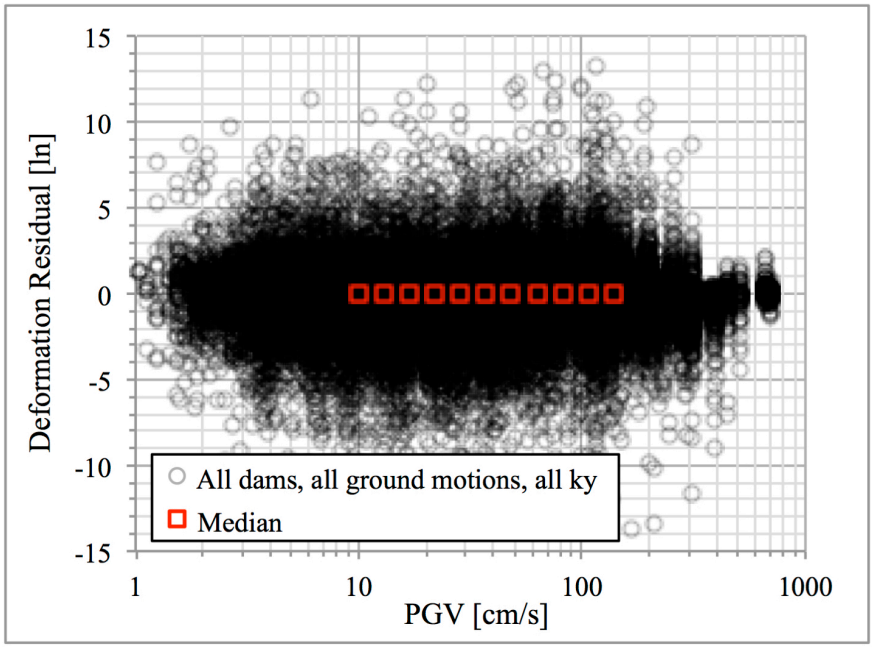

Figure 4.20 **Deformation residuals and median of residuals showing that the transfer-function model is overall unbiased. A residual is calculated as the QUAD4MU deformation – transfer-function model deformation.**

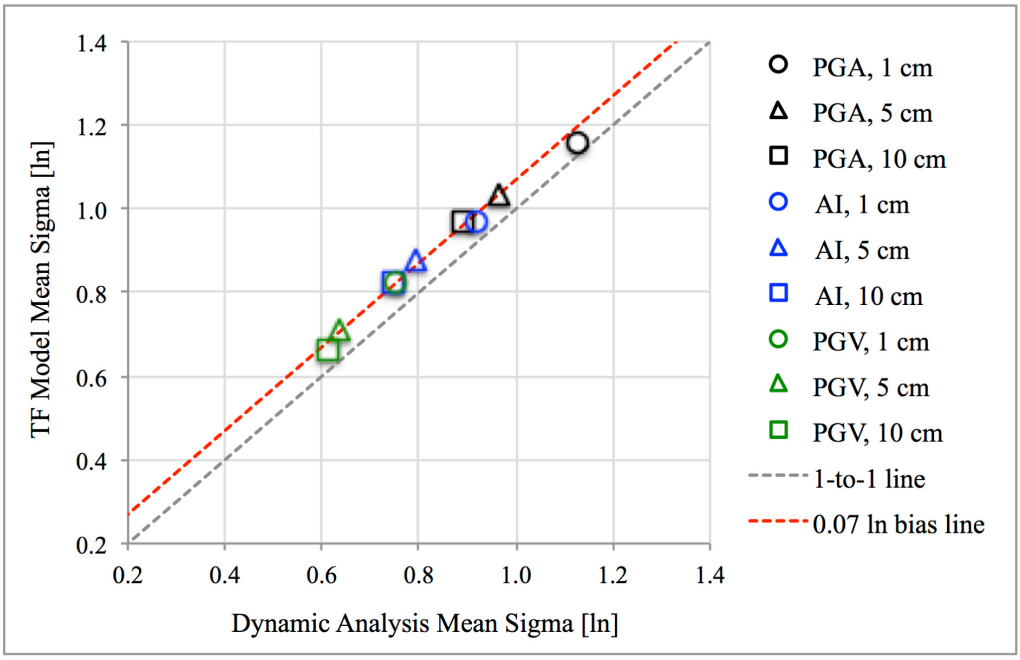

Figure 4.21 **Comparison of standard deviation (sigma) of deformations calculated from dynamic analyses versus transfer-function model showing that the sigma from the transfer-function model is biased slightly high.**

5 MODEL ADJUSTMENTS FOR NONLINEARITY

5.1 Introduction

The original transfer-function model presented in Chapter 4 utilizes the Darendeli (2001) PI=20 shear-modulus reduction and material damping curves with the Yee et al. (2013) adjustment for high strains. The choice of Darendeli curves and use of the Yee et al. (2013) procedure with relatively low shear strengths results in significant softening of the dam materials, leading to a substantial period shift. A series of dynamic analyses were performed with alternative nonlinear curves that model a more moderate strength reduction to understand the sensitivity of the transfer-function model to the choice of nonlinear curves. Because the functional form of the transfer-function model has a physical basis beyond best-fit trends to the selected data, the model can be altered with relatively simple modifications, and adjustments are recommended for different nonlinear curves.

5.2 Alternative Nonlinear Curves

Two alternative nonlinear models were chosen for the sensitivity analysis. The selected shear-modulus reduction and material damping curves are Vucetic and Dobry (1991) PI=30 and Darendeli (2001) PI=50 with the Yee et al. (2013) adjustment for high strains. The Vucetic and Dobry curves were not adjusted at high strains. The two alternative nonlinear curves are plotted in Figure 5.1 along with the nonlinear curves used in the original transfer-function model. Note that the Darendeli curves are confining pressure dependent, while the Vucetic and Dobry curves are not. When assigning nonlinear curves to the finite-element mesh, the Darendeli curves are applied in zones based on confining pressure. For the Vucetic and Dobry curves, the same curve is applied throughout the dam. Another observation from the comparison is that application of the Yee et al. (2013) procedure causes the Darendeli PI=20 and PI=50 G/G_{max} curves to converge at moderate to high levels of shear strains. The two sets of Darendeli G/G_{max} curves are effectively the same at strains beyond about 0.5%. The Vucetic and Dobry G/G_{max} curve is significantly higher at strains beyond about 0.1%.

Both of the alternative nonlinear curves display less nonlinearity than the Darendeli PI=20 curves used in the original transfer-function model. The Darendeli PI=20 curves are highly nonlinear, while the Darendeli PI=50 curves are less nonlinear, and the Vucetic and Dobry PI=30 curves are even more nonlinear. The Vucetic and Dobry curves were chosen, in part, for historical purposes. The Vucetic and Dobry PI=30 relationships have been used to analyze many dams over the years (e.g., East Bay Municipal Utility District, 2008; TERRA /

GeoPentech, 2012; Hadidi et al., 2014) and were also used to generate the dataset for the Bray and Travasarou (2007) simplified procedure.

5.3 Dynamic Analyses and Transfer-Function Parameters

The alternative nonlinear models were applied to the representative dam with a height of 100 *ft* and the medium shear-wave velocity profile (representative dam number 8). Dynamic analyses were performed using QUAD4MU with all 950 input ground motions. For every dynamic analysis, a simplified transfer function was fit to the dynamic-analysis transfer function, resulting in a dataset of simplified transfer functions that can be described by their normalized first-mode period, T_1/T_o, and damping, β. Figure 5.2 plots these parameters as a function of ground-motion intensity for the dynamic analyses.

When the nonlinear curves are changed from Darendeli PI=20 to Darendeli PI=50, there is little difference in the nonlinear behavior of the dam, characterized by a shift in period and increase in damping. In contrast, there are significant differences between the Darendeli results and the Vucetic and Dobry PI=30 results. When the nonlinear curves are changed to Vucetic and Dobry PI=30, the shift in period is reduced, consistent with less nonlinearity. The increase in damping is similarly reduced when the Vucetic and Dobry PI=30 curves are applied, and the damping results don't follow the same "s"-shaped curve. Instead, the damping results from the dynamic analyses run with Vucetic and Dobry show a constant, gradual increase, comparable to the trend in material damping shown in Figure 5.1.

A nonlinear regression was performed on the matched T_1/T_o data in Figure 5.2 using the same functional form as the original model:

$$T_1/T_o = 1 + exp^{c_1(c_2+\ln(SA(T_{NL})))} \tag{5.1}$$

where $SA(T_{NL})$ is the 5% damped pseudo-spectral acceleration of the input ground motion at the nonlinear period of the dam in *g*. Similarly, a regression was performed on the matched β data in Figure 5.2 using the functional form:

$$\ln(\beta) = b_1 + \frac{b_2}{(1+exp^{b_3+b_4\ln(SA(T_{NL}))})} \tag{5.2}$$

In the above equations, T_{NL} is the single period that when used to compute a spectral acceleration, best explains the nonlinear behavior of the dam. T_{NL} is different for each dam, and is calculated as:

$$\ln(T_{NL}) = a_1 \ln(T_o) + a_2 \tag{5.3}$$

where T_o is the small-strain fundamental period of the dam in seconds. The resulting T_1/T_o and β curves are compared in Figure 5.3. The comparison shows that the Darendeli PI=50 curves result in virtually no change from the original model, while the Vucetic and Dobry PI=30 curves deviate from the original model significantly.

5.4 Dynamic Analyses Deformations

Newmark deformations were calculated from the QUAD4MU average acceleration time histories for a suite of yield coefficients. When the shear-induced deformations calculated from the Darendeli PI=50 curves are compared to the original dynamic analyses, there is not a significant difference in the deformations; however, when the dam materials are modeled with the Vucetic and Dobry PI=30 curves, the deformations are about two times larger than the deformations from the original dynamic analyses using the Darendeli PI=20 curves.

The Vucetic and Dobry PI=30 curves, which exhibit less nonlinearity, lead to larger deformations because the dam period shift is reduced, which causes the periods with the most amplification to line up with the periods of the ground motion that have the highest amplitudes. To illustrate this point, the mean period (T_m) of every input ground motion is plotted along with the first-mode period of the dam (T_1) in Figure 5.4. On average, the natural period of the dam is closer to the mean period of the ground motion for the dynamic analyses that use the Vucetic and Dobry PI=30 nonlinear curves, and farther for the Darendeli PI=20 analyses. This is especially true for the highest ground motions, where the Darendeli PI=20 analyses push the first-mode period of the dam to periods significantly longer than the mean period of the input motion. In these cases, the Darendeli PI=20 dynamic analyses amplify periods of the input motion that have relatively low amplitudes, leading to lower deformations. Note that the effect of the dam period shift on the calculated deformations is different for every ground motion and every dam. The trends discussed here are based on the 950 NGA-West2 input motions and the response of representative dam number 8.

In addition to the reduced dam period shift, the Vucetic and Dobry PI=30 curves result in reduced damping. The reduced damping also contributes to the larger estimated deformations because the amplification ratios from the dynamic analyses are higher.

5.5 Recommended Adjustments to Transfer-Function Model

In terms of modifying the transfer-function model for different nonlinear curves, the goal is to make a simple adjustment that accounts for the changes in the transfer-function shape caused by the changes in dynamic material properties. When applied to the same input ground motions, the adjusted model should lead to estimated deformations that are comparable to the shear-induced deformations calculated from the dynamic-analysis results.

The T_1/T_o parameter is modified with the addition of a coefficient in front of the exponential term:

$$T_1/T_o = 1 + \underline{c_3} exp^{c_1(c_2 + \ln(SA(T_{NL})))} \tag{5.4}$$

When c_3 is less than 1 it works as a "reduction factor" and reduces the shift in the first-mode period of the dam, effectively reducing the nonlinear behavior. Adjustment of T_1/T_o for Vucetic and Dobry PI=30 was carried out by fixing c_1 and c_2 equal to their predicted values for the original transfer-function model, and performing a regression to determine c_3. A c_3 value of 0.32 provides the best fit to the dataset generated from the Vucetic and Dobry dynamic analyses. The T_1/T_o model adjusted for the Vucetic and Dobry PI=30 nonlinear curve is shown in Figure 5.5a, along with the T_1/T_o curve from Figure 5.2, and the T_1/T_o dataset from the dynamic

analyses. The close agreement of the model curves in Figure 5.5a means that nothing meaningful was lost by adjusting the original model with c_3 rather than repeating the model building process and regressing on c_1 and c_2.

Adjustment of the damping parameter, β, is more complicated because of the functional form of Eq. 5.2 and the correlation between coefficients $b_1 - b_4$. Additionally, the Vucetic and Dobry PI=30 material damping curve used in the dynamic analyses does not have the same shape as the Darendeli curves used in the original model so adjustment is more than just a simple reduction or shift. The β parameter is modified with the addition of two coefficients that adjust the b_3 and b_4 coefficients:

$$\ln(\beta) = b_1 + \frac{b_2}{(1+exp^{(b_3+\underline{b_5})+(b_4+\underline{b_6})\ln\left(SA(T_{NL})\right)})} \tag{5.5}$$

Although a different functional form is probably better suited to fit the Vucetic and Dobry PI=30 matched damping dataset in Figure 5.2, there are advantages to keeping the "s-shaped" functional form of the original β model. One of the reasons the "s-shaped" curve is favored is because it saturates at high shear strains, rather than continuing to increase damping in an unbounded manner. Additionally, keeping the "s-shaped" curve and modifying the b_3 and b_4 coefficients changes the onset of nonlinearity and the slope of the nonlinear region, while keeping the horizontal asymptotes the same, which is consistent with the change in the dataset observed in Figure 5.2 and ensures that the adjusted model will extrapolate in a reasonable manner when applied to other dams.

Adjustment of β for Vucetic and Dobry PI=30 was carried out by fixing $b_1 - b_4$ equal to their predicted values for the original transfer-function model and performing a regression to determine b_5 and b_6. A b_5 value of -2.0 and b_6 value of -1.0 provides the best fit to the dataset generated from the Vucetic and Dobry dynamic analyses. The β model adjusted for the Vucetic and Dobry PI=30 nonlinear curve is shown in Figure 5.5b, along with the β curve from Figure 5.2, and the β dataset from the dynamic analyses. Again, the close agreement of the model curves in Figure 5.5b means that nothing meaningful was lost by adjusting the original model with b_5 and b_6 rather than repeating the model building process and regressing on $b_1 - b_4$.

The recommended adjustments are based on the dynamic-analysis results of a single dam subjected to all 950 input ground motions. Although dynamic analyses were not carried out for the other representative dams with the alternative nonlinear curves, the adjustments were chosen with extrapolation to all representative dams in mind. The original model serves as a backbone for the change in dam response based on dam height and shear-wave velocity profile, and the adjusted model simply modifies the dam period shift and damping for an alternative nonlinear relationship. The application of the adjustments to the other representative dams should be verified with dynamic analyses in the future.

Given the minimal differences between the matched transfer-function parameters from the original model and the Darendeli PI=50 results, no adjustment is recommended for the Darendeli PI=50 nonlinear curves. The similarity in the results for the Darendeli PI=20 and PI=50 curves is largely due to the application of the Yee et al. (2013) procedure, which results in identical curves at moderate to high shear strains.

5.6 Estimated Deformations and Residuals

The adjustments to the model are based on the transfer functions extracted from the QUAD4MU dynamic analyses run with the Vucetic and Dobry PI=30 nonlinear curves. The adjusted model transfer functions are, therefore, consistent with the dynamic analyses, but it is also necessary to check that the adjusted model provides shear-induced deformations that are similar to the dynamic analyses deformations. The adjusted model was applied to the 950 input ground motions and deformations are calculated for a suite of yield coefficients. Shear-induced deformations were calculated from the QUAD4MU results with the same input ground motions and yield coefficients, and a residual was calculated for every ground motion and yield coefficient combination. The residuals are defined as the observed minus the predicted values where the observed are the QUAD4MU deformations and the predicted are the transfer-function deformations. The median residuals at various ground-motion intensities are displayed in Figure 5.6.

The residuals from the original model for all dams, and the original model for representative dam number 8 only are included for reference. The original model is unbiased when the shear-induced deformations and associated residuals for all dynamic analyses and all yield coefficients are considered. When only dam 8 is considered, the original model shows a small positive bias (over prediction) at smaller PGV values, and the adjusted model for dam 8 shows a similar bias. The bias is not significant and overall, the adjusted model produces deformations that are consistent with the deformations calculated from the QUAD4MU analyses.

The model is not intended for single deterministic analyses and should be applied to a large number of ground motions that appropriately characterize the seismic hazard of the site. For this reason, it is important that the adjusted model provides a distribution of deformations that are similar to the dynamic-analysis deformations when a sufficient number of input ground motions are utilized. Figure 5.7 presents an example of the deformations from the QUAD4MU analyses run with the Vucetic and Dobry PI=30 nonlinear curves alongside the estimated deformations from the adjusted transfer-function model. The results are shown for a single yield coefficient (i.e., for a single dam), which is how the model will be applied. The shear-induced deformations are plotted against the PGV of the ground motion, but other intensity measures can be used on the x-axis. The adjusted transfer-function model produces deformations with a distribution that is consistent with the QUAD4MU dynamic analyses across a wide range of intensity levels. The standard deviation from the transfer-function model is slightly higher than the standard deviation from the QUAD4MU results. This increase is the penalty of using a simplified model. For the example shown in Figure 5.7, the standard deviation for the QUAD4MU results is 0.60 (natural log) and the standard deviation for the transfer-function model results is 0.62. These standard deviations were calculated for deformations greater than 5 *cm*.

5.7 Estimated Transfer Functions

An example deterministic calculation is utilized to observe the change in the estimated transfer function when the model is adjusted for the Vucetic and Dobry PI=30 nonlinear curves. The example applies the model to a hypothetical dam with a height of 50 *ft* and an average shear-

wave velocity of 800 *ft/s*. The input ground motion is a record from the Loma Prieta earthquake with a recorded PGA of 0.28 *g*, which is then scaled up with scale factors of 2 and 4. The transfer-function model is applied to each ground motion and the estimated transfer functions from the original Darendeli model and the model adjusted for the Vucetic and Dobry curves are plotted in Figure 5.8.

For both models, the center of the transfer function moves to lower frequencies and the peak amplification ratio is reduced as the ground-motion intensity increases. The change in the transfer-function shape with increasing ground-motion intensity reflects the nonlinear response of soils, characterized by a shift in the dam period and increased damping. The transfer functions from the model adjusted for the Vucetic and Dobry curves are not shifted as far away from the small-strain fundamental period of the dam (approximately 0.19 *s* or 5.3 *Hz*), and the shift from a scale factor of 1 to 4 is less compared to the Darendeli model. This is because the slope of the T_1/T_o relationship in the nonlinear region of the model adjusted for the Vucetic and Dobry curves is flatter than the Darendeli model. Less nonlinearity means less of a shift in dam period. The transfer functions from the model adjusted for the Vucetic and Dobry curves also have higher peak amplification ratios. Less nonlinearity means less of an increase in damping, leading to more peaked transfer functions.

5.8 Conclusions

Two sets of dynamic analyses were completed with alternative shear-modulus reduction and material damping curves to assess the sensitivity of the transfer-function model to the choice of nonlinear curves employed in the synthetic dataset. Adjustments are recommended to modify the transfer-function model for the nonlinear behavior of the Vucetic and Dobry (1991) PI=30 curves, which includes less elongation of the dam period and less damping (less nonlinearity). The adjustments are described by Equations 5.4 and 5.5 with coefficients listed in Table 5.1. No adjustment is recommended for the Darendeli (2001) PI=50 nonlinear curves with the Yee et al. (2013) procedure for high strains, as the results are nearly the same as the original model.

Table 5.1 Coefficients used in transfer-function model adjustments for nonlinearity (Equations 5.4 and 5.5).

Coefficient	Original Model Darendeli (2001) PI=20 with Yee et al. (2013)	Vucetic and Dobry (1991) PI=30
c_3	1	0.32
b_5	0	-2.0
b_6	0	-1.0

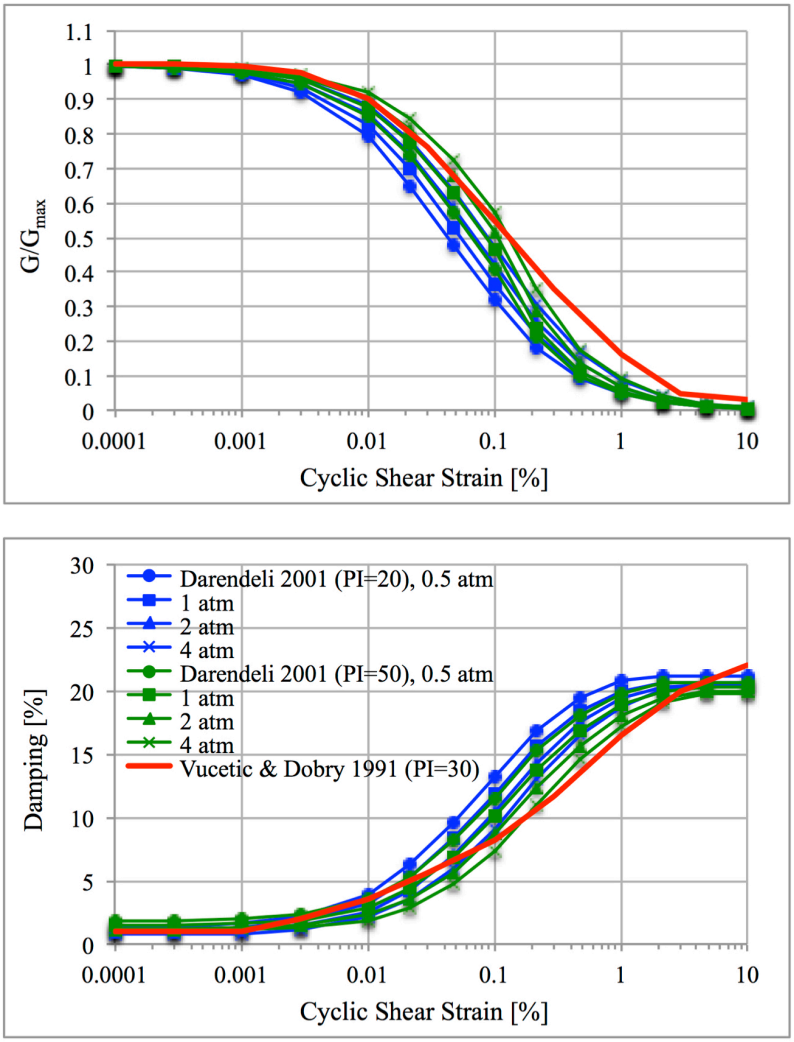

Figure 5.1 **Shear-modulus reduction and material damping curves used in the dynamic analyses to examine the sensitivity of the transfer-function model to alternative nonlinear models.**

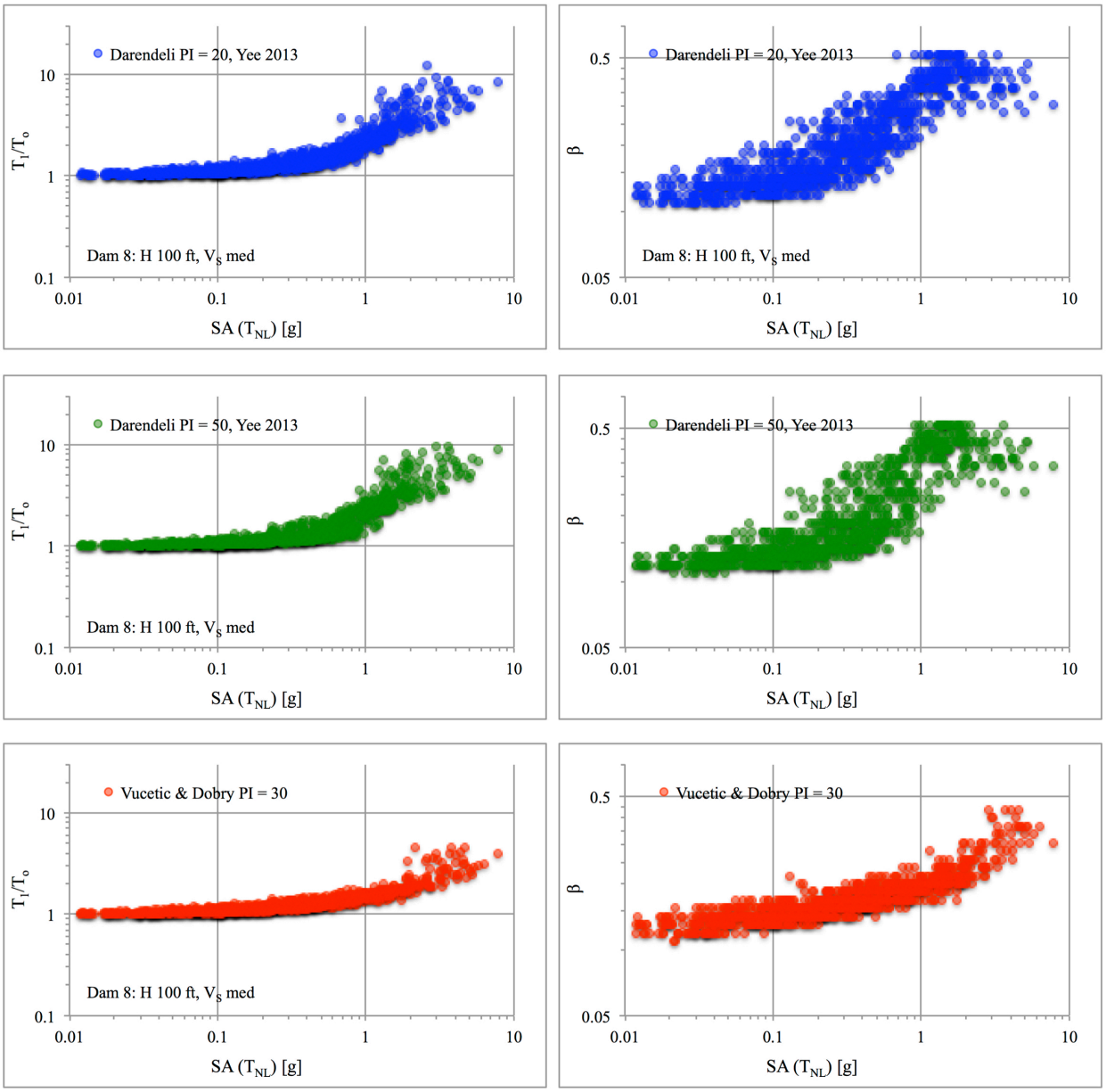

Figure 5.2 **Changes in matched transfer-function parameters T_1/T_o and β when dynamic analyses are run with different shear-modulus reduction and material damping curves.**

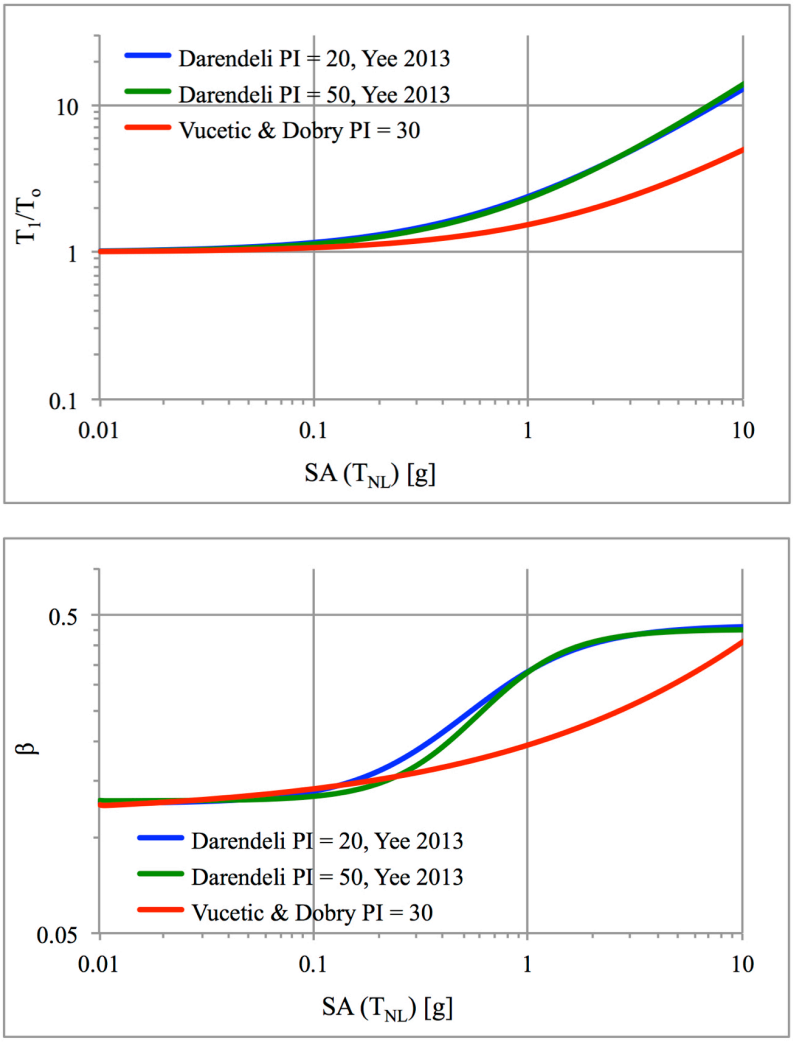

Figure 5.3 Comparison of curves fit through T_1/T_o and β data shown in Figure 5.2.

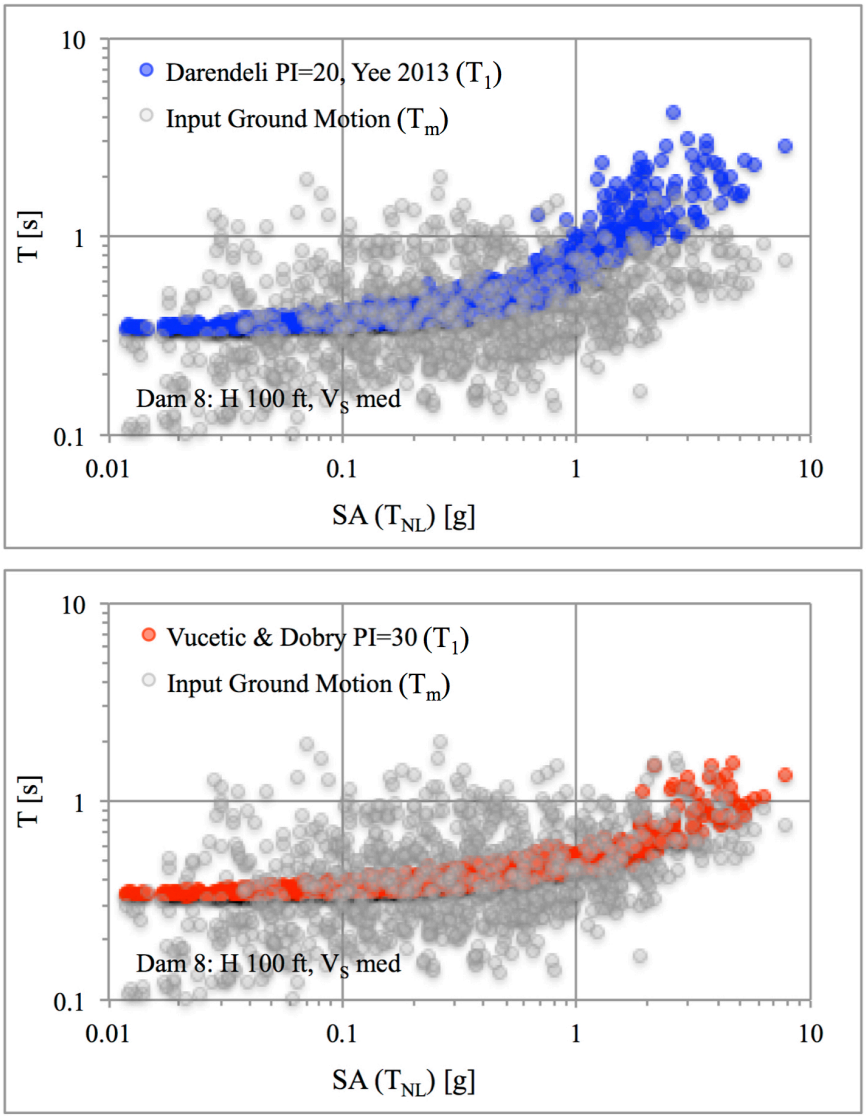

Figure 5.4 **Relation of matched transfer function parameter T_1 to mean period of the input ground motion, T_m, for QUAD4MU dynamic analyses with different nonlinear models.**

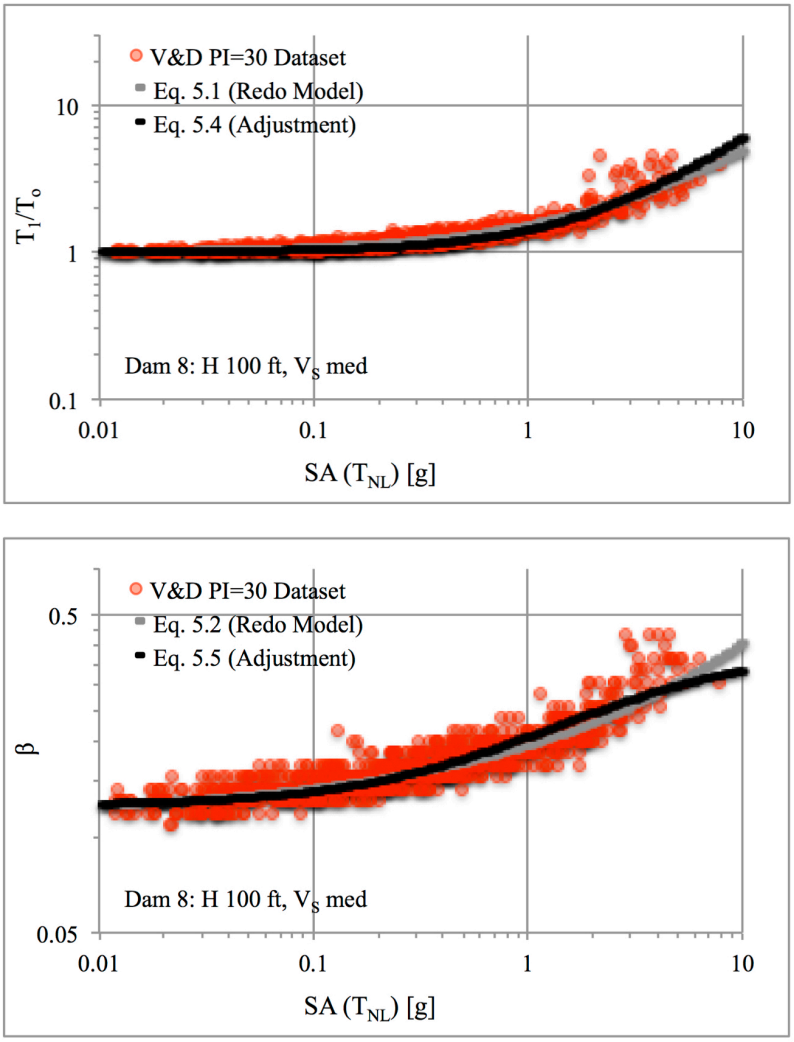

Figure 5.5 **Comparison of fitting Vucetic and Dobry (1991) PI=30 dataset with original transfer-function model equations (Equations 5.1 and 5.2) versus simple adjustments to the original model (Equations 5.4 and 5.5).**

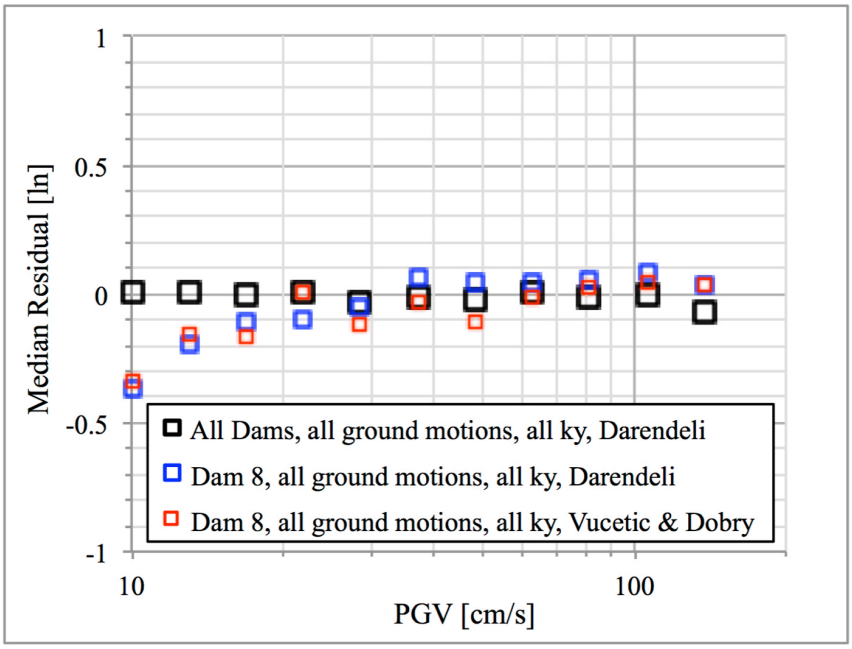

Figure 5.6 **Median residuals of shear-induced deformations showing that the adjusted model is overall unbiased. A residual is calculated as QUAD4MU deformation – transfer-function model deformation.**

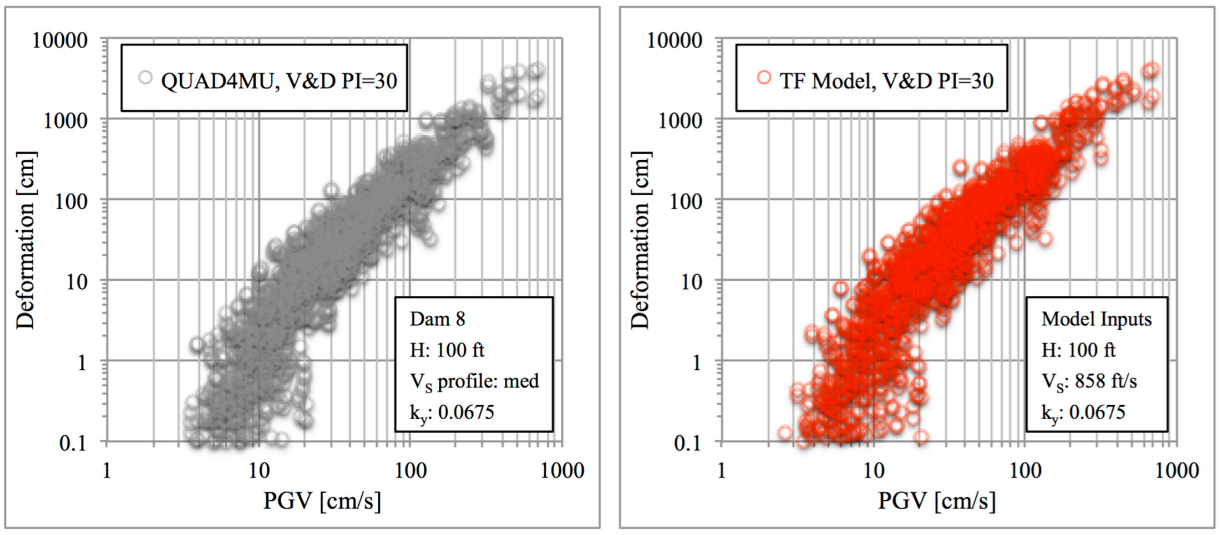

Figure 5.7 **Comparison of shear-induced deformations calculated from QUAD4MU dynamic analyses (left) and transfer-function model (right) for one dam based on the Vucetic and Dobry (1991) PI=30 nonlinear curves.**

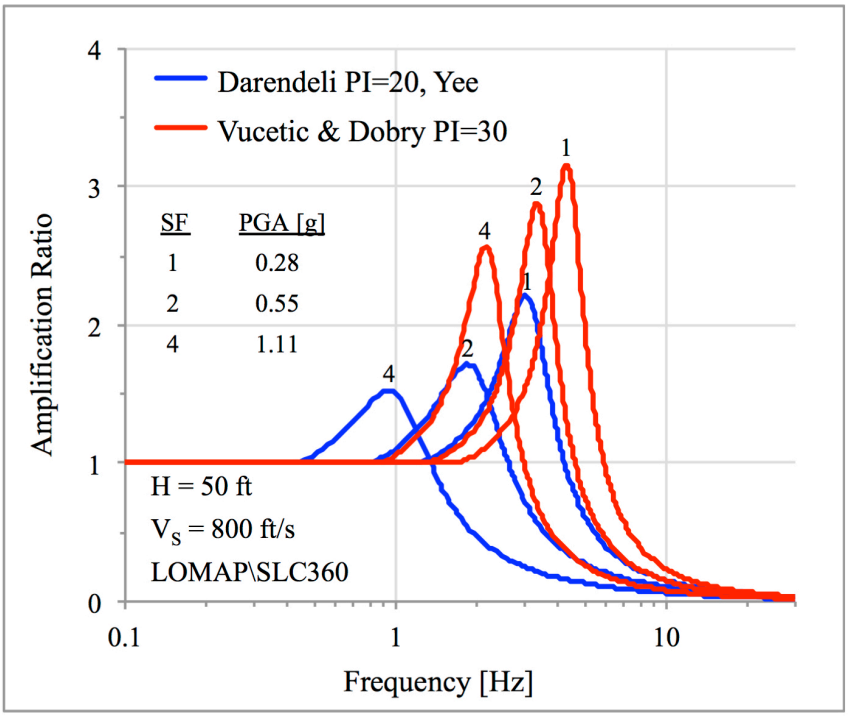

Figure 5.8 **Comparison of estimated transfer functions from original model based on Darendeli (2001) PI=20 nonlinear curves with Yee et al. (2013) procedure and model adjusted for Vucetic and Dobry (1991) PI=30 nonlinear curves.**

6 CASE HISTORY COMPARISONS

6.1 Introduction

The transfer-function model is used to estimate shear-induced deformations for two earthen dams in Northern California. The estimated deformations are compared with observed deformations at these dams following the Loma Prieta earthquake. Despite significant uncertainties in the required inputs, the case histories provide a valuable check on the reasonableness of the estimated deformations from the transfer-function model. The case histories also serve to illustrate the methodology behind the transfer-function model and increase the understanding of the physical basis of the model. A discussion of the results focuses on explaining why the estimated deformations may be low or high compared to the observed deformations.

In the first case history, the largest uncertainty is the input ground motion. Because of this large uncertainty, it is valuable to run multiple input ground motions to obtain a complete picture of the range in potential ground motions and associated shear-induced deformations. The transfer-function model provides an efficient approach for performing a large number of simplified dynamic analyses. The input ground motion also has a large impact on the computed deformation, making it an important input to a deformation analysis. The case history highlights the sensitivity of the shear-induced deformation to the selected input ground motion through use of the transfer-function model, which can accommodate the complete time history of the ground motion and reflect ground motion differences in the estimated deformations. Different approaches are taken to characterize the input ground motion at the dam, including using recorded motions from nearby stations and scaling ground motions to a target range.

In the second case history, a recording of the ground motion at the dam site is available. The uncertainty in the input ground motion is, therefore, significantly reduced, although how well the motion recorded at the abutment represents the foundation motion remains an issue. The case history provides an opportunity to apply the transfer-function model when the small-strain fundamental period of the dam is computed from low levels of ground shaking rather than approximated from a relationship based on properties of the dam. A sensitivity is also performed where the transfer-function model is applied using the first-mode period of the dam calculated from the recording station at the dam during the Loma Prieta earthquake versus the first-mode period estimated by the transfer-function model.

6.2 Austrian Dam

Austrian Dam is a 185-foot-high rolled earth fill dam that sustained damage in the Loma Prieta earthquake. The damage sustained by the embankment included settlement, downstream

movement, and longitudinal and transverse cracking (Harder et al., 1991). The transfer-function model is used to estimate the downstream movement, and a maximum observed shear-induced component of displacement of approximately 48 *cm* is used for this case history comparison (Travasarou, 2003). A dam height of 185 *ft*, average shear-wave velocity of 1400 *ft/s* and yield coefficient of 0.14 were used as inputs in the transfer-function model (Travasarou, 2003). Using the equation $3H/V_S$, the small-strain fundamental period of the dam is estimated as 0.40 seconds.

6.2.1 Recorded Ground Motions

A record of the actual ground shaking at the foundation of Austrian Dam from the Loma Prieta earthquake does not exist. The two stations nearest to Austrian Dam that recorded the ground motions from the Loma Prieta earthquake are the Corralitos station (CLS) and the Los Gatos Presentation Center station (LGP). Figure 6.1 presents a map with these recording stations and the location of Austrian Dam. The epicenter from the Loma Prieta earthquake is also included, as well as the estimated rupture zone inferred from Wald et al. (1991). The CLS station is 14.5 *km* southeast of Austrian Dam and the LGP station is 8.5 *km* northwest of Austrian Dam. Both stations are in the near-field area of the Loma Prieta event with similar distances to the rupture zone. The Joyner-Boore distances are 0.16 *km* (CLS) and 0 *km* (LGP) while the closest distances to the rupture are 3.85 *km* (CLS) and 3.88 *km* (LGP). Note that there are slight discrepancies between these distances (which come from the NGA-West2 flatfile) and the estimated rupture zone inferred from Wald et al. (1991).

The acceleration time histories and response spectra from both horizontal components of the records are displayed in Figure 6.2. A table displaying pertinent ground motion parameters for the records is also included on the figure. The PGV and Arias intensity in particular are included because they correlate well with Newmark deformations (Saygili and Rathje, 2008; Travasarou, 2003; Watson-Lamprey, 2007). Even though the transfer-function model does not explicitly use these ground-motion parameters as inputs, the relationship between them and the estimated shear-induced deformations is preserved because the entire time history is an input to the model. The spectral acceleration at the first-mode period of the dam, SA($T_1 \cong 1.0$ *s*), is an important ground-motion parameter because the transfer function is centered at T_1, amplifying the input motion at T_1 and nearby periods. The table in Figure 6.2 simplistically uses $T_1 \cong 1.0$ *s* to compare the spectral accelerations of the different recorded motions at a single period, rather than computing T_1 for each motion and showing spectral accelerations at different periods. The ground-motion dependent T_1 values for each record, computed from Equation 4.5 are 0.76 *s* (CLS000), 0.66 *s* (CLS090), 1.09 *s* (LGP000), and 0.81 *s* (LGP090).

As shown in Figure 6.2, the acceleration time histories and computed response spectra for the CLS and LGP station records display significant differences. At the CLS station the response spectra shapes between the two horizontal components are markedly different; however, the spectral accelerations near the expected first-mode period of the dam are similar. At the LGP station the response spectra shapes between the two horizontal components are similar, but there is a factor of two difference in the spectral acceleration near the first-mode period of the dam. The CLS station records and the LGP090 record are expected to lead to similar estimated deformations from the transfer-function model because the response spectra near the first-mode period of the dam are similar and the PGV and AI values are similar. The LGP000 record is

expected to lead to larger estimated deformations from the transfer-function model because of the higher spectral accelerations in the long period range, along with the higher PGV and AI values.

The desired input motion is the ground motion that occurs at the foundation of Austrian Dam in the upstream/downstream direction, which is an azimuth of approximately 75°. The ground motions at an azimuth of 75° at the CLS and LGP stations likely have little correlation with the ground motion that occurred at Austrian Dam at the same azimuth. Records several kilometers away from the dam site, particularly along strike and in the near-fault region, are influenced by different radiation patterns and controlled by different high-slip areas of the rupture. It is ultimately unknown how the ground motions were polarized with respect to the dam site; therefore, using only the recorded ground motions rotated to the transverse direction of the dam to estimate deformations is not a reasonable approach. Instead, a suite of rotated input ground motions are generated from the two stations and deformations are estimated for all rotated motions. The horizontal components at each station are rotated in 5° increments to generate records between azimuths of 0° and 175°. This results in thirty-six ground motions per station. Continuing the rotation from 180° to 360° would generate duplicate response spectra, and time histories with the opposite sign. Instead, deformations are calculated for both polarities of the estimated average acceleration time history for a potential sliding mass, effectively covering all azimuths.

6.2.2 Estimated Deformations from Recorded Ground Motions

The transfer-function model is used to estimate a standard polarity and reverse polarity shear-induced deformation for each input ground motion. With thirty-six input ground motions and two deformations per ground motion, this leads to seventy-two individual estimated deformations per station. Results are computed using the original transfer-function model based on the Darendeli PI=20 nonlinear curves. Figure 6.3 presents the response spectra of the rotated motions for the CLS station along with a histogram displaying the deformations estimated from the transfer-function model. Figure 6.4 presents the same results for the LGP station.

The shear-induced deformations from the CLS record are lower and occupy a narrower range than the deformations from the LGP record. In general, the range in deformations considering only two recording stations with rotation to all azimuths is large and can be summarized as follows. When the transfer-function model is applied to the ground motions from a single station, rotated to different azimuths, the range in estimated deformations is more than a factor of three (CLS) and more than a factor of five (LGP). When both stations are considered, the range in deformations is approximately equal to the range from the LGP station, which, for the most part, encompasses the CLS range. The large range in deformations is primarily caused by the large range in spectral acceleration of the input motions near the first-mode period of the dam. There is more variability in the response spectra at a period of 1 second for the rotated LGP motions than there is for the rotated CLS motions, leading to a larger range in estimated deformations.

It is also useful to look at the mean deformation computed from the rotated ground motions so that the magnitude of the average deformation can be compared at different stations. The mean shear-induced deformation at each station is computed from the ground motions

rotated to thirty-six azimuths with deformations from both polarities. The mean is calculated from the log of the deformation. The mean deformation at the CLS station is 9 *cm*, while the mean deformation at LGP is about twice that at 21 *cm*. The higher mean deformation at the LGP station is primarily caused by the higher spectral acceleration of the input motions near the first-mode period of the dam. The spectral accelerations for the LGP record are approximately 50% higher than the CLS station record around T = 1 *s*.

Figure 6.5 presents the results as a function of ground-motion azimuth. The top plot shows the change in spectral acceleration at T = 1 *s* and the bottom plot shows the change in estimated deformation as the input ground motion is rotated from 0° through 175°. The CLS record exhibits relatively little variability with ground-motion azimuth, while the LGP record exhibits more variability, as discussed previously. For each station, the change in deformation with ground-motion azimuth generally follows the same trend as the change in spectral acceleration with ground-motion azimuth. The two stations do not, however, show similar behavior to one another – likely because different patches of slip on the rupture plane influence the records. Austrian Dam is geographically located between the LGP and CLS records, but would have been influenced by a different nearby patch of slip or the same patches of slip polarized in different ways. Based on the sensitivity of the CLS and LGP records to azimuthal direction, it is optimistic to think that the ground motions from a recording several kilometers away at any given azimuth are applicable to a different site at that same azimuth.

6.2.3 Generated Ground Motions

Ground-motion amplitudes are influenced by source, path, and site effects, which coexist to varying degrees in every record. Using a nearby recorded motion assumes that the source, path, and site effects from that station are the same as those at the site of interest, essentially suppressing ground-motion variability to zero. This is a big assumption. Alternatively, a median estimate of the ground motion at Austrian Dam can be calculated from ground-motion prediction equations and the variability about that median can be captured by sampling the distribution defined by the ground-motion sigma, generating a suite of ground motions that reasonably represent the range of possible ground motions at Austrian Dam, where no record exists. This approach is similar to the common industry practice of matching seed records to a target spectrum in a forward modeling application. In this study the records are only modified by scaling and occupy a range rather than being tight matched to the target, which has the benefit of accounting for the variability in addition to capturing the median ground motion.

First an ergodic response spectrum is calculated from the NGA-West2 ground-motion models (Abrahamson et al., 2014; Boore et al., 2014; Campbell and Bozorgnia, 2014; Chiou and Youngs, 2014; and Idriss, 2014). The ergodic response spectrum represents the median prediction based on the NGA-West2 database, which is comprised of RotD50 motions from shallow crustal earthquakes around the world, with some terms regionalized to include California-specific terms. The ergodic response spectrum is presented in Figure 6.6 and the inputs to the ground-motion models are provided in Table 6.1. Response spectra at one standard deviation are also shown and represent the aleatory variability about the median. The RotD50 response spectra from the records at CLS and LGP station are included for reference. The CLS and LGP RotD50 response spectra are both above the ergodic response spectrum at periods between 0.5 *s* and 1.3 *s*. These periods include the range of the expected first-mode period of the

dam and have a large influence on the estimated deformations. Because the earthquake of interest has already occurred, the ergodic response spectrum can be improved by accounting for the Loma Prieta event term.

A target spectrum is generated from the ergodic response spectrum plus the event term from the Loma Prieta earthquake. The event term represents the average shift of the observed ground motions from an individual earthquake from the population median predicted by the ground-motion model (Al Atik et al., 2010). The event term from the Loma Prieta earthquake is positive, meaning that the Loma Prieta earthquake ground motions were larger than the median ergodic target. The target spectrum is presented in Figure 6.7. The within-event standard deviation (ϕ) is used to compute response spectra at one standard deviation about the target. The within-event standard deviation is calculated from the residuals for all records from the Loma Prieta earthquake only. The ergodic median, CLS station, and LGP station response spectra are included on Figure 6.7 for reference. The target spectrum falls between the CLS and LGP RotD50 response spectra at periods between 0.5 and 1.3 *s*.

Twenty records are selected to represent the target median and the distribution about the target. Records were initially screened based on magnitude, distance, and V_{S30}. A second screening removed records with spectral shapes that were significantly different than the target spectrum. The remaining candidate records were then scaled to the target range and a set of twenty scaled records were selected based on how well the median and standard deviation from the set matched the target median and standard deviation. Note that the only modification to the records is scaling – spectral matching techniques are not utilized. The period range of interest for the selection process was 0.1 to 4 seconds. The RotD50 response spectra for the twenty scaled records are presented in Figure 6.8 with the target median and standard deviation for reference. The suit of twenty records has a median and standard deviation that is approximately equivalent to the target median and standard deviation between the periods of interest (see Figure 6.9a).

The record selection is performed on the RotD50 response spectra, and the range about the target spectrum represents the variability in RotD50 motions. To account for the variability in the ground-motion azimuth, which is not captured by RotD50 and is often ignored, the time histories from the two horizontal components of each record are rotated in 5° increments to generate records at thirty-six different azimuths, in the same manner as the recorded motions at CLS and LGP stations. This results in thirty-six ground motions for each of the twenty selected records, for a total of 720 generated ground motions.

The PGV and AI values for the generated ground motions were calculated and compared to the recorded motions at CLS and LGP as an additional check on the generated ground motions. The PGV values from the recorded horizontal components at CLS and LGP stations range from 48 to 96 *cm/s*. The generated ground motions have a geometric mean PGV of 67 *cm/s*. The AI values from the recorded horizontal components at CLS and LGP stations range from 2.6 to 7.9 *m/s*. The generated ground motions have a geometric mean AI of 5.2 *m/s*. The PGV and AI values from the generated records are reasonable.

6.2.4 Estimated Deformations from Generated Ground Motions

The transfer-function model is used to estimate a standard polarity and reverse polarity shear-induced deformation for all 720 generated ground motions, for a total of 1440 estimated

deformations. Figure 6.9b presents a histogram displaying the estimated deformations. The range in deformations when an appropriate range of input ground motions are generated is, not surprisingly, larger than when only one or two records are considered. The mean deformation from the generated ground motions is 14 *cm*.

The estimated deformations from the generated ground motions are plotted against the PGV and SA(T = 1 *s*) of the input ground motion in Figure 6.10. The results for the CLS and LGP records are included for reference. The estimated deformations increase with increasing PGV and SA, as expected. Notably, there is significant scatter in the estimated deformations. This scatter is attributed to the sensitivity of the estimated deformation to the chosen record as well as the azimuthal direction of the record after rotation. To examine the sensitivity of the estimated deformation to the azimuth of the ground motion, a standard deviation is computed from the deformations of all rotated ground motions for a single record. These azimuth standard deviations are presented in Table 6.2. The average azimuth standard deviation from the 20 selected records is considerable at 0.66 natural log units. This is consistent with work by Kramer and Lindwall (2004), who also found that estimated deformations were very sensitive to the assumed azimuthal direction of the input motion.

6.2.5 Discussion

The estimated shear-induced deformations from the transfer-function model applied to the various input ground motions are lower than the maximum observed deformation of 48 *cm* at Austrian Dam. Two potential explanations for this difference are: 1) the ground motion at the foundation of Austrian Dam was on the higher end, and/or 2) the response of Austrian Dam was different than the transfer-function model. These explanations are expanded on further below.

The ground motion is an important input to a deformation analysis and is also typically the input with the largest uncertainty, as is true for this case history. The estimated deformations from the CLS station ground motions are too low. Assuming the transfer-function model provides a reasonable estimate of the dam response, this implies that the ground motions at Austrian Dam were higher than the ground motions at CLS. The estimated deformations from the LGP station ground motions are in better agreement, though still somewhat lower than the maximum observed deformation of 48 *cm*, implying that the ground motions at Austrian Dam site were more similar to the LGP motions than the CLS motions in intensity. One potential explanation for this is a region of high slip north of the epicenter very near the Austrian Dam site, which caused more destructive ground motions at LGP and would cause more destructive ground motions at Austrian Dam than were recorded at CLS station. In particular, the slip amplitudes in the rupture model by Wald et al. (1991) in Figure 6.11 are consistent with this explanation, though alternative rupture models place the areas of high slip at different locations (i.e., Beroza, 1991; Hartzell et al., 1991; Steidl et al., 1991).

When an appropriate range of potential input ground motions are considered, the estimated deformations suggest that the maximum observed deformation of 48 *cm* was above the mean estimated deformation. Higher than average deformations come from higher than average ground motions. About 15% of the generated ground motions lead to estimated deformations that are similar (35 – 65 *cm*) to the observed maximum deformation of 48 *cm*. The response spectra for these ground motions are shown in Figure 6.12. The response spectra of ground motions that

produce deformations between 35 and 65 *cm* are nearly all above the median target response spectrum at periods between 1 and 2 seconds. This implies that the pseudo-spectral accelerations at the first-mode period of the dam (~ 1 *s*) and at the longer periods that neighbor the first-mode period of the dam are important to the estimated deformation from the transfer-function model. The ground motion at the foundation of Austrian Dam may have included above-average pseudo-spectral accelerations at periods between 1 and 2 seconds due to the location of the slip-model asperity, consistent with a maximum observed displacement of about 48 *cm*.

The second potential explanation for why the estimated shear-induced deformations from the transfer-function model are generally lower than the maximum observed deformation is that Austrian Dam responds in a manner that is different than the transfer-function model. Specifically, the transfer-function model is based on the Darendeli PI=20 nonlinear curves with the Yee et al. (2013) strength adjustment, but it can be run with adjustments to approximate other nonlinear curves. To explore the sensitivity of the estimated deformations to different nonlinear curves, the analyses are carried out with three different nonlinear adjustments of the transfer-function model. Figure 6.13 presents the normalized first-mode period, T_1/T_o, and damping, β, for the original model and the adjusted transfer-function models. The original model (NL1) exhibits the most nonlinear behavior, followed by NL2, NL3, and finally the model with the least nonlinear behavior, NL4, which is based on the Vucetic and Dobry PI=30 curves.

The results for the CLS station ground motions are presented in Figure 6.14c. An average transfer function from each nonlinear model is shown in Figure 6.14b and the corresponding first-mode period is annotated on the response spectra in Figure 6.14a. It is useful to look at why changes to the nonlinear model result in different estimated deformations. NL1 exhibits the most nonlinear behavior, which causes the first-mode period to shift the farthest from the small-strain fundamental period and the damping to be relatively high. In contrast, NL4 exhibits the least nonlinear behavior, so the first-mode period is closer to the small-strain fundamental period and the damping is relatively low. The estimated deformations are progressively larger as the nonlinearity in the model is reduced from NL1 to NL4. This is because the transfer function is shifted to a period in the ground motion that has more energy. The transfer function is also more peaked from the lower damping, though the impact on the deformation from the change in damping is secondary to the shift in period. Notably, the change from NL3 to NL4 results in the smallest increase in estimated deformations. This is because the response spectra are relatively flat at the periods where NL3 and NL4 amplify the motion, so there is not the same increase in the ground motion energy that gets amplified as there is when going from NL1 to NL2 or NL2 to NL3.

Similar results for the LGP station ground motions and generated ground motions are presented in Figures 6.15 and 6.16. The results for all nonlinear models and all ground motions are summarized in Table 6.3. Austrian Dam may have responded with less nonlinearity than the original transfer-function model based on the Darendeli PI=20 curves, producing estimated deformations closer to the observed displacement at the dam. Table 6.4 displays the average epsilon at T = 1 *s* for those generated ground motions that lead to estimated deformations similar (35 – 65 *cm*) to the maximum observed deformation for each nonlinear model. Various combinations of input ground motions and nonlinear behavior of the dam result in deformations between 35 – 65 *cm*. For example, it is possible that Austrian Dam's nonlinear behavior is best described by NL3 and the input ground motion was 0.27 standard deviations above the median target.

6.2.6 Austrian Dam Summary

The importance of selecting an appropriate input ground motion cannot be overstated. Even for case histories like Austrian Dam where the event was relatively well recorded near the dam site with multiple recordings at the desired distance to the rupture, the differences between the CLS station record and the LGP station record are large, demonstrating the significant spatial variability of ground motions. Ground motions recorded at nearby stations are single realizations of a random process, and should be part of a larger suite of input ground motions considered. An approach for selecting a set of ground motions with an appropriate median and standard deviation was utilized and the transfer-function model was used to run hundreds of simplified dynamic analyses. The simplified dynamic analyses are run in a matter of seconds, while much more time was spent on the ground-motion selection process. This time allocation is appropriate given the importance of the input ground motion on the resulting deformations.

The estimated shear-induced deformations from the transfer-function model occupy a wide range, depending primarily on the selected input ground motion, and secondarily on the nonlinear curves employed by the transfer-function model. The estimated deformations are not only sensitive to the record chosen to represent the ground motions at the site, but also the azimuth of the input ground motion. The results indicate that the ground motion at the foundation of Austrian Dam likely had significant energy at periods near the natural period of the dam (similar to the ground motions recorded at LGP) and the nonlinearity of the dam is best described by curves that fall somewhere between Darendeli PI=20 with the Yee et al. (2013) adjustment and Vucetic and Dobry PI=30. Various combinations of the ground motion and the nonlinear model produce estimated deformations that are in agreement with the maximum observed deformation of 48 *cm*. More information needs to be brought in to resolve the uncertainties in these inputs, and efforts should focus on improving the constraints on the ground-motion characterization, which has a large impact on the estimated deformations.

6.3 Lexington Dam

Lexington Dam is a 200-foot-high zoned earthen dam that was also damaged in the Loma Prieta earthquake. The damage sustained by the embankment included settlement, downstream movement, and longitudinal and transverse cracking (Harder et al., 1991). The transfer-function model is used to estimate the downstream movement. A maximum observed shear-induced seismic displacement of approximately 15 *cm* is used for this case history comparison (Travasarou, 2003). A dam height of 200 *ft*, average shear-wave velocity of 1600 *ft/s* and yield coefficient of 0.11 were used as inputs in the transfer-function model (Travasarou, 2003).

6.3.1 Recorded Ground Motions

Lexington Dam was instrumented with strong-motion instruments that recorded the ground shaking from the Loma Prieta earthquake. The recording from the left abutment is the Los Gatos Lexington Dam station record (LEX) and is the closest to a foundation input motion. Figure 6.17 presents a map with the location of the Loma Prieta earthquake and Lexington Dam. The dam is near the northeast corner of the rupture zone with a closest distance to the rupture of about 5 *km*. The acceleration time histories and response spectra from both horizontal components of the

LEX record are displayed in Figure 6.18. A table displaying pertinent ground motion parameters for the record is also included on the figure. The acceleration time histories at LEX station display significant long-period energy and relatively short durations. The response spectra from the two horizontal components are similar in shape and peak at a period of about 1 second.

6.3.2 Estimated Deformations

The LEX record with an azimuth of 0° is the ground motion corresponding to the transverse direction of Lexington Dam. Assuming that the recording from the left abutment is an adequate representation of the ground motion at the foundation of Lexington Dam, this motion is used as the input ground motion to the transfer-function model. The transfer-function model is initially applied with no adjustments. Using the equation $3H/V_S$ for the dam period, the small-strain fundamental period of the dam is estimated as 0.38 seconds. The estimated shift in the natural period of the dam with increasing ground-motion intensity is shown in Figure 6.19. The LEX000 record has a spectral acceleration of about 1.0 *g*, and the transfer-function model estimates a first-mode period of about 0.82 *s*. This is a T_1/T_o ratio of approximately 2.2. The estimated shear-induced deformations from the transfer-function model are 57 and 33 *cm* for the standard and reverse polarity of the input motion, or a geometric mean deformation of 43 *cm* (mean of the logs).

Makdisi et al. (1991) used the recordings from the 1989 Lake Elseman earthquake and 1989 Loma Prieta earthquake to analyze Lexington Dam, calculating a small-strain fundamental period of 0.5 seconds and a first-mode period of about 1.4 seconds. This is a T_1/T_o ratio of approximately 2.8. These data points are also plotted on Figure 6.19. The empirical small-strain fundamental period of 0.5 seconds is longer than the period estimated from $3H/V_S$ and the empirical first-mode period is also longer, corresponding to more nonlinearity than the transfer-function model predicts. The transfer-function model can be calibrated with these empirical observations and the modified T_1 relationship is included on Figure 6.19. The modifications to the transfer-function model include using $T_o = 0.5$ *s* directly, and increasing the nonlinearity with a c_3 coefficient of 1.5. The estimated deformations from the calibrated transfer-function model are 36 and 25 *cm* for the standard and reverse polarity of the input motion, or a geometric mean deformation of 30 *cm*.

Figure 6.20 presents the response spectra for the LEX000 record as well as the estimated transfer functions from the model. Transfer functions for the original model and the calibrated model are shown and the estimated first-mode periods are annotated on the response spectra above. The calibrated transfer function leads to a lower estimated deformation because the transfer function is shifted to a period in the ground motion that has less energy. Note that the damping parameter, β, was not modified in the calibrated model.

6.3.3 Discussion

The estimated shear-induced deformations are generally higher than the maximum observed deformation of 15 *cm* at Lexington Dam. Two potential explanations for this difference are: 1) the ground motion at the foundation of Lexington Dam was lower than the motions recorded at the abutment, and/or 2) the response of Lexington Dam was different than estimated by the transfer-function model. These explanations are expanded on further below.

There is some uncertainty regarding how well the ground motion recorded at the left abutment represents the actual ground motion experienced beneath the dam. One concern is that the recorded motion at the abutment was affected by local topographic or geologic conditions that would not have been recorded at the foundation of the dam. It is also possible that the abutment record is contaminated by the response of the nearby dam, such that the abutment includes amplification near the first-mode period of the dam. Without an actual recording from the foundation of Lexington Dam, it is impossible to know with certainty to what degree the response of the dam is present in the abutment record; however, looking at the record more closely may shed light on any unusual characteristics or features of the record.

As shown in Figure 6.20, the shape of the response spectrum for the LEX record is somewhat unusual for a rock motion. An average response spectrum would peak at a period near 0.15 *s*, while the LEX record contains significant long-period energy with a clear peak near T = 1 *s*, close to the natural period of the dam. Figure 6.21a plots the response spectra for the LEX record rotated to all azimuths. The response spectra display a moderate level of azimuthal variability up to a period of about 0.6 *s*, after which the variability increases dramatically. Figure 6.21b displays the change in pseudo-spectral acceleration at the first-mode period of the dam, T = 1.4 *s*, with the azimuth of the ground motion. The azimuthal spectral accelerations at T = 1.4 *s* for the nearby records at Los Gatos Presentation Center (LGP) and Saratoga Aloha Avenue (STG) are also plotted on Figure 6.21b. All three stations are near the northeast corner of the Loma Prieta rupture zone. The LGP and STG records show similar trends with azimuth, while the LEX record differs. The unusual shape of the LEX response spectrum, large azimuthal variability at long periods, and differing behavior of ground-motion azimuth compared to nearby records, do not, by themselves, definitively indicate that the abutment recording is contaminated, but together could suggest that the abutment record contains long-period energy that would not have been present at the foundation of the dam. An input ground motion with lower spectral accelerations near the natural period of the dam would lead to lower estimated deformations from the transfer-function model, moving the estimated deformations closer to the observed deformation of 15 *cm*.

The second potential explanation for why the estimated deformations from the transfer-function model are generally higher than the maximum observed deformation is that Lexington Dam responds in a manner that is different than the transfer-function model. Other studies have been able to reasonably replicate the response spectrum computed from the record at the crest of the dam using the abutment record as a foundation input motion (Makdisi et al., 1991; Mejia et al., 1992). These two studies both utilized the average modulus reduction curve and the lower damping curve proposed by Seed and Idriss (1970) for sands to model the behavior of the dam materials. Figure 6.22 compares the Seed and Idriss nonlinear curves with the Darendeli PI=20 nonlinear curves, which form the basis of the transfer-function model. The Seed and Idriss curves used in the Lexington Dam studies exhibit more nonlinearity than the Darendeli curves from the transfer-function model, which is consistent with the calibration of the transfer-function model for Lexington Dam, where more nonlinearity was required to match the empirical observations of the natural period of the dam. In particular, the chosen Seed and Idriss modulus reduction curve is below the Darendeli PI=20 curves at the level of strains expected in the dam for this case history (0.01 – 1%).

The earlier calibration of the transfer-function model did not modify the damping parameter, β. This is because the original transfer-function model already predicts a β from the

saturated region of the curve based on the high ground-motion intensity. Additionally, the Seed and Idriss damping curve used in the Lexington Dam studies is very similar to the Darendeli PI=20 curves at the strain levels of interest. An increase in β could be applied to the model though, bringing the estimated deformation down further, but does not seem warranted on the basis of the nonlinear behavior of the dam materials. Alternatively, the scale factor, α, could be reduced, which would also result in a transfer function with lower amplification ratios. A reduction in α could be attributed to the shear-wave velocities of the dam and their impact on the amplification of the input motion. Reducing alpha implies that the shear-wave velocities of Lexington Dam cause less amplification of the input motion than the shear-wave velocity profiles of the representative dams used in the transfer-function model. The recorded peak ground accelerations at Lexington Dam are consistent with this explanation. The abutment PGA was 0.45 *g* and the crest PGAs were 0.39 *g* (left crest) and 0.45 *g* (right crest) resulting in an input-to-crest amplification ratio of approximately 1, whereas the representative dams have an average amplification ratio of about 2.5 at the same input motion PGA.

6.3.4 Lexington Dam Summary

The Lexington Dam case history includes a recording of the Loma Prieta earthquake at the dam site. Despite the reduced uncertainty in the input ground motion, there are uncertainties regarding the presence of potential topographic, geologic, and dam amplification effects in the abutment record. More information is necessary to quantify the uncertainty in the input motion given the recording at the left abutment. An approach for calibrating the dam period shift of the transfer-function model with empirical observations was utilized and the transfer-function model was used to run simplified dynamic analyses and estimate shear-induced deformations. The estimated deformations were quite sensitive to the natural period of the dam due to the dramatic differences in the energy of the input motion at the associated periods. The calibrated model brought the estimated deformations (about 30 *cm*) closer to the observed deformation of 15 *cm*.

The empirical observations of the natural period of the dam are consistent with dam behavior that is more nonlinear than the Darendeli PI=20 curves with the Yee et al. (2013) adjustment. The estimated deformations from the transfer-function model indicate that the ground motion at the foundation of Lexington Dam may have had less long-period energy than was recorded at the abutment, and a transfer function with lower amplification ratios, consistent with more damping or less amplification through the dam materials.

6.4 Conclusions

The transfer-function model was used to estimate shear-induced deformations for two earthen dams that experienced horizontal deformations following the Loma Prieta earthquake. The estimated deformations from the transfer-function model are higher than the observed deformations at Austrian Dam and lower than the observed deformations at Lexington Dam. The simplicity and physical basis of the transfer-function model allows the estimated deformations to be tied to the modeled dam period shift, transfer-function damping, and characteristics of the input ground motion. Potential explanations for the differences between the estimated and observed deformations are provided, and alternative input ground motions and reasonable

adjustments to the transfer-function model lead to estimated deformations that are similar to the observed deformations.

In addition to the differences in deformation that are attributed to the input ground motion and model parameters, the transfer-function model is acknowledged as a simplification of the complex process of how soil systems respond to dynamic loading, and it is possible that a limitation of the simplified approach prevents an accurate estimate of the observed deformation. The transfer-function model is based on the results of 2D equivalent-linear analyses utilizing the de-coupled approach, and limitations of this approach are carried through to the transfer-function model. In contrast, the maximum observed displacements are the result of 3D, nonlinear, coupled response. The Newmark sliding block method, while a useful evaluation tool, provides displacements that are approximate in nature, and should be viewed as such. Nonetheless, the transfer-function model provides a framework for carrying out a first-order approximation of shear-induced deformations, and allows for the most information of the input that has the biggest effect on the deformation - the input ground motion. The most sophisticated numerical model of an earthen dam will not solve the problem of large uncertainties in the input ground motion.

The sensitivities presented for the two case histories also provide valuable insights regarding numerical modeling of dams. A common practice in dynamic analyses is to calibrate a numerical model of a dam with a recording from the crest of the dam. A reasonable reproduction of the response spectra at the crest is considered confirmation that the numerical model is adequate, and in particular that the chosen nonlinear curves represent the behavior of the dam materials under dynamic loading. However, the sensitivity of the dam response to the chosen nonlinear curves depends on the input ground motion. If the input ground motion has a low intensity level, the dam response will be in the linear range, where the nonlinear curves are largely all the same. In other words, any nonlinear curve would have given satisfactory results, but any nonlinear curve will not give satisfactory results for future high-intensity ground motions. If the input ground motion used in the calibration has a flat response spectrum near the first-mode period of the system, the results will indicate that the dam response is not sensitive to the selection of nonlinear curves, but future earthquakes with different slopes at those periods will produce meaningfully different responses to different nonlinear curves. Modelers must be careful about the conclusions drawn from one input ground motion and the validity of extending those conclusions to other ground motions, either with higher intensity levels or different spectral shapes.

Table 6.1 Inputs to NGA-West2 ground-motion models for Austrian Dam case history.

Variable	Input
M_w	6.93
R_{RUP} (km)	3.85
R_{JB} (km)	0
R_X (km)	0.25
R_{y0} (km)	0
V_{S30} (m/s)	500
U (BSSA13)	0
F_{RV}	0
F_{NM}	0
F_{HW}	0
Dip (°)	70
Z_{TOR} (km)	3.85
Z_{HYP} (km)	17.48
$Z_{1.0}$ (km)	0.048
$Z_{2.5}$ (km)	0.607
W (km)	18
$V_{S30Flag}$	inferred
FAS	no
Region	California

Table 6.2 **Standard deviation of the estimated deformation considering all azimuthal directions of the generated record for the Austrian Dam case history.**

RSN	Azimuth St. Dev. [ln]
139	1.60
302	0.68
322	0.46
549	0.40
730	0.46
739	0.55
754	1.21
767	0.41
850	0.64
1044	0.66
1063	0.89
1184	0.28
1197	0.52
1512	0.28
1602	0.31
1787	0.84
2625	0.37
2627	1.42
2734	0.50
3473	0.77

Table 6.3 **Austrian Dam case history: summary of estimated deformations from transfer-function model with different nonlinear adjustments.**

Input Ground Motions	Mean Estimated Deformation [cm]			
	NL1	NL2	NL3	NL4
Corralitos, rotated	9	19	28	31
LGPC, rotated	21	33	48	63
20 Scaled to range, rotated	14	22	29	34

Table 6.4 **Average epsilon of generated ground motions for Austrian Dam case history that produce estimated deformations between 35 and 65 cm.**

	NL1	NL2	NL3	NL4
Average ε of ground motion	0.72	0.65	0.27	0.07

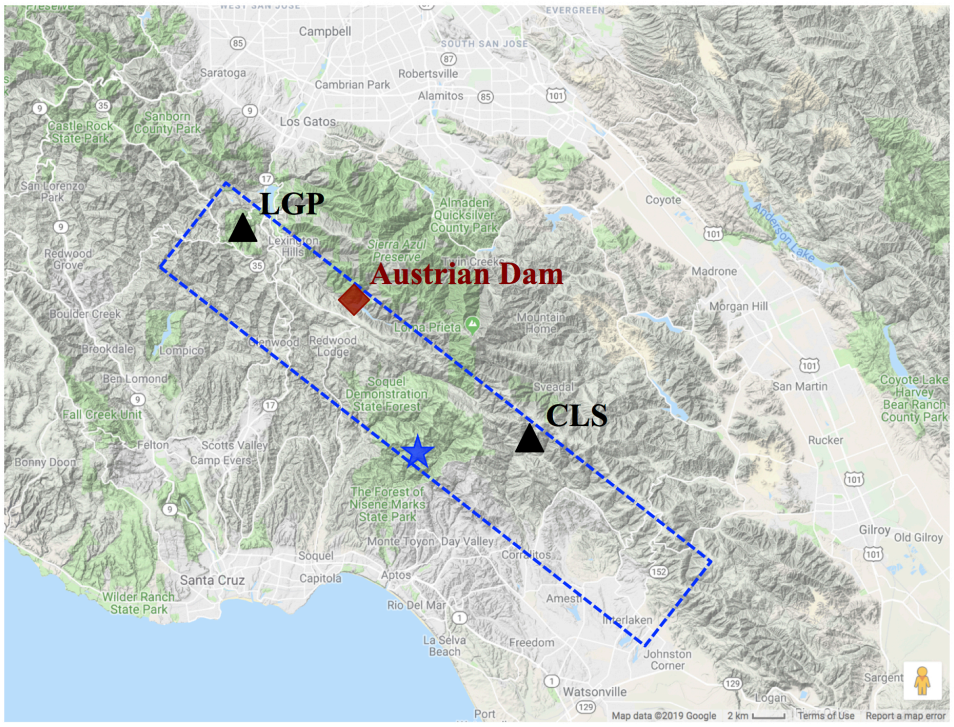

Figure 6.1 **Regional map of Austrian Dam, Loma Prieta earthquake, and nearby recording stations. Blue star indicates location of Loma Prieta epicenter and rectangle is rupture zone inferred from Wald et al. (1991).**

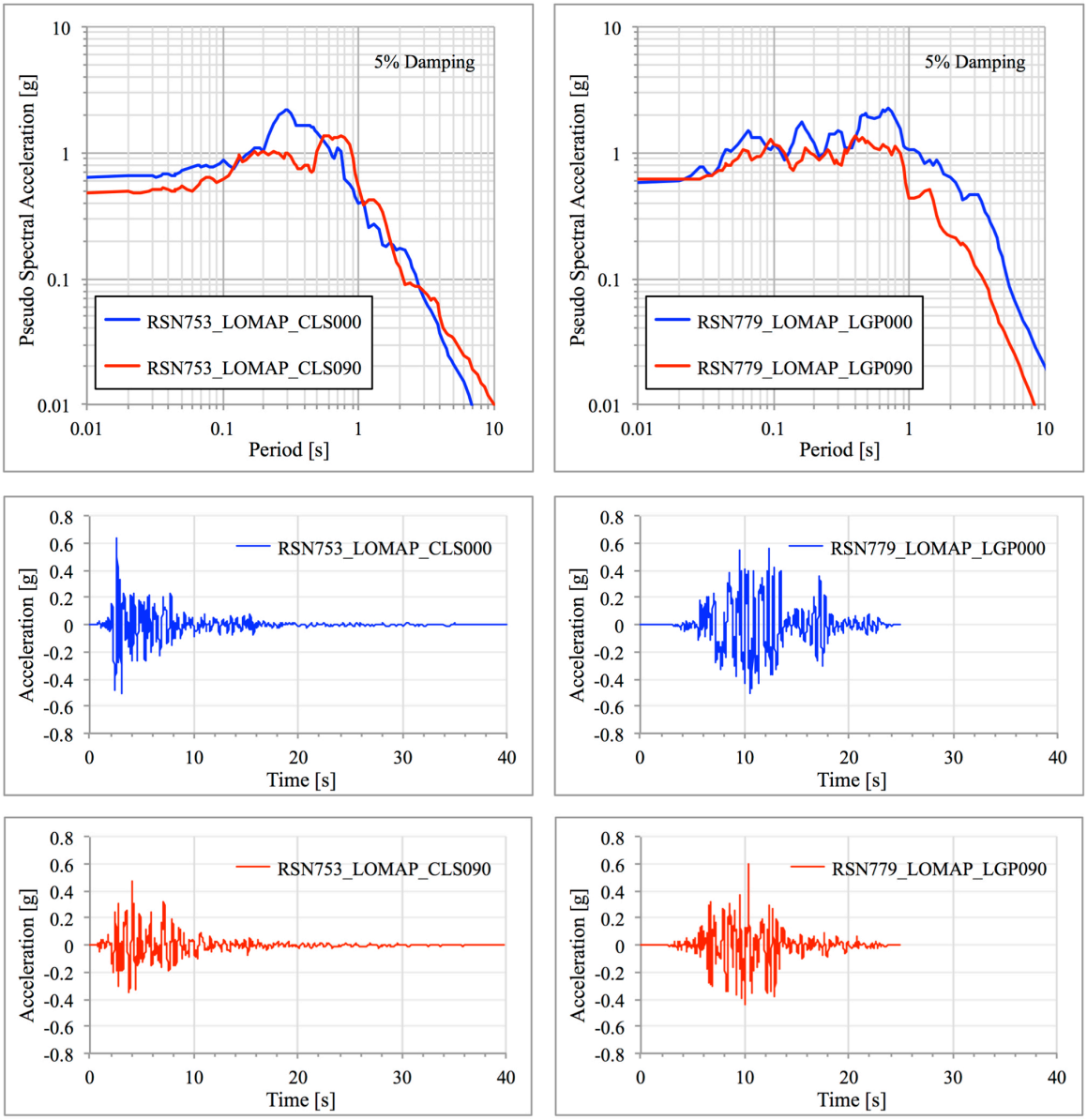

	PGA *g*	PGV *cm/s*	AI *m/s*	$Dur_{5\text{-}75}$ *s*	$SA(T_1 \cong 1.0\ s)$ *g*
RSN753_LOMAP_CLS000	0.64	56	3.2	3.4	0.40
RSN753_LOMAP_CLS090	0.48	48	2.6	4.7	0.55
RSN779_LOMAP_LGP000	0.57	96	7.9	5.5	1.05
RSN779_LOMAP_LGP090	0.61	52	3.1	5.5	0.44

Figure 6.2 **Response spectra and acceleration time histories for two horizontal components recorded at Corralitos station (CLS) and Los Gatos Presentation Center station (LGP) during the Loma Prieta earthquake.**

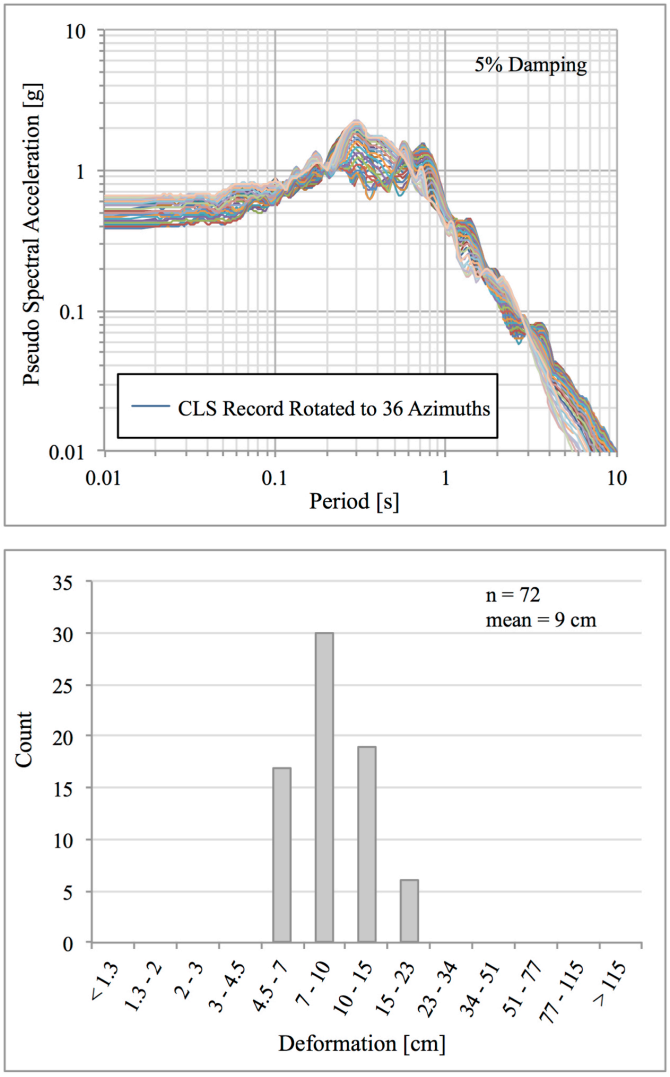

Figure 6.3 **Austrian Dam case history: response spectra for Corralitos station record rotated to various azimuths and resulting deformations when the transfer-function model is applied to those ground motions.**

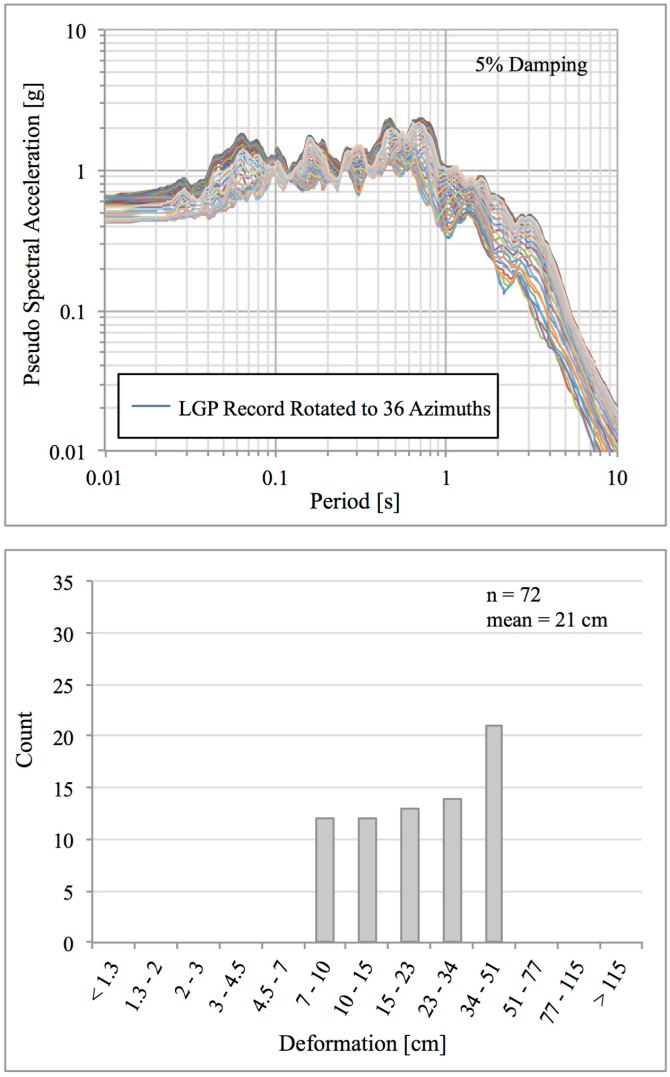

Figure 6.4 **Austrian Dam case history: response spectra for Los Gatos Presentation Center station record rotated to various azimuths and resulting deformations when the transfer-function model is applied to those ground motions.**

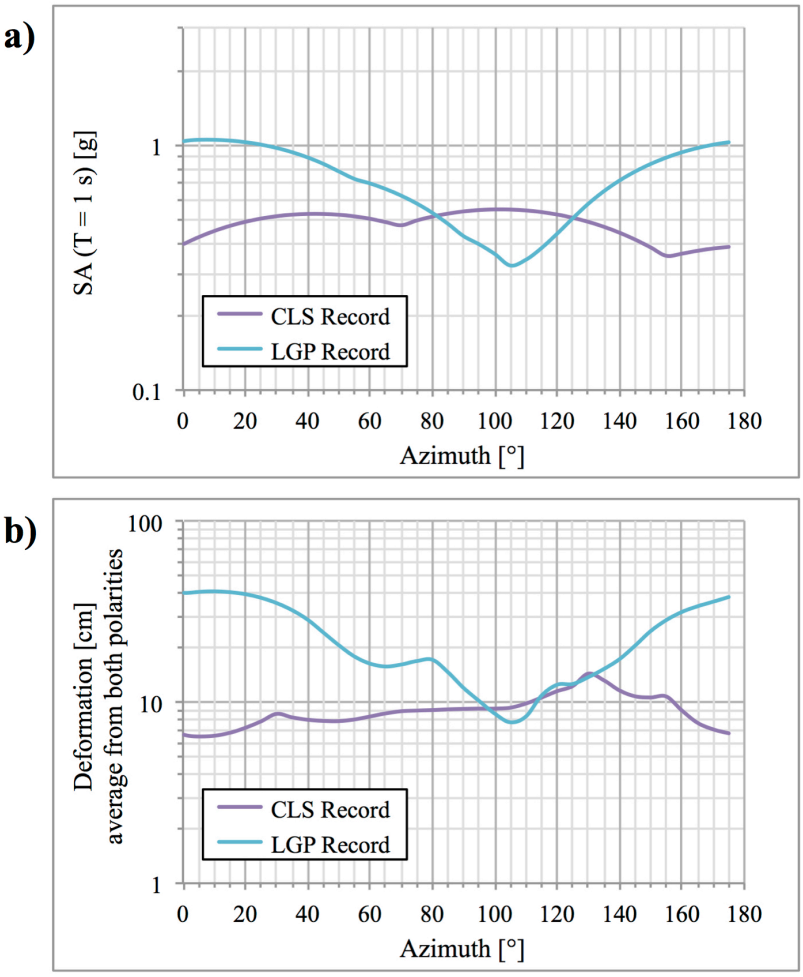

Figure 6.5 **Comparison of a) spectral acceleration of the ground motion and b) estimated deformations versus azimuth of the input ground motion at Corralitos and Los Gatos Presentation Center stations.**

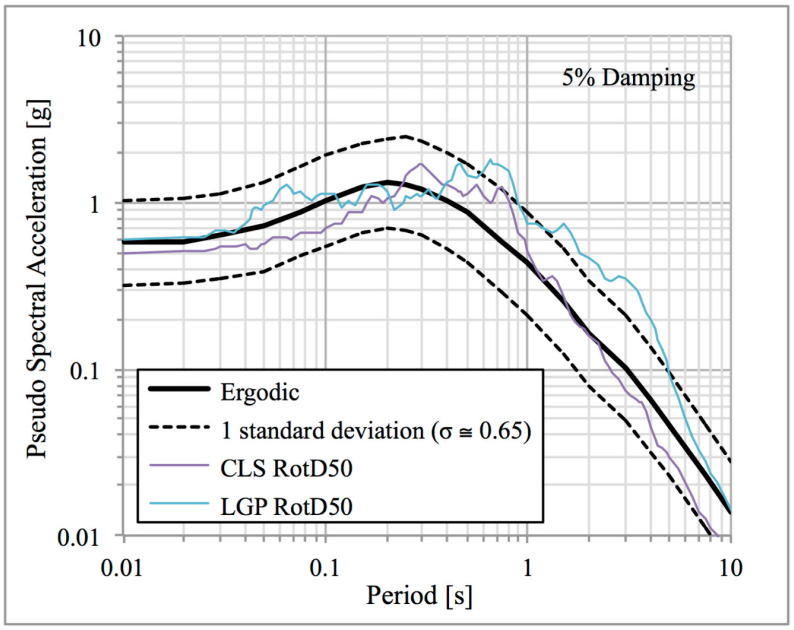

Figure 6.6 **Ergodic target spectrum from NGA-West2 ground-motion models for Austrian Dam site and Loma Prieta event. RotD50 response spectra for Corralitos and Los Gatos Presentation Center records included for reference.**

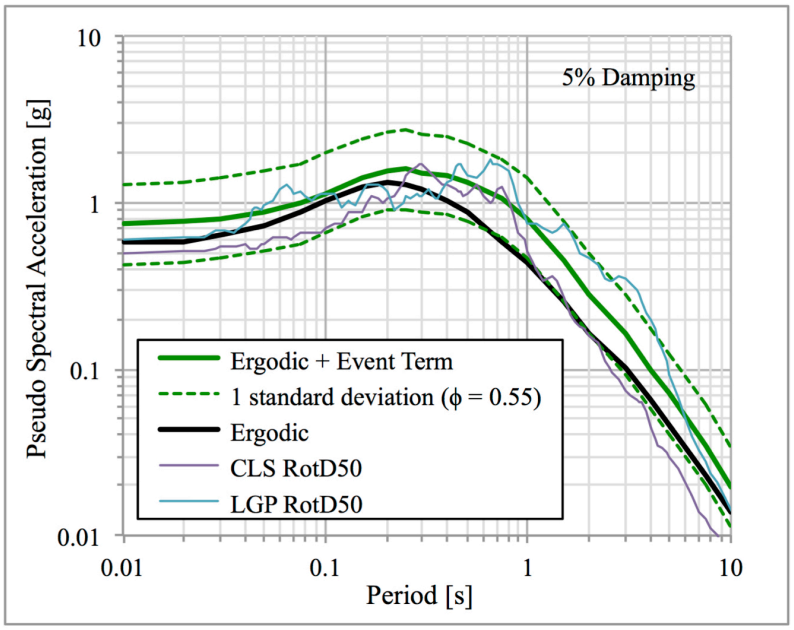

Figure 6.7 **Ergodic target spectrum from NGA-West2 ground-motion models adjusted for the Loma Prieta event term for Austrian Dam site. Ergodic target spectrum and RotD50 response spectra for Corralitos and Los Gatos Presentation Center records included for reference.**

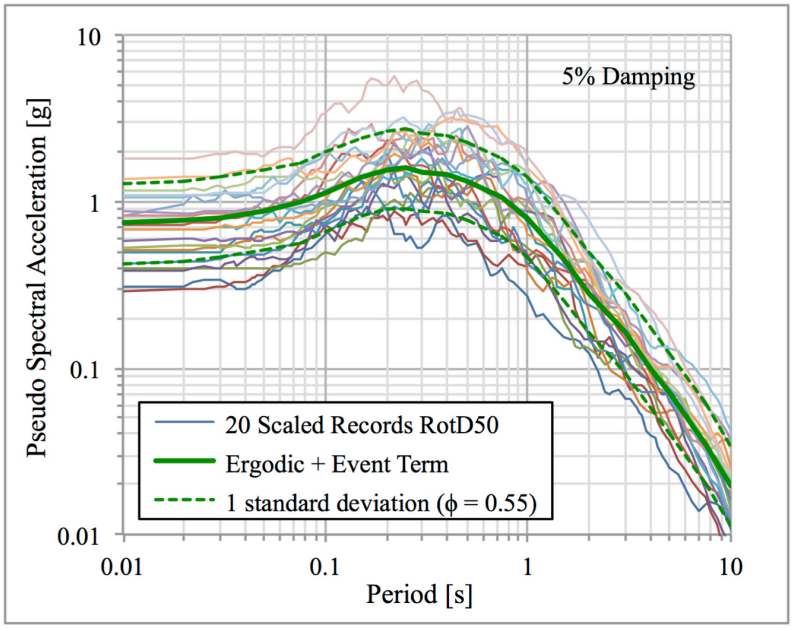

Figure 6.8 **Response spectra for generated ground motions comprised of 20 scaled records that represent the range of possible ground motions at the Austrian Dam site.**

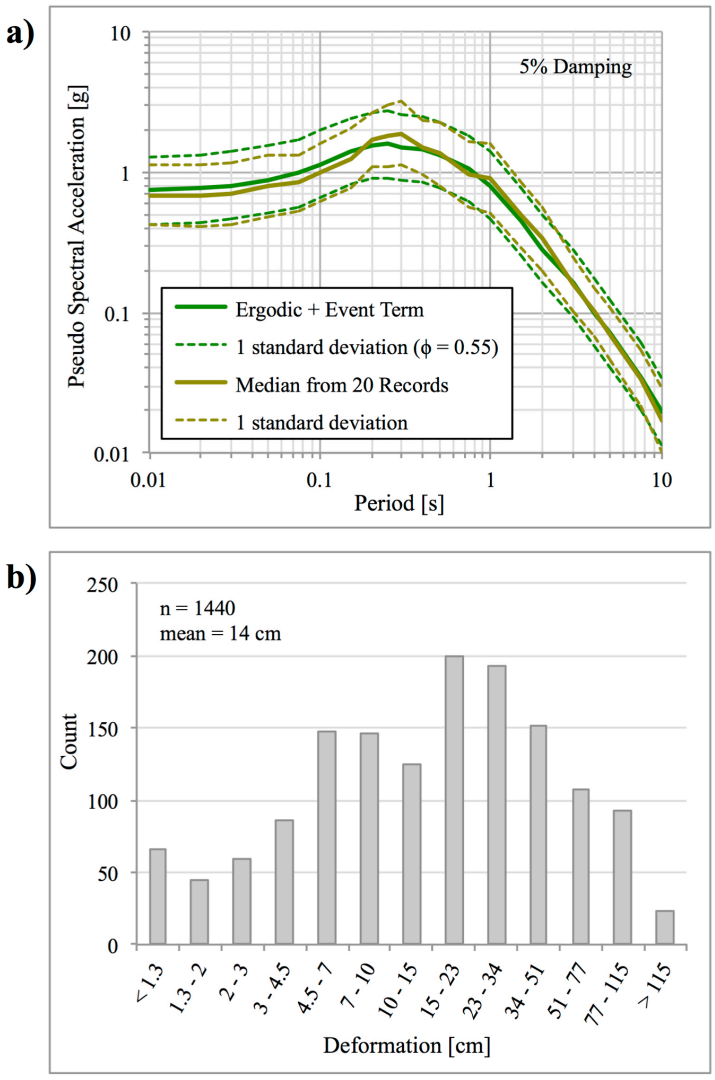

Figure 6.9 **Austrian Dam case history: a) comparison of median target spectrum (Ergodic + Event Term) and one standard deviation range with those calculated from generated ground motions and b) resulting deformations when the transfer-function model is applied to the generated ground motions.**

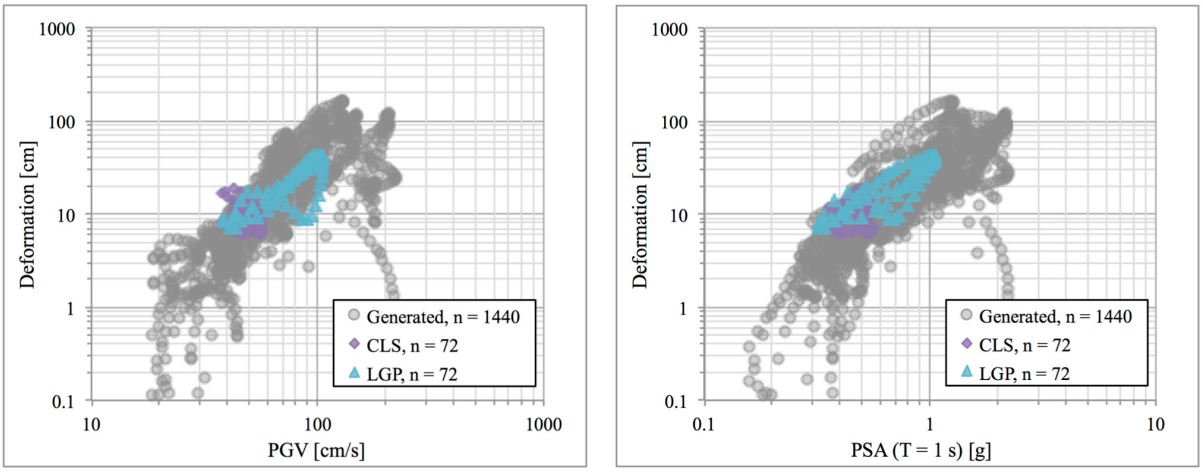

Figure 6.10 **Austrian Dam case history: trends of estimated deformations with input ground motion parameters for generated ground motions.**

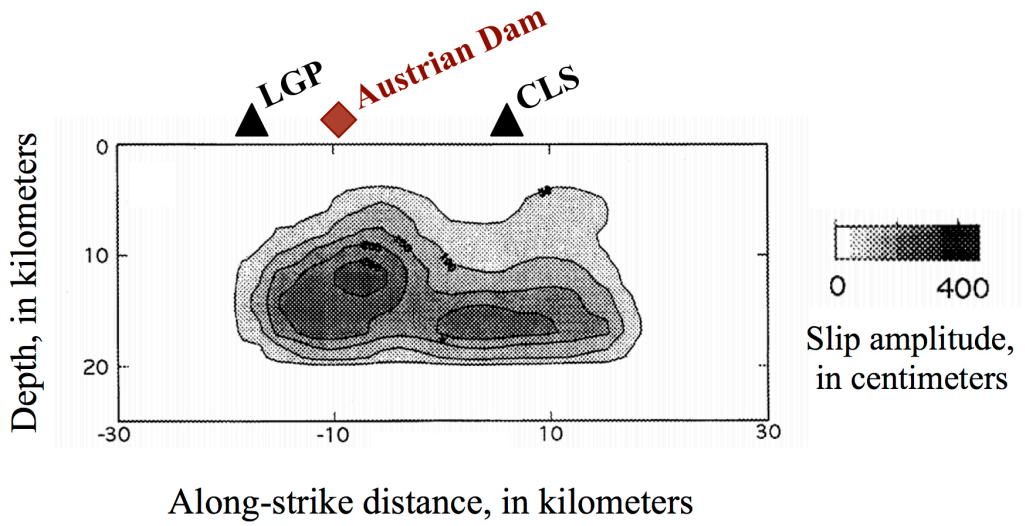

Figure 6.11 **Rupture model depicting slip amplitude of Loma Prieta earthquake from Wald et al. (1991).**

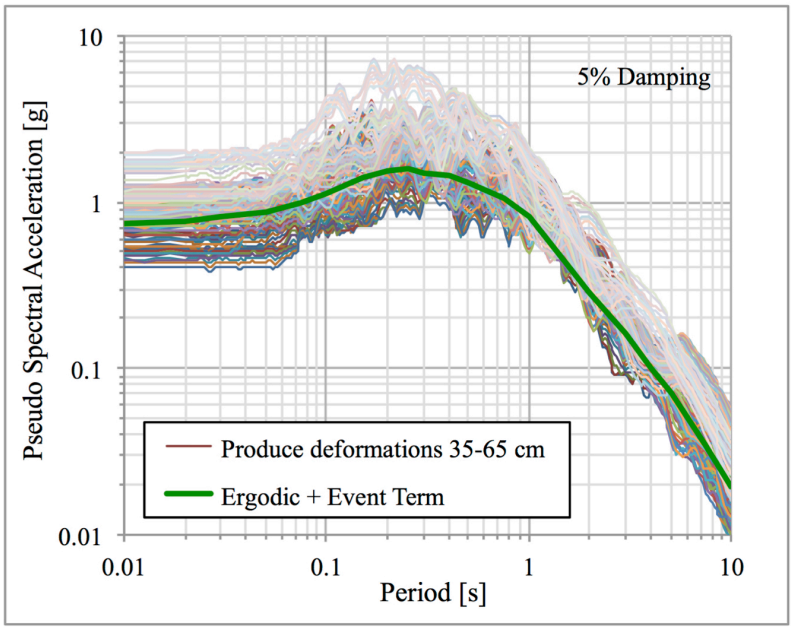

Figure 6.12 **Response spectra for generated ground motions (with rotation) that produce estimated deformations close to the observed maximum deformation at Austrian Dam of 48 *cm*. Median target spectrum (Ergodic + Event Term) included for reference.**

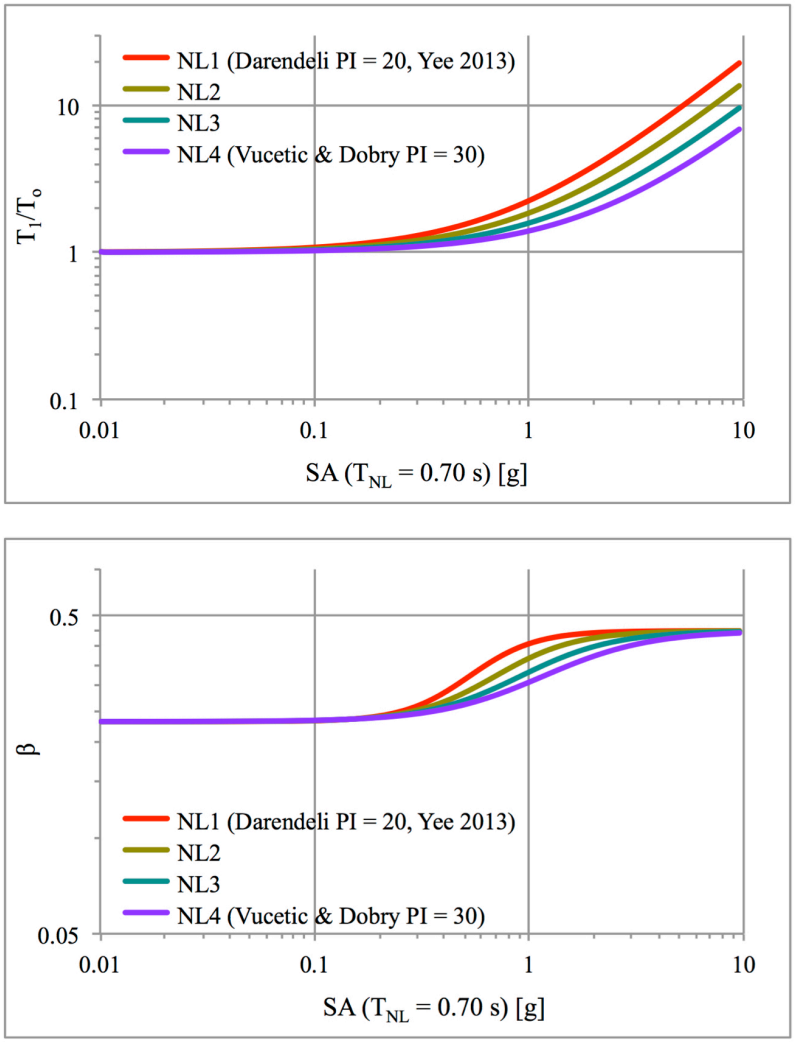

Figure 6.13 **Transfer-function model parameters T_1/T_o and β adjusted for different nonlinear models for Austrian Dam case history.**

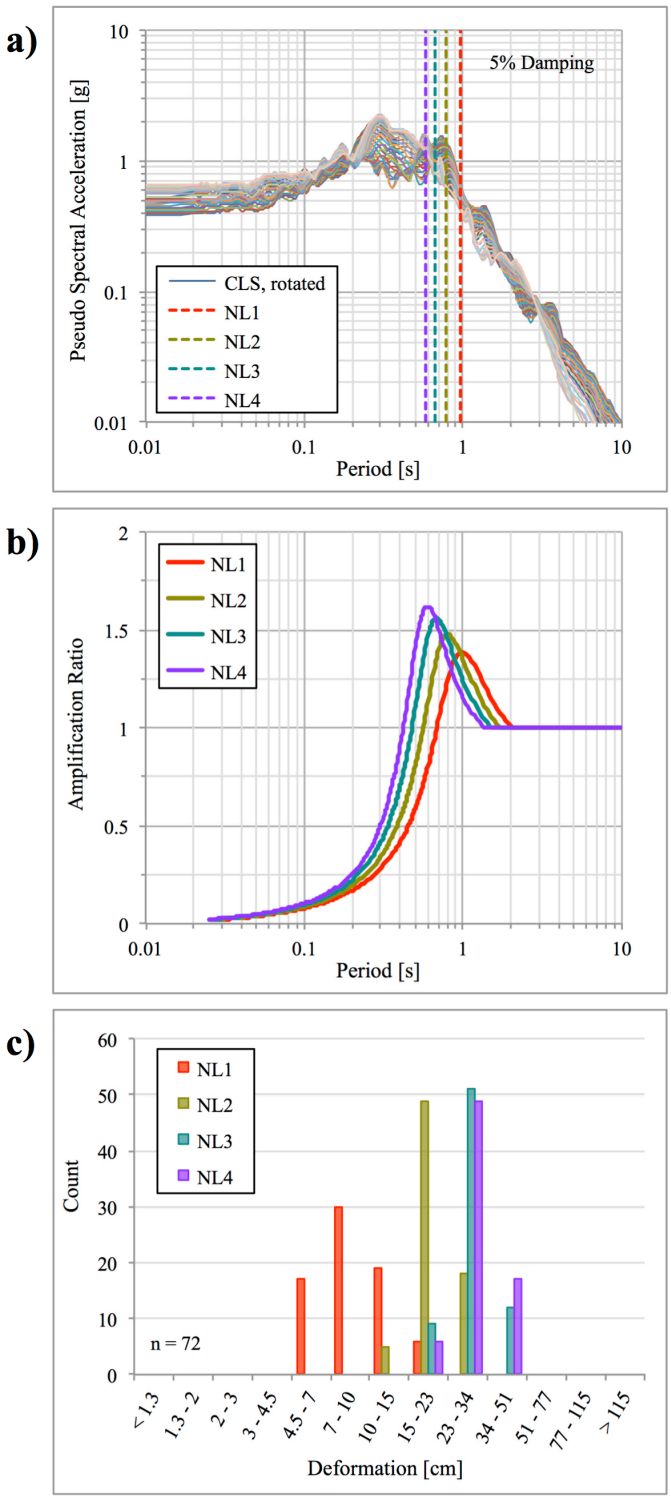

Figure 6.14 **Sensitivity of estimated deformations to nonlinearity of transfer-function model when applied to the Corralitos record for the Austrian Dam case history: a) response spectra of input ground motions annotated with T_1 of average transfer function, b) average transfer function from each nonlinear model, and c) estimated deformations.**

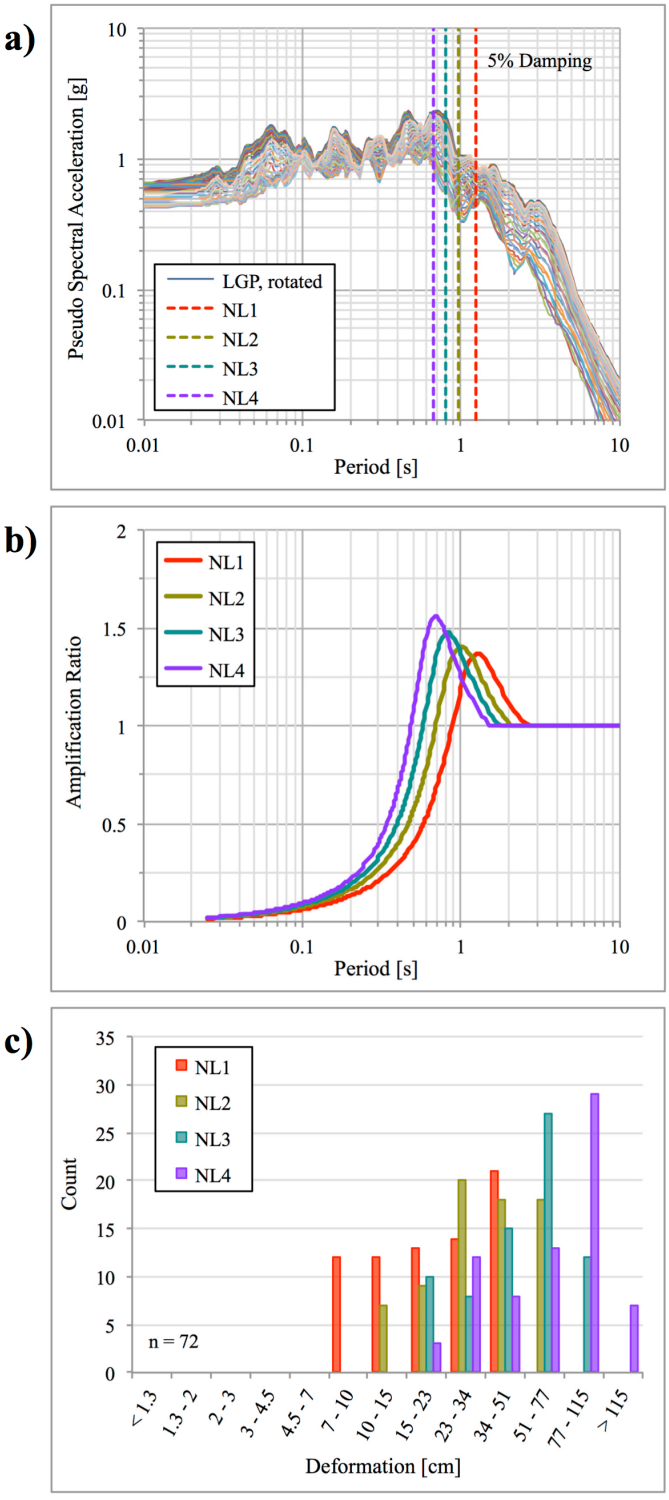

Figure 6.15 **Sensitivity of estimated deformations to nonlinearity of transfer-function model when applied to the Los Gatos Presentation Center record for the Austrian Dam case history: a) response spectra of input ground motions annotated with T_1 of average transfer function, b) average transfer function from each nonlinear model, and c) estimated deformations.**

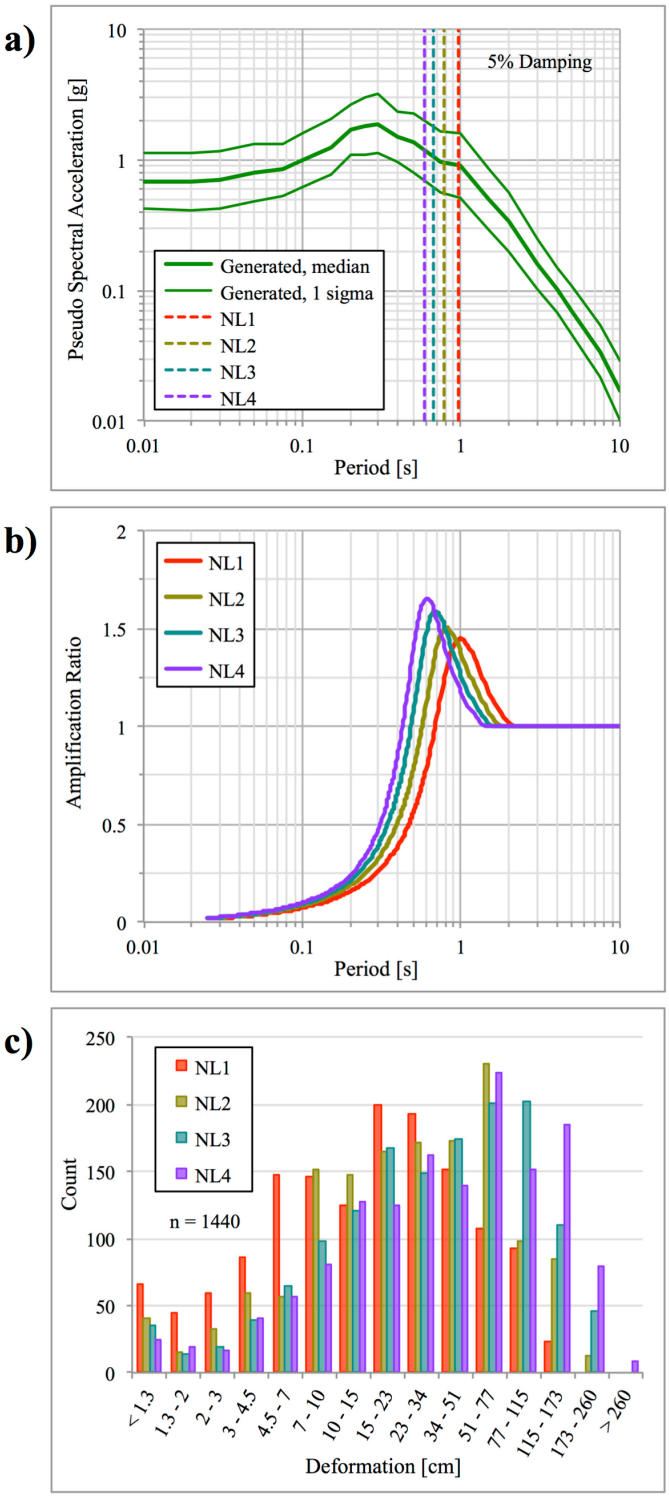

Figure 6.16 **Sensitivity of estimated deformations to nonlinearity of transfer-function model when applied to the generated ground motions for the Austrian Dam case history: a) response spectra annotated with T_1 of average transfer function, b) average transfer function from each nonlinear model, and c) estimated deformations.**

Figure 6.17 **Regional map of Lexington Dam (with recording station) and Loma Prieta earthquake. Blue star indicates location of Loma Prieta epicenter and rectangle is rupture zone inferred from Wald et al. (1991).**

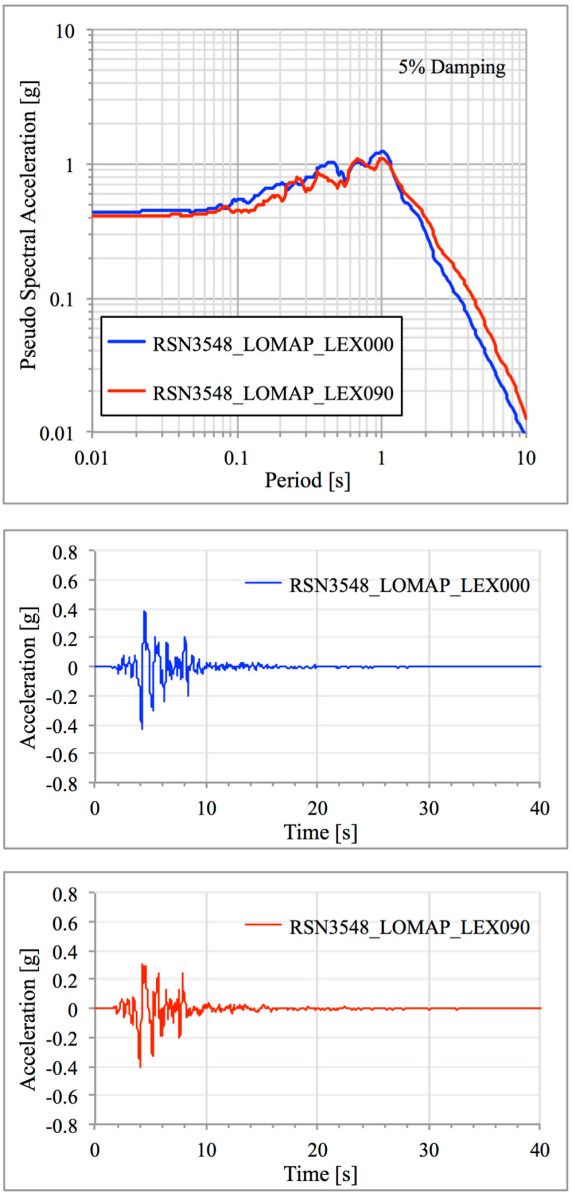

	PGA *g*	PGV *cm/s*	AI *m/s*	$Dur_{5\text{-}75}$ *s*	$SA(T_1 \cong 1.0\ s)$ *g*
RSN3548_LOMAP_LEX000	0.44	86	1.9	2.1	1.22
RSN3548_LOMAP_LEX090	0.41	96	1.8	1.9	1.10

Figure 6.18 **Response spectra and acceleration time histories for two horizontal components recorded at Lexington Dam station (LEX) during the Loma Prieta earthquake.**

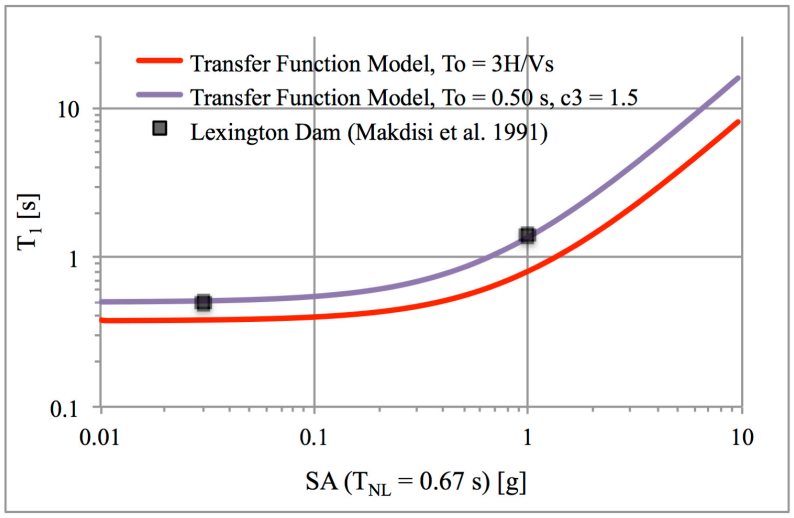

Figure 6.19 **Lexington Dam case history: first-mode period, T_1, estimated by the original transfer-function model (red line) and the modified transfer-function model (purple line) after calibration with empirical observations from Makdisi et al. (1991).**

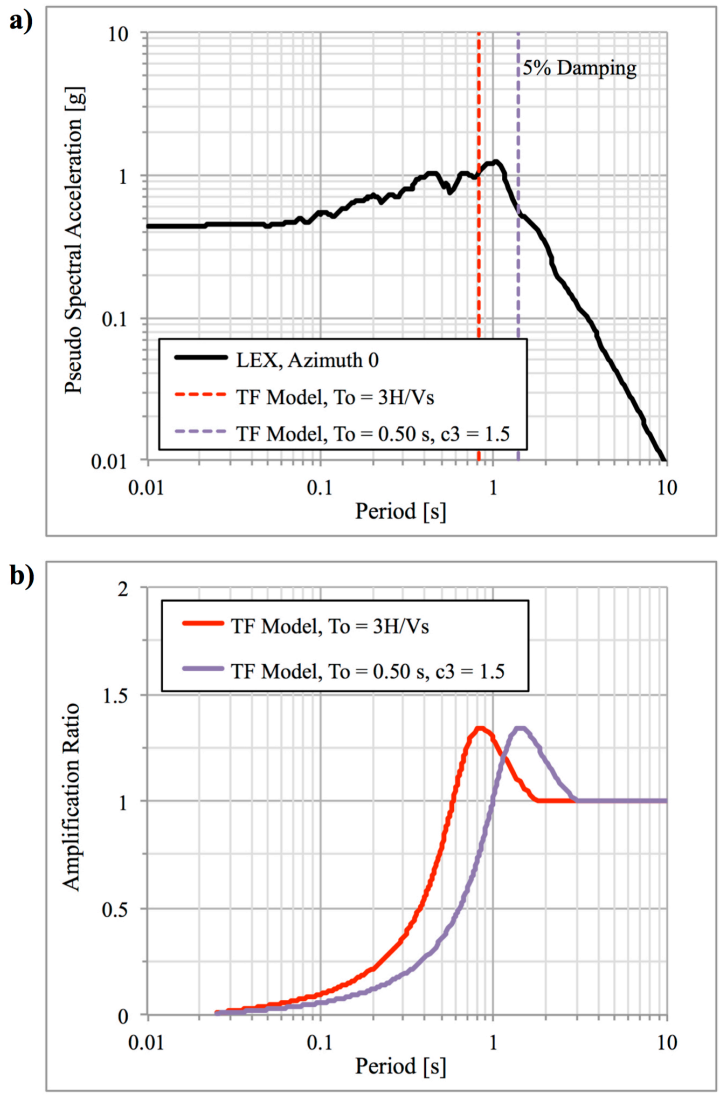

Figure 6.20 **Lexington Dam case history: a) response spectra for Lexington Dam station record annotated with T_1 of transfer function and b) transfer function from original model and calibrated model.**

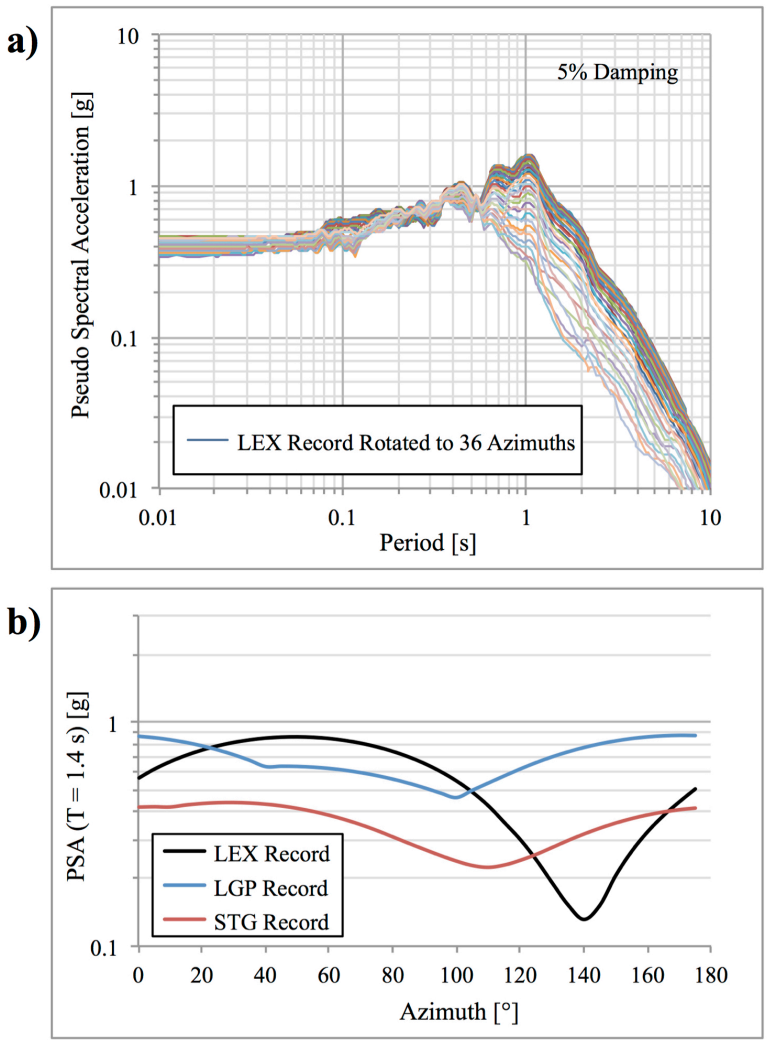

Figure 6.21 **Lexington Dam case history: a) response spectra for Lexington Dam station record rotated to various azimuths and b) change in spectral acceleration of the ground motion with azimuthal direction at Lexington Dam and nearby Los Gatos Presentation Center and Saratoga Aloha Avenue stations.**

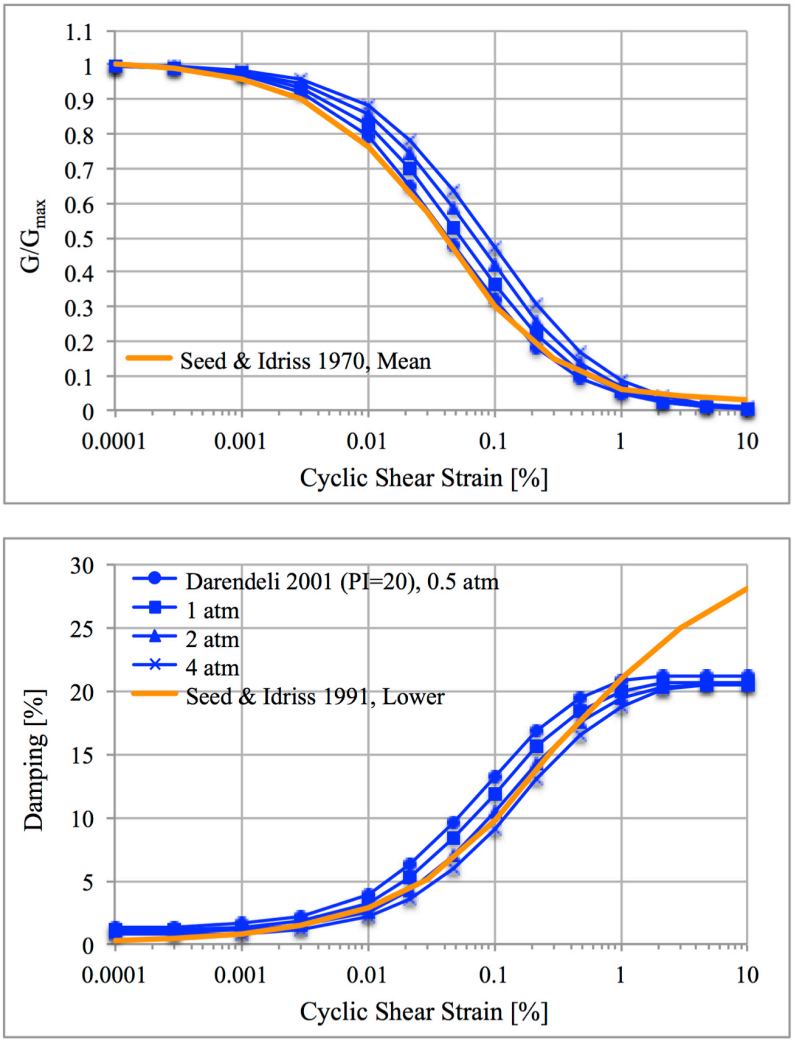

Figure 6.22 **Lexington Dam case history: comparison of Darendeli (2001) curves used in transfer-function model and Seed and Idriss (1970) curves used in other studies of Lexington Dam.**

7 CHARACTERIZING SEISMICALLY INDUCED DEFORMATION HAZARD FOR EARTHEN DAMS

7.1 Introduction

Dam owners and regulators are interested in characterizing the hazard for their dams due to potential future earthquakes. The question is – what hazard? Seismic hazard has historically been characterized in terms of a ground-motion intensity measure, and the most common intensity measure is elastic pseudo-spectral acceleration. The reasons for this are two-fold. First, for many structures, the spectral acceleration is the best indicator for how the building will respond to ground shaking. Second, probabilistic seismic hazard codes are set up to run spectral acceleration, so a practitioner can compute the spectral acceleration hazard without having to modify the code. There are also many available ground-motion models for spectral acceleration and the models are robust, whereas there are generally few published models for other intensity measures and the models that are available are often outdated and not developed with the same level of rigor or physical basis as the spectral acceleration models. Though hazard is most commonly computed for spectral acceleration, fundamentally hazard should be calculated for something that is a proxy for damage to the structure. An appropriate parameter that is a proxy for damage to an earthen dam is the shear-induced deformation.

Shear-induced deformations are estimated in this chapter using the transfer-function model. A series of deterministic deformation analyses are used to demonstrate the application, physical basis, and flexibility of the transfer-function model. Application of the transfer-function model in a probabilistic framework is then presented to characterize the deformation hazard for an earthen dam. The results from a site-specific probabilistic seismic hazard analysis are used to capture the expected ground motions at a hypothetical dam site, the transfer-function model is used to perform incremental dynamic analyses for the dam, and the seismic hazard results are combined with the dynamic analyses results to compute deformation hazard curves. Finally, epistemic uncertainty in the seismic hazard and dam response is presented through a sensitivity analysis leading to alternative deformation hazard curves.

7.2 Deterministic Deformation Analysis

Although the transfer-function model is not intended for use with a single input ground motion, the model is used here with a deterministic earthquake scenario to illustrate its application in estimating seismically induced Newmark deformations. An appropriate input ground motion is selected for the deterministic analysis. The transfer-function model is used to estimate the transfer function for a potential sliding mass, and that transfer function is applied to the input

ground motion to obtain the time history of the average acceleration for the potential sliding mass. The Newmark sliding block method is then applied to the average acceleration time history, along with the yield coefficient, to obtain an estimate of the Newmark deformation.

It is important to define the specific transfer function estimated by the model and emphasize that this definition of a transfer function is unique and is not typically calculated or presented in dam seismic stability evaluation reports. The transfer function utilized in this study is defined as the ratio of the Fourier transform of the average acceleration time history of the potential sliding mass to the Fourier transform of the input ground motion time history. This transfer function is not the transfer function between the crest and input motion (i.e., the spectral ratio) as is typical when analyzing vibration periods of dams, and it is not the amplification factor between the crest and input motion response spectra as is typical in site response. The transfer function in this study is between the average acceleration time history of the potential sliding mass and the input ground motion.

7.2.1 Single Ground Motion

The process of applying the transfer-function model to calculate a Newmark deformation is summarized in Figure 7.1 using a record from the Loma Prieta earthquake with a recorded PGA of 0.46 *g*. The entire acceleration time history of the ground motion, which is an outcropping motion, is an input to the model (see Figure 7.1a). A fast Fourier transform is performed to obtain the amplitude and phase of the ground motion. The Fourier amplitude spectrum of the ground motion is shown in Figure 7.1b. The amplitude and phase of the input ground motion are multiplied by the amplitude and phase of the estimated transfer function. The estimated transfer function is specific to the properties of the dam as well as the properties of the ground motion and is shown in Figure 7.1c for this example. In particular, the properties of the hypothetical dam are a height of 50 *ft* and an average shear-wave velocity of 800 *ft/s*. Note that although the phase of the ground motion and the phase of the transfer function are not shown in Figure 7.1, they are calculated and are necessary to go back to the time domain. An inverse Fourier transform is performed to obtain the estimated average acceleration time history for a potential sliding mass along a deep failure surface, as shown in Figure 7.1d. The Newmark sliding block method is applied to the average acceleration time history, along with a yield coefficient of 0.12, to obtain an estimate of the Newmark deformation. The estimated deformations from the standard and reverse polarities for this example are 50 and 46 *cm* and are reported on Figure 7.1d.

A key attribute of the transfer-function model is that it only simplifies the dynamic response of the dam. The model utilizes the framework of a traditional de-coupled analysis, which can be broken down into three components: 1) the input ground motion, 2) the dynamic response of the earthen dam, and 3) the estimation of the shear-induced deformation. With the transfer-function approach, only the dynamic response of the earthen dam is simplified. The input ground motion is not simplified, and the Newmark sliding block method is not simplified. The model is used to estimate the transfer function for the potential sliding mass, which is a compact description of how the earthen dam amplifies and filters input motions at different frequencies. This estimated transfer function replaces a detailed numerical model of the dam, often requiring the construction of a finite-element mesh and significant computational time.

7.2.2 Single Ground Motion with Scale Factors

To observe the change in the estimated transfer-function shape over a range of ground-motion intensities, a single input ground motion is scaled up and down with five scale factors. The five scaled input ground motions represent five deterministic earthquake scenarios. This example utilizes the same hypothetical dam and the same record from the Loma Prieta earthquake. The range in PGAs after the scale factors are applied is 0.14 – 0.68 *g*, and the five estimated transfer functions are plotted in Figure 7.2.

As illustrated in Figure 7.2, as the intensity of the input ground motion increases, there is a shift in the first-mode frequency of the transfer function to lower frequencies, or longer periods. The transfer-function model provides a continuous degradation of the first-mode period of the dam across a wide range of ground-motion intensities. Additionally, as the ground-motion intensity increases, the shape of the transfer function becomes less peaked, and the amplification factor at the first-mode frequency is reduced due to increased damping. This behavior demonstrates that the functional form of the transfer-function model has a physical basis that captures the key mechanisms through which nonlinearity affects soil behavior, including dam period shift and damping increase.

7.3 Probabilistic Deformation Hazard Analysis

A probabilistic deformation hazard analysis is fundamentally a large number of deterministic deformation analyses with a rate assigned to each deformation scenario. In contrast to a deterministic analysis, a probabilistic hazard analysis provides a framework in which aleatory variability and epistemic uncertainty are identified and combined to provide a more complete picture of the deformation hazard for a particular dam. In this section, the results from a site-specific probabilistic seismic hazard analysis are used to capture the expected ground motions at a hypothetical dam site, the transfer-function model is used to perform incremental dynamic analyses for the hypothetical dam, and the seismic hazard results are combined with the dynamic analyses results to compute shear-induced deformation hazard curves.

One of the considerations for a deformation hazard analysis is maintaining a similar level of detail on both the ground motion and dam response sides. It's important to recognize that in performing a seismic hazard analysis, simplified models are utilized. The complicated dynamic rupture process of an earthquake is modeled with a single magnitude and the 3D wave propagation through the crust is often modeled with a single distance measure in ground-motion prediction equations. The better ground-motion prediction equations are based on the Brune (1970) point-source model to provide a physical basis for the models and ensure proper extrapolation beyond the range of the empirical data. On the dam response side, the dynamic response of soil systems such as earth dams is a complex process, and estimating the response and shear-induced permanent deformation of the dam with a transfer function and Newmark-like procedure is likewise acknowledged as utilizing a simplified model. Similar to the physical basis behind the ground-motion prediction equations, the transfer-function model is based on the nonlinear response of soils, and the transfer function captures the key mechanisms through which nonlinearity affects soil behavior, including dam period shift and damping increase.

7.3.1 Probabilistic Seismic Hazard Analysis

The seismic hazard at the dam site can be characterized by performing a probabilistic seismic hazard analysis (PSHA). The output of the PSHA analysis is a suite of hazard curves. Each hazard curve provides the annual rate of exceedance for the pseudo-spectral acceleration at a given period. The hypothetical dam is located in Northern California and the hazard was run using the PSHA computer program HAZ-45 (Abrahamson, 2018) with a 2018 model for the seismic source and ground-motion characterization of the Sierra Mountain Region.

The results of the PSHA are summarized in Figure 7.3. Figure 7.3a shows a map view of the site, and includes the location of the hypothetical dam as well as five nearby sources that have the largest contribution to the hazard. Figure 7.3b shows the mean total hazard for the site, along with the hazard from each of the five nearby sources, at a period of T = 0.5 *s*. The seismic hazard from the five nearby sources makes up about 75% of the total hazard at a spectral acceleration of 1 *g* at this period. Figure 7.3c shows the same mean total hazard for the site with epistemic uncertainty. The epistemic uncertainty is characterized here by the 10^{th} and 90^{th} fractile curves. This epistemic uncertainty in the hazard comes from a logic tree with alternative models for the seismic source and ground-motion inputs. Figure 7.3d shows the uniform hazard spectrum (UHS) at a return period of 10,000 years. The uniform hazard spectrum is constructed by plotting the spectral acceleration at the 1E-4 hazard level from each hazard curve against the period for that hazard curve. In this example application the uniform hazard spectrum represents the target spectrum for ground-motion selection.

7.3.2 Ground-Motion Selection

The development of site-specific ground motions is informed by the seismic hazard analysis, and the selected ground motions are used as input motions to evaluate the response of the earthen dam. The selection criteria used depend on what ground-motion properties are important for the evaluation of the structure. For the case of evaluating an earthen dam for shear-induced deformations, important ground-motion properties include the intensity of shaking, the duration of shaking, and the frequency content of the ground motion. The selected ground motions should therefore have a hazard-consistent magnitude, distance, target spectrum shape, and target spectrum amplitude. The magnitude and distance both capture the duration of shaking, and the shape and amplitude of the target spectrum ensures that the selected ground motions have appropriate frequency content and intensity.

The deaggregation information for the example application indicates that the hazard at the 10,000-year return period is dominated by events with magnitudes from 6.5 to 6.75 at distances of about 5 *km*. The deaggregation results are consistent at short and long periods. These selection criteria, along with the shape of the UHS target spectrum are used to select the candidate ground motions. Ten records were selected, each with two horizontal components, for a total of twenty acceleration time histories. The magnitudes of the records range from 6.3 to 7.0 with a mean magnitude of 6.7 and the closest distance to the rupture ranges from 6.2 to 28.3 *km* with a mean distance of 13.3 *km*. Though the distances are somewhat larger than the desired distance, the duration added to the record by going out an additional 5 or even 15 *km* is not significant. The duration scales approximately as 0.05 x duration (in seconds) so going out an additional 5 or 15 *km* only adds 0.25 or 0.75 *s* to the record.

A single scale factor is then applied to both horizontal components from a given record, such that the geomean of the peak ground accelerations (PGA) matches the target spectrum. Finally, the horizontal components from a given record are spectrally matched as a pair, such that the geomean of the two horizontal components matches the target spectrum. This last step is different than the typical process of modifying each time history individually to match the target spectrum. Rather than modifying each time history to match the target, the set of horizontal components is modified together to satisfy two criteria. First, the recorded variability between the two horizontal components is maintained. Second, the geomean of the two horizontal components matches the target spectrum. The reason for maintaining the recorded variability between the two horizontal components is that this variability occurs in real earthquakes, but is not in the hazard calculations. Hazard is calculated with ground-motion models that provide the average horizontal ground motion, known as RotD50. Matching individual components to a target spectrum developed from average horizontal ground motions would suppress the real variability that we observe in records. Modifying ground motions so that the recorded variability between the two horizontal components is maintained and their geomean matches the target spectrum is consistent with RotD50 hazard and consistent with the observed variability between horizontal components. The spectral matching was performed using a modified version of the computer program RSPMatch (Abrahamson, 2019).

The modification of the recorded ground motions to develop site-specific ground motions is summarized in Figure 7.4. Figure 7.4a shows the response spectra for the two recorded horizontal components from one of the selected records. The record is from the Loma Prieta earthquake with a magnitude of 6.9 and a closest distance of 12.8 *km*. The response spectra shape is similar to the UHS target spectrum. Figure 7.4b shows the response spectra for the same two horizontal components after the time histories have been scaled and matched using the process described in the previous paragraph. Note that the variability (i.e., the vertical distance) between the two recorded horizontal components is approximately preserved between the two matched components at all periods. Figure 7.4c demonstrates that the geomean of the response spectra for the two modified time histories shown in Figure 7.4b matches the target spectrum. Figure 7.4d shows the response spectra for the twenty developed ground motions.

7.3.3 Incremental Dynamic Analysis

The developed ground motions were selected and modified based on the seismic hazard at the 10,000-year return period; however, to develop a deformation hazard curve, the intensities of the ground motions need to span the full range of expected ground motions, not just a single target level. Following the incremental dynamic analysis approach, the set of ground motions that were selected based on the target return level are scaled up and down to sample the full seismic hazard curve. A key assumption in incremental dynamic analysis is that the selection criteria used to select ground motions at the target return level are reasonably applicable to the rest of the hazard curve. Figure 7.5a-c demonstrates that the magnitude, distance, and target spectrum shape for the seismic hazard at this example application site do not change significantly from seismic hazard levels of 1E-1 to 1E-6.

The primary change in the expected ground motions going from 1E-1 to 1E-6 hazard is the epsilon of the ground motion. Figure 7.5d shows that the mean epsilon needed to exceed the ground motion at the 1E-2 hazard level is approximately 0, and at 1E-6 the mean epsilon is 3. An

epsilon of 0 corresponds to an average ground motion, and an epsilon of 3 corresponds to a very rare ground motion at three standard deviations above the mean. Because the primary change in the hazard curve is the epsilon of the ground motion, scale factors can be used to modify the set of ground motions developed for the 10,000-year return period so that they are applicable at other return periods. Fifteen scale factors were used to scale the ground motions up and down to sample the pseudo-spectral accelerations associated with seismic hazard ranging from 1E-1 to 1E-6.

Figure 7.6 shows the average spectral acceleration of the twenty time histories at each of the fifteen hazard levels, along with the spectral acceleration of the individual time histories. The average from each set is consistent with the hazard curve, while the range from the individual time histories represents the aleatory variability between the two horizontal components, which is not otherwise captured in the hazard. Note that the average is calculated from the log of the peak spectral acceleration.

The twenty time histories and fifteen scale factors are used to create 300 input ground motions for the dynamic analysis. For each of the 300 input ground motions, a transfer function is estimated using the transfer-function model, the average acceleration time history for a potential sliding mass is computed from the input ground motion and the transfer function, and shear-induced Newmark deformations are calculated. Two deformations are calculated for each time history – one for the standard polarity and one for the reverse polarity.

7.3.4 Deformation Hazard Calculation

The shear-induced deformation hazard is calculated by first selecting the deformation test values that span the x-axis of the deformation hazard curve. These deformations are denoted here as z, and for this example range from $z = 0.1$ *cm* to $z = 1000$ *cm*. Each of the 300 input ground motions from the incremental dynamic analysis is considered a possible earthquake that can occur at the dam site, and each resulting deformation is a possible deformation scenario of the dam. With 300 input ground motions and two possible polarities, there are 600 deformation scenarios. The annual rate of exceedance for the shear-induced Newmark deformation hazard is calculated from:

$$Haz(def > z) = \sum_{SC=1}^{SC=n} Rate_{SC} * P(def > z \mid TH, POL) \tag{7.1}$$

where $Rate_{SC}$ is the rate of occurrence of the deformation scenario and $P(def > z \mid TH,POL)$ is the conditional probability that the deformation exceeds the test value, given that the ground-motion time history occurs with a particular polarity of the average acceleration time history. The conditional probability that the deformation exceeds the test value for a given time history and polarity is calculated with a Heaviside step function equal to 1 if the estimated deformation is greater than or equal to z, and equal to 0 if the estimated deformation is less than z. The rate of occurrence of the deformation scenario is calculated from:

$$Rate_{SC} = Rate_{SA} * P(TH) * P(POL) \tag{7.2}$$

where $Rate_{SA}$ is the rate of occurrence of the spectral acceleration from the seismic hazard, $P(TH)$ is the probability of the time history, and $P(POL)$ is the probability of the positive or

negative polarity. In this example, the twenty developed time histories are treated as a uniform distribution such that $P(TH) = 1/20$ for each time history, and the positive and negative polarity of the average acceleration time history is treated as a uniform distribution such that $P(POL) = 1/2$ for each polarity. The marginal deformation hazard is summed up over all scenarios for each deformation test value, z. Note that what is typically calculated in seismic hazard is the rate of exceedance of the spectral acceleration, and what is needed in equation 7.2, $Rate_{SA}$, is the rate of occurrence of the spectral acceleration. This rate of occurrence can be calculated for each of the 15 target spectra by taking the difference between the rates of exceedance for UHS that would be located at the midpoint on either side of the target spectrum.

7.3.5 Epistemic Uncertainty in Deformation Hazard

The inputs used to characterize the earthen dam in the shear-induced deformation hazard calculation include the average shear-wave velocity of the dam and the yield coefficient of the sliding mass. Additionally, the transfer-function model can be run with different nonlinear models to describe the shear-modulus reduction and material damping properties of the dam. The suite of input ground motions and their associated rates of occurrence from the PSHA constitute the inputs needed to characterize the seismic hazard for the deformation hazard calculation. Each of these inputs has uncertainty, leading to uncertainty in the deformation hazard curve. A sensitivity analysis was carried out to examine how the deformation hazard curve changes with different inputs. The baseline case uses an average shear-wave velocity of 800 *ft/s*, a yield coefficient of 0.10, the nonlinear behavior based on Darendeli (2001) PI=20 with the Yee et al. (2013) adjustment (referred to as "more nonlinear"), and the developed ground motions scaled to the mean seismic hazard.

Figure 7.7 presents the change in the deformation hazard curve when these inputs are varied. As shown in Figure 7.7a, the impact on the deformation hazard curve is small when the average shear-wave velocity of the dam is changed from 600 *ft/s*, to 800 *ft/s*, to 1000 *ft/s*. The average shear-wave velocity of the dam is used to calculate the estimated small-strain fundamental period of the dam, T_o, and influences how the dam period shifts and the damping increases with increasing ground-motion intensity, but the applied range of shear-wave velocities leads to significant overlap in the estimated deformations, and ultimately very similar deformation hazard curves.

As shown in Figure 7.7b, the impact on the shear-induced deformation hazard curve is notable when the yield coefficient is changed from 0.08, to 0.10, to 0.12. Note that changing the yield coefficient does not impact the transfer-function model. The estimated average acceleration time histories for all earthquake scenarios are the same, but the threshold for shear-induced movement used in the Newmark procedure is changed, leading to different deformations. The entire deformation hazard curve shifts to the right as the yield coefficient is reduced, reflecting a lower threshold for shear-induced movement and resulting in larger accumulated deformations.

Figure 7.7c compares the deformation hazard curves when the transfer-function model is run with the adjustment for the Vucetic and Dobry (1991) PI=30 nonlinear curves (referred to as "less nonlinear"). When the nonlinear properties of the dam are less nonlinear, the deformation hazard is higher compared to the deformation hazard based on more nonlinear behavior. This is caused by differences in the dam period shift and differences in damping between the two

nonlinear models. Figure 7.8b compares the average transfer function for the ground motions scaled to the UHS at 1E-4 for each of the nonlinear models. The corresponding first-mode period is annotated on the UHS in Figure 7.8a. When the transfer-function model is run with less nonlinearity, the transfer function is centered at a period of the ground motion with higher amplitudes, leading to larger estimated deformations. The average transfer function with less nonlinearity also has lower damping which results in more amplification, also contributing to the larger estimated deformations.

Figure 7.7d compares the deformation hazard curves when the seismic hazard at the site is characterized by different fractile curves. When a different seismic hazard curve is utilized, the change to the calculation of the deformation hazard is that the developed ground motions are scaled to the pseudo-spectral accelerations associated with the seismic hazard range of interest for the new hazard curve. As shown in Figure 7.7d, the epistemic uncertainty in the seismic hazard has a large impact on the deformation hazard. For instance, at a deformation of 100 *cm*, there is a factor of 18 difference in the deformation hazard between the analyses utilizing the seismic hazard at the 10^{th} and 90^{th} fractiles.

7.3.6 Alternative Deformation Hazard Curves

To quantify the uncertainty in the shear-induced deformation hazard associated with the inputs described above, a logic tree is used to describe the range of possible values for each input parameter. The logic tree for these inputs is relatively simple with only four nodes used to capture the uncertainty in the average shear-wave velocity of the dam, yield coefficient of the sliding mass, nonlinearity of the dam materials, and seismic hazard. Weights are assigned to each branch of the logic tree, and the branch weights at each node must sum to unity. The weights on the branches of the log tree reflect scientific judgment in the relative merit of each input or alternative model due to limited data. The weights used in this example are for illustrative purposes – more work is necessary to robustly assess the uncertainties and assign logically consistent weights.

There is no correlation between branches on the logic tree, resulting in fifty-four possible alternative deformation hazard curves. Figure 7.9 describes the logic tree used to quantify the epistemic uncertainty in the deformation hazard for the hypothetical dam and Figure 7.10 shows the resulting alternative deformation hazard curves along with the mean deformation hazard. The mean deformation at a return period of 10,000 years is approximately 75 *cm*. The uncertainties in the deformation hazard for the hypothetical dam are substantial – at this same mean deformation of 75 *cm*, the return period could be anywhere from 5,000 years to 500,000 years based on which alternative hazard curve is correct.

7.3.7 Comparison with Bray and Travasarou (2007)

In addition to the uncertainties in the dam properties and seismic hazard, there is uncertainty in the simplified model used to calculate the deformations. The deformation hazard curve calculated from the transfer-function model is compared with a deformation hazard curve calculated from the simplified procedure by Bray and Travasarou (2007). The comparison is made with the transfer-function model adjusted for less nonlinear behavior based on the Vucetic

and Dobry (1991) PI=30 curves, as these curves were also utilized in the analyses performed by Bray and Travasarou (2007).

To implement the Bray and Travasarou (2007) model, the annual rate of exceedance for the shear-induced deformation hazard is calculated from:

$$Haz(def > z) = \sum_{SA=1}^{SA=n} Rate_{SA} * P(def > z \mid SA) \tag{7.3}$$

where $Rate_{SA}$ is the rate of occurrence of the ground motion from the seismic hazard and $P(def > z \mid SA)$ is the conditional probability that the deformation exceeds the test value, given that the spectral acceleration occurs. This conditional probability follows a log normal distribution and utilizes the median displacement and the standard deviation of that displacement provided by the model. For this application, the median displacement was scaled by the probability that the displacement was not negligible (i.e., multiplied by $1–P(D=0)$). A single magnitude of 6.7 was used to estimate the median displacement at all ground motion intensity levels, which is consistent with the incremental dynamic analysis approach. The marginal deformation hazard is summed up over all spectral acceleration levels for each deformation test value, z.

As shown in Figure 7.11, the Bray and Travasarou (2007) model leads to a higher estimate of deformation hazard compared to the transfer-function model. The difference in deformation hazard comes primarily from differences in the estimated deformations. Figure 7.12 compares the deformations estimated by each model. The Bray and Travasarou (2007) model provides an estimate of the median deformation and the standard deviation of that deformation, which is a constant 0.66 natural log units. In this application of the transfer-function model, standard and reverse polarity deformations are estimated for each of the 300 input ground motions, resulting in a distribution of deformations across the range of intensities.

Differences in the models include one-dimensional analyses using a fully coupled stick-slip sliding model in Bray and Travasarou (2007) versus two-dimensional finite-element analyses using a decoupled approximation in the transfer-function model. Additionally, the variability in the Bray and Travasarou (2007) deformations (represented by the standard deviation) is largely a reflection of the variability in their ground motion database, while the variability in the transfer-function model deformations is a reflection of the variability in the ten hazard-consistent ground motions, the variability between horizontal components of those motions, and the variability between the standard and reverse polarity of each motion. More work is needed to fully explain the difference in deformations estimated from the two models.

7.4 Conclusions

The transfer-function model was used to perform a deterministic shear-induced deformation analysis with a single ground motion, followed by a series of deterministic analyses that demonstrate the behavior of the model with increasing ground-motion intensity. The transfer-function model was then used to perform a probabilistic deformation hazard analysis. Site-specific ground motions were developed with an approach that produces a set of ground motions

that are consistent with RotD50 seismic hazard and preserves the observed aleatory variability between horizontal components.

In the probabilistic example application, the transfer-function model was applied using the incremental dynamic analysis approach to run simplified dynamic analyses and calculate deformation hazard. For cases where the key assumptions of incremental dynamic analysis are not met (e.g., when the seismic hazard is split between very different sources), the transfer-function model can be applied to a suite of ground motions developed using conditional-spectrum based approaches (e.g., Baker, 2011; Arteta and Abrahamson, 2019).

The transfer-function model is efficient enough to run hundreds of simplified dynamic analyses, and repeat these analyses for all paths on a logic tree to quantify the epistemic uncertainty in the deformation hazard. Quantifying the epistemic uncertainty is a critical component to characterizing the deformation hazard for an earthen dam. When the analysis is limited to best-estimate inputs and the resulting deformation hazard curve is used to make dam safety decisions and prioritize resources without characterizing the epistemic uncertainty, decisions are made based on the magnitude of the engineering judgments that went into deciding the inputs, without regard for the reliability of those input values. When the epistemic uncertainty in the deformation hazard is quantified and shown, decision makers can base decisions on the mean hazard as well as the range in the hazard, and consider whether or not the current state of knowledge supports the decision at hand.

The probabilistic deformation hazard analysis presented here can be extended to a portfolio of dams. The dams in the portfolio can be grouped based on the earthquake scenarios that dominate the hazard at the site, such that ground motions do not need to be selected for each dam individually. Instead, sites with similar ground-motion selection criteria, like magnitude and distance, can utilize the same set of selected ground motions, and those motions can be scaled for each dam site to generate a set of site-specific ground motions. When used to calculate deformation hazard for a portfolio of dams, the transfer-function model provides a consistent approach that provides a basis for comparisons.

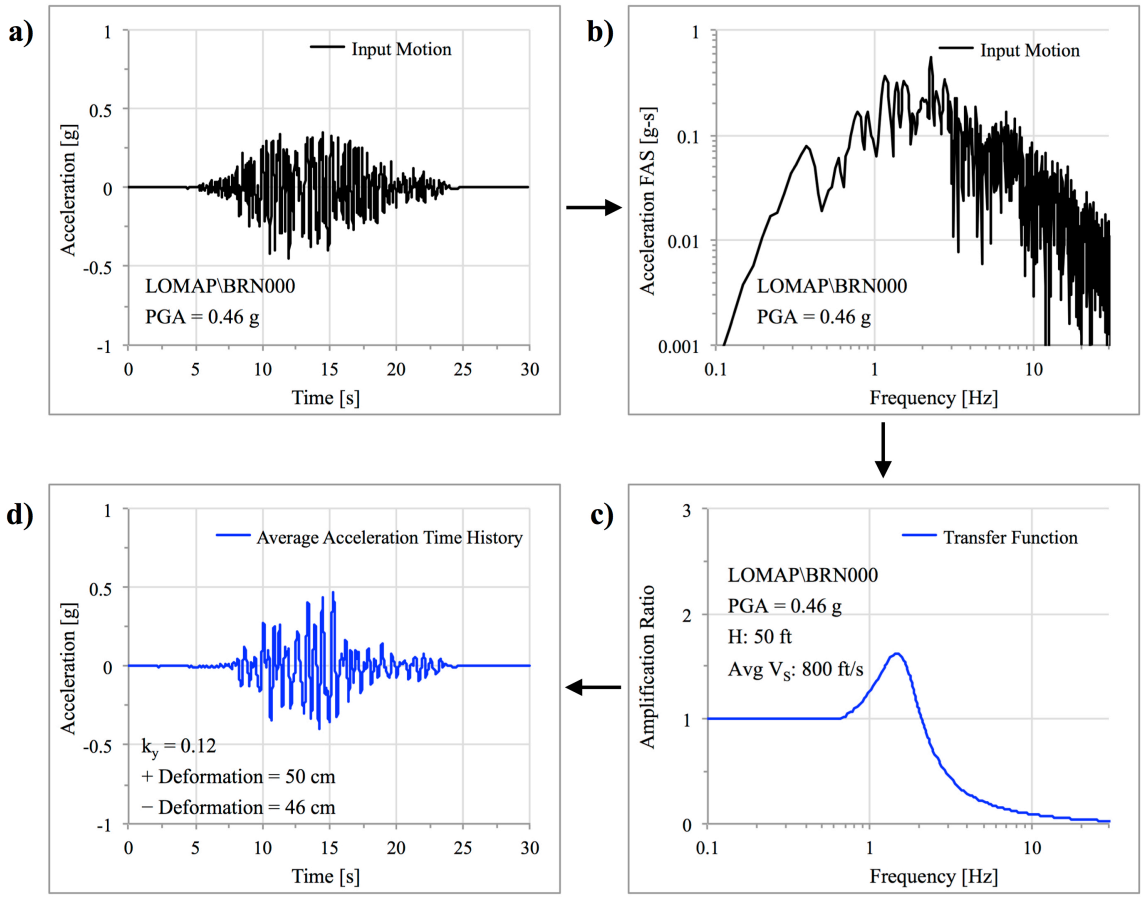

Figure 7.1 **Illustration of transfer-function model applied to a ground motion to estimate an average acceleration time history for a potential sliding mass and calculate Newmark deformations.**

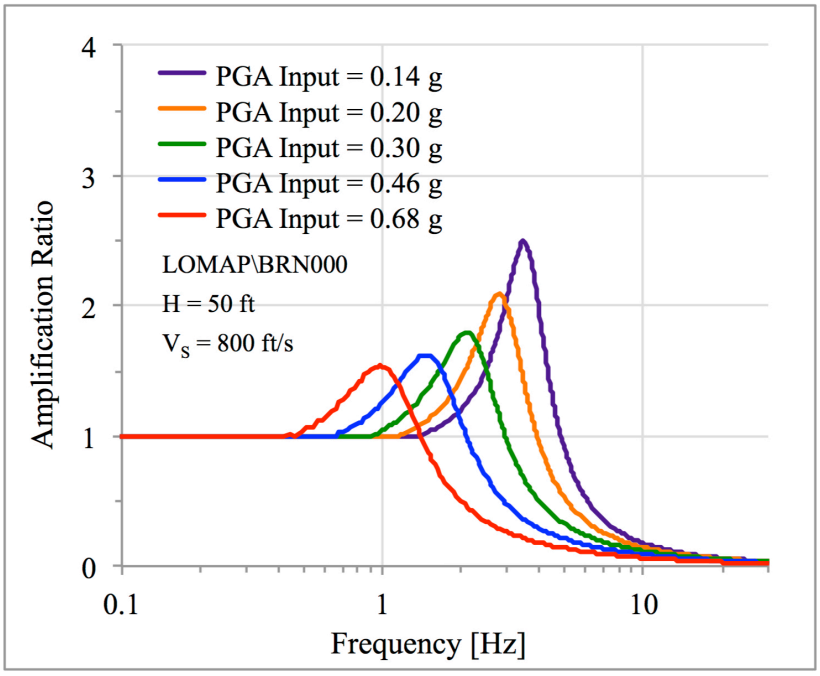

Figure 7.2 **A single input ground motion is scaled up and down to illustrate the shift in the natural period and an increase in damping that occurs with the transfer-function model when the ground-motion intensity increases.**

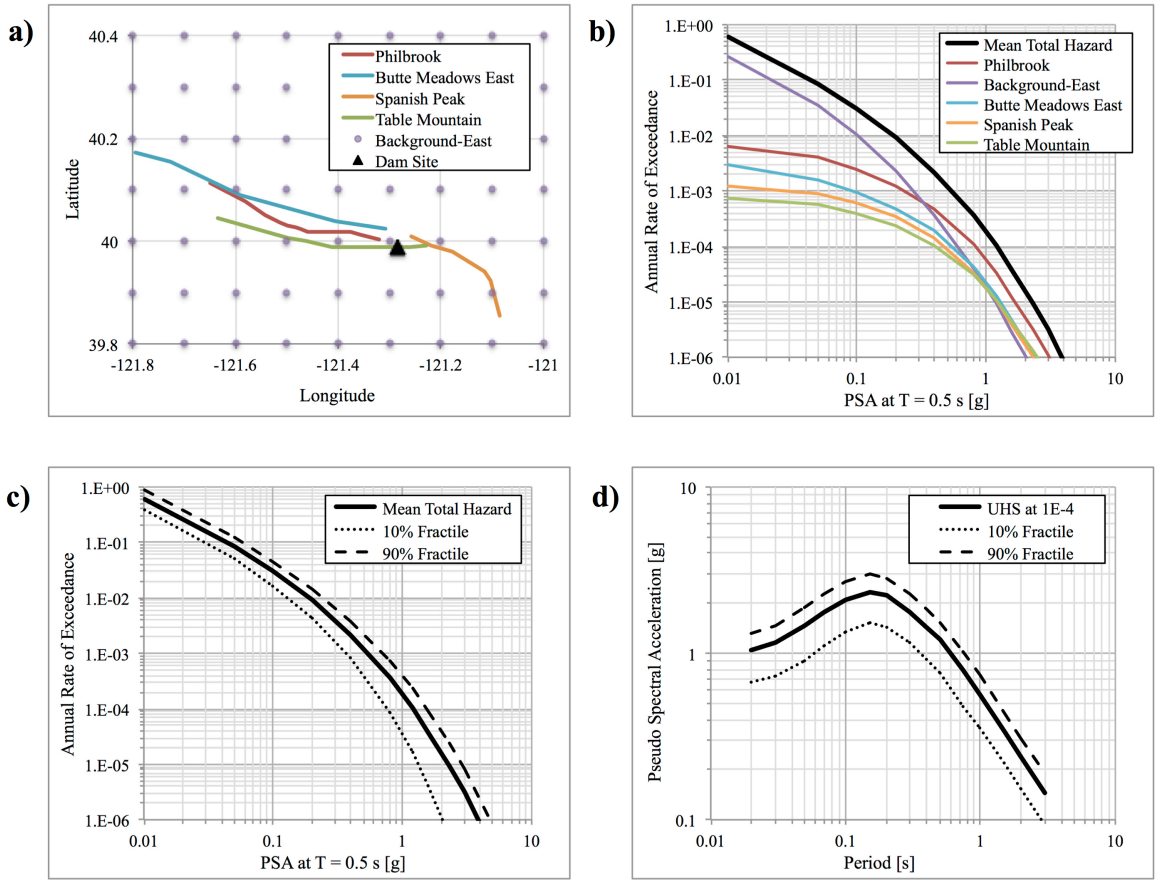

Figure 7.3 **Summary of probabilistic seismic hazard analysis for hypothetical dam site including a) map view of site with nearby sources, b) hazard curves, c) fractiles, and d) uniform hazard spectra.**

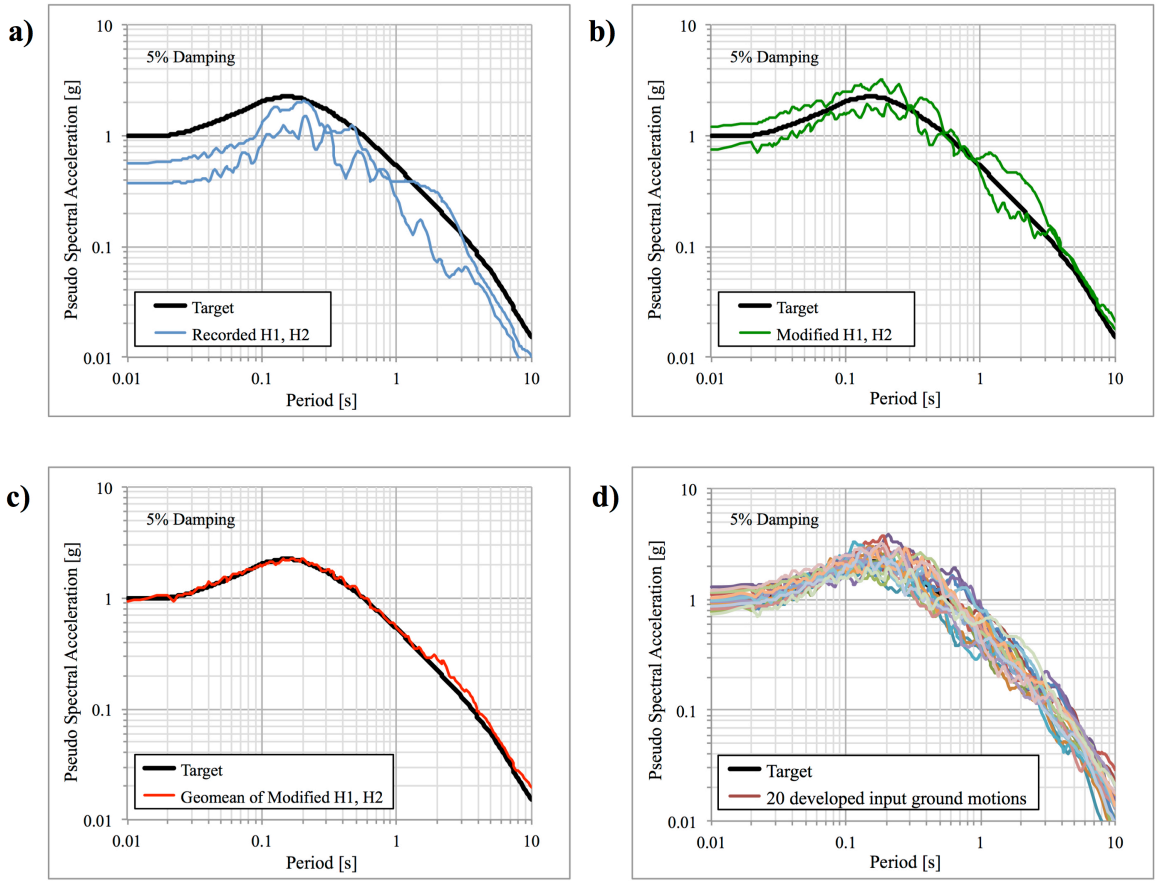

Figure 7.4 **Example of matching horizontal components as a pair to maintain variability between components: a) as-recorded horizontal motions, b) after scaling and matching, c) geomean of modified records matches target, and d) response spectra for all developed ground motions.**

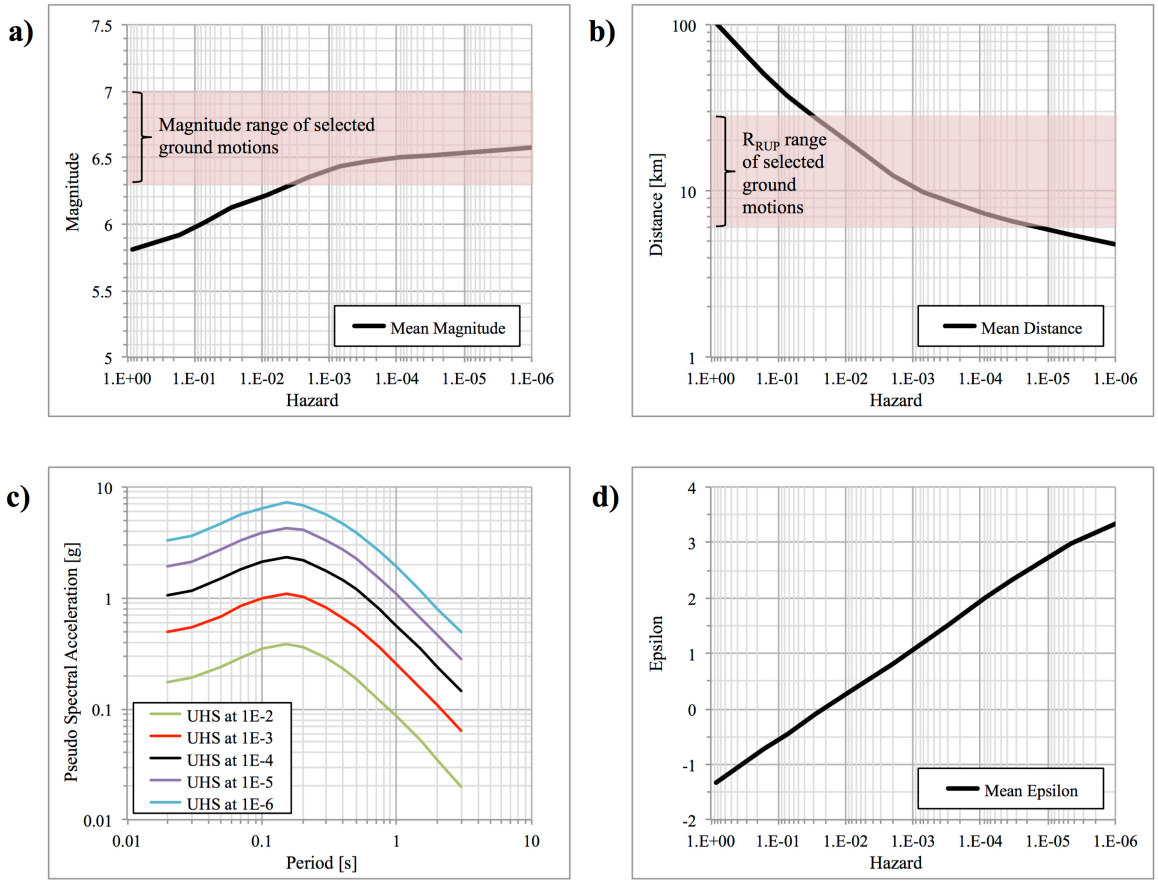

Figure 7.5 **Mean magnitude (a), mean distance (b), spectral shape (c), and mean epsilon (d) from probabilistic seismic hazard analysis.**

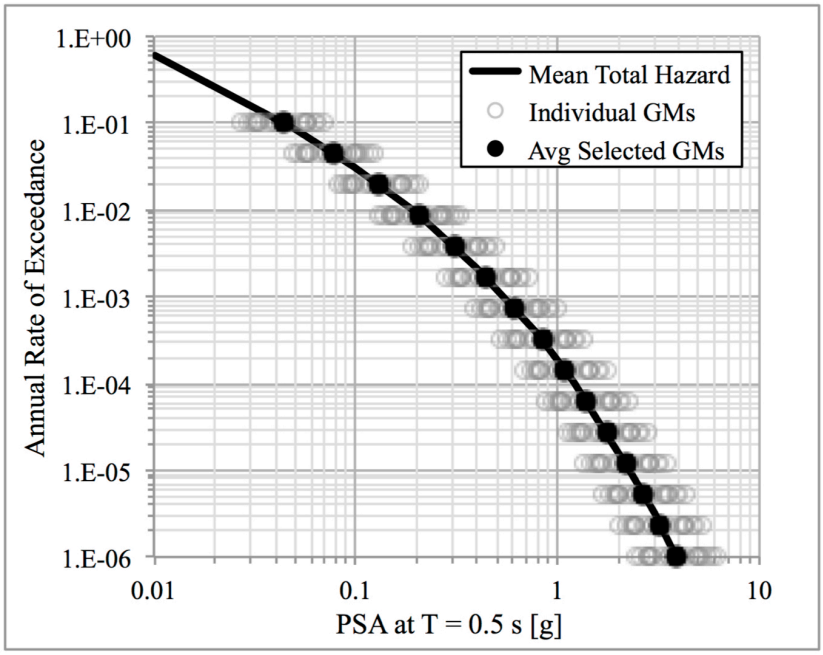

Figure 7.6 **Individual and average spectral accelerations of the twenty time histories at each of the fifteen hazard levels.**

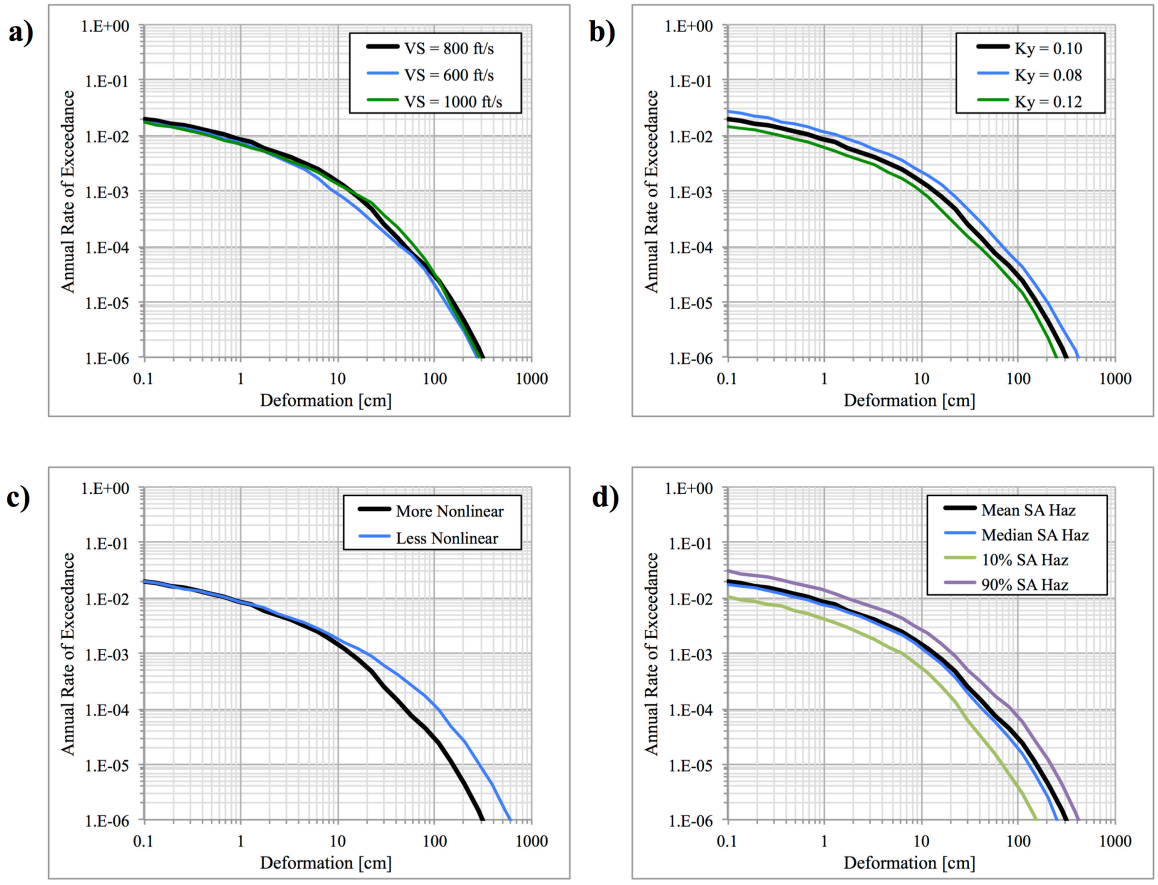

Figure 7.7 **Sensitivity of deformation hazard to a) average shear-wave velocity of dam, b) yield coefficient of dam, c) nonlinear behavior of dam materials, and d) epistemic uncertainty of seismic hazard.**

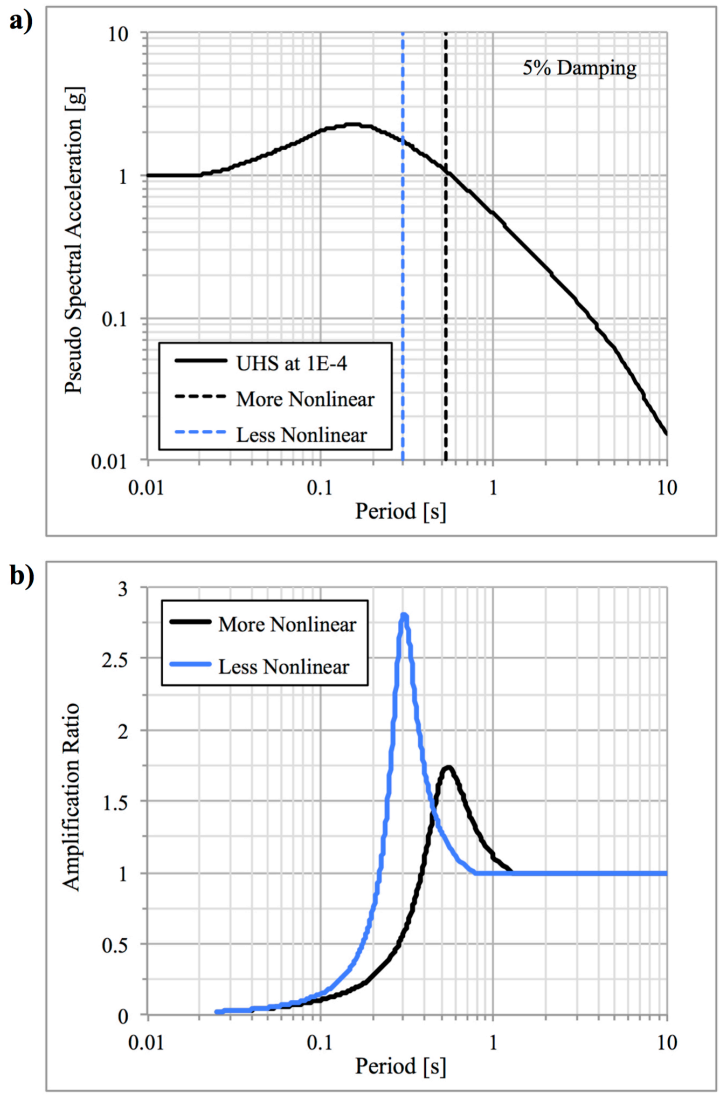

Figure 7.8 **Comparison of transfer function from different nonlinear models used in deformation hazard sensitivity: a) uniform hazard spectrum at 1E-4 annotated with T_1 of average transfer function, and b) average transfer function from each nonlinear model for the ground motions scaled to the UHS 1E-4 level.**

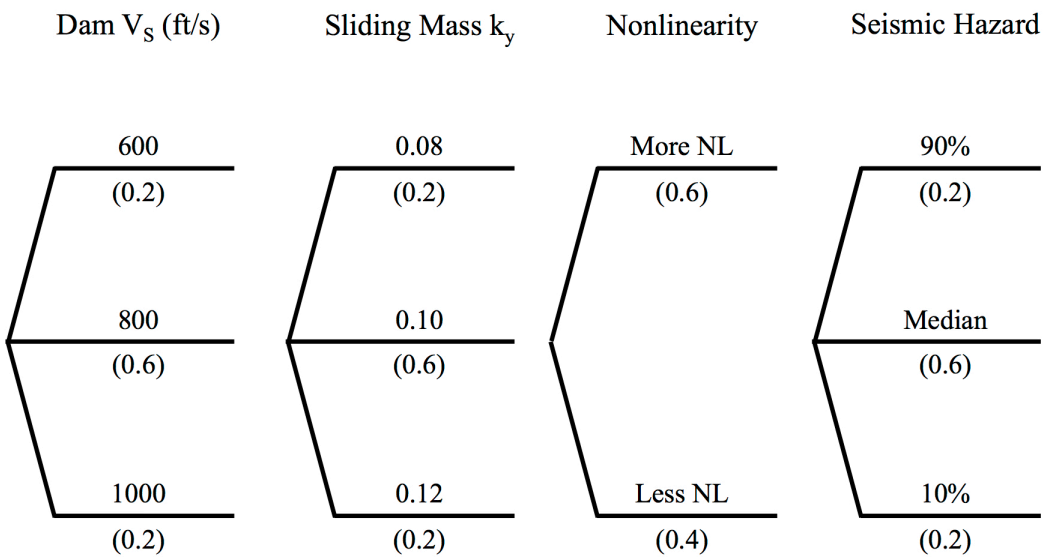

Figure 7.9 **Logic tree illustrating epistemic uncertainty in deformation hazard inputs.**

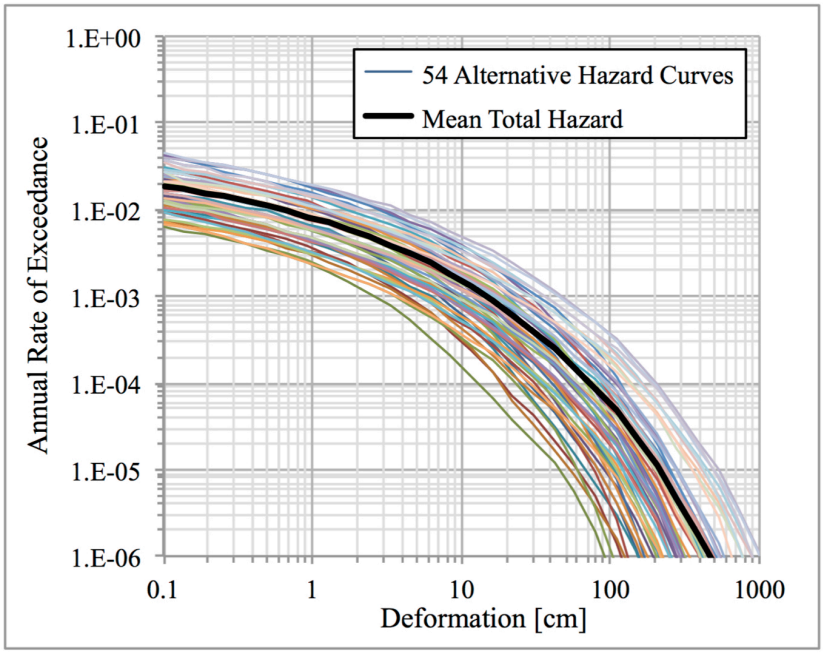

Figure 7.10 **Alternative deformation hazard curves and mean total deformation hazard from logic tree.**

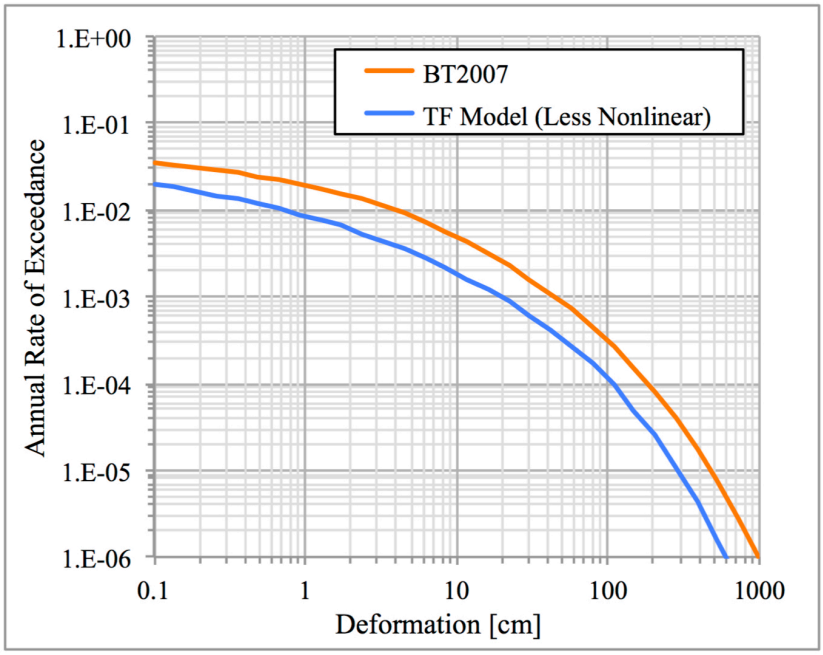

Figure 7.11 **Comparison of deformation hazard curves when deformations are estimated from transfer-function model and Bray and Travasarou (2007) simplified procedure.**

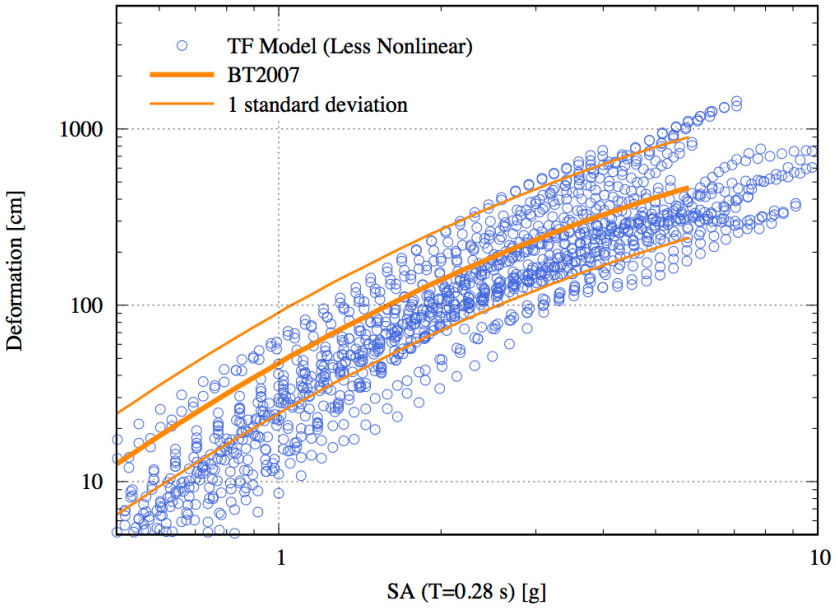

Figure 7.12 **Comparison of deformations estimated from transfer-function model and Bray and Travasarou (2007) simplified procedure.**

8 CONCLUSIONS

8.1 Summary and Conclusions

The aim of this work was to develop a simplified method to estimate shear-induced deformations for earthen dams that maximizes information about the input ground motion. The developed model estimates the transfer function for a potential sliding mass of an earthen dam, which is applied to the input ground motion to estimate the time history of average acceleration for the potential sliding mass and calculate a shear-induced Newmark deformation. Application of the transfer-function model utilizes the de-coupled approach to accommodate the full description of an input ground motion.

The modeled transfer functions, which are a simplification of the transfer functions extracted from a series of two-dimensional equivalent-linear dynamic analyses, capture the key mechanisms through which nonlinearity affects soil behavior, including dam period shift and damping increase. The functional form of the model defines the transfer function at all frequencies, and allows for adjustments of the nonlinear behavior.

The model is an ideal tool for performing simplified dynamic analyses for dams whose materials are not well-characterized or the state-of-knowledge of the as-built condition is limited, because the model relies on relatively simple parameters like the dam height and an estimate of the shear-wave velocity of the embankment materials. When used with the results of probabilistic seismic hazard analyses, the transfer-function model addresses the need to perform site-specific deformation hazard analyses for a large number of dams with a consistent methodology that provides a basis for comparisons between dams. Moreover, use of the transfer-function model with probabilistic seismic hazard analyses (which are based on simplified models of the seismic sources and ground motions) maintains a similar level of detail between the ground motion and dam response.

The modeled transfer functions are recognized as a simplification of the complex process of how soil systems respond to dynamic loading, and the simplified dynamic analyses are not intended to replace sophisticated dynamic analyses. Instead, the transfer-function model provides a rational approach for performing hundreds of simplified dynamic analyses to gain insights, calculate deformation hazard curves, and quantify epistemic uncertainty.

8.2 Future Work

8.2.1 Expansion of Transfer-Function Model

Dynamic analyses were performed with a deep failure surface and a shallow failure surface, but only the deep failure surface results were used to develop the transfer-function model. Future work can expand the model for the shallow failure surface. Preliminary results indicate that the model can be adjusted for the shallow failure surface by increasing alpha to reflect stronger amplification that occurs in the upper half of the dam, where the shallow failure surface is located. Thought should also be given to how the estimated deformations from different failure surfaces are used to calculate deformation hazard curves for a dam. Do the different failure surfaces represent aleatory variability, epistemic uncertainty, or something else?

In Chapter 5, the equivalent-linear dynamic analyses were repeated with two additional nonlinear models for a single representative dam. Adjustments to the transfer-function model to reflect the nonlinearity by Vucetic and Dobry (1991) for PI=30 are recommended based on these results. Future work includes running the dynamic analyses with the Vucetic and Dobry (1991) PI=30 nonlinear model for all representative dams to better constrain the recommended adjustments when applied to other dam heights and shear-wave velocity profiles.

With the equations and coefficients in Chapter 4 and the adjustments to the model presented in Chapter 5, the transfer-function model can be applied with two different nonlinear models – one with more nonlinearity based on Darendeli (2001) PI=20 with the Yee et al. (2013) procedure and one with less nonlinearity based on Vucetic and Dobry (1991) PI=30. Future work includes performing dynamic analyses for additional nonlinear models that represent the center, body, and range of credible nonlinear models so that the transfer-function model can be run with various adjustments to characterize the epistemic uncertainty in the nonlinear behavior of earthen dams. Where recordings from high intensity ground motions at earthen dams are available, future work should also aim to tie the shift in the natural period of the dam observed empirically to the different nonlinear models.

8.2.2 Calibration with Advanced Analyses

The transfer-function model is based on the results from dynamic analyses using the equivalent-linear procedure. Many of the dynamic analyses used to develop the transfer-function model resulted in effective shear strains that exceed the typical range where the equivalent-linear procedure is considered applicable. Future work includes running dynamic analyses for the representative dams and ground motions using fully nonlinear methods to calibrate the model for high intensity ground motions where the induced shear strains are large. The advanced analyses also provide an opportunity to identify and address other shortcomings of the simplified approach.

Exploratory research was conducted in collaboration with Kleinfelder Inc. and Pacific Gas and Electric Company where thirty ground motions were propagated through the representative dam with a height of 100 *ft* using the computer program FLAC Version 8.0 (Itasca Consulting Group, Inc., 2016). The following issues, questions, and areas for future research were identified:

- What is the desired deformation from the nonlinear analysis? Consider deformations at the crest on the upstream side (x and y direction), a maximum deformation at any location in the dam (x and y direction), and others.
- Will the desired deformation be used to evaluate freeboard or does it represent a performance metric? The answer to this question has implications on the fragility curves and their compatibility with the desired deformation.
- What is missed by using the de-coupled approach and Newmark procedure? When the shear-induced deformations from the transfer-function model are combined with volumetric-induced deformations from an appropriate simplified procedure (e.g., Tokimatsu and Seed, 1987), how do these deformations compare to the nonlinear deformations?
- What deformation from the nonlinear analysis provides the best point of comparison to the Newmark deformation from the transfer-function model? How should the two Newmark deformations from the standard and reverse polarity be combined or handled for the comparison?
- When ground motions span the full range of intensities, how does the scaling of the nonlinear deformations with ground-motion intensity compare to the scaling of the transfer-function model deformations?
- When multiple ground motions have the same intensity level, how does the standard deviation of those deformations from the nonlinear analysis compare to the standard deviation of deformations estimated from the transfer-function model? Are the nonlinear deformations more or less sensitive to details of the input ground motion?

Future research should aim to answer these questions and provide recommendations on calibrating the transfer-function model or applying a correction for identified biases. Early results indicate that the deformations from the transfer-function model compare well with the deformations from the nonlinear analysis at the crest in the x direction, but are biased low compared to the deformations at the crest in the y direction and the maximum deformations in the body of the dam (presumably due to missing the volumetric-induced component). The scaling of the deformations from the transfer-function model with ground-motion intensity is very similar to the scaling from the nonlinear results. The comparison is not worse for high-intensity ground motions, indicating that the equivalent-linear approach is acceptable for this application despite the large induced strains. Finally, early results point to the nonlinear deformations being less sensitive to details of the input ground motion. This is potentially due to the transfer-function model applying the same nonlinear behavior to the entire time history, rather than the dam experiencing a shift from small-strain nonlinear behavior to large-strain nonlinear behavior throughout the duration of shaking. Future work on an improved version of the transfer-function model should consider if a broader transfer function (the width of the transfer function in frequency) produces deformations that are less sensitive to details of the input ground motion, consistent with the nonlinear results.

8.2.3 Probabilistic Deformation Hazard Analysis and Risk

With additional work, the transfer-function model can be directly incorporated into a deformation hazard analysis, where the probability of exceeding a deformation is estimated for every earthquake scenario. For this implementation, each earthquake scenario in the probabilistic

seismic hazard analysis would be described by a model of its amplitude and phase. The transfer-function model would then be applied with the Newmark procedure using random vibration theory to calculate the probability of exceeding a given deformation. This methodology would eliminate the need to select time histories. An empirical model for Fourier amplitude spectra using the NGA-West2 database was recently developed by Bayless and Abrahamson (2018) and could be used in this application to describe the ground-motion amplitudes. A random phase model over a time duration related to earthquake size and propagation distance (i.e., Boore, 1983) could be used to describe the ground motion phase. A phase derivative model that can accommodate directivity (i.e., Baglio, 2017) can also be utilized in this application.

In Chapter 7, the epistemic uncertainty in the deformation hazard included alternative inputs or models for the shear-wave velocity of the dam, yield coefficient of the sliding mass, nonlinear behavior of the dam, and seismic hazard at the site. In addition to these uncertainties, there is uncertainty in the simplified model used to calculate the deformations. Similar to using multiple ground-motion models to capture the epistemic uncertainty in the ground-motion estimates for seismic hazard, alternative deformation models should be used to capture the epistemic uncertainty in the deformation estimates for deformation hazard. A deformation hazard curve was computed using the Bray and Travasarou (2007) model as an example of this epistemic uncertainty. These results and the resuts from additional alternative deformation models should be utilized and incorporated on the logic tree.

Preliminary implementation of alternative deformation models shows that the shear-induced deformations estimated from the transfer-function model are lower than those estimated from other simplified methods. Other studies (Saygili and Rathje, 2008) have similarly found significant differences between the deformations estimated from various simplified procedures (Bray and Travasarou, 2007; Jibson, 2007; Watson-Lamprey and Abrahamson, 2006), though these comparisons have focused on the rigid sliding block case. One of the main differences between the transfer-function model and alternative deformation models is that the transfer-function model is not a simplified procedure with proxies for the ground motion and dam, but rather a way to run a simplified dynamic analysis with the full description of the ground motion and proxies to help describe the nonlinear behavior of the dam. Additionally, the transfer-function model is based on the results of 2D earthen dams, rather than 1D soil columns, and utilizes the de-coupled approximation, rather than the more complete coupled response interaction. It is important to understand the differences in the alternative deformation models and how these differences impact the estimated deformations. More work is needed to fully understand these differences and future research should compare the deformation hazard curves generated from the alternative deformation models with a focus on explanations for the resulting differences.

Finally, the transfer-function model was used with a probabilistic seismic hazard analysis and the incremental dynamic analysis approach to calculate deformation hazard curves. Characterizing the seismic performance of a dam by computing the deformation hazard is a significant improvement over the seismic hazard alone or using the seismic hazard and a qualitative assessment of dam response. The probabilistic deformation hazard approach also provides a framework for identifying and combining aleatory variability and epistemic uncertainty for a more complete picture of the deformation hazard. To move to risk, fragility curves relating the deformation of the dam to the probability of a damage state are needed.

Development of a family of fragility curves for use with earthen dams is an area for future research.

REFERENCES

Abrahamson, N. A. (2018). PSHA computer program, HAZ-45.

Abrahamson, N. A. (2019). Spectral matching computer program, RSPMatch.

Abrahamson, N. A., Silva, W. J., and Kamai, R. (2014). Summary of the ASK14 ground motion relation for active crustal regions, *Earthq. Spectra*, 30(3): 1025-1055.

Al Atik, L., Abrahamson, N., Bommer, J. J., Scherbaum, F., Cotton, F., and Kuehn, N. (2010). The variability of ground-motion prediction models and its components, *Seismological Research Letters*, 81(5): 794–801.

Ambraseys, N. N. (1960). On the shear response of a two-dimensional truncated wedge subjected to an arbitrary disturbance, *Bull. Seism. Soc. Am.*, 50(1): 45-56.

AMEC Geomatrix, Inc. (2011). Anderson Dam seismic stability evaluation report. Prepared for Santa Clara Valley Water District. *Consulting Report*.

Ancheta, T. D., Darragh, R. B., Stewart, J. P., Seyhan, E. Silva, W. J., Chiou, B. S.-J., Wooddell, K. E., Graves, R. W., Kottke, A. R., Boore, D. M., Kishida, T., and Donahue, J. L. (2014). NGA-West2 Database, *Earthq. Spectra*, 30(3): 989-1005.

Armstrong, R. J. (2017). Relationship between earthquake ground motion intensity measures and embankment dam deformations. *Proceedings of Strong Motion Instrumentation Program (SMIP) 2017 Seminar on Utilization of Strong Motion Data*, Berkeley, CA.

Arteta, C. A. and Abrahamson, N. A. (2019). Conditional Scenario Spectra (CSS) for Hazard-Consistent Analysis of Engineering Systems. *Earthq. Spectra*, 35(2): 737-757.

Baglio, M., Abrahamson, N., and Cimellaro, G. P. (2017). Stochastic ground motion method combining a Fourier amplitude spectrum model from a response spectrum with application of phase derivatives distribution prediction. *Master's thesis*. University of California, Berkeley.

Baker, J. W. (2011). Conditional mean spectrum: tool for ground-motion selection. *Journal of Structural Engineering*, 137(3): 322-331.

Bayless, J. and Abrahamson, N. A. (2018). An Empirical Model for Fourier Amplitude Spectra using the NGA-West2 Database, *PEER Report No. 2018/07*, Pacific Earthquake Engineering Research Center, University of California, Berkeley, CA.

Beroza, G. C. (1991). Near-source modeling of the Loma Prieta earthquake; evidence for heterogeneous slip and implications for earthquake hazard, *Bull. Seism. Soc. Am.*, 81(5): 1603–1621.

Boore, D. M. (1983). Stochastic Simulation of High-frequency Ground Motions Based on Seismological Models of the Radiated Spectra. *Bull. Seism. Soc. Am.*, 73: 1865—1894.

Boore, D. M., Stewart, J. P., Seyhan, E., and Atkinson, G. M. (2014). NGA-West2 equations for predicting PGA, PGV, and 5% damped PSA for shallow crustal earthquakes, *Earthq. Spectra*, 30(3): 1057–1085.

Branum, D., Chen, R., Petersen, M., and Wills, C. (2016). Earthquake Shaking Potential for California. *California Geological Survey*, Map Sheet 48.

Bray, J. D. and Macedo, J. (2019). Procedure for estimating shear-induced seismic slope displacement for shallow crustal earthquakes. *J. Geotech. Geoenviron. Eng.*, 145(12): 04019106.

Bray, J. D., Macedo, J., and Travasarou, T. (2018). Simplified procedure for estimating seismic slope displacements for subduction zone earthquakes. *J. Geotech. Geoenviron. Eng.*, 144(3): 04017124.

Bray, J. D. and Rathje, E. R. (1998). Earthquake-induced displacements of solid-waste landfills. *J. Geotech. Geoenviron. Eng.*, 124(3): 242-253.

Bray, J. D. and Travasarou, T. (2007). Simplified procedure for estimating earthquake-induced deviatoric slope displacements. *J. Geotech. Geoenviron. Eng.*, 133(4): 381-392.

Brune, J. (1970). Tectonic stress and spectra of seismic shear waves from earthquakes, *J. Geophys. Res.*, 75: 4997-5009.

Cameron, W. I. (1996). U.S. Army Engineer Waterways Experiment Station (WES) data, *US Army Corps of Engineers,* NUREG/CR-5741.

Campbell, K. W. and Bozorgnia, Y. (2014). NGA-West2 ground motion model for the average horizontal components of PGA, PGV, and 5% damped linear acceleration response spectra, *Earthq. Spectra*, 30(3): 1087–1115.

Chiou, B. S.-J. and Youngs, R. R. (2014). Update of the Chious and Youngs NGA model for the average horizontal component of peak ground motion and response spectra, *Earthq. Spectra*, 30(3): 1117–1153.

Conkle, C. (2017). Stability Analysis of a Concrete-Faced Rockfill Dam using Parametric Evaluations. *United States Society on Dams (USSD) Annual Conference and Exhibition*, Anaheim, California.

Darendeli, M. B. (2001). Development of a new family of normalized modulus reduction and material damping curves, *Ph. D. dissertation*, The University of Texas at Austin.

Division of Safety of Dams (2018). Dams within jurisdiction of the state of California: dams listed alphabetically by dam name. September, 2018.

Du, W., Wang, G., and Huang, D. (2018). Evaluation of seismic slope displacements based on fully coupled sliding mass analysis and NGA-West2 database, *J. Geotech. Geoenviron. Eng.*, 144(8): 06018006.

East Bay Municipal Utility District (2008). Seismic Stability Evaluation Report Central Reservoir Main Dam, Oakland, California.

Federal Emergency Management Agency (2005). Federal Guidelines for Dam Safety: Earthquake Analyses and Design of Dams (FEMA-65). May 2005.

Foster, M., Feel, R., and Spannagle, M. (2000). The statistics of embankment dam failures and accidents. *Canadian Geotechnical Journal*, 37: 1000-1024.

GEO-SLOPE International, Ltd. (2008). Stability Modeling with SLOPE/W 2007, GEO-SLOPE International Ltd., Calgary, Alberta, Canada.

Hadidi, R., Moriwaki, Y., Barneich, J., Kirby, R., and Mooers, M. (2014). Seismic deformation evaluation of Lenihan Dam under 1989 Loma Prieta Earthquake. *Tenth U.S. National Conference on Earthquake Engineering*, Frontiers of Earthquake Engineering.

Harder, L. F. (1991). Performance of earth dams during the loma prieta earthquake. *Second International Conference on Recent Advances in Geotechnical Earthquake Engineering and Soil Dynamics*, 2: 1613-1628, St. Louis, Missouri.

Harder, L. F., Bray, J. D., Volpe, R. L., and Rodda, K. V. (1998). Performance of Earth Dams During Loma Prieta Earthquake. *The Loma Prieta, California, Earthquake of October 17, 1989 – Earth Structures and Engineering Characterization of Ground Motion*. 3-26.

Hartzell, S. H., Stewart, G. S., and Mendoza, C. (1991). Comparison of L_1 and L_2 norms in a teleseismic waveform inversion for the slip history of the Loma Prieta, California, earthquake, *Bull. Seism. Soc. Am.*, 81(5): 1518–1539.

Hatanaka, M. (1955). Fundamental Considerations on the Earthquake Resistant Properties of the Earth Dam. Part I On the Vibration of Earth Dam. *Bulletins-Disaster Prevention Research Institute, Kyoto University*, 11, 1-22.

Hayati, H. and Moss, R. E. S. (2017). Site response analysis considering strain compatible site period. *Soil Dynamics and Earthquake Engineering*, 92: 551-560.

Hudson, M. B., Idriss, I. M., and Beikae, M. (1994). QUAD4M: User's manual for a computer program to evaluate the seismic response of soil structures using finite-element procedures and incorporating a compliant base. *Center for Geotechnical Modeling*, University of California, Davis.

Hudson, M. B., Idriss, I. M., and Beikae, M. (2003). QUAD4MU: Addendum to user's manual for QUAD4M for updates to the QUAD4MU version. March 4, 2003.

Idriss, I. M. (2014). An NGA-West2 empirical model for estimating the horizontal spectral values generated by shallow crustal earthquakes, *Earthq. Spectra*, 30(3): 1155–1177.

Idriss, I. M., Lysmer, J., Hwang, R., and Seed, H. B. (1973) QUAD4: A computer program for evaluating the seismic response of soil structures by variable damping finite-element procedures. *Earthquake Engineering Research Institute*, University of California, Berkeley, Report 73-16.

Itasca Consulting Group, Inc. (2016) FLAC – Fast Lagrangian Analysis of Continua, Ver. 8.0. Minneapolis: Itasca.

Jibson, R. W. (2007). Regression models for estimating coseismic landslide displacement. *Engineering Geology*, 91: 209-218.

Kottke, A. R. and Rathje, E. M. (2008). Technical Manual for Strata, *PEER Report No. 2008/10*, Pacific Earthquake Engineering Research Center, University of California, Berkeley, CA.

Kramer, S. L. (1996). *Geotechnical earthquake engineering.* Upper Saddle River, N.J: Prentice Hall.

Kramer, S. L. and Lindwall, N. W. (2004). Dimensionality and Directionality Effects in Newmark Sliding Block Analyses, *J. Geotech. Geoenviron. Eng.*, 130(3): 303-315.

Kramer, S. L. and Smith, M. W. (1997). Modified Newmark model for seismic displacements of compliant slopes. *J. Geotech. Geoenviron. Eng.,* 123: 635-644.

Lysmer, J. and Kuhlemeyer, R. L. (1969). Finite dynamic model for infinite media. *Journal of the Engineering Mechanics Division, Proceedings of the American Society of Civil Engineers*. EM4: 859-877.

Makdisi, F. I., Chang, C. Y., Wang, Z. L., and Mok, C. M. (1991). Analysis of the recorded response of Lexington Dam during various levels of ground shaking. *Proceedings of Strong Motion Instrumentation Program (SMIP) 1991 Seminar on Seismological and Engineering Implications of Recent Strong-Motion Data*, Sacramento, CA.

Makdisi, F. I. and Seed, H. B. (1977). A simplified procedure for estimating earthquake-induced deformations in dams and embankments. *Earthquake Engineering Research Center,* Report No. UCB/EERC-77/19.

Makdisi, F. I. and Seed, H. B. (1978). Simplified procedure for estimating dam and embankment earthquake-induced deformations. *J. Geotech. Geoenviron. Eng.*, 104(7): 849-867.

Mejia, L. H., Sun, J. I., Salah-mars, S., Moriwaki, Y., and Beikae, M. (1992). Nonlinear dynamic response analysis of Lexington Dam. *Proceedings of Strong Motion Instrumentation Program (SMIP) 1992 Seminar on Seismological and Engineering Implications of Recent Strong-Motion Data*, Sacramento, CA.

Mejia, L., Wu, J., Newman, E., and Mooers, M. (2014). Seismic Stability Evaluation of Dam Underlain by Coarse-Grained Alluvium. *Proceedings of United States Society on Dams (USSD) Annual Meeting and Conference*, San Francisco, California.

Newmark, N. M. (1965). Effects of Earthquakes on Dams and Embankments, *Géotechnique*, 15(2): 139-160.

Öner, M. and Erdik, M. (1981). Dynamic Properties of Embankment Dams, *International Conference on Recent Advances in Geotechnical Earthquake Engineering and Soil Dynamics*, 15.

Park, D. S. and Kishida, T. (2019). Seismic response of embankment dams based on recorded strong-motion data in Japan. *Earthq. Spectra*, 35(2): 955-976.

Phalen, J. and Wagner, N. (2017). Seismic Deformation Fragility Analysis of an Embankment Dam for a Probabilistic Risk Assessment. SAGE Engineers. *UC Berkeley GeoSystems Wednesday Seminars*, March 8, 2017.

Rathje, E. M. and Antonakos, G. (2011). A unified model for predicting earthquake-induced sliding displacements of rigid and flexible slopes. *Eng. Geol*., 122: 51-60.

Rathje, E. M. and Bray, J. D. (2000). Nonlinear coupled seismic sliding analysis of earth structures. *J. Geotech. Geoenviron. Eng.*, 126(11): 1002-1014.

Rathje, E. M. and Saygili, G. (2009). Probabilistic assessment of earthquake-induced sliding displacements of natural slopes. *Bull. of the New Zealand Society for Earthquake Engineering,* 42(1): 18-27.

Sawada, Y. and Takahashi, T. (1975). Study on the material properties and the earthquake behaviors of rockfill dam. *Proceedings of 4th Japan Earthquake Engineering Symposium*, pp. 695-702.

Saygili, G. and Rathje, E. M. (2008). Empirical predictive models for earthquake-induced sliding displacements of slopes. *J. Geotech. Geoenviron. Eng.*, 134(6): 790-803.

Seed, H. B. and Idriss, I. M. (1970). Soil Moduli and Damping Factors for Dynamic Response Analyses, Report No. EERC 70-10, University of California, Berkeley, California, December.

Sirles, P. C. (1988a). Shear wave velocity measurements before and after dynamic compaction of cohesionless soil deposits. *58th Ann. Internat. Mtg., Soc. Expl. Geophys., Expanded Abstracts.*

Sirles, P. C. (1988b). Shear wave velocity measurements in embankment dams. *U.S. Bureau of Reclamation*.

Spencer, E. (1967). A method of analysis of embankments assuming parallel inter-slice forces. *Géotechnique*, 17(1): 11-26.

Steidl, J. H., Archuleta, R. J., and Hartzell, S. H. (1991), Rupture history of the 1989 Loma Prieta, California, Earthquake, *Bull. Seism. Soc. Am.*, 81(5): 1573–1602.

Strenk, P. M. (2010). Evaluation of Analytical Procedures for Estimating Seismically Induced Permanent Deformations in Slopes, *Ph. D. dissertation*, Drexel University.

Sykora, D. W. (1987). Creation of a Data Base of Seismic Shear Wave Velocities for Correlation Analysis, *US Army Corps of Engineers*.

TERRA / GeoPentech (2012). Seismic stability evaluation of Stevens Creek Dam. Prepared for Santa Clara Valley Water District. *Consulting Report*. Report No. SC-3.

Tokimatsu, K. and Seed, H. B. (1987). Evaluation of Settlements in Sands Due to Earthquake Shaking. *J. Geotech. Geoenviron. Eng.*, 113(8).

Travasarou, T. (2003). Optimal ground motion intensity measures for probabilistic assessment of seismic slope displacements, *Ph. D. dissertation*, University of California, Berkeley.

URS Corporation (2006). Dynamic stability analysis of Estates Dam. Prepared for East Bay Municipal Utility District. *Consulting Report*.

US Army Corps of Engineers (2017). National Inventory of Dams.

Vucetic, M. and Dobry, R. (1991). Effect of soil plasticity on cyclic response, *J. Geotech. Eng.*, 117(1): 89-107.

Wald, D. J., Helmberger, D. V., and Heaton, T. H. (1991). Rupture model of the 1989 Loma Prieta earthquake from the inversion of strong-motion and broadband teleseismic data. *Bulletin of the Seismological Society of America*, 81(5): 1540–1572.

Watson-Lamprey, J. (2007). Selection and Scaling of Ground Motion Time Series, *Ph. D. dissertation*, University of California, Berkeley.

Watson-Lamprey, J. and Abrahamson, N. (2006). Selection of ground motion time series and limits on scaling. *Soil Dynamics and Earthquake Engineering*, 26: 477-482.

Yee, E., Stewart, J. P., and Tokimatsu, K. (2013). Elastic and Large-Strain Nonlinear Seismic Site Response from Analysis of Vertical Array Recordings, *J. Geotech. Geoenviron. Eng.*, 139(10): 1789-1801.

Yu, L., Kong, X., and Xu, B. (2012). Seismic Response Characteristics of Earth and Rockfill Dams. *Proceedings of the 15th World Conference on Earthquake Engineering*, Lisbon, Portugal. Paper ID 2563.

APPENDIX A SENSITIVITY ANALYSES

A.1 Poisson's Ratio of Foundation

The dynamic analyses of the representative dams utilized a Poisson's ratio of 0.3 for the foundation material. The foundation material is below the phreatic surface, and is, therefore, more accurately modeled with a Poisson's ratio of 0.47, reflective of a condition near saturation. A sensitivity analysis was performed where the Poisson's ratio for the foundation was changed to 0.47. The sensitivity analysis was run using the representative dam with a height of 100 *ft* and the medium shear-wave velocity profile (representative dam number 8). Dynamic analyses were completed for a subset of 30 ground motions from the original 950 ground motions. The 30 ground motions span the range of intensities of the full set of 950 ground motions.

The results of the dynamic analysis were evaluated in terms of the difference in the dam response as well as the computed deformations. A transfer function was computed for the potential deep failure surface. The first-mode period (where the transfer function is centered) and the peak amplification factor (the maximum amplification ratio) were computed for each transfer function. These values are compared to the base case for the same 30 ground motions in Figure A.1. A comparison of the full transfer function for one of the ground motions is presented in Figure A.2. Newmark deformations were also computed for the potential deep failure surface using yield coefficients ranging from 0.05 – 0.30. The resulting deformations are compared to the base case for the same ground motions and yield coefficients in Figure A.3. The results indicate that the change from a Poisson's ratio of 0.3 to 0.47 for the foundation material has a negligible effect on the dynamic analyses.

A.2 Weathered Rock Zone

The representative dams were modeled with a foundation zone that has a shear-wave velocity of 3200 *ft/s*. The foundations for many dams are comprised of a weathered rock zone sitting atop a more intact rock material. A sensitivity analysis was performed where the top 15 *ft* of the foundation was modeled as a weathered rock zone with a shear-wave velocity of 2000 *ft/s*, and the shear-wave velocity of the deeper foundation was kept at 3200 *ft/s*. The sensitivity analysis was run using representative dam number 8 and the same 30 ground motions used in the previous sensitivity analysis.

The transfer functions for the potential deep failure surface are compared to the base case via their first-mode period, T_1, and peak amplification factor, A_1 in Figure A.4. Newmark deformations are compared to the base case for the same ground motions and yield coefficients

ranging from 0.05 – 0.30 in Figure A.5. The results indicate that the change from a foundation with a single shear-wave velocity of 3200 *ft/s* to a foundation that includes a weathered rock zone has a negligible effect on the dynamic analyses. Note that this sensitivity analysis is limited to changing the shear-wave velocity of the upper 15 *ft* of the foundation zone, and does not include changing the shear-modulus reduction and material damping curves for the foundation.

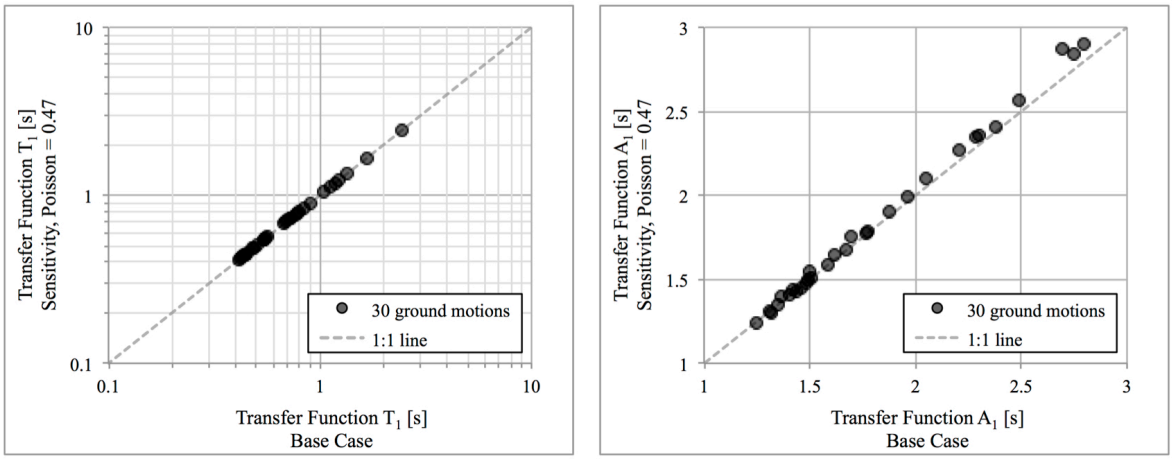

Figure A.1 **First-mode period and peak amplification factor of transfer functions for deep failure surface from dynamic analyses run for the base case and the sensitivity with a Poisson's ratio = 0.47 for the foundation zone.**

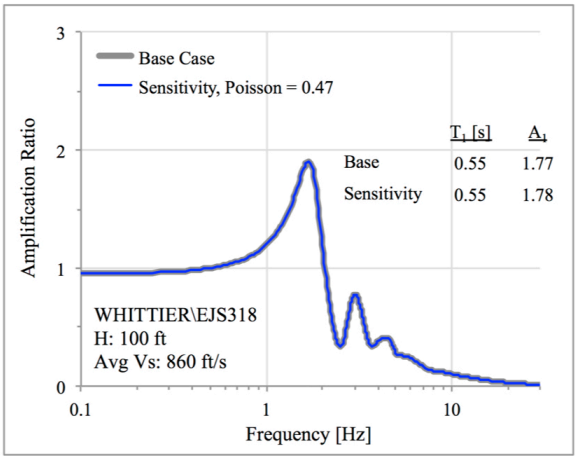

Figure A.2 **Example transfer functions for deep failure surface from dynamic analyses run for the base case and the sensitivity with a Poisson's ratio = 0.47 for the foundation zone.**

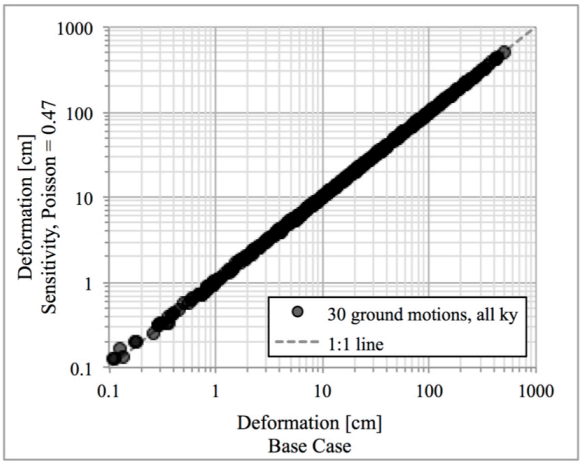

Figure A.3 **Comparison of Newmark deformations computed for the base case and the sensitivity with a Poisson's ratio = 0.47 for the foundation zone.**

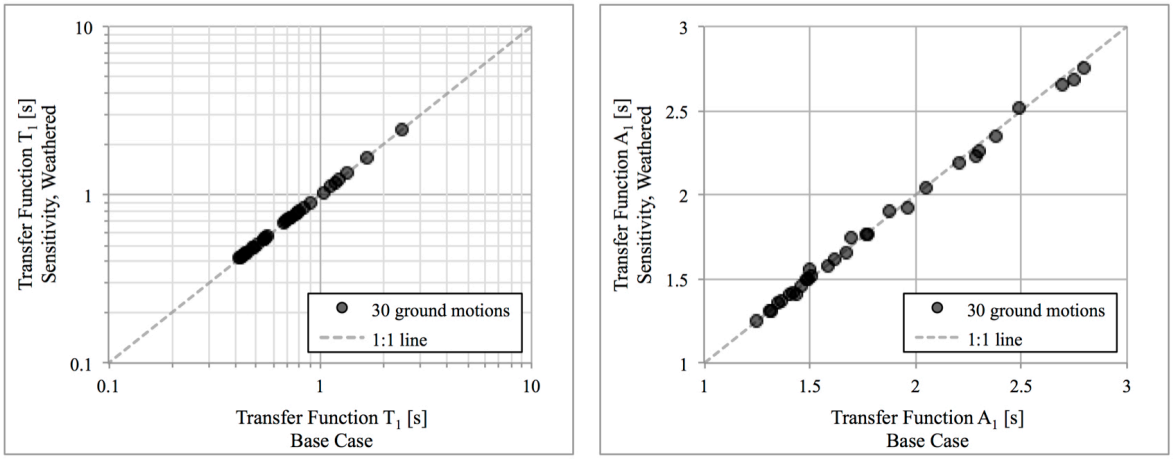

Figure A.4 **First-mode period and peak amplification factor of transfer functions for deep failure surface from dynamic analyses run for the base case and the sensitivity with a weathered rock zone.**

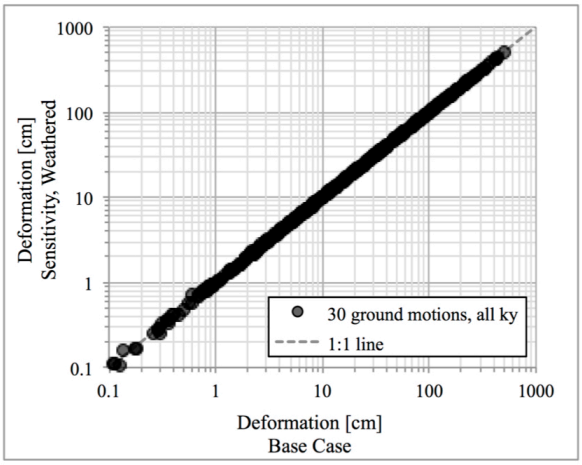

Figure A.5 **Comparison of Newmark deformations computed for the base case and the sensitivity with a weathered rock zone.**